THE UNIVERSITY OF TEXAS AT AUSTIN
CENTER FOR TRANSPORTATION RESEARCH

TECHNICAL REPORT 0-7041-1
TxDOT PROJECT NUMBER 0-7041

Development of NextGen Texas Bridge Decks

Hwa-Ching Wang
Aidan Reed
Christian Galvin
Dylan Gentry
Jongkwon Choi
Zach Webb
Juan Murcia-Delso
Elias Saqan
Oguzhan Bayrak

May 2024

Published January 2025

https://library.ctr.utexas.edu/ctr-publications/0-7041-1.pdf

Technical Report Documentation Page

1. Report No. FHWA/TX-25/0-7041-1	2. Government Accession No.	3. Recipient's Catalog No.
4. Title and Subtitle Development of NextGen Texas Bridge Decks		5. Report Date Submitted: May 2024
		6. Performing Organization Code
7. Author(s) Hwa-Ching Wang, Aidan Reed, Christian Galvin, Dylan Gentry, Jongkwon Choi, Zach Webb, Juan Murcia-Delso, Elias Saqan, Oguzhan Bayrak		8. Performing Organization Report No. 0-7041
9. Performing Organization Name and Address Center for Transportation Research The University of Texas at Austin 3925 W. Braker Lane, 4th Floor Austin, TX 78759		10. Work Unit No. (TRAIS) 11. Contract or Grant No. 0-7041
12. Sponsoring Agency Name and Address Texas Department of Transportation Research and Technology Implementation Division 125 E. 11th Street Austin, TX 78701		13. Type of Report and Period Covered Technical Report September 2020 – May 2024 14. Sponsoring Agency Code
15. Supplementary Notes Project performed in cooperation with the Texas Department of Transportation and the Federal Highway Administration.		

16. Abstract

Project 0-7041 represents a significant endeavor aimed at developing the NextGen Texas Bridge Deck system. Utilizing panel pairs reinforced with wire trusses, the need of bracket-supported deck overhangs is expected to be eliminated, which will reduce construction time and effort. Through a comprehensive research approach encompassing experimental testing and advanced analysis techniques, the project sought to evaluate the feasibility and performance of this innovative bridge construction method. Experimental tests conducted on wire truss partial-depth panels provided valuable insights into structural behavior under various loading conditions, revealing a ductile load response and highlighting the influence of wire truss span on overhang deflections. Full-scale bridge deck tests demonstrated the feasibility of implementing the system and the confidence about the strength/serviceability. Furthermore, fatigue testing elucidated the system's endurance under cyclic loading, informing recommendations for reinforcement strategies and material selection. The culmination of these efforts resulted in a set of design recommendations and guidelines offering practical insights for implementing the NextGen Texas Bridge Deck system in accordance with TxDOT standards. These recommendations cover wire truss spacing, reinforcement details, panel dimensions, and construction considerations, providing engineers with valuable tools to streamline bridge construction processes and enhance overall project efficiency. Moving forward, the findings and recommendations from Project 0-7041 have the potential to transform bridge construction practices in Texas and beyond, offering a viable alternative to traditional methods and paving the way for safer, more efficient, and resilient transportation networks.

17. Key Words Accelerated bridge construction, Bridge Engineering, Bridge decks, Wire trusses, Precast concrete, Fatigue tests	18. Distribution Statement No restrictions. This document is available to the public through the National Technical Information Service, Alexandria, Virginia 22312; www.ntis.gov.

19. Security Classif. (of report) Unclassified	20. Security Classif. (of this page) Unclassified	21. No. of pages 206	22. Price

Form DOT F 1700.7 (8-72) Reproduction of completed page authorized

THE UNIVERSITY OF TEXAS AT AUSTIN
CENTER FOR TRANSPORTATION RESEARCH

Development of NextGen Texas Bridge Decks

Hwa-Ching Wang
Aidan Reed
Christian Galvin
Dylan Gentry
Jongkwon Choi
Zach Webb
Juan Murcia-Delso
Elias Saqan
Oguzhan Bayrak

CTR Technical Report:	0-7041-1
Report Date:	Submitted: May 2024
Project:	0-7041
Project Title:	Development of NextGen Texas Bridge Decks
Sponsoring Agency:	Texas Department of Transportation
Performing Agency:	Center for Transportation Research at The University of Texas at Austin

Project performed in cooperation with the Texas Department of Transportation and the Federal Highway Administration.

Center for Transportation Research
The University of Texas at Austin
3925 W. Braker Lane, 4th floor
Austin, TX 78759

http://ctr.utexas.edu/

Disclaimers

Author's Disclaimer: The contents of this report reflect the views of the authors, who are responsible for the facts and the accuracy of the data presented herein. The contents do not necessarily reflect the official view or policies of the Federal Highway Administration or the Texas Department of Transportation (TxDOT). This report does not constitute a standard, specification, or regulation.

Patent Disclaimer: There was no invention or discovery conceived or first actually reduced to practice in the course of or under this contract, including any art, method, process, machine manufacture, design or composition of matter, or any new useful improvement thereof, or any variety of plant, which is or may be patentable under the patent laws of the United States of America or any foreign country.

Engineering Disclaimer

NOT INTENDED FOR CONSTRUCTION, BIDDING, OR PERMIT PURPOSES.

Project Engineer: Oguzhan Bayrak
Professional Engineer License State and Number: Texas No. 106598
P.E. Designation: Research Supervisor

Acknowledgments

The authors express deep appreciation to the Texas Department of Transportation (TxDOT) for providing the funds and support to conduct this research study. The contributions of the project manager Martin Dassi (RTI Division) and other members of the Project Monitoring Committee – Ahmed Al-Basha, Jason Tucker, Joe Roche, Jorge Carrasco, Leon Flournoy, Rachel Larcom, and Taya Retterer – facilitated great improvements to the outcome of this project.

Table of Contents

List of Tables

List of Figures

Chapter 1. Background

1.1. Overview

The construction of bridges plays a pivotal role in infrastructure development, connecting communities, and facilitating economic growth. In recent years, there has been a growing emphasis on enhancing the safety and efficiency of bridge construction processes. One innovative approach being explored by the Texas Department of Transportation (TxDOT) involves the use of full-width precast partial-depth panels as a means to streamline deck construction. This project explores the feasibility associated with implementation of this NextGen Texas bridge deck system.

Traditional Bridge Deck Construction

In conventional bridge deck construction in Texas, the process typically involves the use of precast partial-depth panels that span between bridge girders, serving as bottom forms [Figure 1-1(a)]. This approach is effective in many aspects, but it encounters challenges when it comes to deck overhangs that extend outside the first girders on each side of the bridge. This situation necessitates extra forming and bracing, leading to a considerable amount of fieldwork [Figure 1-1(b)], which can slow down the construction process. In some cases, these challenges can even offset the advantages gained from using precast partial-depth panels.

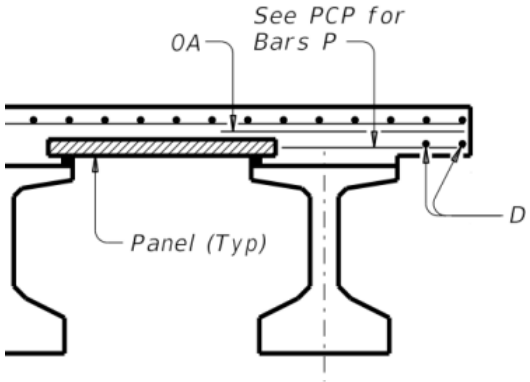

(a) Typical detailing (TxDOT standard)

(b) Brackets and supporting formwork (Clifton and Bayrak, 2008)

Figure 1-1 TxDOT Typical precast panel decks and cast-in-place overhang

Taking Inspiration from Spain

The NextGen Texas bridge deck system draws inspiration from Spanish bridge deck construction techniques. In Spain, full-width precast partial-depth panels connected by lattice girders have been successfully installed (see Figure 1-2). What sets this approach apart is that, instead of dealing with extra forming for deck overhangs, the precast partial-depth panels span across the entire width of the bridge deck. This innovative design eliminates the need for additional forming and bracing, significantly simplifying the construction process.

Figure 1-2 Bridge deck system in Spain (courtesy of Dr. David Fernández-Ordóñez)

Key Advantages

Simplified Construction: The implementation of partial-depth deck panels spanning the entire width of the bridge deck simplifies the construction process, reducing the need for extensive fieldwork and additional formwork.

Cost Reduction: By eliminating the requirement for extra forming and bracing, the deck system can potentially reduce construction costs, making infrastructure projects more financially feasible.

Accelerated Project Delivery: Streamlining the construction process not only reduces costs, but also accelerates project delivery. Faster completion means reduced disruption to communities and faster access to improved transportation routes.

Research Initiative

To bring this innovative bridge deck system to fruition, TxDOT has embarked on a comprehensive research initiative (TxDOT 0-7041). This study aims to develop a NextGen Texas bridge deck system that utilizes full-width precast partial-depth panels. The research project includes a thorough experimental investigation into the behavior of these panels and a full-scale bridge deck system. Non-linear finite element analysis is included to ensure structural integrity and safety.

The NextGen Texas bridge deck system represents a promising step forward in bridge construction technology. By drawing inspiration from successful international practices, TxDOT is exploring innovative ways to streamline construction processes, reduce costs, and accelerate project delivery. As research and development efforts continue, the potential benefits of this approach are becoming increasingly apparent. The future of bridge construction in Texas may well be defined by the efficient and cost-effective NextGen Texas bridge deck system.

1.2. Project Objectives

Establish a Comprehensive Standard Design: Develop a standard design for Texas that outlines the utilization of full-width partial-depth deck panels, covering the entire width of the bridge superstructure. This standard will serve as a foundational guide for future bridge construction projects.

Experimental Validation: Conduct a rigorous series of large-scale and full-scale tests to comprehensively evaluate the behavior of full-width partial-depth panels under construction loads. This validation process will encompass several critical aspects:

- Construction Procedure: Examine the behavior of wire trussed full-width partial-depth panels under construction loads, especially regarding the overhang design and analysis.
- Serviceability Performance Assessment: Assess the performance of the full-scale bridge decks under expected service loads, ensuring they meet structural and functional requirements.
- Ultimate Strength Evaluation: Determine the ultimate strength characteristics of the NextGen bridge deck system to ensure it can withstand extreme loads and conditions.
- Fatigue Strength Analysis: Investigate the fatigue strength of the bridge deck system to gauge its long-term durability and resilience against cyclic stresses.
- Feasibility Demonstration: Verify the feasibility of the NextGen bridge deck system through real-world testing, providing evidence of its practicality and efficacy.
- Comparative Analysis: Conduct a direct and thorough comparison between the existing deck system and the NextGen bridge decks, highlighting the advantages and improvements offered by the latter.

Nonlinear Finite Element Analysis: Complement the experimental program with advanced nonlinear finite element analysis. This computational approach will provide in-depth insights into modeling techniques for the NextGen bridge deck system under various loading scenarios.

Provide Comprehensive Design Guidelines: Develop comprehensive design guidelines that incorporate the optimized design details. These guidelines will offer practical recommendations and best practices for engineers and practitioners involved in future bridge construction projects, promoting the widespread adoption of the NextGen bridge deck system.

1.3. Organization of the Report

This report is structured to systematically present the objectives, significance, and innovative aspects of the research on NextGen bridge deck, including eight chapter as follows:

Chapter 1: Introduction

- Provides an overview of the research objectives, significance, and the need for innovation in bridge deck construction.
- Outlines the structure and organization of the report.

Chapter 2: Literature Review

- Offers a comprehensive review of existing literature, including the current Texas bridge deck system design.
- Compares and contrasts the Texas bridge deck system with the successful Spanish bridge deck system.
- Highlights key findings from previous research and identifies gaps that this study aims to address.

Chapter 3: Partial-Depth Precast Panel Pairs

- Introduces the experimental program designed to evaluate the behavior of full-width partial-depth panel pairs.
- Describes the methodology, instrumentation, and data collection procedures used in the experiments.
- Presents test results, data analysis, and design methods that support the feasibility of using full-width partial-depth panels.

Chapter 4: Full-Scale Bridge Deck Structural Test

- Presents the full-scale bridge deck test conducted to assess the performance of the developed NextGen deck system.
- Provides detailed insights into the testing procedures, results, and their implications.
- Analyzes the results of experiments related to the serviceability performance and ultimate strength of the NextGen deck system.

Chapter 5: Investigation into Fatigue Behavior

- Examines the results of an experimental investigation focused on the fatigue behavior of NextGen deck strips.
- Discusses the implications of the findings in terms of the long-term durability and reliability of the NextGen deck system.

Chapter 6: Design Recommendations

- Summarizes the key findings of the study.
- Demonstrates the design guidelines and procedures developed based on the research findings.
- Offers practical recommendations for engineers and practitioners to implement the NextGen deck system effectively.

Chapter 7: Conclusion

- Summarizes the project.
- Highlights the significance of the research in advancing bridge construction technology.
- Provides future work recommendations.

Chapter 8: Value of Research

- Summarizes the key contributions of the study.
- Discusses the impact of implementing the NextGen Texas bridge decks.

Chapter 2. Literature Review

2.1. Behavior of Bridge Decks

In this section, research studies contributing to the understanding of bridge-deck behavior are summarized. Studies pertaining to the punching-shear capacity of bridge slabs and the effects of arching action on slab capacity are discussed.

In 1952, Ockleston tested a three-story, reinforced concrete building in Johannesburg, loading the flat plate slabs of various sizes to failure. This early research program examined the failure loads and failure mechanisms of slabs, finding that the tested capacities exceeded predictions based on plastic analysis. Several explanations for this were considered. Ockleston stated that although the measured and predicted capacities did not agree, the observed cracking patterns and slab deflections agreed well with the predicted collapse mechanisms. Ockleston believed that the discrepancy between observed and predicted capacities could be accounted for by the effects of compressive membrane action (also referred to as "arching action"), but he could not predict the extent to which this would increase slab capacity. In 1963, Christiansen published a detailed theory of the mechanics of arching action that could be used to predict the magnitude of membrane stresses and the effects of these stresses on slab capacity. The phenomenon of arching action refers to in-plane forces generated after the flexural cracking of laterally restrained slabs. Once flexural cracking occurs, a compression field emanating from the load point spreads to the supports (see Figure 2-1). Equilibrium is maintained by a tension hoop around the compression field, as well as by bottom reinforcement in the slab that acts as tension ties.

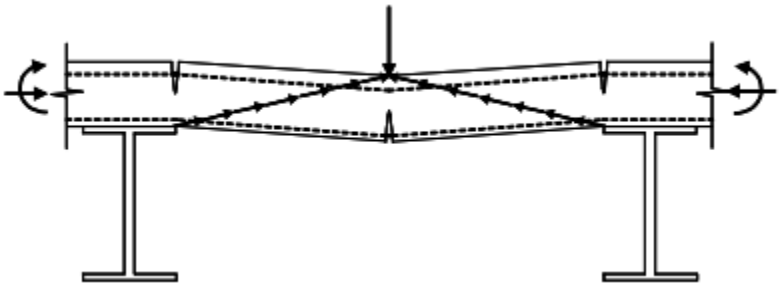

Figure 2-1 Arching action

The extent of arching action depends on several factors, including lateral restraint of the supports, material properties, and slab thickness. Full lateral restraint of the supports is not necessary to develop in-plane forces, as continuous deck slabs on girders can exhibit arching action. Slab thickness and plan extent must be sufficient, however. In the 1960s, the Ontario Ministry of Transportation and Communications sponsored a series of tests on bridge slabs performed at Queen's University in Kingston, Ontario. These tests focused on the presence of compressive membrane action in bridge slabs, the resulting increase in the flexural capacity of those slabs, and their consequent reserve strength. In the 1970s, Batchelor and Hewitt published several articles

discussing these studies, with several additional authors building on their findings in later publications. Those articles are discussed here as follows:

Batchelor and Hewitt (1976)

To develop a method to predict bridge slabs' ultimate out-of-plane flexural capacity, Batchelor and Hewitt performed 31 tests on eight 1/8th-scale bridge specimens. Those specimens had different percentages and arrangement of reinforcement, and their decks had different span-to-thickness ratios. The test specimens were modeled after two prototype bridge slabs, 80-ft long and 7-in. thick, designed for HS-20 and HS-44 loads. Based on these two full-scale designs, eight 4-girder scaled test specimens were fabricated. Indented wire reinforcement with a diameter of 0.0915 in. was used to simulate flexural reinforcement in reinforcement ratios from 0% to 0.6%; nails (3- in. long) simulated shear studs. Four diaphragms were installed in each specimen at slab ends and intervals of 2.5 ft along the girders. The average 14-day compressive strength of the concrete was 5000 psi. Loads were applied to a ½-in. (13-mm) thick, elliptical steel plate, scaled to represent the contact area of tires of large trucks. The loads were applied at midspan between girders in the transverse direction and equidistant between two diaphragms in the longitudinal direction. To study the effects of transverse cracking on punching shear capacity, cracking was deliberately introduced in the deck of one specimen, but the effects of the induced cracks were negligible. With only two exceptions, loaded areas failed in punching shear. For all tests, the average capacity was approximately 16 kips per load point, 22 times the scaled AASHTO HS-20 truck load. Results from that test program indicated that the location of the tested panel in the specimen and the magnitude of dead-load stresses had little to no influence on the capacity. They also showed that punching-shear capacity decreased with decreasing percentage of flexural reinforcement. However, the punching-shear capacity of an unreinforced test section was still ten times the HS-20 design load. Because these bridge decks designed for flexure actually failed in punching shear at loads far greater than predicted, Batchelor and Hewitt asserted that AASHTO LRFD flexural-design provisions were excessively conservative, and the arching action would, in general, increase flexural capacity enough to make punching shear the controlling failure mechanism. They advocated using only 0.2% isotropic reinforcement placed at the center of the slab, as required by AASHTO LRFD provisions for temperature and shrinkage reinforcement.

Arching Action and the Ontario Design Method

Under the auspices of the Ontario Ministry of Transportation, Csagoly, Holowka, and Dorton (1978) sought to verify the high reserve strength predicted by Batchelor and Hewitt by testing in-service bridges in the Province of Ontario. Csagoly et al. agreed with Batchelor and Hewitt that arching action increased the flexural capacity of slabs, causing their failure to be governed by punching shear rather than flexure. They also agreed that bridge slabs could be adequately reinforced using only 0.3% isotropic reinforcement placed at the mid-depth of the slab. To verify the results of Batchelor and Hewitt, Csagoly et al. field-tested 40 existing bridge decks in the Province of Ontario, Canada. Based on the results of those field tests and additional tests by Dorton, Holowka, and King (1977) on the Conestogo River Bridge, constructed with 0.3%

isotropic reinforcement, the Ontario Ministry of Transportation developed new design provisions, anticipating vast savings through the significant reduction of flexural reinforcement and a potential increase in service life due to diminished corrosion potential. Some of the subsequent research studies on bridge decks can be regarded as attempts to further investigate the results of Batchelor and Hewitt and the Ontario design method based on those results. In the 1980s, several studies on isotropic bridge decks were performed, and results were published in the early 1990s.

Kuang and Morley (1992)

While arching action is generally believed to enhance the flexural capacity of slabs, Kuang and Morley investigated its effect in enhancing punching shear capacity. They conducted tests of the punching-shear capacities of slabs with varied amounts of support restraint. Twelve 1/5th-scale, square slab specimens were supported, and 24 were restrained on all four sides by monolithic edge beams of varying widths and stiffnesses. Specimens were constructed with 1.6%, 1.0%, and 0.3% ratios of flexural reinforcement. Slabs with thicknesses of 2.4 in. and 1.6 in. were constructed, representing 12-in. and 8-in. full-scale decks, respectively. All deck specimens had a clear span of 47 in. in both directions, resulting in span-to-depth ratios of 20 and 30. At 28 days, the concrete compressive strength was 6525 psi. The specimens were supported by pedestals at each corner and were loaded at the center by a square plate measuring 4.7 in. on each side. All specimens failed in punching shear rather than flexure, and Kuang and Morley observed that increased edge restraint resulted in an increase in punching shear capacity for otherwise identical specimens. During testing, lateral bowing of the edge beams was observed, confirming the compressive membrane action and the associated in-plane lateral deformations of the restrained deck. In addition, Kuang and Morley found that as the percentage of isotropic flexural reinforcement was increased from 0.3% to 1.0% and then to 1.6%, punching-shear capacity also increased, though it increased very little from the 1.0% specimen to the 1.6% specimen. This trend indicated to Kuang and Morley that punching-shear capacity did not increase linearly with increasing isotropic flexural reinforcement ratios. Test results confirmed that while slab thickness was an important factor in punching shear strength, increases in slab thickness did not result in proportional increases in punching-shear capacity. All punching-shear capacities exceeded those predicted by ACI provisions.

Azad, Baluch, Mandil, Sharif, and Kareem (1993)

Azad et al. hypothesized that the punching-shear capacity of a cracked slab is diminished if the cracks form a zone of weakness near the point of load application. A test program was developed to examine the punching-shear behavior of slab panels with simulated flaws. Three 3.5-in. deep square panels were constructed on two parallel girders, spaced 39 in. between centerlines. All top reinforcement bars were 0.23 in. in diameter. Bottom reinforcing bars oriented perpendicular to girders were 0.39 in. in diameter, and bars oriented parallel to girders were 0.31 in. in diameter. To introduce crack flaws, a thin-walled conical metallic insert was cast into the panels beneath the point of load application. The inclination angle of the insert varied from 20º to 90º and its height varied from 1.2 in. to 2.5 in. All panels failed in punching shear, and Azad et al. observed trends

between flaw geometry and punching-shear capacity. As the angle of inclination of the flaw increased, the punching shear capacity approached that of a panel with no flaw. For panels with flaws constructed at 90º, punching-shear capacities were similar to that of the panel with no flaw, regardless of the flaw height or diameter. For flaws with diameters smaller than the diameter of the loading plate, punching-shear capacities were similar to that of the panel with no flaw. Most panels failed along the flaw, and punching shear capacity was greatly diminished for panels with flaws that crossed the failure plane. Azad et al. concluded that progressive crack growth influenced slab capacity, and a critical crack-surface orientation with regard to loaded area maximizes the decrease in punching-shear capacity.

Miller, Aktan, and Shahrooz (1994)

Miller at al. tested a three-span skewed reinforced concrete bridge that was to be decommissioned by the Ohio Department of Transportation. Non-destructive and destructive tests were performed on the deck to determine its out-of-plane stiffness as a function of distance from the slab end and also its ultimate capacity. The test bridge had a three-span, skewed, reinforced concrete deck of 18- in. thick. The outer spans were 32 ft long, and the interior span was 40 ft long. Grade 40, 25 No. 9 reinforcing bars were spaced in a 15-in. orthogonal grid on the top mat and a 24-in. orthogonal grid on the bottom mat. The average yield strength of the reinforcement was 48 ksi. The concrete compressive strength of core samples was 7650 psi, and the average splitting strength was 750 psi. To load the bridge to failure, two load plates were anchored with prestressing tendons to bedrock below the bridge. The plates were placed approximately 15 ft from the edge. A flexural shear failure occurred at a total load of 720 kips, approximately 22 times the AASHTO HS-20 design load.

Azad, Baluch, Abbasi, and Kareem (1994)

In 1994, Azad et al. published a discussion of further investigation of the punching-shear capacity of bridge decks. Decks were loaded to failure, and experimental capacities were compared with those predicted by ACI code provisions and the Jiang-Shen model for punching shear (Jiang and Shen 1986). Twelve 2.7-in. thick decks were constructed with two 28-in. wide bays in the transverse direction and a longitudinal dimension of 59 in. Diaphragms were attached at the slab ends. Concrete compressive strength was approximately 3860 psi. The test decks were isotropically reinforced, with varying ratios of flexural reinforcement: four decks had 0.24%, four had 0.54%, and four had 0.98%. For each reinforcement ratio, the specimens were loaded over rectangular areas measuring 3 by 6 in., 4 by 8 in., 4 by 16 in., and 8 by 20 in. All test specimens failed in punching shear, with the failure plane at an inclination between 20º and 35º from the plane of the deck. Azad et al. concluded that the ACI punching shear equation was conservative, predicting capacities between 98% and 58% of the actual failure load. Test specimens with higher percentages of reinforcement had smaller crack widths at similar loads. Increased flexural reinforcement, while beneficial, did not appreciably increase punching shear capacity. Azad et al. also observed that as the area of the loading footprint was increased, the punching shear capacity increased, though not proportionately.

Ebeido and Kennedy (1996)

Ebeido and Kennedy sought to quantify the effects of several factors on ultimate deck capacity, including girder spacing, angle of skew, reinforcement ratio, deck thickness, load position, shear stud connectors, size of longitudinal girders, and size of cross-bracing. While their study was conducted primarily using ABAQUS, seven, 1/8th-scale bridge specimens were constructed to verify the finite-element models. The scaled specimens were constructed with high early-strength concrete and were exaggerated in the vertical direction to accommodate the reinforcement used. Girder spacings varied from 8 in. to 13.25 in., representing full-scale girder spacings of 5.3 ft to 8.3 ft. The slab specimen depths were 2 in. for six of the specimens and 1.5 in. for one of the specimens, corresponding to full-scale depths of 16 in. and 12 in., respectively. Specimens were loaded at multiple locations by a single elliptical plate with major and minor dimensions of 2 in. (52 mm) and 1.4 in. (36 mm), respectively. Based on their analytical and experimental study results, several trends of slab deck behavior were identified: (i) punching-shear capacity increases as girder spacing decreases; (ii) punching-shear capacity decreases as skew angle increases; (iii) punching-shear capacity increases as isotropic flexural reinforcement increases; (iv) punching-shear capacity increases as deck thickness increases; (v) punching-shear capacity increases as load is applied closer to the end diaphragm; and (v) punching-failure capacity is not affected by the presence of cross-bracing. The capacities of test specimens exceeded those predicted by AASHTO, BS-8110, and CEB-FIP punching-shear provisions, and the researchers suggested modifications to the British standard provisions (BS-8110) to account for the effects of skew and the ratio of the longitudinal bending stiffness of a girder to the transverse bending stiffness of the slab.

Youn and Chang (1998)

Youn and Chang studied the effects of static and fatigue loading on bridge decks, varying the location of the applied load. In that study, five 1/3rd scale, 1.5-in. (38-mm) deep decks were reinforced with 0.13-in. (5-mm) diameter reinforcing bars. The average 28-day strength of concrete samples was 3920 psi (27 MPa). In each specimen, one bay with two overhangs was constructed with two I-shaped steel girders. Diaphragms were installed at the slab ends and at the third-points of the test specimen. To determine how load plate proximity to a girder and deck edge affects punching-shear capacity, a series of tests were performed on the specimens of identical layouts. Test results indicated that punching-shear capacity decreased as the loading position moved away from the supports. The authors attributed this decrease to the reduction in compressive in-plane forces (arching action). They also found that the punching-shear capacity of the exterior panel did not differ significantly from that of the interior panel.

Graddy, Kim, Whitt, Burns, and Klingner (2002)

Graddy et al. studied the punching-shear behavior of bridge decks under static and fatigue loads, using full-scale cast-in-place and precast, prestressed panel specimens. Cast-in-place (CIP) test specimens and precast-prestressed panel (PCP) specimens topped with 4 in. of cast-in-place concrete were fabricated and tested. The concrete used for the CIP specimens and the topping of the PCP specimens had an average cylinder strength of 6000 and 5000 psi, respectively. Flexural

capacities were calculated using yield-line analysis, and compressive membrane forces, estimated using finite-element analysis and the results of previous research, were used in calculations of flexural capacity. In addition, predicted AASHTO LRFD and ACI 318-95 punching-shear capacities were calculated for both the predicted and observed failure modes. Graddy et al. found that AASHTO and ACI punching-shear provisions were conservative and could be improved based on the assumed configuration of the punching shear failure surface.

Coselli et. al (2006), Wood et al. (2008)

Research conducted by Coselli et al. provided information on the behavior of bridge decks at expansion joints. Details were developed that have the potential to simplify bridge deck construction, reduce construction costs, and improve worker safety. Although the primary purpose of the study was to evaluate expansion joint performance under design tandem loads, which are representative of the truckloads observed on roads in Texas that carry heavy traffic between the U.S. and Mexico, various slab end details were studied. Full-scale tests of bridge decks demonstrated that a uniform-thickness (8-in.) cast-in-place deck (UTSE) with additional reinforcement at the edge exhibited essentially the same performance as decks with the IBTS detail that is commonly specified for Texas bridges. The IBTS detail consists of a cast-in-place thickened edge in a deck. The interior portion of the deck is generally constructed using precast, prestressed panels and a cast-in-place topping slab. The cast-in-place edge requires extra formwork and poses higher risks for the workers as well as for the traffic beneath if the roadway remains open to traffic during construction. Because the uniform-thickness, cast-in-place deck detail (UTSE) performed well, an alternative construction procedure was studied in which precast panels were placed adjacent to the expansion joint, and the cast-in-place topping slab was added. Once again, the performance was excellent, and the results indicated that temporary formwork could be replaced with the stay-in-place precast panels. Decks designed using this detail are safer to construct and less costly.

Another variable studied by Coselli et al. involved skewed edges. In skewed bridges, the clear span between girders along the edge increases as the skew increases for the same girder spacing. The stresses at the edge also increase. The findings of Coselli et al. indicated that the performance of the two cast-in-place edge details (IBTS and UTSE) was satisfactory for a skew angle of 45 degrees. With skewed edges, however, the option of using precast panels up to the edge is eliminated unless an innovative technique can be developed to permit the use of precast panels that incorporate a skew angle. In a follow-up TxDOT research project (0-5367), skewed panels were development. Skewed panels with skew angles up to 45 degrees were built and tested at the FSEL of UT Austin. In addition, panels with details developed at UT Austin were also fabricated at commercial precast yards and tested at UT Austin. The test results and constructability study conducted at a precast panel fabrication provided justification for including standard skewed panel details in TxDOT standards for slab ends at expansion joints.

2.2. Serviceability of Bridge Decks

In this section, research studies contributing to the understanding of bridge-deck serviceability are summarized.

Krauss and Rogalla (1996)

Krauss and Rogalla summarized the conclusions of their investigation into the transverse deck cracking in NCHRP Report 380. The authors studied transverse cracking with theoretical analyses, field instrumentation, and laboratory research. In a survey sent to all U.S. DOTs, several transportation agencies in Canada, and overseas, Krauss and Rogalla sought to identify the perceived extent of serviceability problems with bridge decks. While more than 100,000 bridges in the United States were reported to have developed transverse cracking, only 62% of the bridge owners considered such cracking problematic; 24% did not consider it a problem, and 14% had no opinion in this regard. Typical acceptable crack widths in locations where deicing chemicals are used ranged between 0 and 0.008 in. Krauss and Rogalla reported that Denmark, Japan, and Switzerland specify a maximum crack width of 0.008 in. for their conventionally reinforced concrete decks. Two U.S. DOTs were found to have maximum crack width specifications. While one of them limits crack widths to a maximum of 0.007 in., the other requires that the maximum length of cracks wider than 0.02 in. be limited to 50 ft. It is important to recognize that the laboratory component of their study was focused on the materials aspect of the problem rather than the structural issues.

Frosch, Blackman, Radabaugh (2003)

After numerous bridges in the state of Indiana were identified with concrete deck cracking, the Indiana Department of Transportation funded a research study at Purdue University. In that study, Frosch et al. investigated bridge-deck cracking in various bridge superstructure systems. Cracking was observed in the negative and positive moment regions of bridge decks on both the top and bottom surfaces and was reported to appear before or shortly after the opening of the structure to live loads. Frosch et al. observed significant crack widths and various degrees of cracking in different bridge decks supported on both concrete and steel girders. The authors attributed transverse deck cracking to restrained shrinkage of the concrete and longitudinal cracking to a combination of factors, including restrained shrinkage and a construction detail involving a steel shelf angle supporting the permanent metal deck forms (PMDF). Based on their experimental and field studies, Frosh et al. recommended that (i) the wet curing time of decks should be increased to 7 days; (ii) shrinkage-reducing admixtures could be used; (iii) concrete mixture designs should be adjusted to minimize shrinkage; (iv) cement content of mixture designs should be reduced; and (v) maximum bar spacing should be limited to 6 in. to limit crack widths to 0.016 in. The researchers further concluded, "*Additional reinforcement above current practice is required to control the crack widths in concrete decks*" (Frosch et al.). More specifically, for Grade 60 reinforcing bars and 4000 psi concrete, the recommended amount of deck steel was 0.63% of the cross-sectional area, which is more than three times the amount required by ACI 318 or AASHTO

LRFD Specifications. Frosch et al. made further recommendations against the use of PMDF and for the use of plywood forms.

Shoemaker, Fowler, and Whitney (2002)

Shoemaker et al. investigated the long-term behavior of high-performance concrete bridge decks. The following bridges were monitored during the course of their research study:

Lubbock:

- 82nd St. overpass on US 82/62
- Loop 289 and Frankford St. Bridge
- IH 27 New Deal Bridge

Amarillo:

- FM 1061 overpass on Loop 335
- Amarillo Creek Bridge on Loop 335

Houston:

- SH 249 & Louetta Rd. Bridge

San Angelo:

- US 87 & N. Concho River Bridge

While some of the bridge decks and spans inspected by Shoemaker et al. exhibited no visible cracks at the time of inspection, others were cracked. The typical cracks observed by Shoemaker et al. are shown in Figure 2-2. Those decks were of high-strength concrete. However, similar cracking was observed by the research team members in bridge decks of normal-strength concrete in Austin, Houston, Dallas, and San Antonio. These studies showed that, while some bridge decks in Texas have longitudinal and transverse cracks, these cracks are typically very narrow and do not constitute major serviceability problems.

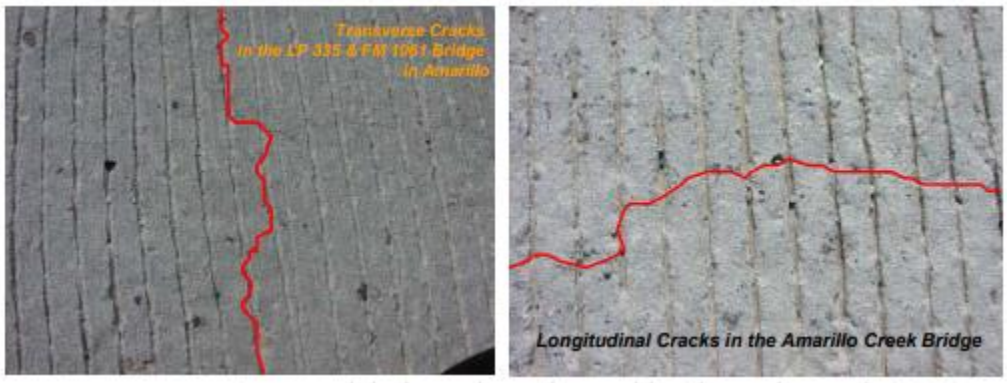

Figure 2-2 Typical deck cracking observed by Shoemaker et al. (2002)

Folliard, Smith, Sellers, Brown and Breen (2003)

In a project titled "Evaluation of Alternative Materials to Control Drying-Shrinkage Cracking in Concrete Bridge Decks," Folliard et al. conducted a "small field investigation," in their own terms,

and comprehensive material testing. After inspecting the Louetta Road Overpass in Houston, Texas, and the Dow Barge Canal Bridge in Freeport, Texas, the researchers identified "concrete materials and mixture proportions as the most critical aspect to prevent transverse drying shrinkage cracks" and, as such, bridge design, detailing and construction methods were not considered. The deck cracking observed by Folliard et al. is exemplified in Figure 2-3. The longitudinal "paired cracks" are roughly positioned over the girders and near the edges of the precast prestressed concrete deck panels.

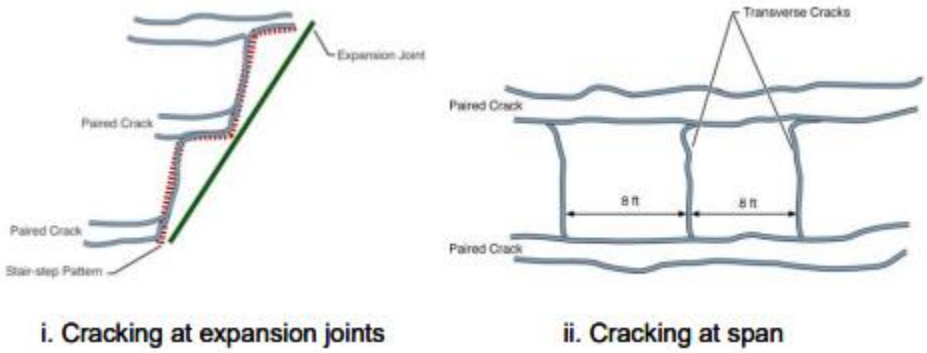

Figure 2-3 Deck cracking observed by Folliard et al. (2003)

The free shrinkage of several "control" mixtures was studied by Folliard et al. (2003), and those mixtures were based on the TxDOT Specification for Class S concrete, typically used for bridge decks. Since restrained drying shrinkage of concrete is the primary cause of the transverse cracking observed in bridge decks, it is interesting to note the maximum shrinkage strains recorded by Folliard et al. While those free-drying shrinkage strains of approximately 0.0005 to 0.0006 in./in. do not directly represent restrained shrinkage strains, they are related to such strains. Free shrinkage strains of 0.0005 to 0.0006 are prevalent for many normal-strength concrete mixtures, including TxDOT Class S mixture.

2.3. Partial- and Full-Depth Panel Systems in Texas

Texas engineers and contractors are familiar with the design and construction of bridge decks utilizing partial-depth precast concrete panels and cast-in-place concrete topping. A majority of bridge construction in Texas employs this method to erect most of the area of the deck between fascia girders. The primary impediment to a full-width deck of this type is the deck overhang. Currently, the normal procedure is to construct the overhang as a monolithic cast-in-place element (as seen in Figure 2-4) using temporary formwork and falsework. The integration of partial-depth panels into the design of the overhang is crucial to the development of the NextGen Bridge Deck. This section reviews the current state of partial-depth deck panel design and investigate the difficulties in extending partial-depth panels to the overhangs.

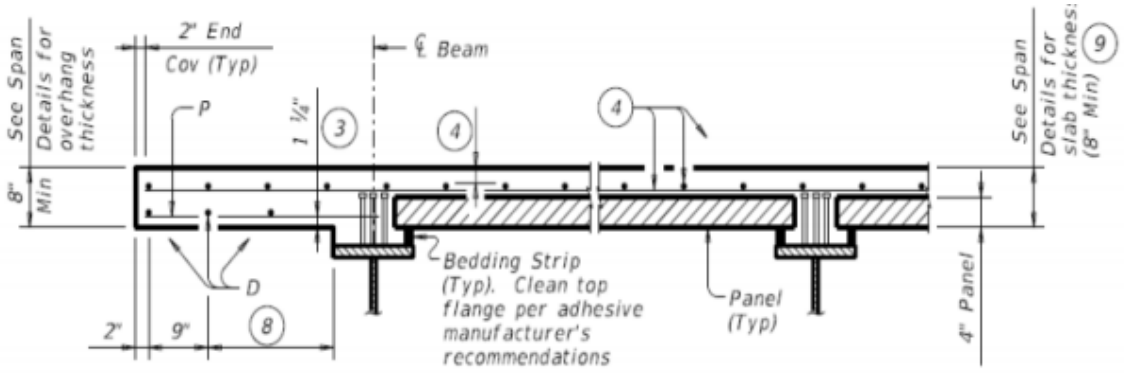

Figure 2-4 Example of typical overhang design (Turco, 2018)

The literature review conducted revealed the following facts about the development of Texas bridge decks with regard to partial-depth panels:

1. The behavior and performance of bridge decks have been well-documented through experimental research and field performance studies. These key concepts were established concerning general bridge deck behavior: (i) The ultimate capacity of bridge decks is typically governed by punching shear. (ii) The strength limit state, in this regard, is less critical than serviceability.

2. TxDOT's current deck details that employ partial-depth deck panels have been developed on the basis of experimental research. Those details have been refined over the years by evaluating the field performance of decks. As an example of this refinement, Foster (2010) determined that current TxDOT standards for longitudinal top mat reinforcement are well optimized; alternatively, welded wire reinforcement or a reduced bar size could be utilized in the transverse direction for sufficient crack control with reduced reinforcement usage. Additionally, Bayrak et al. (2013) accomplished an array of tasks: confirmed the findings of Foster; determined that the initial PCP prestress level could be reduced by 20 ksi; determined that the assumed lump-sum prestress loss could be reduced by 20 ksi; observed that the width and spacing of collinear PCP cracks may be reduced by placement of additional transverse reinforcement near the edge of the panel; developed a new equation for prediction of prestress loss, which takes into account aggregate type and initial prestress level; and established that the Double Punch Test (DPT) is effective and efficient for the performance evaluation of Steel Fiber Reinforced Concrete (SFRC).

3. In recent years, partial-depth deck panel details have been developed to expand the use of panels from expansion joint to expansion joint (i.e., from the beginning of a bridge deck to the end of that deck). Coselli et al. (2006) demonstrated that partial-depth panel decks could be utilized all the way to the expansion joint on non-skewed bridges, exhibiting similar behavior to traditional decks and a strength capacity exceeding design loads. Wood (2008) expanded on the concept and likewise showed that partial depth panels can be used adjacent to the expansion joints for skewed bridges. Furthermore, it was found in this study that the

panels provided outstanding fatigue responses for both skewed and non-skewed shapes. These developments have been embraced by the construction industry since they enhance worker safety and expedite construction.

4. Precast overhang solutions have also been sought over the years. The need for composite action between decks and girders complicates the overhang design for a full-width PCP deck system, as the connection between decks and fascia girders must provide both horizontal and torsional restraint (Culmo, M.P., 2009). TxDOT's current details regarding a precast overhang utilize full-depth panels with shear pockets, developed and tested at Texas A&M University and implemented in some projects with success (Trejo et al. (2011) and Mander et al. 2010). A model of the design is shown in Figure 2-5 and an implementation is shown in Figure 2-6.

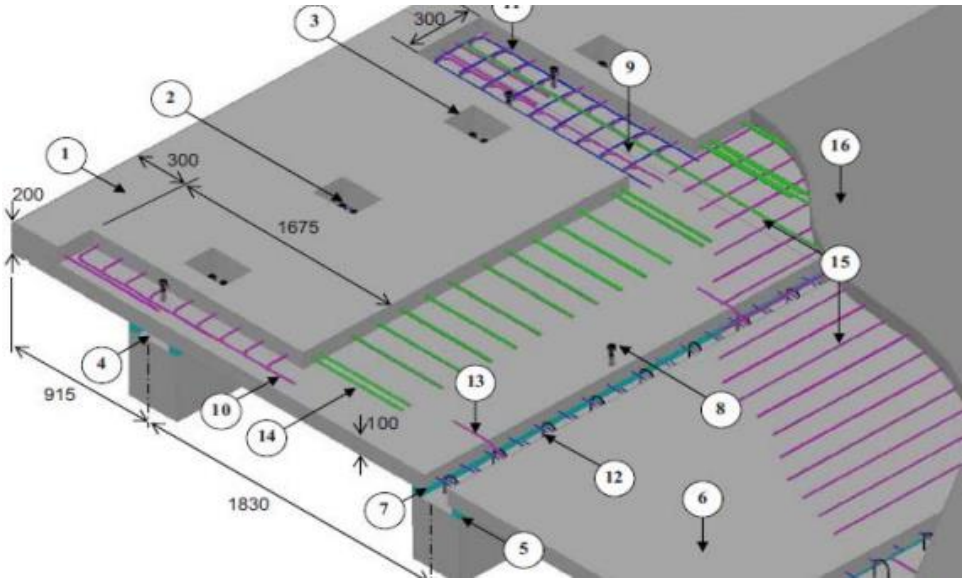

Figure 2-5 Full-depth PCP overhang design with shear pocket (Mander et al., 2010)

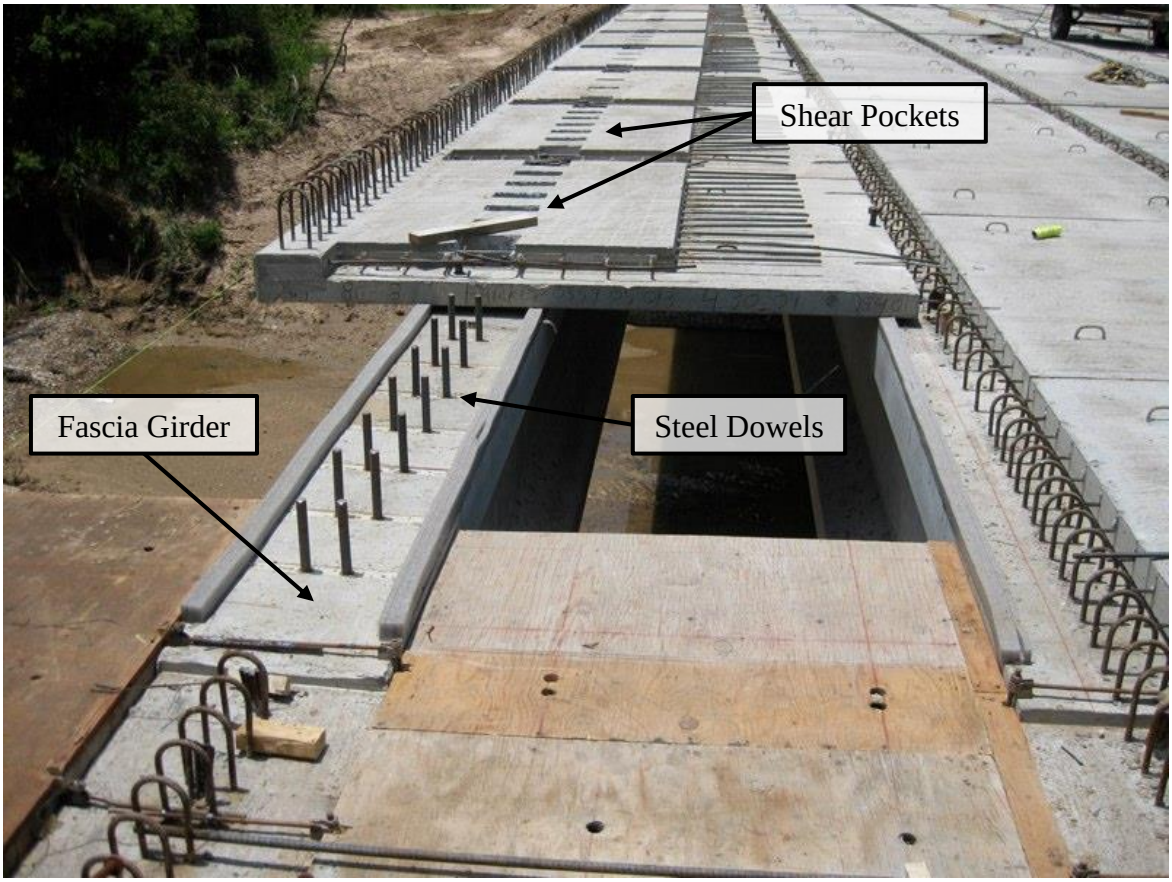

Figure 2-6: Full-depth PCP overhang design with shear pocket (Trejo et al. 2011)

Clifton et al. (2008) devised and constructed a new precast overhang design using partial-depth panels cast compositely with the fascia girder. The overhang, modeled below in Figure 2-7, was load tested and determined to be approximately five to ten times stiffer than the conventional monolithic cast-in-place overhang. The cracking load was found to be roughly double the expected load given by AASHTO LRFD. The novel method was considered to be only a preliminary probe, and various disadvantages were identified as needing further research and review, namely, the construction of a consistent slab edge form, the provision of a space for workers to stand, and general improvements to the efficiency of the system. However, the research team observed a significant potential for a decrease in construction time and material cost, as well as an increase in worker safety, through the use of partial depth precast overhang methods.

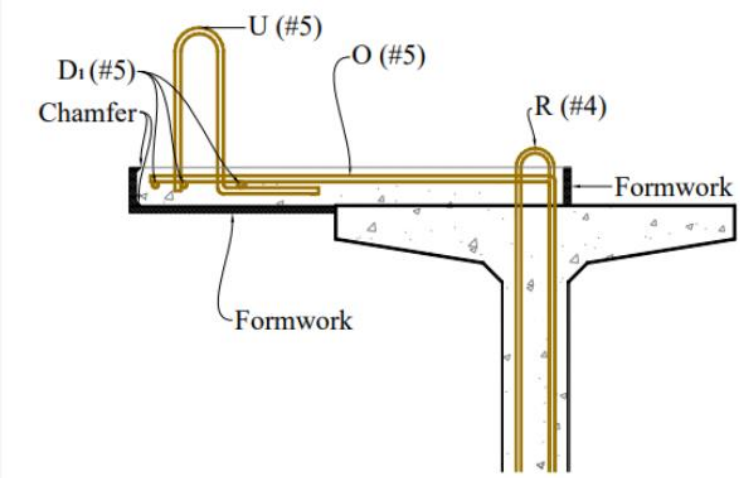

Figure 2-7 Partial-depth precast concrete overhang design before cast-in-place pour (Clifton, 2008)

2.4. Behavior and Characteristics of Lattice Girder Decks

The NextGen Bridge Deck draws inspiration from a particular partial-depth PCP deck system, which is applied in many Spanish bridge decks and various buildings worldwide. This deck design utilizes steel lattice girders (Figure 2-8) as reinforcement with bottom chords embedded in the PCP. Within the Spanish decks that employ this system, the lattice girders are continuous over the fascia girder in order to transfer moment forces during construction before the cast-in-place concrete topping is cured (Figure 2-9). The concrete panels themselves are not continuous over any girder. The lattice girders are enveloped within the cast-in-place topping and act as top mat reinforcement in the transverse direction. Thus, a partial-depth PCP overhang is successfully implemented.

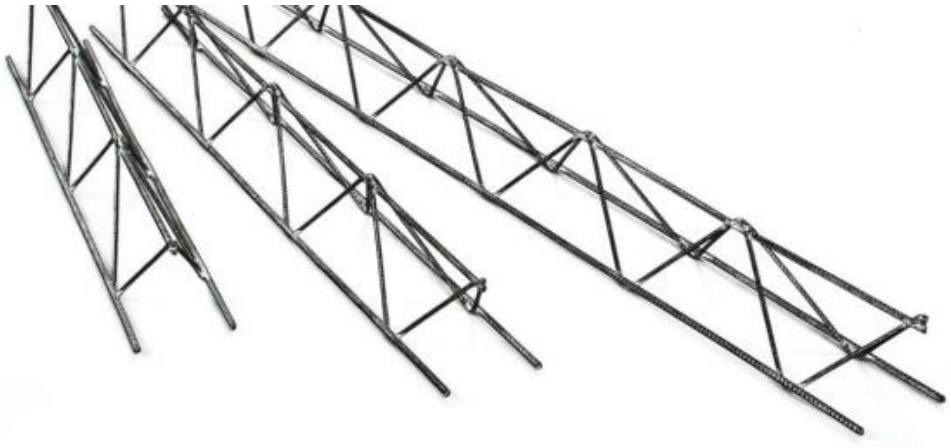

Figure 2-8 Lattice Girders Sidenor, <https://sidenor.gr/en/products-and-solutions/sd-concrete-reinforcing-steel/ilektrosygkollimena-diktyomata/> (June 27, 2020).

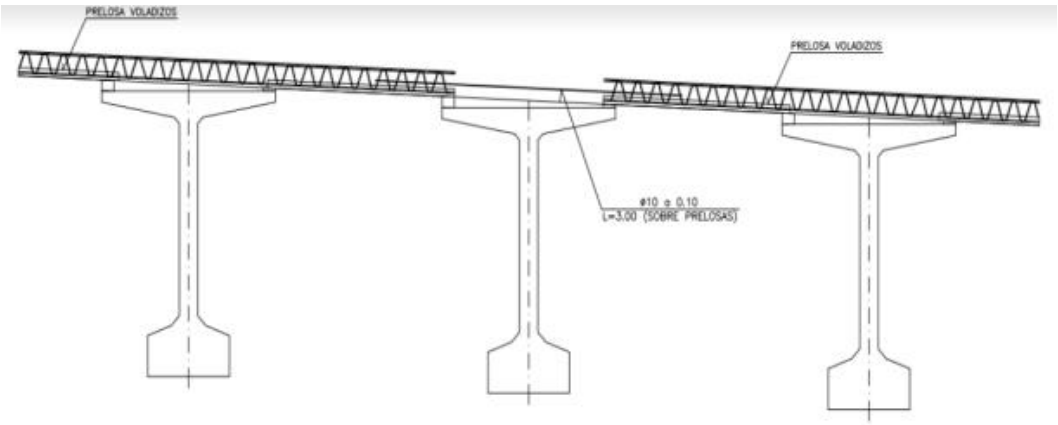

(a)

Figure 2-9 Lattice girders continuous over the fascia girder (a)courtesy of Roads and Bridges LLC, (b) courtesy of Dr. David Fernández-Ordóñez

Newell, S., and Goggins, J. (2019)

Newell, S., and Goggins, J. (2019) tested six lattice girder deck specimens without a cast-in-place topping in order to investigate behavior during building construction and develop an understanding of primary characteristics governing serviceability and ultimate limit states when used as a one-way or two-way building slab. The load testing is pictured below in Figure 2-10. The simply supported planks were loaded under a displacement-controlled actuator while deflections and strains were measured.

Figure 2-10 Load testing of lattice girder deck element (Newell and Goggins, 2019)

Chief findings were as follows: significant stiffness reduction occurs at first cracking when the midspan deflection of the tests reached approximately 1/1000 of the span. After significant cracking occurred, system stiffness was primarily given only by the lattice girder and panel reinforcement. The research team attempted to predict the initial stiffness of the system by transforming the steel sections into equivalent concrete sections. This method was proven valid, but tended to significantly underestimate initial stiffness for planks with relatively low-height girders. Upon initial loading, compressive forces were taken by the top and bottom chord of the lattice girder, as well as the top of the concrete panel and the panel reinforcement. Only the soffit of the panel was subjected to tension. Once the panel began to crack, then tension was shifted to the panel reinforcement and the bottom chord of the girder. Regarding the ultimate limit state, the panels tended to fail via top chord buckling or compression buckling of the diagonal web members. It is noted that planks with shorter lattice girders will likely experience less buckling of web members due to their shorter lengths. Predicted values of buckling load using Eurocode 3, which utilizes Euler's critical load method, were uniformly conservative, producing safety factors of 2.08 to 3.26. All of the specimens reached their assigned serviceability limit state of deflection larger than the span divided by 100 before their ultimate limit state, so it was concluded that serviceability tends to control the design of these types of panels.

Löfgren et al. (2001)

This research study investigated the behavior of partial-depth PCP lattice girder elements in order to refine their design as permanent formwork in cast-in-place concrete construction. Two identical, simply supported elements were subjected to four-point bending until failure (Figure 2-11). The research team used the data to test an analytical model developed to estimate element stiffness and flexural capacity. The model assumes that element stiffness can be determined by transforming the steel sections into equivalent concrete sections and was found to predict these parameters accurately.

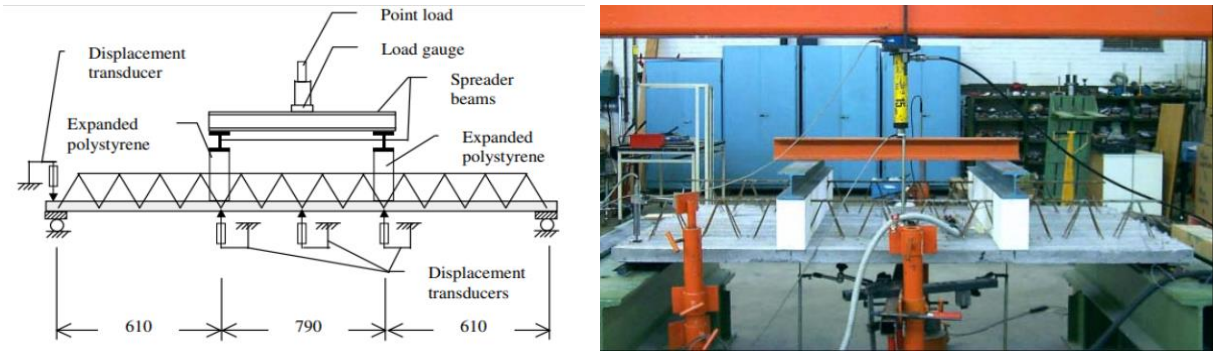

Figure 2-11 Loading test setup for four-point bending (Löfgren et al., 2001)

During the first phase of testing, the concrete in the panel remained uncracked, and the element displayed a relatively linear load-deformation curve. The stiffness during this phase could be estimated by transforming the steel sections into equivalent concrete sections. For the second phase of the tests, the panel concrete began to crack, decreasing the element stiffness. The load-deformation curve lost linearity. In this phase, it was assumed that the concrete panel's contribution to element stiffness was negligible. In the final phase, the top chord of the lattice girder began to buckle, initiating ultimate failure. The buckling load was primarily controlled by the slenderness of the top chord. Figure 2-12 illustrates the internal forces of the elements before and after the concrete in the panel initially begins to crack. Once the concrete cracks, it is assumed to contribute no tensile resistance.

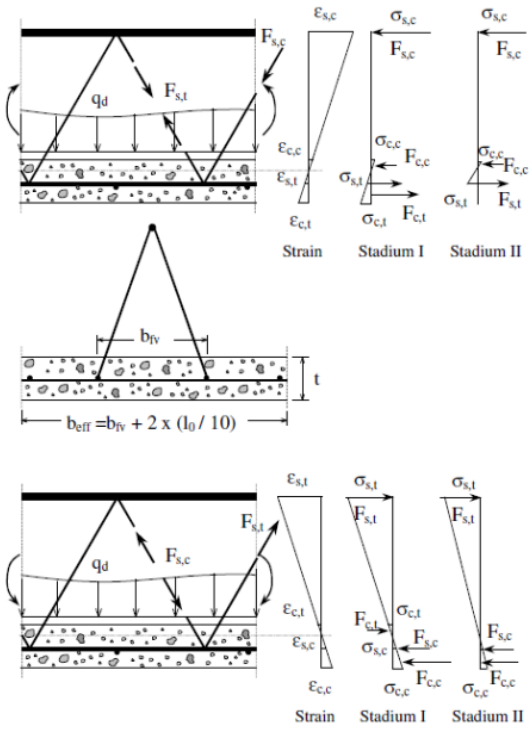

Figure 2-12 Diagrams of forces present before and after initial cracking of panel concrete (Löfgren et al., 2001)

Tapan (2014)

Tapan (2014) investigated the behavior of monolithic concrete beams with lattice girders as reinforcement (Figure 2-13), comparing that behavior to beams with traditional mild reinforcing bars. Although this subject matter is not directly representative of a partial-depth PCP deck system, the findings are relevant to the general behavior of concrete members reinforced with lattice girders, such as a completed partial-depth panel bridge deck with lattice girders. Researchers tested six beams, half of which were reinforced with lattice girders and half with traditional reinforcing bars. All six beams rested simply supported, loaded with a point load at the mid-span until failure. All six beams were found to have roughly the same initial stiffness and initial cracking loads. However, the beams reinforced with lattice girders were found to maintain a significantly higher stiffness after initial cracking and sustained much higher ultimate loads. On average, the lattice girder beams withstood approximately 44% higher loads before failing. The researchers attributed this to the higher stiffness after cracking, which likely comes from the web members of the lattice girder. While the traditional beams relied solely on concrete compressional strength and longitudinal reinforcement members to resist bending strains, those with lattice girders had diagonal members, giving additional restraint as truss elements.

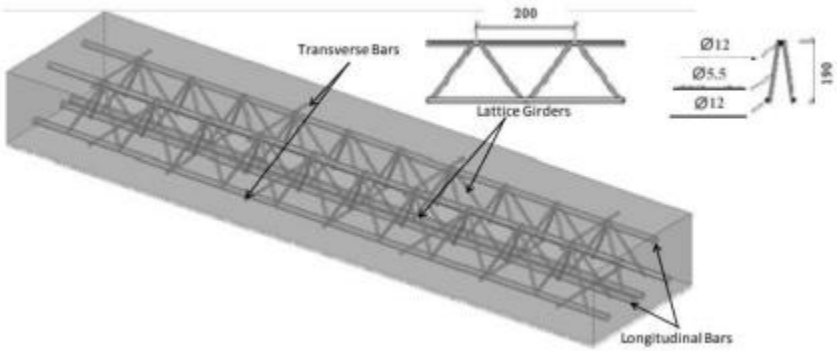

Figure 2-13 Monolithic concrete beam with lattice girders as reinforcement (Tapan, 2014)

Bridges and Roads, LLC.

Information about a full-width partial-depth bridge deck executed in Spain by Bridges and Roads, LLC. was obtained and reviewed. The research team probed the drawings of this project to comprehend specifics about the full-width design and seek items that differ significantly from current bridge construction practice in Texas to aid in future designs. Several of the key differences between the Spanish system and the current Texas design standard are summarized below:

As seen in Figure 2-14, the Spanish system utilizes additional longitudinal reinforcement along transverse joints between panels. The reinforcement is placed directly on the panel and likely serves to stiffen the joint. It is unknown whether this is primarily for the purpose of strength or serviceability requirements.

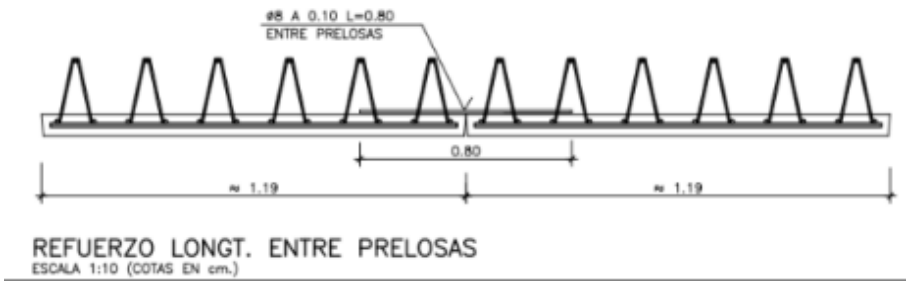

Figure 2-14 Additional longitudinal reinforcement laid across transverse panel joints. Translation: "Longitudinal Reinforcement Between Panels" (courtesy of Bridges and Roads, LLC.)

Also seen in Figure 2-14, the precast panel appears relatively shallow compared to the depth of the planned cast-in-place portion. Whereas Texas bridge decks tend to be approximately half precast panel and half cast-in-place concrete, the panels in the Spanish deck appear to be approximately 25% to 33% of the total deck depth. Figure 2-15 shows a dimensioned view of the lattice girders, which clarifies this concept. Overall deck depth appears roughly similar to the 8-inch (20.32 cm) depth commonly used in Texas, if not marginally thinner. Presumably, the Spanish system considers the precast deck temporary formwork only and does not include its contribution to in-service design after the CIP deck has cured.

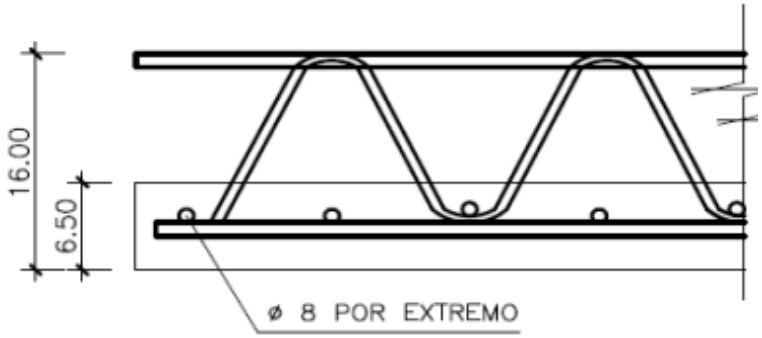

Figure 2-15 Structural configuration of panel reinforced with lattice girder

Transversally, lattice girders appear to be placed every 20 cm (7.9 in.) on center (Figure 2-16). Top mat reinforcement is therefore spaced at 7.9 in. on center, less than TxDOT's 9 inch maximum spacing. Because there are two bottom bars per lattice girder, this equates to a bottom mat reinforcement spacing of approximately 4 in., which is less than the 6-inch spacing between prestressing 12 strands currently used by TxDOT. Bar sizes for the top and bottom chords of the lattice girder are called out as being 10 mm in diameter (Figure 2-16), roughly the same size as the No. 4 bars normally used in Texas bridges. Longitudinally, there seems to be the same bottom mat spacing of 10 cm (approximately 4 in.) (Figure 2-17), also less than TxDOT's 6-inch maximum. The bars are called out as 8 mm in diameter, slightly smaller than the No. 4 bars specified by TxDOT. It is unclear what bar size and spacing are used for top mat longitudinal bars. No girder spacings or overhang lengths are shown in the given drawings.

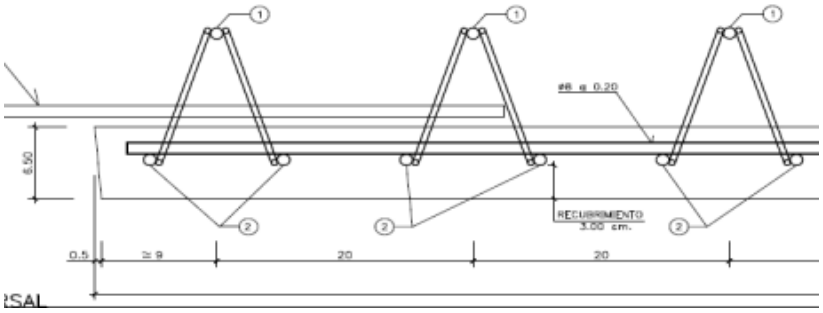

PRELOSA TIPO	①	②
VOLADIZO	ø10	ø10
CENTRAL	ø10	ø10
COMPLETA	ø10	ø10

Figure 2-16 Lattice girder spacing detail (courtesy of Bridges and Roads, LLC.)

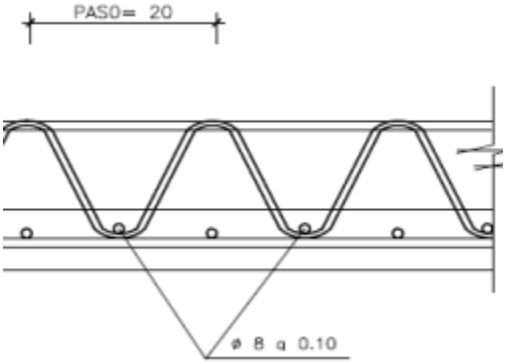

Figure 2-17 Longitudinal PCP reinforcement spacing (courtesy of Bridges and Roads, LLC.)

2.5. Fatigue Behavior

Sparse literature exists on the fatigue properties of steel trusses embedded into concrete slabs. Therefore, the majority of the literature review for fatigue behavior was focused on the previous research on the behavior of reinforcement in beams and slabs instead.

NCHRPR (1976)

This report covers a series of fatigue tests on miniature, reinforced concrete beams. The beams were subjected to 3-point, load-controlled tests while being recorded for midspan deflection. The loading was applied at a frequency of 4-8 Hz and an amplitude and mean set by the test. A total of 353 fatigue tests were performed on the beams that each contained a single reinforcement bar. Reinforcement diameters of No. 5, No. 6, No. 10, and No. 11 were tested. Grades 40 through 75 were tested. The specimens were cast in the shape of T-beams with the reinforcement present near the bottom of the stem. The report focused on the effects of stress range, minimum stress, bar size, grade, and geometry. This report found that the stress range that the reinforcement bars endured was the primary factor leading to the fatigue life of the beams. This stress range must put the bars into tension to achieve a failure, as there were no failures when the reinforcement was subjected to only compression. Stress range had a reduced impact when the maximum stress approached the tensile strength of the reinforcement. Increasing the minimum stress level that the bars endured

showed a reduced fatigue life for both short-term and long-term fatigue tests. As the diameter of the bar decreased, its fatigue life increased. This is credited to the additional manufacturing effort put into forming smaller bars as well as the decreased chance of having an imperfection present in the bar. The grade of the reinforcement had a positive effect on the fatigue life of the reinforcement. This was shown by the test results; however, the researchers could not observe any regular trend. Previous research has also disagreed on the amount of positive effect that material grade has on fatigue life. Finally, the bar geometry, or how the bar was deformed, had significant impacts on how fatigue cracking initiated. Sharp corners or edges promoted fracture cracking, which would induce an earlier fatigue failure.

The following equation was developed which applied to most of the specimens tested. This equation will be used to determine the truss's approximate fatigue life of the precast panels.

$$Log\ N = 6.9690 \pm 0.3586 - 0.0383\ f_r \qquad (2\text{-}1)$$

N refers to the number of cycles the specimen is expected to withstand before failure and f_r refers to stress range that the specimen is subjected to in ksi.

Raithy (1976)

This experimental program consisted of fatigue testing on plain concrete beams. Three different mixes were tested in which were than cured in a series of 10 ways. This series included wet curing for 26 weeks, surface coatings, impermeable barriers, air curing in controlled humidity, and traditional wet curing followed by exposure to air. The specimens were tested at loading rate of 20 Hz. The researchers noted that the loading frequency can impact the behavior of the concrete when the induced stresses are high enough to cause microcracking in the matrix. When the induced stress is below, the rate of loading did not have any effect on beams.

Tilly (1979)

This paper gave a review of the knowledge surrounding the fatigue of reinforcement in concrete structures and a history of the research performed that supports current practices. Tilly states that fatigue failure has never occurred on any highway in service, but fatigue failure can be unexpected beyond cracking in the concrete. This clean record can be attributed to the serviceability limit state and others that ensure stresses remain at minimal levels while cyclic loading is applied. There is still research conducted on this topic however as fatigue fractures have occurred in large research projects such as the AASHO Road Test in which reinforcement failed earlier than was expected from laboratory testing. Additional research has been conducted with the introduction of higher grades of steel and probing into durability issues which can reduce expected life dramatically.

Fatigue testing methods falls into two major categories. The first testing method is axial testing which is performed on a single bar held in two grips that cycle it. This cycling can reach frequencies as high as 150 Hz before the results become dependent on the frequency itself. This

high frequency loading allows these tests to reach high cycle counts in a short amount of time. However, axial testing has issues with how the bar is gripped, as significant local stresses caused by the grips can cause fracture in the bar before the undisturbed region reaches failure. Additionally, the lack of an interface with concrete leads to a separation from real conditions. This has been attempted to be remedied by casting a casing of concrete around the bar, but this additional material exacerbates the issues found with the stresses induced from the grips. The second testing method is flexural testing of reinforced beams. This method involves casting concrete beams that includes a single reinforcement bar located in the tension region of the beam. This test has an advantage as there us a realistic steel-to-concrete interface. Frequency must be limited due to the large deflections and local heating due to friction in cracks. Therefore, tests are run at low frequencies on the order of 3 Hz which requires long stretches of time to complete. Additionally, assumptions must be made about the properties of the concrete and placement of the reinforcement. Flexural tests are subjected to sinusoidal, load controlled cycles at a low frequency. Researchers may cast a strip of material into the beams to control where cracking will occur to better align with assumptions, however this will artificially increase the fatigue life.

Welding of reinforcement has shown to reduce the strength of the bars. This is prominent in axial tests, where it can reduce strength by up to 50%. Flexural tests may not be impacted by welding. This is attributed by where cracking in the concrete occurs as it may not coincide with where joint welds are placed. Therefore, strength is impacted by welding, which is relevant in axial tests with no concrete interface, and not as relevant in flexural tests have concrete to influence its behavior.

AASHTO LRFD 2020

The AASHTO LRFD Bridge Design Specifications detail when reinforcement in concrete elements is expected to have a finite fatigue life under stress ranges defined by the engineer. This is found in section 5.5.3 – Fatigue Limit State. The section further defines whether the reinforcement under scrutiny has cross-welds present in 5.5.3.2 – Reinforcing Bars and Welded Wire Reinforcement. If welds are not present, Eq. (2-2) governs, else Eq. (2-3) governs.

$$(\Delta F)_{TH} = 26 - \frac{22 f_{min}}{f_y} \tag{2-2}$$

$$(\Delta F)_{TH} = 18 - 0.36 f_{min} \tag{2-3}$$

$(\Delta F)_{TH}$ (ksi) refers to the constant-amplitude fatigue threshold, which governs the stress range that reinforcement is permitted to cycle between before a finite life is predicted. f_{min} (ksi) refers to the minimum live-load stress combined with unfactored permanent loads. This value is positive if tension, negative if compression. f_y (ksi) is the minimum yield strength of the reinforcement, with limits of 60 ksi and 100 ksi.

As the trusses are made by welding the chords to the webs, they fall under Eq. (2-2). These values will be calculated later in this paper to set the loading on the specimens. It should be noted that

$(\Delta F)_{TH}$ represents a minimum stress range before finite life, and therefore stress ranges that slightly exceed this value are likely to still perform with infinite life.

2.6. Summary and Research Needs

This chapter analyzed existing literature regarding the current state of partial-depth precast concrete panel bridge deck construction in Texas to understand what difficulties are encountered in extending such a system to be utilized as a full-width design. It has also presented a novel design technique to achieve this goal, inspired by current Spanish bridge design, which makes use of steel lattice girders embedded into the panels. The primary findings of this literature review are as follows:

- Partial-depth precast concrete panel bridge deck design and behavior are generally well understood within the boundaries of the fascia girders. Outside of the previously discussed problems associated with creating the overhang, the current design standards utilized by TxDOT appear to be sufficient to create a uniform full-width bridge deck design.

- The chief concern associated with the creation of a uniform full-width partial-depth bridge deck design is the transfer of moment forces over the fascia girder during construction. Alongside this moment transfer, the final constructed deck must still act compositely with the girder in order to provide horizontal shear resistance. Although there have been attempts to design for these requirements, there are new logistical problems generated through these attempts that still need to be worked out to implement anything new in the field.

- There is significant potential for safety improvement, cost savings, and greater design efficiency in full-width partial-depth precast concrete overhang design and construction.

- Concrete sections with lattice girder reinforcement show greater stiffness after initial concrete cracking occurs due to the truss action of lattice girder web members. This could lead to a more durable and resilient concrete structure.

- During the construction phase, when the cast-in-place topping has not cured, precast concrete panels with lattice girders tend to fail by compression buckling in the top chord and/or web of the girder. Estimation of buckling load using Eurocode 3, which utilizes Euler's critical buckling load method, tends to produce conservative results by a factor of roughly 2 to 3. For girders of lower height, web member buckling is less likely. This is true when considering a deck element subjected solely to positive moment; therefore, for the purposes of the NextGen deck, it is important to probe failure possibilities under negative moment as well. For instance, buckling of web members or tensile failure of the top chord may control the overhang design.

- Serviceability limits such as maximum deflection tend to be reached before ultimate failure during construction. Accordingly, serviceability limit states will likely govern design.

- Deflection behavior and overall section stiffness, in general, are heavily dependent on crack formation. Once cracking occurs, overall section stiffness sharply decreases.

- It is essential to obtain an accurate prediction of stiffness for the system in order to design for serviceability limits. Before curing the cast-in-place concrete, one can obtain a conservative estimate of element stiffness by transforming the steel sections into equivalent concrete sections, but estimates may be increasingly conservative for lattice girders of lower heights.

- The research team is aware of some noticeable differences (besides the use of lattice girders) between the current Texas partial-depth panel deck design and that of the Spanish type: namely, the Spanish system has additional longitudinal reinforcement laid directly on top of transverse panel joints; its precast panels make up roughly 1/3 of the total deck depth as opposed to Texas's 1/2; its transverse and longitudinal reinforcing bar spacings, in general, tend to be smaller than TxDOT standard maximum spacings; and its longitudinal bottom mat bar sizes are slightly smaller than those found in Texas bridges.

- Existing methods for predicting the number of fatigue cycles in literature or in AASHTO LRFD are applicable for regular rebar, plain concrete, or rebar embedded in concrete. Wire trusses, on the other hand, have different configuration and made with different welding technique. It is unclear if the existing equations are still applicable for wire trusses or composite wire truss panel decks.

Chapter 3. Partial-Depth Precast Panels

This chapter presents an experimental program that was developed to investigate the behavior of precast wire trussed partial depth panel pairs under flexural bending moments or shear forces. Test variables included unbraced length of wire trusses, production of wire trusses, and the presence of auxiliary compression reinforcement.

3.1. Introduction

The project aims to develop a full-width partial-depth precast concrete panel (PCP) deck for Texas bridges. These PCPs utilize partially embedded wire trusses (see Figure 3-1) to connect two or multiple panels. Wire trusses, in general, consist of a top chord and two bottom chords joined with inclined web members. Connected concrete panels are referred to as wire trussed partial depth precast concrete panels (WTPD PCPs).

WTPD PCPs are usually fabricated to have two panels, which are also named as precast panel pairs. These precast panel pairs are placed onto bridge bent caps, with one of the panels serving as the deck overhang support and the other as interior deck support. The cast-in-place concrete topping is then cast onto those panels and fills in the haunch and ties the deck to the rest of the superstructure to complete the construction of bridge decks. After cast-in-place a concrete topping is cast, the wire trusses act as deck reinforcement, as shown in Figure 3-1 schematically. During construction, the wire trusses between the panels are able to transfer moments generated by screed and construction loads on the bridge overhangs to eliminate the need for overhang brackets and formwork. The system is expected to significantly accelerate construction and reduce the impact to transportation.

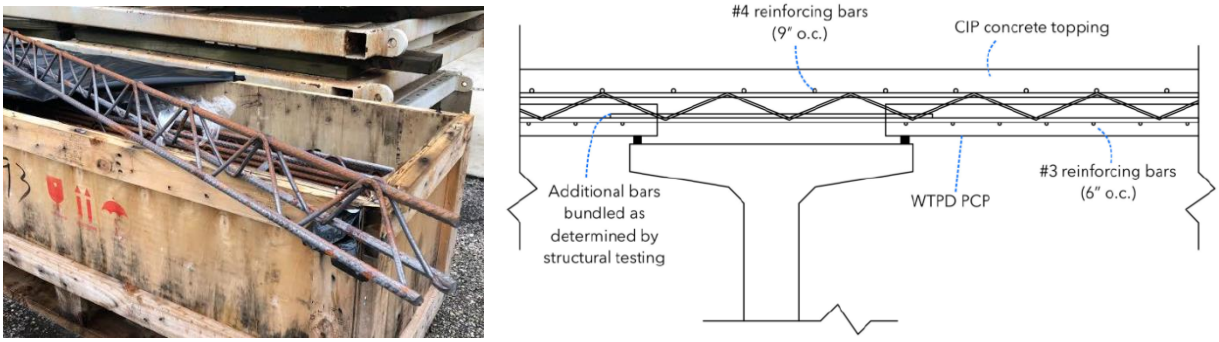

Figure 3-1 Wire trusses and typical design of NextGen decks with wire trusses

The successful implementation of this system relies on the behavior and performance of the precast panel pairs under construction and screed loads before cast-in-place concrete topping is finished. As mentioned above, the wire trusses between the two concrete panels are resisting bending moment generated from construction and screed loads. In other words, the top chords are under

tension while the bottom chords are under compression. In addition, the web members are resisting shear force. Unbraced, the wire trusses become the weakest link of the system.

It is identified that the wire truss has three primary probable failure modes: yielding of the top chord, local or global buckling of the bottom chords, or yielding/buckling of web members caused by shear forces. These controlling failure mechanisms for the system dictate the magnitude of construction and screed loads that can be applied onto the overhang when under construction. Therefore, an experimental program was needed to evaluate the structural viability of the PCPs with various design parameters.

The study presented in this chapter aims to experimentally investigate the behavior of WTPD PCPs. In the experimental program, twenty-four specimens of precast panel pairs were tested. Test variables included the unbraced length, additional reinforcement for bottom chords, and the welding methods for producing wire trusses (electro-welding versus hand-welding). The specimens were tested under four-point flexural bending or cantilever bending.

3.2. Experimental Program

3.2.1. Specimen Design and Test Matrix

As shown in Figure 3-2, the basic specimen configuration in the experimental program consisted of two concrete panels with a thickness of 4 in. connected by four partially embedded wire trusses spaced at 9 in. Other than the wire trusses, No. 3 bars spaced at 6 in. are distributed transversely to the wire trusses, serving as temperature reinforcement on the bottom. The two concrete panels had an identical width of 3 ft. The length of the panels (denoted as A1 and A2) and the unbraced length of the wire trusses (denoted as B) varied as summarized in the test matrix shown in Table 3-1.

In total 24 specimens were developed and categorized into six series, as shown in Table 3-1. Specimens in the first three series were reinforced with electro-welded wire trusses while specimens in the other three series were reinforced with hand-welded wire trusses. Series I aimed to investigate the effect of the unbraced length on the overall strength and behavior of panel pairs under negative bending moments. It was considered that the bottom chords are predisposed to buckle before the yielding of the top chord with a long-unbraced length. In other words, whether yielding or buckling controlled might depend on the length of the span. To investigate the relationship between the unbraced span and failure mode, the length of the span varied from 6 in. to 49 in. Lengths were chosen based on TxDOT girder designs such that each unbraced span corresponds to the flange width of a concrete or steel beam that appears in the TxDOT Bridge Design Standards.

Specimens in Series II were reinforced with additional steel bars bundled alongside the bottom chords of the wire truss to investigate the effect on buckling behavior as well as overall strength

and ductility. It was believed that additional bottom reinforcement would resist compression together with the bottom chords, preventing a premature buckling failure. The specimens in Series II had the same geometry as those in Series I with the unbraced length longer than 30 in. to determine how buckling capacity and behavior was affected by the additional bundled bars.

Series III was developed to investigate the shear behavior in the unbraced lengths of the specimens. These specimens were designed to be supported such that the maximum shear was concentrated in the panel or in the unbraced span of the trusses so that the shear behavior could be sufficiently investigated. Shear resistance in the truss was primarily provided by the diagonal web members. Anticipated failure modes included yielding or buckling of the diagonal web members within the shear span. Among the three specimens in this series, the first specimen was to be loaded for maximizing shear in the panel and the remaining two specimens were to be loaded to make the web members of the wire trusses resist shear force.

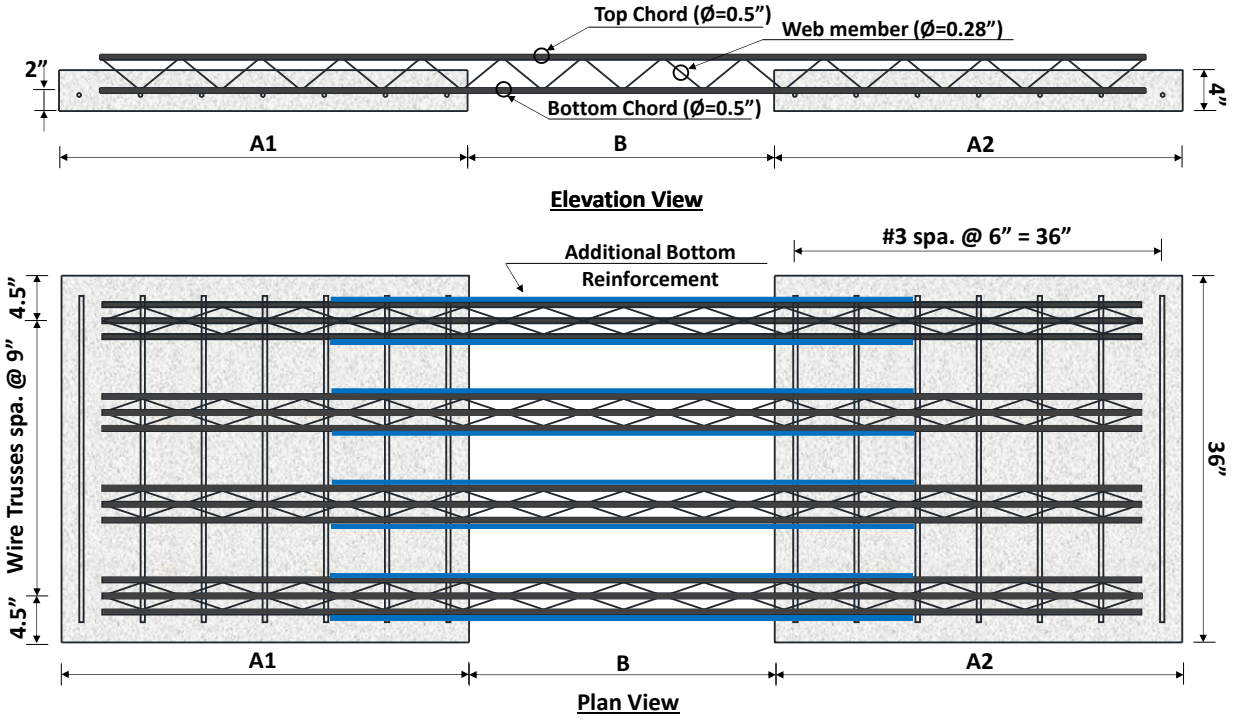

Figure 3-2 Specimen design

Table 3-1 Specimen schedule

Series	Specimen ID	Truss Type	A1 (in.)	A2 (in.)	B (in.)	Addt'l Reinf.
I	I-E-U30	Electro-welded	40	40	30	-
	I-E-U12		41.5	41.5	12	-
	I-E-U38		28.5	28.5	38	-
	I-E-U6		44.5	44.5	6	-
	I-E-U49		23	23	49	-
II	II-E-U30-#4		40	40	30	#4 bars
	II-E-U38-#4		28.5	28.5	38	#4 bars
	II-E-U49-#4		23	23	49	#4 bars
	II-E-U49-#5		23	23	49	#5 bars
III	III-E-U6-SC		12	12	6	-
	III-E-U6-SW-C		12	24	6	-
	III-E-U12-SW		12	24	12	-
IV	IV-H-U30	Hand-welded	40	40	30	-
	IV-H-U12		41.5	41.5	12	-
	IV-H-U38		28.5	28.5	38	-
	IV-H-U6		44.5	44.5	6	-
	IV-H-U49		23	23	49	-
V	V-H-U30-#4		40	40	30	#4 bars
	V-H-U38-#4		28.5	28.5	38	#4 bars
	V-H-U49-#4		23	23	49	#4 bars
	V-H-U49-#5		23	23	49	#5 bars
VI	VI-H-U6-SW-C		12	24	6	-
	VI-H-U6-SW-T		12	24	6	-
	VI-H-U12-SW		12	24	12	-

Specimens in Series I and II were to be placed in four-point negative bending, as shown in Figure 3-3(a). Pin-roller supports were to be placed underneath the specimen and loads were to be applied at ends of the specimen, creating negative bending moment in the unbraced length. In Series III, the first specimen was to be loaded the same as shown in Figure 3-3(a) to create shear force in the concrete panel without failing the unbraced length. The remaining two specimens, on the other hand, were to have one of the panels supported by a pin and a roller while being loaded at both ends, as shown in Figure 3-3(b). In this way, the unbraced length was subjected to shear.

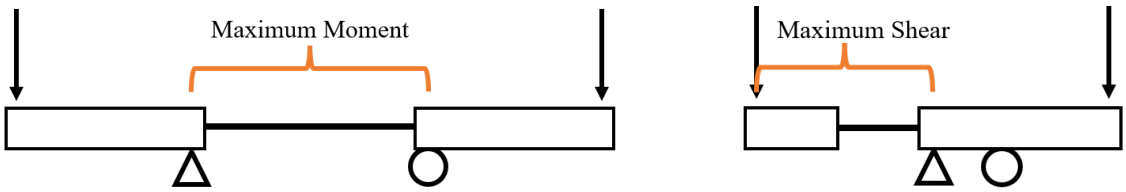

(a) Flexural test setup (b) Shear test setup

Figure 3-3 Flexural and shear test setups

Unlike specimens in the previous series, which were reinforced with electro-welded wire trusses, Specimens in Series IV through VI were reinforced with hand-welded wire trusses. The structural configurations were mostly duplicates of the Series I through III, respectively, with one exception: Specimen VI-H-U6-SW. The specimen had a larger panel to accommodate the embedment of the wire trusses after unexpected issues were encountered in the test of Specimen III-E-U6-SC. Also, Series VI specimens were fabricated with trusses oriented such that one specimen would test the web members in compression, one would test the web members in tension, and one would test them in both orientations simultaneously (see Figure 3-4).

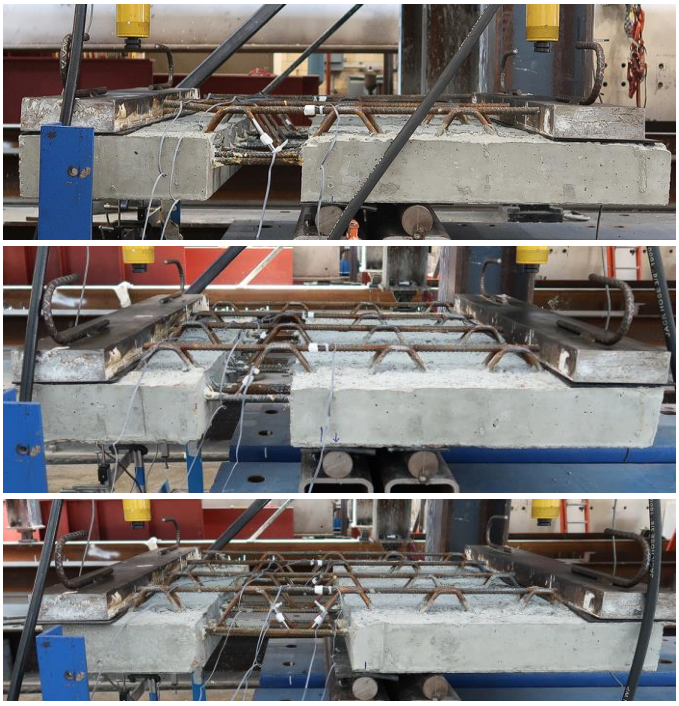

Specimen VI-H-U6-SW-C tested web members in compression

Specimen VI-H-U6-SW-T tested web members in tension

Specimen VI-H-U12-SW tested web members in both orientations

Figure 3-4 Different web orientations for Series VI specimens

3.2.1.1. Nomenclature

A naming system was developed for identifying the test specimens, as presented in Figure 3-5. The nomenclature consisted of six parts. The first part was the series number; the second part indicated the weld method; the third part indicated the unbraced length of the wire trusses at the mid-span; the forth part, which was for Series II and IV, indicated the size of additional reinforcing bars bundled with the bottom chords; the fifth part, which was for Series III and VI, indicated that

the specimen was tested for shear capacity; and the sixth part, which was for Series III and VI, indicated the orientation of the web members that resisted the applied shear force.

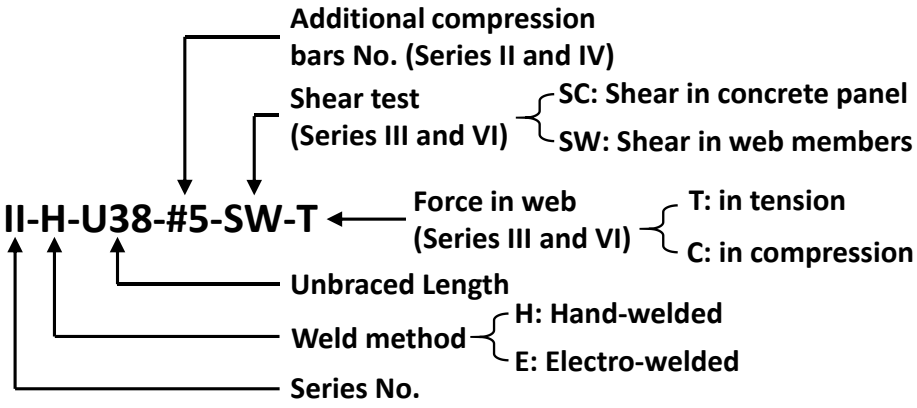

Figure 3-5 Nomenclature

3.2.2. Specimen Fabrication

3.2.2.1. Wire Trusses

As discussed in previous sections, the research team sourced two different wire truss products with a similar configuration (see Figure 3-6) for testing. The first one was electro-welded trusses (see Figure 3-6(a)) and the other was hand-welded (see Figure 3-6(b)). The wire trusses consisted of one top chord and two bottom chords (13 mm or 0.5 in. in diameter) welded with continuous web members (7 mm or 0.375 in. in diameter).

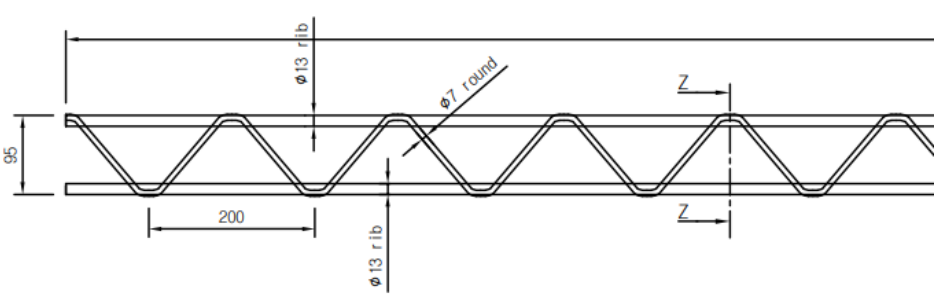

(a) Electro-welded truss (Company A): elevation view (units: mm.)

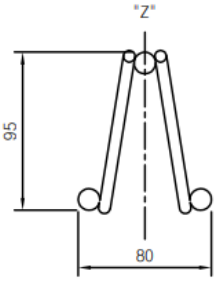

(b) Section Z

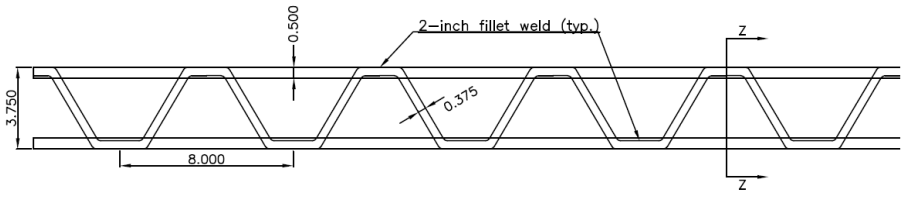

(c) Hand-welded truss (Company B): elevation view (units: in.)

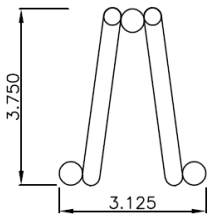

(d) Section Z

Figure 3-6 Configuration of wire trusses

The first trusses were produced with a machine to automatically form and electro-weld the trusses en masse, as shown in Figure 3-7. Welds were small and precise, and the addition of imperfections to the overall geometry of the truss from welding was negligible. The chords were 13 mm in diameter, and the webs 7 mm. The fabricator provided documentation for strength testing of the steel in the trusses, stating that the chords were a steel with approximately 78.0 ksi yield strength and the web was a steel wire with yield strength of 90 ksi. In addition, the web members had a yield strength of 91.2 ksi and an ultimate strength of 98.9 ksi.

Figure 3-7 Electro-welded trusses

The second trusses were manufactured by hand-weld, as shown in Figure 3-8. This fabricator did not have the same machine that automatically forms and welds the trusses. As such, the trusses comprised ASTM A706 weldable Grade 60 deformed rebars for chords and Grade 70 1018 drawn wire for the web. These welded joints were large fillet welds. Independent tensile tests performed by the research team resulted in a yielding strength of 68.6 ksi and an ultimate strength of 98.9 ksi for the chord members of the truss.

Figure 3-8 Hand-welded trusses

3.2.3. Laboratory Fabrication

All five specimens in Series I were fabricated in the Ferguson Structural Engineering Laboratory (FSEL). Formwork was constructed with lumber as presented in Figure 3-9(a) with inner partition walls that allowed trusses to pass through specially cut channels. Expanding foam and tape were

used to seal the channels after the trusses were in place [see Figure 3-9(b)]. The partition walls were uninstalled and reinstalled in different locations to accommodate different geometries of panel for fabrication.

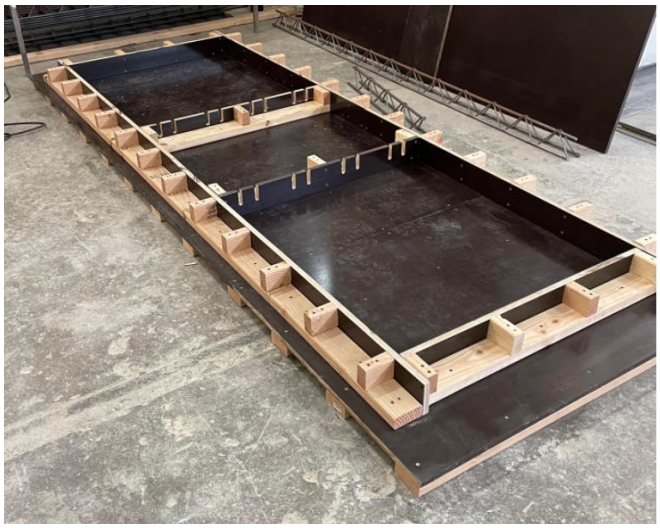

(a) lateral walls and partitions

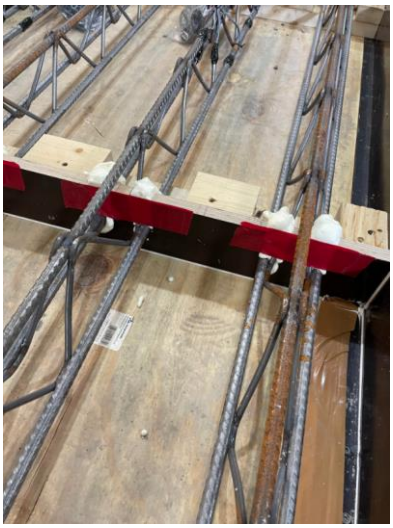

(b) Expanding foam and tape

Figure 3-9 Typical wood formwork for specimens in Series I through III

Casting of these specimens took place in the lab. Figure 3-10 shows two specimens cast by the research team shortly after a concrete pour. Information about concrete strength for these specimens can be found in Table 3-2.

(a) Specimen I-E-U30

(b) Specimen I-E-U6

Figure 3-10 Specimens on casting day

Table 3-2 Compressive strength of concrete for Series I

Series	Specimen	Concrete Strength f'_c (psi)
I	I-E-U30	3600
	I-E-U12	4670
	I-E-U38	4670
	I-E-U6	3730
	I-E-U49	3730

3.2.4. Outsourcing Fabrication

All specimens for Series II through Series VI were fabricated by a precast reinforced concrete fabricator located in Texas, as shown in Figure 3-11. This allowed for a greatly expedited fabrication pace. Specimens were fabricated according to detailed drawings provided by the research team. Members of the research team regularly met with the fabricators to discuss the process and view specimens. Concrete cylinders were cast for each specimen and delivered to the research team for the purpose of obtaining concrete strength, as listed in Table 3-3.

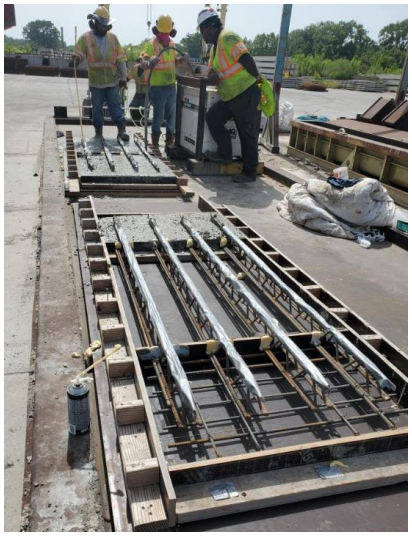

Figure 3-11: Texas precast fabricator pouring and vibrating research specimens

Table 3-3 Compressive strength of concrete for Series II through Series VI

Series	Specimen	Concrete Strength f'_c (psi)
II	II-E-U30-#4	6340
	II-E-U38-#4	7480
	II-E-U49-#4	7620
	II-E-U49-#5	10190
III	III-E-U6-SC	7570
	III-E-U6-SW-C	10990
	III-E-U12-SW	-
IV	IV-H-U30	8150
	IV-H-U12	9770
	IV-H-U38	7820
	IV-H-U6	10900
	IV-H-U49	10900
V	V-H-U30-#4	9950
	V-H-U38-#4	10000
	V-H-U49-#4	10000
	V-H-U49-#5	9950
VI	VI-H-U6-SW-C	8590
	VI-H-U6-SW-T	8590
	VI-H-U12-SW	-

3.2.5. Test Setup

3.2.5.1. Design of the Test Frame

The loading frame for the experimental program in the current study was designed to provide four-point bending to induce negative bending in the midspan of the specimen, as illustrated in Figure 3-12. The loading frame had flexibility to reposition the loading and supports as necessary to accommodate different specimen geometries. This also allowed for Series III and VI to be tested for shear capacity of specimens that were not symmetric nor the same size as the other Series' specimens.

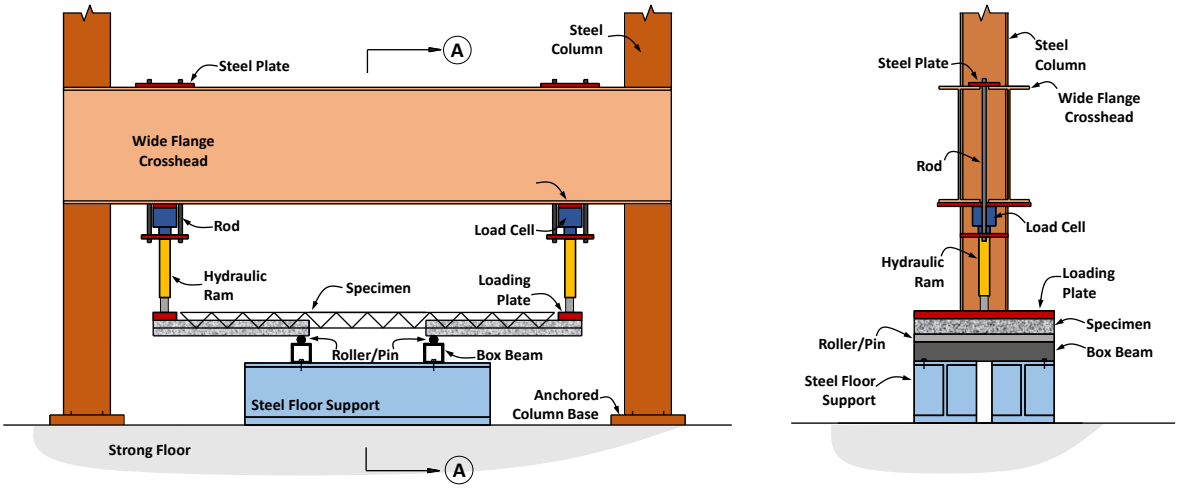

(a) Elevation View (b) Section A-A

Figure 3-12 Test Frame

The loading frame consisted of a steel portal frame mounted with two hydraulic cylinders. Each of the hydraulic cylinders were mounted upside down and hang from a pair of coped beams using threaded rods and a fashioned steel plate (see Figure 3-13), along with one 25-kip load cell per ram to measure loading force. Each cylinder had a 30-kip capacity and 10-inch stroke. Steel loading pads were fabricated in the lab to distribute the point load from the loading rams into a line load along the ends of the specimen.

(a) Ram mounting plates

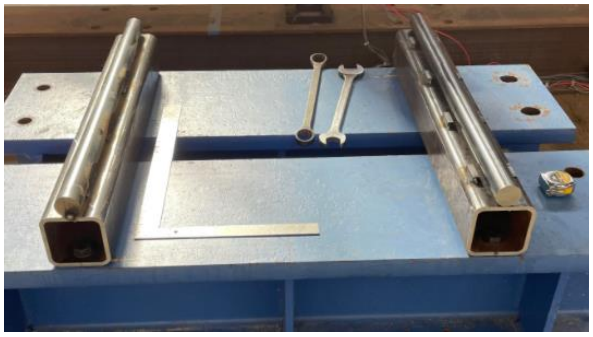

(b) Pin and roller

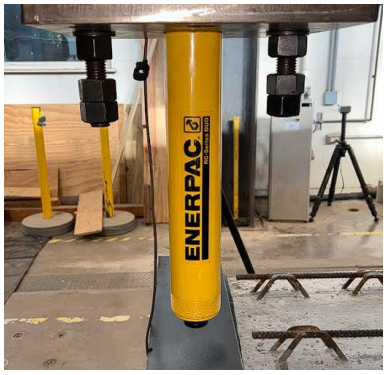

(c) Hydraulic cylinder ram

(d) Mounted hydraulic ram and load cell

Figure 3-13: Components of the testing frame

The specimen was supported by a pin and a roller [Figure 3-13(b)]. The pin was welded onto a box beam while the roller was placed onto a box beam with multiple stoppers on each side. The box beams were anchored to two support beams to transfer load onto the strong floor. Rubber padding was used at steel-concrete interfaces to distribute forces into the panel and ensure evenly distributed contact. If a concrete surface was too rough for rubber to properly distribute forces, then gypsum cement was used instead to create a strong interface.

The pin and the roller were placed at a position that was approximately 2 in. away from the edge of the panel in compliance with standard PCP drawings published by TxDOT. Each of the rams was centered at the steel load pad when applying loads, creating a moment arm that varied in dependence of the unbraced length. Table 3-4 summarizes the moment arms for analysis in the later sections.

Table 3-4: Distance between load points and support points for each specimen

Series	Specimen ID	Lever arm (in.)
I	I-E-U30	37.0
	I-E-U12	36.5
	I-E-U38	23.5
	I-E-U6	39.5
	I-E-U49	18.0
II	II-E-U30-#4	35.5
	II-E-U38-#4	20.5
	II-E-U49-#4	15.0
	II-E-U49-#5	15.5
III	III-E-U6-SC	7.0
	III-E-U6-SW	15.5
	III-E-U12-SW	19.0
IV	IV-H-U30	32.0
	IV-H-U12	37.0
	IV-H-U38	23.5
	IV-H-U6	39.5
	IV-H-U49	18.0
V	V-H-U30-#4	35.0
	V-H-U38-#4	23.5
	V-H-U49-#4	18.0
	V-H-U49-#5	18.0
VI	VI-H-U6-SW-C	19.0
	VI-H-U6-SW-T	19.0
	VI-H-U12-SW	19.0

When testing specimens in Series III (except for Specimen III-E-U6-SC) and Series VI for shear behavior, the rams and the load cells were re-arranged as shown in Figure 3-14 to create shear in the unbraced length. Moment arms for these specimens are also found in Table 3-4.

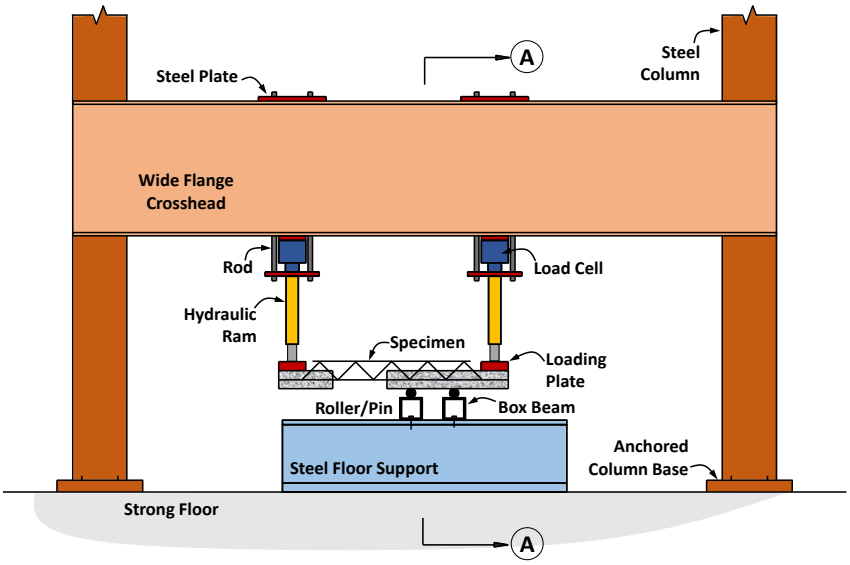

Figure 3-14 Arrangement of loading rams and supports to generate shear in the wire trusses

3.2.5.2. Frame Erection Procedure

The columns of the loading frame resisted the applied ram load by reacting against the floor in tension. They were therefore bolted to the strong floor of the lab with threaded anchor rods. To ensure that the columns do not lift off the ground during testing as the anchor rods deform, the columns were pretensioned through the base plates to the strong floor with a total of 30 kips per column.

The coped beams were connected to the columns with steel bolts to a slip-critical condition to prevent slipping during testing. Specimen supports were anchored to the strong floor to provide horizontal stability in case of extreme deflection. The test setup is shown in Figure 3-15.

Figure 3-15 Test setup

3.2.5.3. Instrumentation

Other than load cells were mounted with the rams for measuring loads on the specimen, other sensors were also used. Firstly, string potentiometers were placed under the test specimen at specified positions, as shown in Figure 3-16. This allowed for the monitoring and recording of end deflections and midspan deflections during testing.

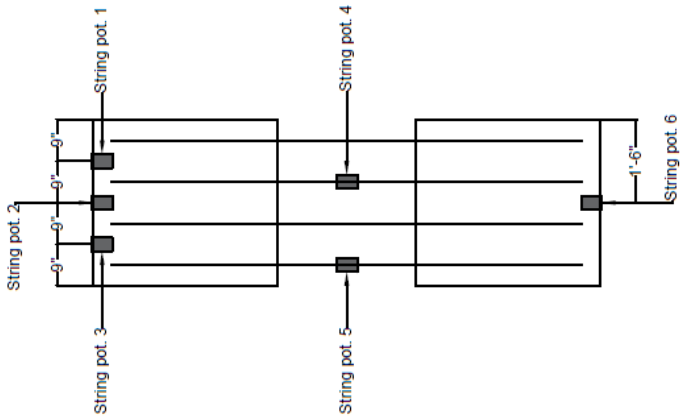

Figure 3-16 String potentiometer locations

One end of each specimen had three equally spaced potentiometers to detect any potential torsional action or otherwise uneven displacements. The other end contained one potentiometer to confirm that deflections were similar on both sides. The midspan had two potentiometers hooked to the trusses to investigate midspan deflection up to and during failure.

For Series IV though VI, the string potentiometers [see Figure 3-17(a)] were replaced with linear potentiometers [see Figure 3-17(b)] as it was found that the linear potentiometers provide more stable measurement with the data logger. The linear potentiometers were calibrated to the data logger and placed in the same spots as the previous string potentiometers.

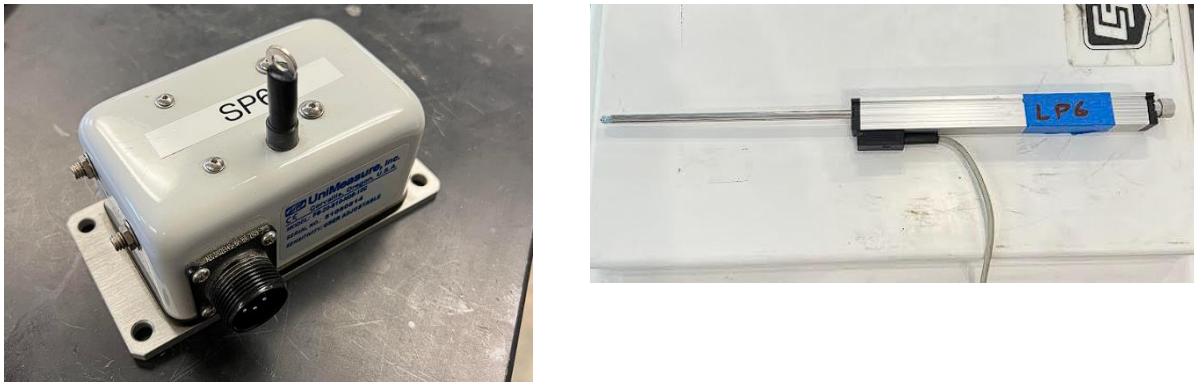

(a) String potentiometer (b) Linear potentiometer

Figure 3-17 Potentiometers used in the load testing program

Each specimen was strain gauged at locations of interest to investigate the distribution of internal forces during load testing. Figure 3-18 shows the strain gauge diagram as an example. In the figure, W indicates strain gauges on web members; T indicates strain gauges on top chords; and B indicates strain gauges on bottom chords. In general, specimens subjected primarily to flexural testing contained gauges that monitor the top and bottom chords of the trusses, and specimens subjected primarily to shear testing contained gauges on the web members of the trusses. Early specimens (i.e., Series I specimens) contained an abundance of both chord and web member gauges, as the research team was interested in confirming that flexural forces are resisted primarily by the chords in the midspan and shear forces primarily by the web near the loading points.

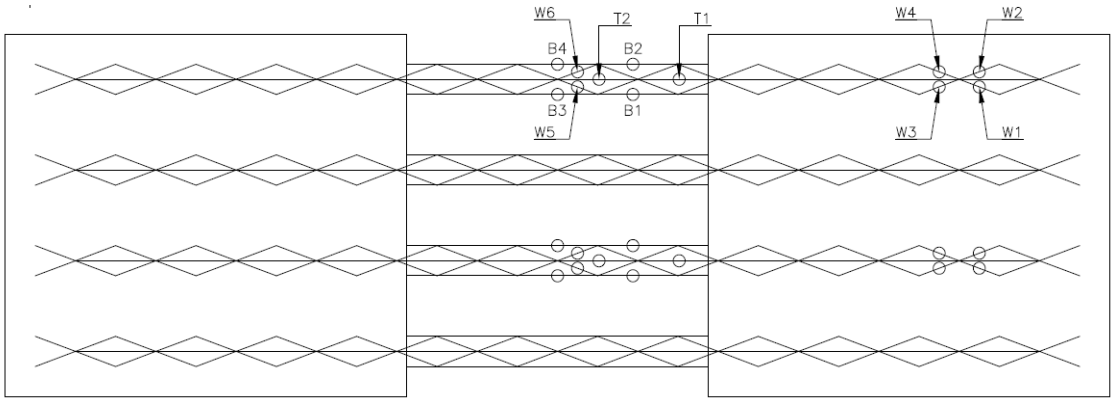

Figure 3-18 Strain gauge diagram

A data acquisition machine was used to monitor instrumentation readings and record data, as shown in Figure 3-19(a). All potentiometers and load cells were calibrated to this data acquisition

machine in the Lab before the testing program began. After the completion of Series I through III, the research team switched to a Campbell Scientific datalogger [see Figure 3-19(b)] to monitor instrumentation for purposes related to lab resources and to speed up the testing process. The datalogger performed the same job as the data acquisition machine. All previously calibrated instrumentation was recalibrated to the data logger before testing Series IV through VI.

(a) Data Acquisition Machine

(b) Data logger

Figure 3-19 Data acquisition hardware

3.2.6. Testing Procedure

Testing was performed with a manual hydraulic pump. The research team loaded the specimen at a rate of approximately 20 pounds per second. Load steps were at every 1 kip of total load, i.e., 500 pounds applied per side. At each load step, the research team maintained the current load while photographing the specimen, noting the current displacement state, and searching for signs of concrete cracking or steel failure. Throughout the test, the data acquisition machine took readings from every strain gauge, string potentiometer, and load cell once per two-seconds. The data was collected into a single file which the research team processed after testing was complete.

3.3. Experimental Results and Discussion

Results of this load testing task are presented herein. In general, it was found that concrete strength did not play a noticeable role in the strength or behavior of the specimens under any type of loading conducted for this task, with the exception of Specimens III-E-U6-SC and VI-H-U6-SW, which experienced cracking as a result of inadequate reinforcement near the loading point. As may be expected for adequately reinforced specimens, the weakest and most flexible location was the unbraced span of truss where there was no concrete. Additionally, the welding points of the specimens did not show any signs of breaking, cracking, or any other type of failure as a result of any tests conducted.

3.3.1. Specimens with Electro-Welded Wire Trusses

Here are presented the results of the load testing program on the specimens which were fabricated using the electro-welded trusses – Series I, II, and III.

3.3.1.1. Series I

Moment-deflection curves are provided in Figure 3-20 for Series 1 specimens. Moment provided in the figure was determined by multiplying the applied load by the lever arm of the specimen. In addition, Table 3-5 summarizes the test results of Series I specimens. In the table, test moments (M_{test}) are the peak moment in the mid-span, which was calculated by multiplying the peak applied (P_{test}) by the lever arm (see Table 3-5) of the specimen.

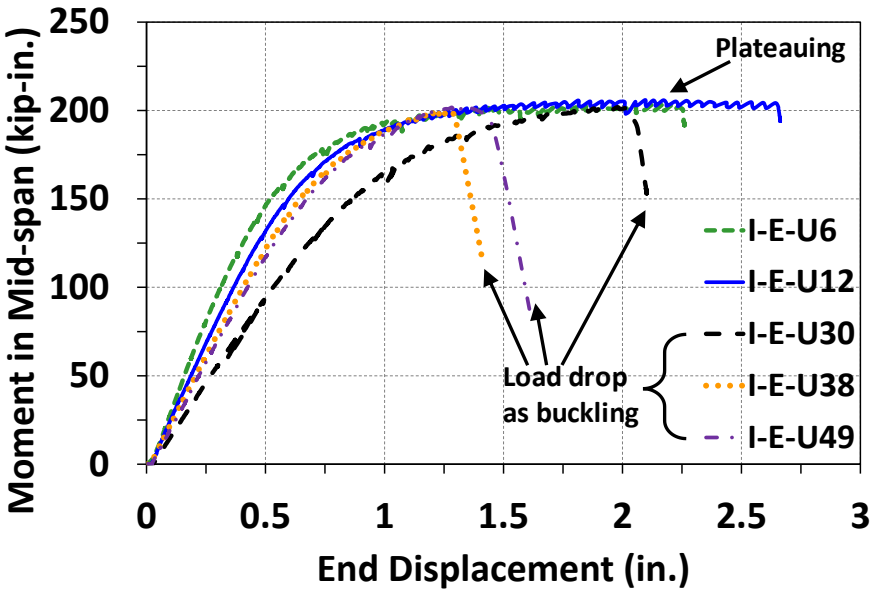

Figure 3-20 Moment-deflection curves for Series I specimens

Table 3-5 Test moments achieved by Series I specimens

Specimen ID	P_{test} (kip)	Lever Arm (in.)	M_{test} (kip-in.)
I-E-U30	5.456	37	193.7
I-E-U12	5.638	36.5	205.8
I-E-U38	8.464	23.5	198.9
I-E-U6	5.154	39.5	203.6
I-E-U49	11.256	18	202.6

It can be seen from Figure 3-20 that specimens with unbraced lengths of 6 in. and 12 in. exhibited plateauing after a linear load-deflection behavior. The plateauing was considered resulting from yielding of the top chords. These tests ended when deflections were too large and the tilt saddles attached to the loading rams were reaching their maximum tilt. Figure 3-21 provides a visual of this type of deflection. No sign of buckling of the bottom chords was observed before the end of the tests.

Figure 3-21 Extreme deflection prompts the end of a load test

Unlike specimens with shorter unbraced lengths, specimens with unbraced lengths of 30 in., 38 in., and 49 in. ultimately failed by buckling of the bottom chords, companied by a sharp decline in the load-carrying capacity seen in Figure 3-20. The buckling of the bottom chords was generally be characterized as global buckling along the mid-span, as shown in Figure 3-22. In all three cases, however, the bottom chord buckling occurred after the specimen began to exhibit load plateauing. The degree of load plateauing seemingly decreased as the unbraced length was longer. Regardless of whether the specimens buckled or not, similar test moments were achieved for all specimens in Series I, because the buckling of the bottom chords occurred after end of the linear behavior was reached.

Specimen I-E-U30 Specimen I-E-U49

Figure 3-22 Global buckling of the bottom truss chords

3.3.1.2. Series II

Similarly, moment-deflection curves of specimens in Series II were plotted, as shown in Figure 3-23. Test moments and peak load are presented in Table 3-6. It can be seen from Figure 3-23 that no specimen in this series exhibited a sudden load-drop. Instead, Specimens generally experienced load plateau before halting of testing, except for Specimen II-E-U49-#4. Testing of these specimens was halted when displacements were considered by the research team to be unsafe (i.e., when it appeared that the tilt saddles of the loading rams were near their maximum tilt).

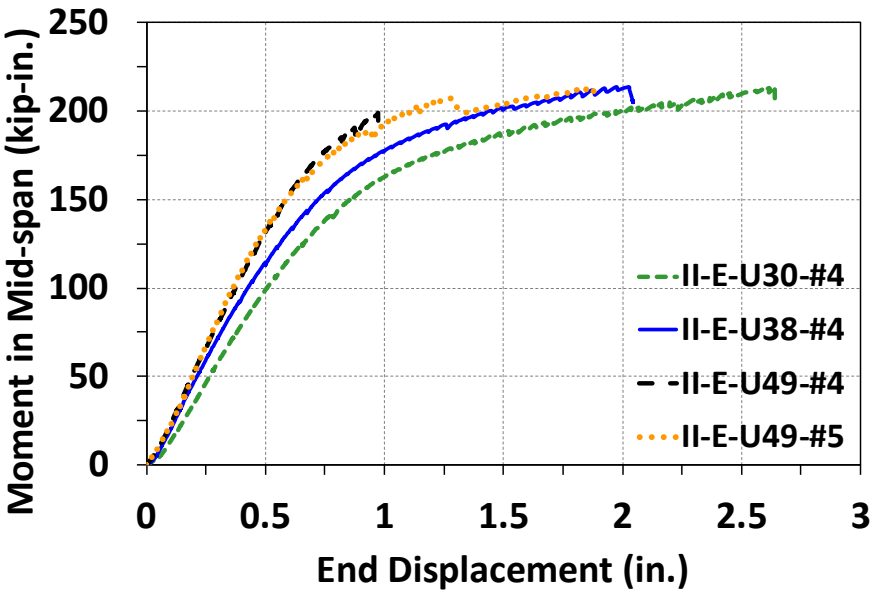

Figure 3-23 Moment-deflection curves for Series II specimens

Table 3-6 Test moments achieved by Series II specimens

Specimen	P_{test} (kip)	Lever Arm (in.)	M_{test} (kip-in.)
II-E-U30-#4	6.025	35.5	213.9
II-E-U38-#4	10.415	20.5	213.5
II-E-U49-#4	13.287	15	199.3
II-E-U49-#5	13.742	15.5	213.0

No specimens in the series failed via buckling of the truss bottom chords. Each unbraced span tested in this series showed significantly more displacement before halting of testing compared to the Series I counterparts. Figure 3-24 shows an example of the significant deflection of Specimen II-E-U49-#5 just before the end of load testing. The test results reveal that the additional compression bundled reinforcing bars contribution to preventing the buckling of the bottom chords.

Figure 3-24 Specimen II-E-U49-#4 exhibits large deflections without buckling of trusses

3.3.1.3. Series III

For this series, shear force resisted in the concrete panel or in the unbraced wire trusses was plotted regarding the end displacement, as shown Figure 3-25. Test loads, which were taken right before a significant load drop or the peak load the specimen reached, are provided in Table 3-7.

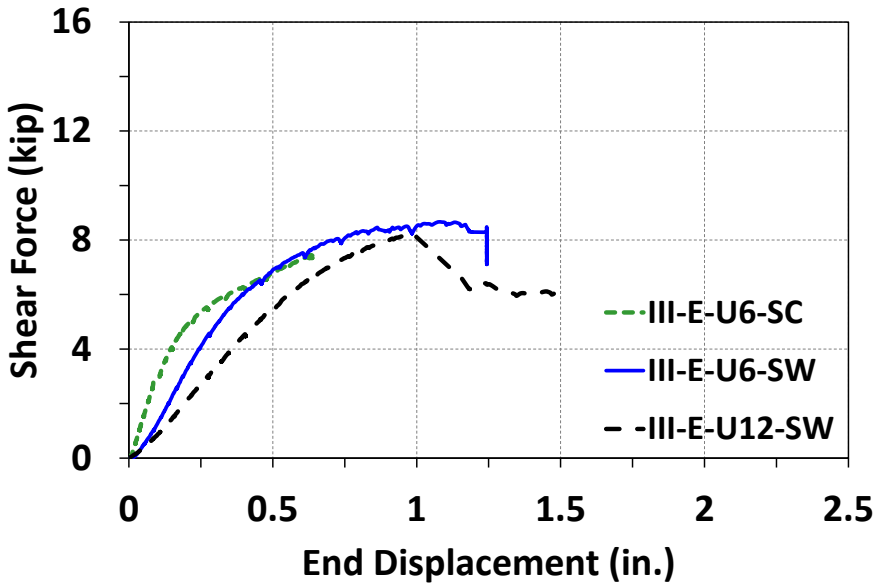

Figure 3-25 Load-deflection curves for Series III specimens

Table 3-7 Test loads achieved by Series III specimens

Specimen ID	P_{test} (kip)
III-E-U6-SC	7.452
III-E-U6-SW	8.663
III-E-U12-SW	8.254

Specimen III-E-U6-SC was intended to be tested for shear behavior in the concrete panels. Testing of Specimen III-E-U6-SC halted prematurely as the trusses did not develop fully into the panel and thus began to slip out of the panel while loading. A photograph of this effect is provided in Figure 3-26.

(a) After failure

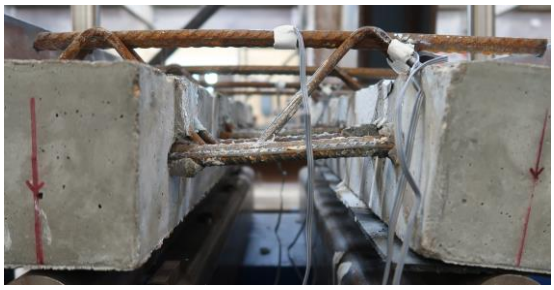

(b) Wire trusses slip out of the panels during loading

Figure 3-26 Status of Specimen III-E-U6-SC after end of test

Unlike Specimen III-E-U6-SC, Specimens III-E-U6-SW and III-E-U12-SW were meant to investigate the shear resistance of the web members. Both specimens failed by buckling of the web members in compression at just over 8 kips of applied load. Figure 3-27 shows the buckled web members after load testing was completed in Specimen III-E-U6-SW.

Figure 3-27 Web members buckle during shear testing of Specimen III-E-U6-SW

3.3.2. Specimens with Hand-Welded Wire Trusses

This section presents the results of the load testing program on the specimens which were fabricated using the hand-welded trusses – Series IV, V, and VI.

3.3.2.1. Series IV

Moment-deflection curves are provided in Figure 3-28 for Series IV specimens. It should be noted that the string potentiometers on Specimen IV-H-U6 did not have appropriate noise cancelling, resulting in a more erratic set of deflection data. Test moments (M_{test}) are provided in Table 3-8. The test moment was calculated by multiplying the highest applied load by the lever arm of each specimen.

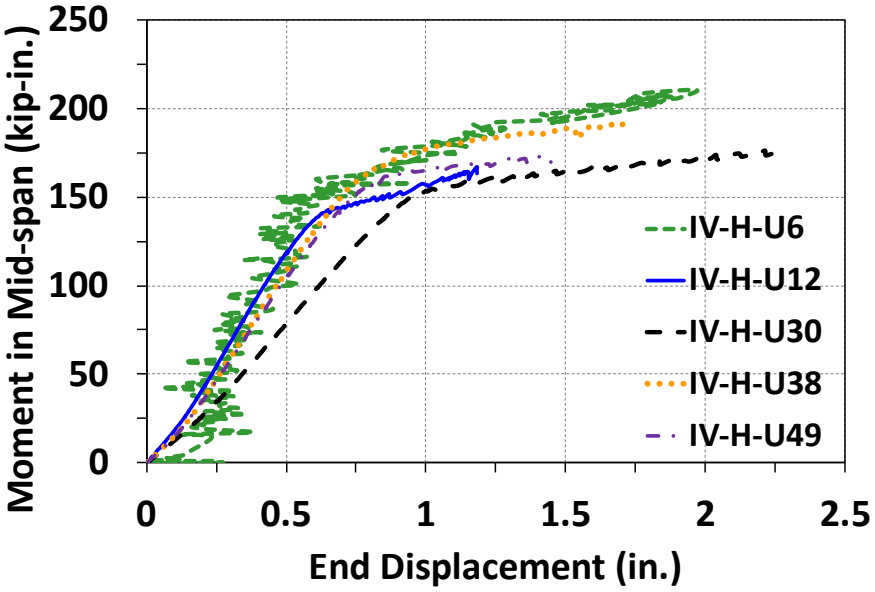

Figure 3-28 Moment-deflection curves for Series IV specimens

Table 3-8 Test moments achieved by Series IV specimens

Specimen ID	P_{test} (kip)	Lever Arm (in.)	M_{test} (kip-in.)
IV-H-U30	5.048	32	161.5
IV-H-U12	4.527	37	167.5
IV-H-U38	8.128	23.5	191.0
IV-H-U6	5.337	39.5	210.8
IV-H-U49	9.613	18	173.0

All specimens in Series IV experienced a load plateau, which was considered resulting from yielding of the top chord. All specimens in this series did not reach their ultimate failure because the tests were halted when the research team determined from observation that the tilt saddles on the loading rams were at or very near their maximum tilt. The observatory and safety-focused nature of this failure mode led to some discrepancies in what maximum displacement was reached by each specimen before halting each test.

Contrary to Series I, no specimen in Series 4 exhibited a sudden drop in load due to global buckling of bottom truss chords. However, buckling of some bottom truss chords did still occur during load testing, albeit fewer. Specifically, global buckling of the bottom chord occurred in one out of four trusses during the testing of Specimen IV-H-U38 (with a 38-inch unbraced truss length) and one out of four trusses during the testing of Specimen IV-H-U49 (with a 49-inch unbraced truss length), as shown in Figure 3-29. These are the two specimens with the largest unbraced truss lengths, and

therefore the two highest propensities for bottom chord compression buckling in negative moment. In both cases, the moment-deflection curves suggest that the buckling of a single truss did not have a significant effect on the overall behavior of the specimen during load testing, as the load plateaus continued to develop with no significant drops in load-carrying capacity. Tests of both specimens were also halted due to high deflections resulting from yielding of the top chords.

(a) Specimen IV-H-U38

(b) Specimen IV-H-U49

Figure 3-29 One truss buckles globally in Specimens IV-H-U38 and IV-H-U49

3.3.2.2. Series V

Moment-deflection curves are provided in Figure 3-30 for Series V specimens. Test moments (M_{test}) are provided in Table 3-9. The test moment was calculated by multiplying the highest applied load (P_{test}) by the lever arm of each specimen.

Table 3-9 Test moments achieved by Series 5 specimens

Specimen ID	P_{test} (kip)	Lever Arm (in.)	M_{test} (kip-in.)
V-H-U30-#4	8.331	20.0	166.6
V-H-U38-#4	8.062	23.5	189.5
V-H-U49-#4	9.757	18.0	175.6
V-H-U49-#5	11.135	18.0	200.4

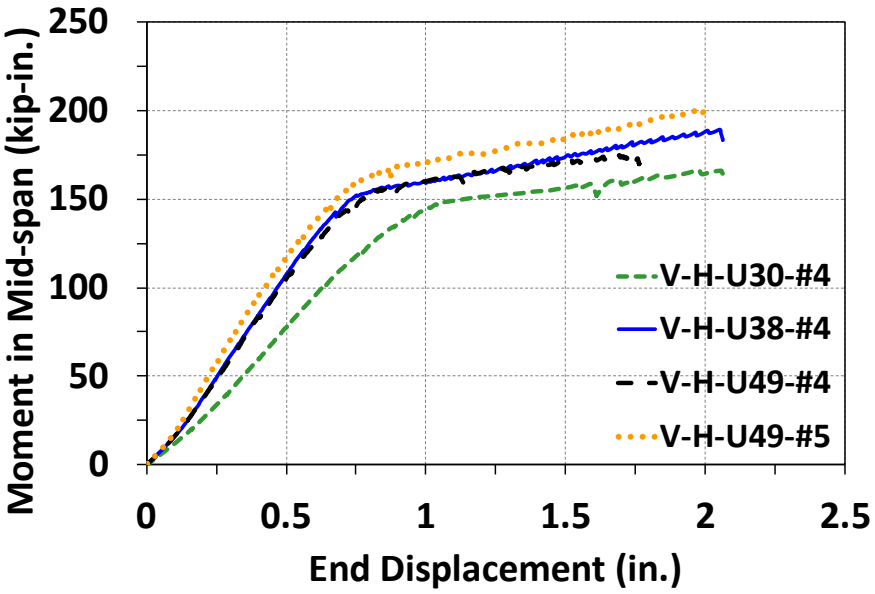

Figure 3-30 Moment-deflection curves for Series V specimens

Each of the specimens in Series V demonstrated no buckling of the bottom chords before the test was halted due to large deflection and the tilt saddles being maxed out (see Figure 3-31). Before the end of the test, the specimen had experienced extensive yielding of the top chords and a load plateau.

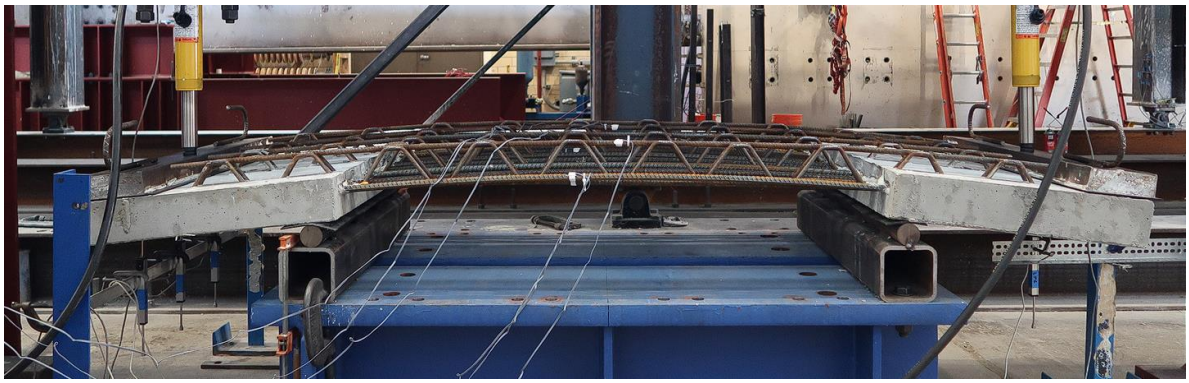

Figure 3-31 Specimen V-H-U49-#5 achieves extreme deflections prior to halting the load test

3.3.2.3. Series VI

Load-deflection curves are provided in Figure 3-32 for Series VI specimens. Test loads (P_{test}), which were taken right before a significant load drop or the peak load the specimen reached, are provided in Table 3-10.

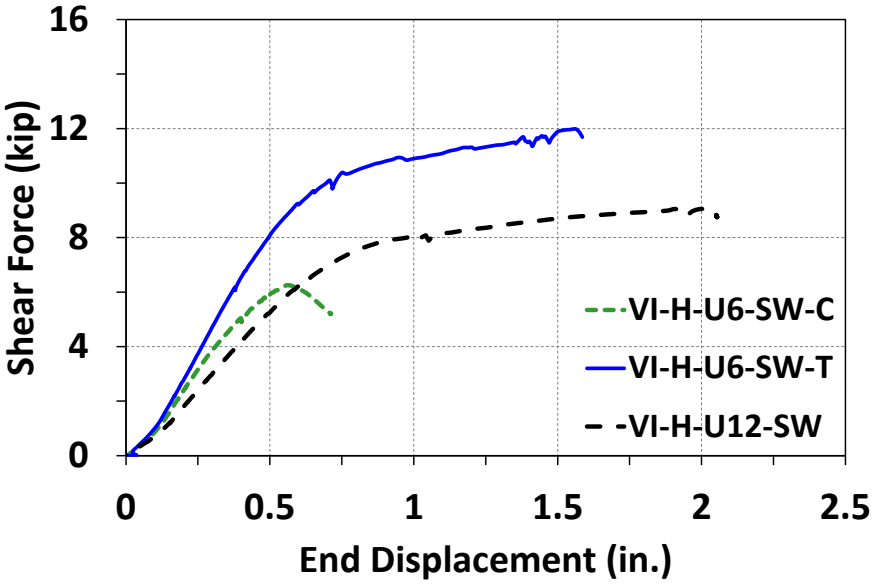

Figure 3-32 Load-deflection curves for Series 6 specimens

Table 3-10 Test loads achieved by Series 6 specimens

Specimen ID	P_{test} (kip)
VI-H-U6-SW-C	6.3
VI-H-U6-SW-T	12.0
VI-H-U12-SW	9.1

Specimen VI-H-U6-SW-C was the first and only specimen in this load testing task to experience signs of flexural and shear cracking in the concrete as a result of applied load. The wire trusses in this specimen were placed in such a way that one side of the specimen did not have the trusses developing deep into the concrete. As a result, flexural and shear effects were not adequately transferred to the trusses, and flexural cracks emerged in the top side of the panel, connecting to shear cracks emerging on the sides of the panel. There was very little reinforcement to arrest the cracks due to a lack of adequate embedment of the trusses in the panel. The failure mode of Specimen VI-H-U6-SW-C was considered to be a flexural and shear failure of the concrete due to inadequate reinforcement in the panel that was loaded in shear. Figure 3-33 shows Specimen VI-H-U6-SW-C before and after the cracks developed.

(a) Before testing (the trusses do not extend far into the right-side panel of the specimen)

(b) After flexural and shear cracks develop in concrete during load testing

Figure 3-33 Flexural cracks develop in Specimen VI-H-U6-SW-C due to inadequate truss reinforcement in the panel

Load testing found that both Specimens VI-H-U6-SW-T and VI-H-U12-SW experienced a significant load plateau with no sign of buckling in the web members unlike their counterparts in Series III. Both specimens reached a load plateau and tests were halted because the tilt saddles on the rams reached their maximum tilt (see Figure 3-34). The hand-welded trusses, by virtue of lower yield strengths and stiffer web member geometry, avoided shear failure in the unbraced span, instead exhibiting ductile flexural behavior. Without a shear failure, both specimens attained a better ductility and a higher load-carrying capacity than their counterparts.

(a) Specimen VI-H-U6-SW-T

(b) Specimen VI-H-U12-SW

Figure 3-34: Series VI specimens fail in flexure due to extreme deflection

3.4. Evaluation of Strength and Analytical Method

This section presents an evaluation of specimen performance and a discussion about factors that affected strength and behavior. Analytical methods for flexural strength, web buckling, and the global buckling of bottom chords are presented.

3.4.1. Flexural Behavior

3.4.1.1. Formulation

Based on the results of the load testing program, specimen behavior could be generally well described by a sectional analysis. It was assumed that moments in the unbraced span would be

resisted by the top and bottom chords of the trusses, and that shear forces would be resisted by the web members of the trusses in conjunction with the concrete panel near the load points. As it was observed that the buckling of bottom chords occurred after the wire trusses entered a load plateau, taking the yielding of the top chords as the controlling failure mode in the analysis was legitimate.

Considering a wire truss under negative moment (M) shown in Figure 3-35, per elastic sectional analysis, tensile stress in the top chord at the outermost fiber (f_s) can be calculated by

$$f_s = \frac{Mc}{I} \tag{3-1}$$

where c is the distance between the neutral axis and the outermost fiber; I is the second moment of inertia of the cross-section. The value of c can be determined by calculating the depth of the neutral axis. In this case without additional bundle bars with the bottom chords, the neutral axis is located at two third of the center-to-center height (h) below the center of the top chord; therefore, the value of c is given by

$$c = \frac{2}{3}h + \frac{1}{2}d_b \tag{3-2}$$

In addition to the value of c, the value of I can be determined by considering the second moment of inertial of the top chord and the bottom chords about the neutral axis. Per parallel axis theorem, the second moment of inertia I given by

$$I = \left[\frac{\pi d_b^4}{64} + \frac{\pi d_b^2}{4}\left(\frac{2}{3}h\right)^2\right] + 2\left[\frac{\pi d_b^4}{64} + \frac{\pi d_b^2}{4}\left(\frac{1}{3}h\right)^2\right] = \frac{3\pi d_b^4}{64} + \frac{\pi d_b^2 h^2}{6} \tag{3-3}$$

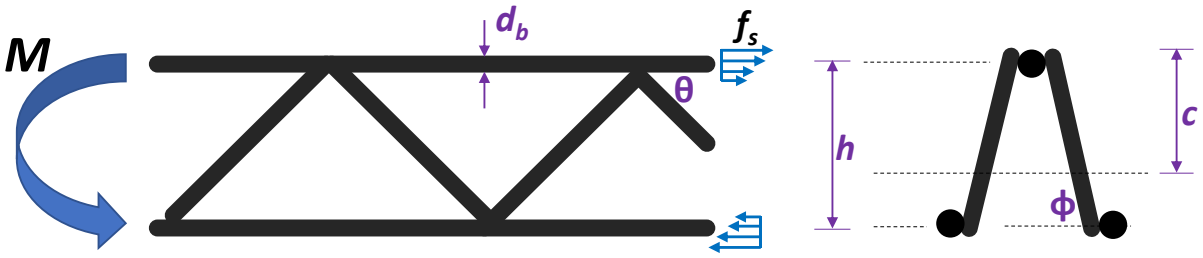

Figure 3-35 Wire truss under bending moment

With Eqs. (3-1) through (3-3), when tensile stress at the outermost fiber reaches the yield strength f_y, the corresponding moment, the yield moment M_y, can be expressed as

$$M_y = \frac{f_y\left(\frac{3\pi d_b^4}{64} + \frac{\pi d_b^2 h^2}{6}\right)}{\frac{2}{3}h + \frac{1}{2}d_b} \tag{3-4}$$

When the moment keeps increasing after reaching the yield moment, plastic analysis can be used to determine the plastic moment M_p. It is assumed that both the top chord and the bottom chords fully yield, resulting in a simplified system of loads shown in Figure 3-36. It should be noted that the resultant force in the bottom chords is slightly deeper than the center of the bottom chords; however, the simplified load system shown in Figure 3-36 provides a simple and conservative estimate of the plastic moment M_p.

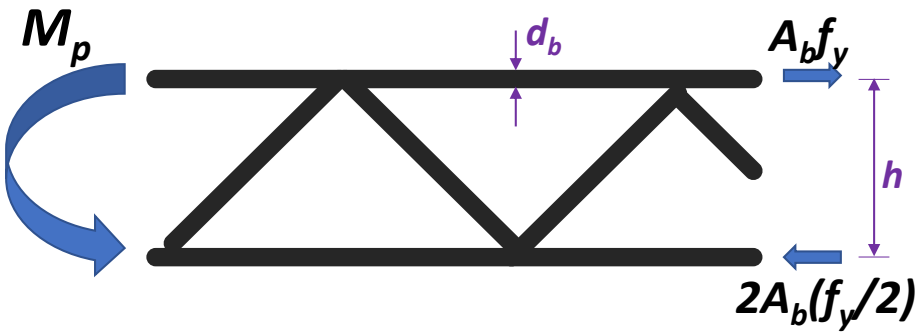

Figure 3-36 Plastic analysis of wire trusses

The flexural stresses in the system are therefore resolved in the midspan by a force couple generated by the top and bottom chords, where the top chord is in tension and the bottom chords are in compression. The force couple is in equilibrium with the acting plastic moment. Consequently, the plastic moment can be calculated given by

$$M_p = A_b f_y h \tag{3-5}$$

where A_b is the area of individual bar, assuming the top chord has the same size as the bottom chord. Eqs. (3-4) and (3-5) are for individual wire truss. It is needed to consider the number of wire trusses that are provided within the width of interest.

If additional bundled bars are used, the same method can be used with necessary modifications to the calculation of neutral axis and second moment of inertia. It should be noted that additional bundled bars were not considered in later analysis, as the research team suggested that additional bundled reinforcing bars were not contributing to the strength during the design process.

3.4.1.2. Specimens with Electro-Welded Trusses

Table 3-11 and Table 3-12 present the comparisons of the estimated moment capacity (both M_y and M_p) per Eqs. (3-4) and (3-5) to the actual test moments M_{test} achieved by each specimen for Series I and II. It can be seen from the tables that the analysis per Eqs. (3-4) and (3-5) delivered accurate and somewhat conservative results for what test moment will be achieved by the flexural specimens. Firstly, the ratio of M_{test} to M_y ranged from 1.11 to 1.15 for Series I and 1.12 to 1.2 for Series II. The average of the ratio is 1.13 for Series I and 1.18 for Series II. The analysis reveals that as long as buckling of the bottom chords does not occur earlier than plateauing, taking the yield moment M_y per Eq. (3-4) to estimate as a design baseline for WTPD PCP pairs is acceptable. As observed in the load testing, no specimens exhibited buckling of the bottom chords prior to reaching M_y, indicating that Eq. (3-4) is valid for unbrace lengths up to at least 49 in., whether additional reinforcing bars exist or not.

Table 3-11 Test vs calculated moments for Series I specimens

Specimen ID	f_y (ksi)	d_b (in.)	A_b (in.^{2})	h (in.)	M_{test} (kip-in.)	M_y (kip-in.)	M_{test}/M_y	M_p (kip-in.)	M_{test}/M_p
I-E-U30	78	0.5	0.20	3.23	201.8	178.5	1.13	201	1.01
I-E-U12	78	0.5	0.20	3.23	205.8	178.5	1.15	201	1.02
I-E-U38	78	0.5	0.20	3.23	198.9	178.5	1.11	201	0.99
I-E-U6	78	0.5	0.20	3.23	203.6	178.5	1.14	201	1.01
I-E-U49	78	0.5	0.20	3.23	202.6	178.5	1.14	201	1.01

Table 3-12 Test vs calculated moments for Series II specimens

Specimen ID	f_y (ksi)	d_b (in.)	A_b (in.^{2})	h (in.)	M_{test} (kip-in.)	M_y (kip-in.)	M_{test}/M_y	M_{calc} (kip-in.)	M_{test}/M_{calc}
II-E-U30-#4	78	0.5	0.20	3.23	213.9	178.5	1.20	201	1.06
II-E-U38-#4	78	0.5	0.20	3.23	213.5	178.5	1.20	201	1.06
II-E-U49-#4	78	0.5	0.20	3.23	199.3	178.5	1.12	201	0.99
II-E-U49-#5	78	0.5	0.20	3.23	213.0	178.5	1.19	201	1.06

Moreover, the plastic moment M_p also provided accurate estimation of the ultimate moment capacity for WTPD PCP pairs. It can be seen from Table 3-11 and Table 3-12 that the ratio of M_{test} to M_p ranged from 0.99 to 1.02 for Series I and from 0.99 to 1.06 for Series II. The average of the ratio is 1.01 for Series I and 1.04 for Series II. The method per Eq. (3-5) was generally accurate with one unconservative count for both Series I and Series II; the unconservative count in Series II was Specimen II-E-U49-#4, of which the test was halted early and the ratio was 0.99. The test moment would have been potentially higher if the load had continued. In Series I, the

unconservative prediction in the cast of I-E-U38, although undergoing buckling of the bottom chords, was insignificant.

Preventing the buckling of the bottom chords is essential in order to apply Eqs. (3-4) and (3-5), and the addition of No. 4 or No. 5 reinforcing bars bundled to the bottom chords effectively added some moment capacity to the system and increased the ductility, as illustrated in Figure 3-37. In the Figure 3-37, the moment capacity is presented in terms of the ratio of the test moment to the yield moment; the level of M_p and ductility ratio are also provided; the ductility was defined as the maximum end displacement divided by the deflection corresponding to M_y. Except for Specimen II-E-U49-#4, of which the test was stopped for safety, other specimens reached a higher test moment than their counterparts in Series I. The observation can be attributed to the fact that buckling of the bottom chords were delayed or prevented, resulting in a more substantial post-yield behavior. The bundled bars may be used in cases where the designer intends to prevent bottom chord buckling after a yield plateau develops.

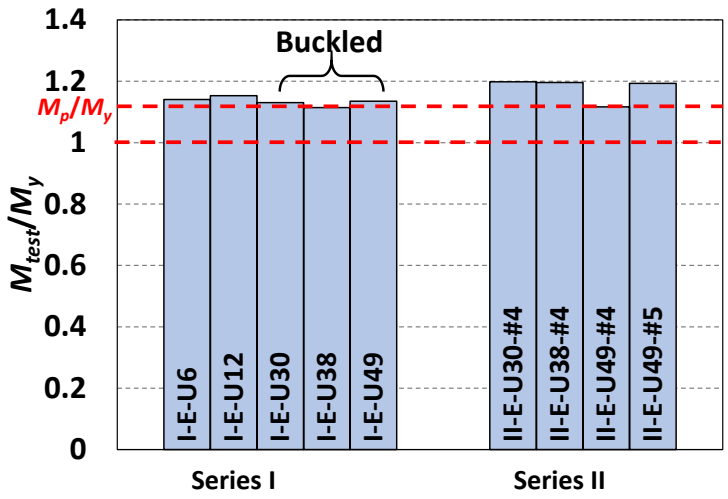

Figure 3-37 Comparison of moment capacity and ductility between Series I and II

3.4.1.3. Specimens with Hand-Welded Trusses

Similarly, Table 3-13 and Table 3-14 present comparisons of the calculated moments, M_y and M_p to the test moments achieved by each specimen, M_{test}, in Series IV and V. It can be once again seen that Eqs. (3-4) and (3-5) also demonstrated great predictive abilities in estimating the moment capacities for the specimens reinforced with hand-welded wire trusses. Regarding the yield strength, the specimens in Series IV were able to reach moment capacities 1.02 to 1.33 times the M_y. The average ratio of the moment capacity to the yield moment was 1.14. For Series V, the ratio ranged from 1.05 to 1.27 with an average of 1.16. It should be noted that the results would possibly have been higher as the tests of the specimens in Series IV and V did not reach the ultimate failure for safety reasons.

Table 3-13: Test vs calculated moments for Series 4 specimens

Specimen ID	f_y (ksi)	d_b (in.)	A_b (in.^{2})	h (in.)	M_{test} (kip-in.)	M_y (kip-in.)	M_{test}/M_y	M_p (kip-in.)	M_{test}/M_p
IV-H-U30	68.6	0.5	0.20	3.25	161.5	158	1.02	178	0.91
IV-H-U12	68.6	0.5	0.20	3.25	167.5	158	1.06	178	0.94
IV-H-U38	68.6	0.5	0.20	3.25	191.0	158	1.21	178	1.07
IV-H-U6	68.6	0.5	0.20	3.25	210.8	158	1.33	178	1.18
IV-H-U49	68.6	0.5	0.20	3.25	173.0	158	1.09	178	0.97

Table 3-14: Test vs calculated moments for Series 5 specimens

Specimen ID	f_y (ksi)	d_b (in.)	A_b (in.^{2})	h (in.)	M_{test} (kip-in.)	M_y (kip-in.)	M_{test}/M_y	M_{calc} (kip-in.)	M_{test}/M_{calc}
V-H-U30-#4	68.6	0.5	0.20	3.25	166.6	158	1.05	178	0.94
V-H-U38-#4	68.6	0.5	0.20	3.25	189.5	158	1.20	178	1.06
V-H-U49-#4	68.6	0.5	0.20	3.25	175.6	158	1.11	178	0.99
V-H-U49-#5	68.6	0.5	0.20	3.25	200.4	158	1.27	178	1.13

Regarding the predictability of Eq. (3-5), the ratio of M_{test}/M_p ranged from 0.91 to 1.18 with three unconservative counts for Series IV; the ratio ranged from 0.94 and 1,13 with two unconservative counts for Series V. Nonetheless, the method still showed great predictability, given the average ratio being 1.02 for Series IV and 1.03 for Series V. The results are not considered decisive because test specimens in Series IV and V would have attained a higher load-carrying capacity if the tests had not halted early. Nevertheless, Eq. (3-5) is considered applicable for these hand-welded WTPD PCP pairs.

As can be seen in Figure 3-38, the addition of bundled No. 4 or No. 5 bars on the bottom truss chords in Series V specimens once again produced test moments that are slightly higher than the Series IV counterparts without additional bars, except for Specimen V-H-U38-#4, which had a test moment of 189.5 kip-in lower than that of its counterpart Specimen V-H-U38. Nevertheless, both of the specimens did not reach a load drop; the comparison is not decisive. In addition, bottom chord buckling was already minimal in Series IV specimens, so the additional bundled bottom chord bars did not have a significant effect in raising the test moment by virtue of preventing buckling-type failures. However, the additional bundled bottom chord bars did succeed in completely eliminating any buckling whatsoever in the specimens tested for this series.

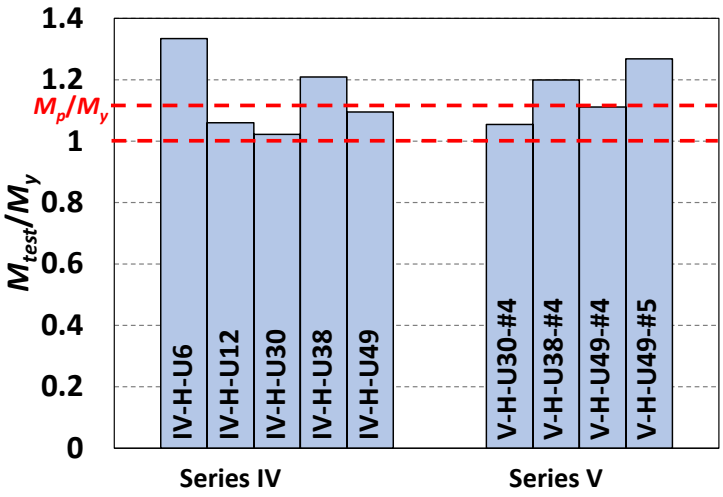

Figure 3-38 Comparison of moment capacity and ductility between Series IV and V

3.4.2. Shear Behavior

3.4.2.1. Formulation

Shear behavior was similarly estimated using a simplified analytical model, as shown in Figure 3-39. Per equilibrium, external shear forces are resisted by the web members of the wire truss. Depending on the orientation, the web members can be in tension or in compression. When the web members are in tension, the maximum internal force in each web member is limited to the tensile yield strength (F_y), as illustrated in Figure 3-39(a). In addition, when in compression, the web members' capacity is limited by the buckling load (F_{cr}) or compressive yield strength, which is assumed the same as the tensile yield strength. Therefore, the shear capacity can be determined by the equilibrium of the structure with the lesser of F_y and F_{cr}.

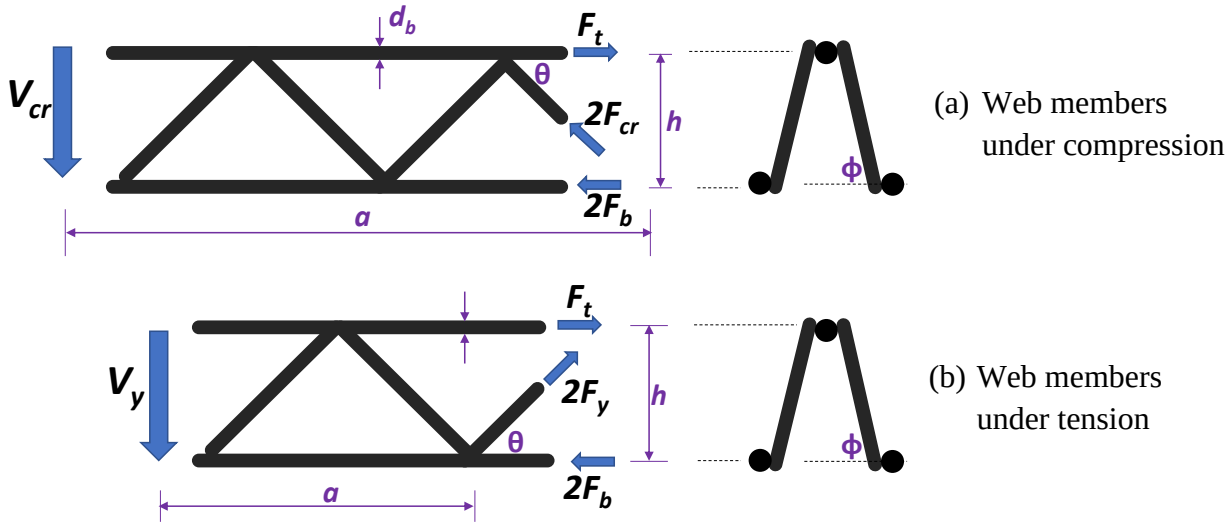

Figure 3-39 Wire trusses under shear force

As the section has two inclined web members with angles of θ and ϕ, equilibrium of an individual wire truss can be established and expressed for the calculated shear capacity V_y (controlled by yielding) or V_{cr} (controlled by buckling), given by

$$V_y \text{ or } V_{cr} = 2 \times \min\{F_y, F_{cr}\} \times \sin\theta \sin\varphi \tag{3-6}$$

in which

$$F_y = f_y A_w \tag{3-7}$$

$$F_{cr} = \frac{\pi^2 EI}{(KL)^2} \tag{3-8}$$

where θ and ϕ are angles of the web member; A_w is the area of the web member; EI is the flexural rigidity of the web member; L is the length of the web member; K is the effective length factor. The K factor for the web members depends on the boundary conditions on both ends, which is related to the weld size and other influential factors. There was no simple way to determine the K factor analytically; instead, it was determined based on the experimental method, which is introduced in later sections.

In addition, flexural bending would potentially cause the top chord yield before the web members reach their strength. The corresponding shear force V_p can be determined by moment equilibrium, given by

$$V_p = \frac{A_b f_y h}{a} \tag{3-9}$$

where A_b is the area of the top chord; a is the moment arm shown in Figure 3-39. Consequently, the calculated shear capacity V_{calc} of an individual wire truss is the lessor of V_y, V_{cr}, and V_p. Of course, it is needed to account for the number of wire trusses embedded within a width in consideration to determine the total shear capacity.

3.4.2.2. Specimens with Electro-Welded Trusses

It was found in testing that compression buckling of web members was the controlling failure mode in shear for the electro-welded trusses; it was therefore used to calibrate the K factor against the test data. Using the data from the load tests, it was determined that a K-factor of 1.1 consistently matched the calculated loads to the test loads fairly well for each specimen tested. The research team finds this effective length factor to be reasonable, as it represents a fixed-fixed connection with some potential for small translation and rotation. A comparison of calculated loads to test loads for Series III specimens is given in Table 3-15. It should be noted that Specimen III-E-U6-SC is not included because of the slippage failure. In the table V_{test} is controlled by V_{cr}; V_y was 14.6

kip and V_p was 11.8 kip for Specimen III-E-U6-SW-C and 9.6 kip for Specimen III-E-U12-SW. A bar chart that compares the test results and failing loads is presented in Figure 3-40.

Table 3-15 Calculated vs test loads for Series III specimens

Specimen ID	f_y (ksi)	A_w (in.^{2})	EI (k-in.^{2})	L (in.)	θ (rad)	ϕ (rad)	K	V_{test} (kip)	V_{calc} (kip)	V_{test}/ V_{calc}
III-E-U6-SW-C	91.2	0.06	8.26	6.64	0.76	1.36	1.1	8.663	8.2	1.06
III-E-U12-SW	91.2	0.06	8.26	6.64	0.76	1.36	1.1	8.254	8.2	1.01

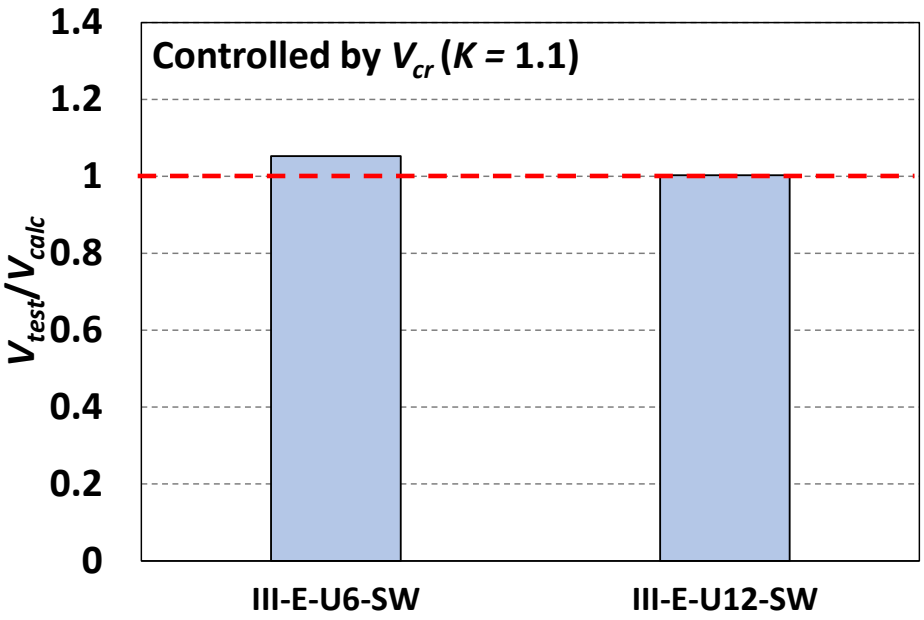

Figure 3-40 Comparison of test and analytical results for Series III

The static analysis described provides a reasonably accurate estimate of the shear strength of the specimens. Although it would not be expected in the field for the NextGen WTPD PCP pairs to encounter significant shear in the unbraced span of trusses, a baseline for shear performance was established. It was determined that the shear strength for these specimens can be calculated using Eqs. (3-6) through (*3-9*) with effective length factor for web members K = 1.1 for buckling of web members.

3.4.2.3. Specimens with Hand-Welded Trusses

Using the same calculation procedure described in Eq. (3-6) with K = 1.1, it was found that the estimated failure loads for the hand-welded trusses were 26.0 kip for V_y and 48.3 for V_{cr}. The V_{calc} for this case was limited by V_p, which was 10.5 kip for Specimen VI-H-U6-SW-T and 7.7 for Specimen VI-H-U12-SW, as listed in Table 3-16. A bar chart that compares the test results and

failing loads is presented in Figure 3-41. Specimen VI-H-U6-SW-C is not included due to premature concrete failure.

Table 3-16 Calculated vs test loads for Series VI specimens

Specimen ID	V_{test} (kip)	Lever Arm (in.)	V_{calc} (kip)	V_{test}/V_{calc}
VI-H-U6-SW-T	11.987	17	10.5	1.14
VI-H-U12-SW	9.067	23	7.7	1.17

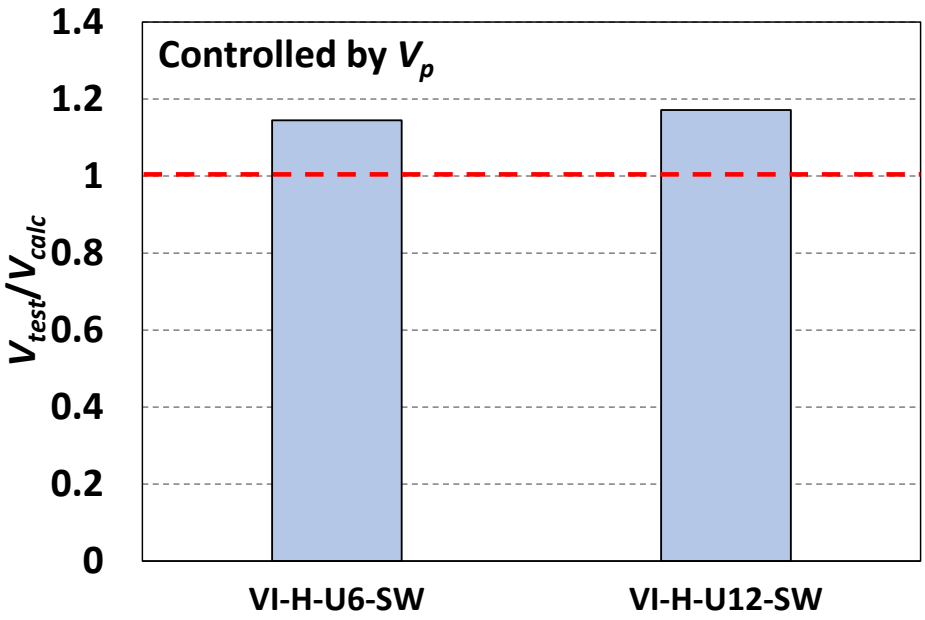

Figure 3-41 Comparison of test and analytical results for Series IV

It is revealed that Eq. (3-6) demonstrates conservative and accurate predictive ability. The controlling failure mode was also successfully reflected. The ratio V_{test}/V_{calc} is 1.14 and 1.17 for Specimens VI-H-U6-SW-C and VI-H-U12-SW, respectively based on V_p. As long as web members do not fail in buckling nor yielding under shear demand, the unbraced length can still be treated as a flexural member and evaluated using Eq. (3-6).

3.4.3. Buckling of Bottom Chords

Test results showed that bottom chords of wire trusses within the unbraced length are susceptible to buckling when subjected to negative moments. Although almost always happening after the moment that caused the yield of the top chords was reached during the tests, it is still essential to investigate affecting factors and understand conditions that plausibly lead to early buckling. In this section, an analytical model for determining the buckling load of the bottom chords is presented.

Key factors related to the configurations of wire trusses are discussed, and a testing method on wire truss segments for preventing premature buckling is also recommended.

3.4.3.1. Formulation

The spatial three-dimensional configuration of wire trusses increased the difficulty of developing an analytical method. For instance, factors such as the inclination of web members and welded connections between web members and chords, as shown in Figure 3-42, prevented a simple analytical model. Nevertheless, a few simplifications were made to avoid involving the complicated geometry of the web members.

Consider a wire truss with a total unbrace length of L, within which $(N\text{-}1)/2$ wave lengths are contained, as shown in Figure 3-42. To facilitate the analysis, a numbering system is applied to represent the positions of each of the intersections between web members and chords. For intersections of the top chord and web members, odd numbers are assigned so that the intersections have horizontal coordinates of x_1, x_3, x_5,…, $x_{(\text{odd number})}$, …, and x_N. On the other hand, even numbers are assigned to intersections of the bottom chords and web members so that the intersections have horizontal coordinates of x_2, x_4, x_6,…$x_{(\text{even number})}$,…, and $x_{N\text{-}1}$. Furthermore, after deforming, the lateral displacement of each intersection on top chord is assumed y_1, y_3, y_5, …, $y_{(\text{odd number})}$, …, and y_N, and that on bottom chords is assumed y_2, y_4, y_6, …, $y_{(\text{even number})}$, …, and $y_{(N\text{-}1)}$.

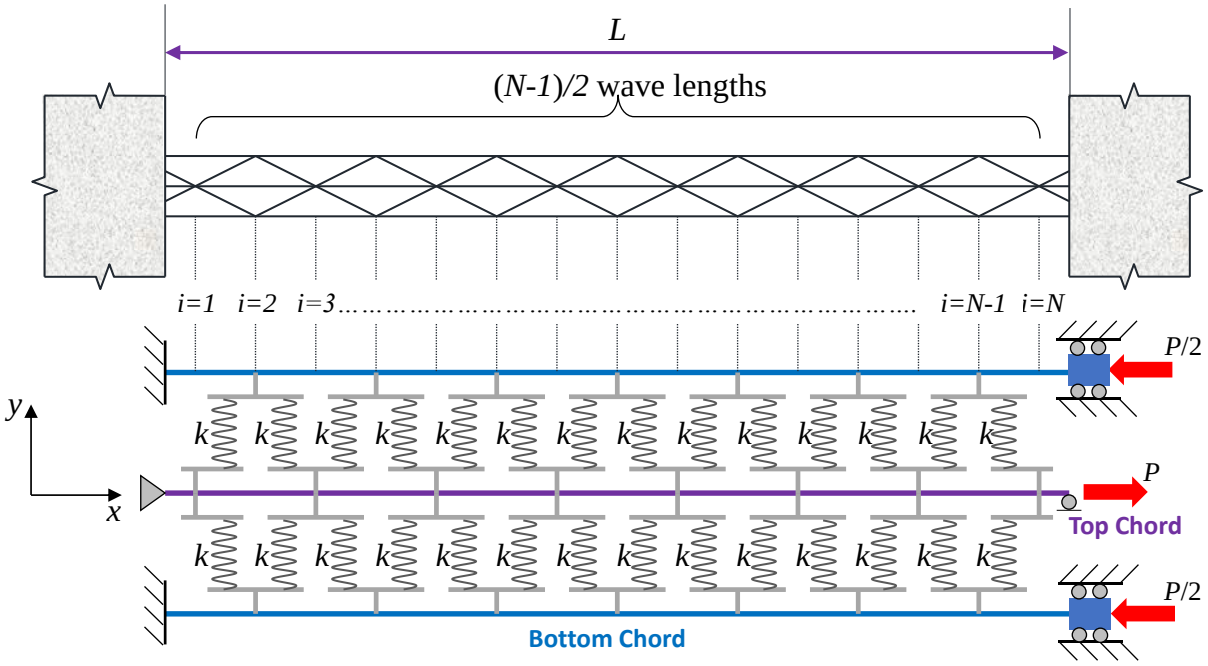

Figure 3-42 Analytical model of unbraced wire truss under constant moment

As web members serve the purpose of preventing the bottom chords and the top chords from laterally deforming, and as the web members can be assumed behaving linear-elastically, it is legitimate to model the web members as springs with a stiffness of k. The value of k is believed to

be related to the material properties, the second moment of inertia, the inclination, the length, and the fixity at both ends of the web member. The stiffness *k*, thus, can be an indication of wire trusses' quality, which will be introduced in later sections. Admittedly, the stiffnesses of the first and the last springs are expected to be higher than *k* because the first and the last web members have shorter lengths and connect to a fixed end. Nevertheless, the difference is not anticipated to be significant. Neglecting the potential higher stiffness is considered conservative.

From the typical configuration of the wire truss shown, each of the intersections is attached to two of the springs. To reflect the fact that each intersection has only one lateral displacement and the compatibility with the ends of the two connected springs, a rigid T-shaped element is placed in between. With the well-positioned T-shape elements, the displacement difference of both ends of each spring can be determined, as shown in Figure 3-43. For instance, for the two springs attached to the T-shape element at *i*, the left one has a displacement difference Δ_{il} as shown in Eq. (3-10); while the right one Δ_{ir} as shown in Eq. (3-11). It should be noted that the values of y_0 and y_{N+1} are both assumed zero because they are located at the fixed ends where no lateral displacement is allowed.

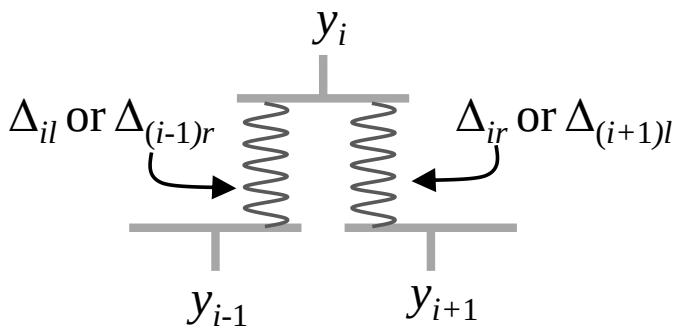

Figure 3-43 relative displacement in springs

$$\Delta_{il} = \Delta_{(i-1)r} = y_i - y_{i-1} \tag{3-10}$$

$$\Delta_{ir} = \Delta_{(i+1)l} = y_i - y_{i+1} \tag{3-11}$$

When the unbraced length is taking a constant moment, *M*, transferred from the concrete spans, the top chord is assumed taking a tension of *P*. By force equilibrium and symmetry, each of the bottom chords is taking a compression of *P*/2. As mentioned in early sections, the value of *P* is equal to the moment divided by the height of the wire truss, *M*/*h*.

To solve for the critical load P_{cr} and the corresponding critical moment M_{cr}, Rayleigh-Ritz approximation can be applied to avoid cumbersome differential equations. The fundamental concept behind Rayleigh-Ritz approximation is that given assumed deformation functions that satisfy boundary conditions, one can determine the structural responses by taking the variation of the total potential energy of the system as zero, as described in Eq. (3-12). It should be noted that

a bar on the top of each term in the equation indicates that the total energy is not the true value but an approximation.

$$\delta \bar{I} = \delta(\bar{U} + \bar{V}) = 0 \tag{3-12}$$

To begin with, it is necessary to assume lateral displacements of top and bottom chords as functions of *x* with boundary conditions satisfied. For the top chord, a typical choice can be a sinusoidal function as shown in Eq. (3-13). The parameter *b* is a constant.

$$y_t = b \sin\frac{\pi x}{L} \tag{3-13}$$

For the bottom chords, the same function is chosen for both bottom chords due to symmetry and for simplicity. To satisfy the boundary conditions, a typical choice can be expressed as Eq. (3-14) in which the parameter *a* is also a constant.

$$y_b = a(1 - \cos\frac{2\pi x}{L}) \tag{3-14}$$

With the chosen displacement functions [Eqs. (3-13) and (3-14)], the lateral displacement at the intersection *i* can be easily determined by substituting *x* with x_i as shown in Eq. (3-15) or Eq. (3-16) depending on whether the intersection is on the top chords or on the bottom chord. The stretch of the attached two springs can also be determined using Eqs. (3-10) and (3-11). In the meantime, the strain energy of the two springs can be determined using Eq. (3-17).

$$y_i = a\left(1 - \cos\frac{2\pi x_i}{L}\right) \text{ if } i \text{ is an even number} \tag{3-15}$$

$$y_i = b\left(\sin\frac{\pi x_i}{L}\right) \text{ if } i \text{ is an odd number} \tag{3-16}$$

$$\overline{U_{si}} = \frac{1}{2}k\Delta_{il}^2 + \frac{1}{2}k\Delta_{ir}^2 = \frac{1}{2}k(y_i - y_{i-1})^2 + \frac{1}{2}k(y_i - y_{i+1})^2 \tag{3-17}$$

Thus, the total strain energy of all springs can be determined by taking the summation of the strain energy of all springs on both sides, which can be expressed as Eq. (3-18).

$$\overline{U_s} = 2\sum_{i=1,3,5,\ldots}^{N} \frac{1}{2}k[(y_i - y_{i-1})^2 + (y_i - y_{i+1})^2] \tag{3-18}$$

On the other hand, strain energy is also stored in the top chords and both bottom chords as they are subjected to bending deformation. The general form of strain energy in terms of bending deformation can be expressed as Eq. (3-19), where *E* and *I* are the elastic modulus and the second moment of inertia of the member, respectively.

$$\int_0^L \frac{1}{2} EI(y'')^2 dx \tag{3-19}$$

Substituting the curvature y'' with the second derivative of the assumed displacement functions for the top chord and the bottom chords [Eqs (3-13) and (3-14)] and taking the summation deliver the total strain energy of all chords as Eq. (3-20). Expanding Eq. (3-20) obtains Eq. (3-21).

$$\overline{U_b} + \overline{U_t} = 2\int_0^L \frac{1}{2} EI \frac{d^2}{dx^2}[a\left(1 - \cos\frac{2\pi x}{L}\right)]^2 dx + \int_0^L \frac{1}{2} EI \frac{d^2}{dx^2}[b \sin\frac{\pi x}{L}]^2 dx \tag{3-20}$$

$$\overline{U_b} + \overline{U_t} = \frac{8a^2 EI\pi^4}{L^3} + \frac{b^2 EI\pi^4}{4L^3} \tag{3-21}$$

On the other hand, potential energy is equal to negative work done by the external forces of the system. It can be seen in Figure 3-42 that a force $P/2$ is acting on the end of each bottom chord where the axial shortening at the end can be generally expressed as Eq. (3-22) and therefore the total potential energy of the two can be calculated using Eq. (3-23).

$$\Delta_{\text{end}} = \int_0^L \frac{1}{2}(y')dx \tag{3-22}$$

$$\overline{V_b} = 2 \times \left[-\frac{1}{2} P \int_0^L \frac{1}{2} a \frac{d}{dx}\left(1 - \cos\frac{2\pi x}{L}\right) dx\right] = -a^2 P \frac{\pi^2}{L} \tag{3-23}$$

Similarly, the potential energy caused by the external forces acting on the end of the top chords can be calculated by multiplying P with the axial displacement. However, because the force P has a direction opposite to that of the axial displacement, the work done by the force has a negative sign which cancels out the negative sign of the potential energy, as shown in Eq. (3-24).

$$\overline{V_t} = \left[-(-P)\int_0^L \frac{1}{2} b \frac{d}{dx}\left(\sin\frac{\pi x}{L}\right) dx\right] = \frac{1}{4} b^2 P \frac{\pi^2}{L} \tag{3-24}$$

With Eqs. (3-18), (3-21), (3-23), and (3-24), one can determine the total potential energy of the system $\bar{I}$ by taking the summation of $\overline{U_b}$, $\overline{U_t}$, $\overline{U_s}$, $\overline{V_b}$, and $\overline{V_t}$, as shown in Eq. (3-25), where y_i is defined as Eqs. (3-15) and (3-16).

$$\bar{I} = \frac{8a^2 EI\pi^4}{L^3} + \frac{b^2 EI\pi^4}{4L^3} + \sum_{i=1,3,5,\ldots}^{N} k[(y_i - y_{i-1})^2 + (y_i - y_{i+1})^2] + \frac{1}{4} b^2 P \frac{\pi^2}{L} - a^2 P \frac{\pi^2}{L} \tag{3-25}$$

According to Rayleigh-Ritz method, the critical load P_{cr} can be determined by equating the partial derivatives of $\bar{I}$ with regard to a and b to zero individually, which are expressed as Eqs. (3-26) and (3-27).

$$\frac{\partial I}{\partial a} = a\left[\frac{16EI\pi^4}{L^3} - 2P\frac{\pi^2}{L} + 4k\sum_{i=2,4,6,\ldots}^{N-1}\left(\cos\frac{2\pi x_i}{L} - 1\right)^2\right] + b\left\{2k\sum_{i=1,3,5,\ldots}^{N}\sin\frac{\pi x_i}{L}\left[\left(\cos\frac{2\pi x_{i-1}}{L} - 1\right) + \left(\cos\frac{2\pi x_{i+1}}{L} - 1\right)\right]\right\} = 0 \quad (3\text{-}26)$$

$$\frac{\partial I}{\partial b} = b\left[\frac{EI\pi^4}{2L^3} + \frac{1}{2}P\frac{\pi^2}{L} + 4k\sum_{i=1,3,5,\ldots}^{N}\sin^2\left(\frac{\pi x_i}{L}\right)\right] + a\left\{2k\sum_{i=1,3,5,\ldots}^{N}\sin\frac{\pi x_i}{L}\left[\left(\cos\frac{2\pi x_{i-1}}{L} - 1\right) + \left(\cos\frac{2\pi x_{i+1}}{L} - 1\right)\right]\right\} = 0 \quad (3\text{-}27)$$

Rewriting Eqs. (3-26) and (3-27) as a matrix form yields Eqs. (3-28) through (3-32).

$$\begin{bmatrix} K_{11} & K_{12} \\ K_{21} & K_{22} \end{bmatrix}\begin{bmatrix} a \\ b \end{bmatrix} = \begin{bmatrix} 0 \\ 0 \end{bmatrix} \quad (3\text{-}28)$$

in which

$$K_{11} = \frac{16EI\pi^4}{L^3} - 2P\frac{\pi^2}{L} + 4k\sum_{i=2,4,6,\ldots}^{N-1}\left(\cos\frac{2\pi x_i}{L} - 1\right)^2 \quad (3\text{-}29)$$

$$K_{21} = 2k\sum_{i=1,3,5,\ldots}^{N}\sin\frac{\pi x_i}{L}\left[\left(\cos\frac{2\pi x_{i-1}}{L} - 1\right) + \left(\cos\frac{2\pi x_{i+1}}{L} - 1\right)\right] \quad (3\text{-}30)$$

$$K_{12} = 2k\sum_{i=1,3,5,\ldots}^{N}\sin\frac{\pi x_i}{L}\left[\left(\cos\frac{2\pi x_{i-1}}{L} - 1\right) + \left(\cos\frac{2\pi x_{i+1}}{L} - 1\right)\right] \quad (3\text{-}31)$$

$$K_{22} = \frac{EI\pi^4}{2L^3} + \frac{1}{2}P\frac{\pi^2}{L} + 4k\sum_{i=1,3,5,\ldots}^{N}\sin^2\left(\frac{\pi x_i}{L}\right) \quad (3\text{-}32)$$

Regarding Eq. (3-28), as both *a* and *b* equal to zero becomes a trivial solution, it should be solved by taking the determinant of the matrix $\begin{bmatrix} K_{11} & K_{12} \\ K_{21} & K_{22} \end{bmatrix}$ as zero. Therefore, it becomes a quadratic equation of P_{cr}, and one can solve the equation for P_{cr} with known *k*, *EI*, *L* and x_i, expressed as

$$P_{cr} = f(k, EI, L, x_i) \quad (3\text{-}33)$$

3.4.3.2. Discussion

The applicability of Eq. (3-35) was discussed using properties of the wire trusses used in specimens that failed in buckling. Three unbraced lengths (*L*) in the equation (30 in, 38 in. and 49 in) were used. The coordinates x_i were determined by assuming a symmetric configuration and $x_{n+1} = x_n +$

web spacing/2, where the web spacing was 7.87 in. x_1 was assumed to be 3.195 in. for the case of 30 in; 3.26 in. for the case of 38 in.; 0.89 in. for the case of 49 in. Other than parameters of lengths and coordinates, the rigidity of one individual bottom chord was also necessary, which was calculated as 29000 kip/in.^{2} × $\pi(0.5)^4/64$ = 88.97 kip-in.^{2} With the determined parameters, the critical load P of the system, which corresponded to twice the force in one individual bottom chord or equaled the force in the top chord, was plotted regarding the stiffness k ,as shown in Figure 3-44.

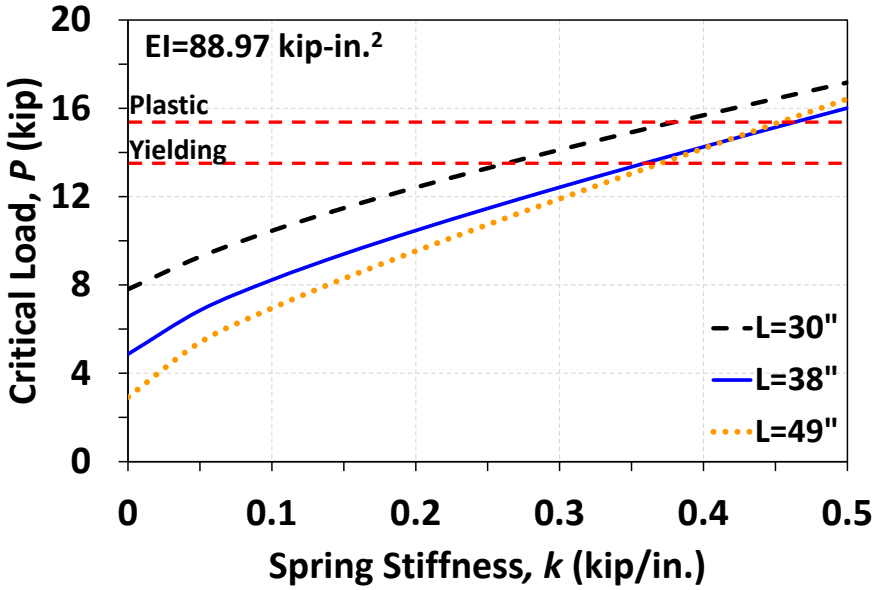

Figure 3-44 Critical load of the wire truss regarding web stiffness

It can be seen in Figure 3-44 that increasing the spring stiffness increases the critical load. When k is equal to zero, the critical loads are 7.8 kips, 4.9 kips, and 2.9 kips for the case of 30 in., 38 in., and 49 in., respectively; the values correspond to the exact Euler load of the bottom chords with those unbraced lengths and the fixed-fixed non-sway boundary condition.

Moreover, loads that correspond to the yield moment and plastic moment (assuming f_y = 78 ksi) are indicated in Figure 3-44 to demonstrate required spring stiffness that prevents buckling of bottom chords before reaching the yield or plastic moment. For the case of 30 in. the required spring stiffness is 0.251 kips/in. and 0.382 kips/in. for yield and plastic moments, respectively. For the case of 38 in., the required spring stiffness is 0.351 kips/in. and 0.455 kips/in. for yield and plastic moments, respectively. For the case of 49 in., the required spring stiffness is 0.368 kips/in. and 0.440 kips/in. for yield and plastic moments, respectively.

Associating the spring stiffness with the web member stiffness is not straightforward, as mentioned previously. Nevertheless, the structural configuration of web members can be simplified as bars connected with rotational springs under loads and tested, as shown in Figure 3-45. From the structural model in the figure, it can be determined that the spring stiffness has a range, given by

$$\frac{3EI}{l^3} < k < \frac{12EI}{l^3} \tag{3-34}$$

where *EI* and *l* are based on the web members. However, the value of *l* was still challenging to be determined as the weld size and actual configuration were affecting it. Taking *l* as 4.5 in. and using Eq. (3-34), the electro-welded wire trusses were expected to have a *k*-value between 0.289 kip/in. and 1.152 kip/in. and the hand-welded wire trusses had a *k*-value between 0.926 kip/in. and 3.707 kip/in. A squeeze test shown in Figure 3-45 indicated that the electro-welded wire trusses had a *k*-value of 0.95 kip/in. and the hand-welded wire trusses, 2.69 kip/in.

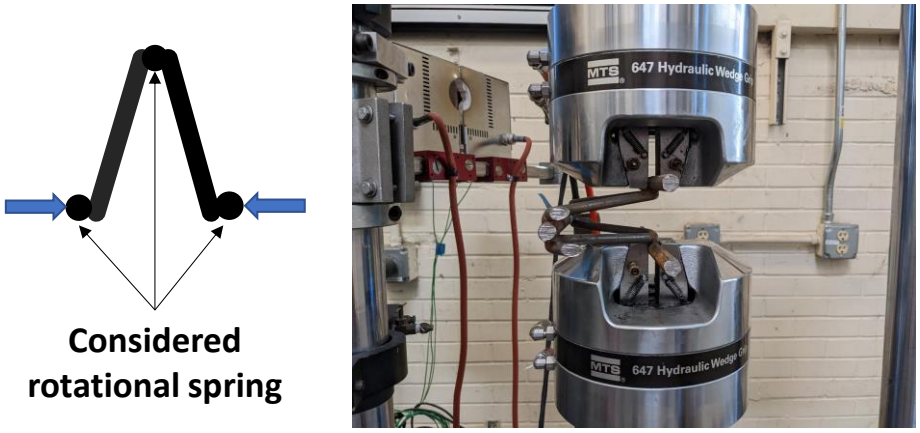

Figure 3-45 Simplified model and test for the determination of spring stiffness

As the *k*-values of the electro-welded wire trusses and the hand-welded wire trusses were higher than the required *k*-values to reach yield moment, it is explained that all wire trusses were able to exhibit the yield moment before buckling of the bottom chords. In addition, the *k*-value of the hand-welded wire trusses was larger than that of the electro-welded wire trusses, indicating that it had a higher critical load and therefore harder to cause buckling of the bottom chords. The analytical results were in good agreement with the experimental observations. It should be noted that the squeeze test was a demonstration and had no available standard procedure to follow. The introduced concept here is preliminary and needs further research.

3.4.4. Factor of Safety

To investigate the factor of safety for WTPD concrete panels, the first step was to study the relationship between the moment applied in the unbraced length and the end displacement. As mentioned in the previous sections, the yield moment of the unbraced span can be reasonably taken as a design baseline. Another important design consideration is the deflection of the overhang. Test results of specimens in Series I and Series IV were therefore normalized with regard to M_y and the shear span, as shown in Figure 3-46.

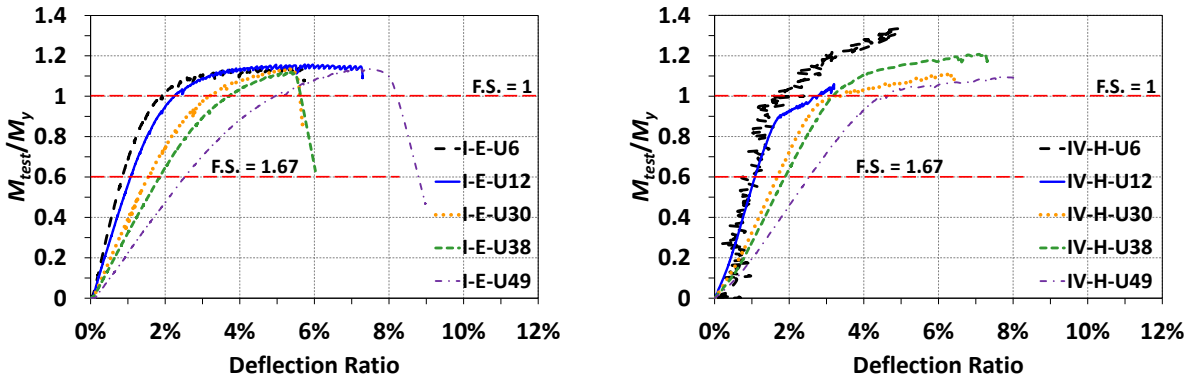

(a) Series I specimens (b) Series IV specimens

Figure 3-46 Moment-deflection ratio plots

In Figure 3-46, the vertical axis is the ratio of the test moment to the yield moment (M_{test}/M_y). The yield moment, according to the sectional analysis introduced in previous sections, is again shown for convenience as Eq. (3-35).

$$M_y = \frac{f_y\left(\frac{3\pi d_b^4}{64} + \frac{\pi d_b^2 h^2}{6}\right)}{\left(\frac{2}{3}h + \frac{1}{2}d_b\right)} \tag{3-35}$$

Per Eq. (3-35), the value of M_y is 178 kip-in. for electro-welded wire trusses; 158 kip-in. for hand-welded wire trusses. As M_y is considered the design baseline here, the reciprocal of the normalized moment, namely the value of M_y/M_{test}, is equivalent to the factor of safety (F.S.) at a certain magnitude of the applied moment.

In addition, the horizontal axis is the deflection ratio, defined as the ratio of the measured end displacement to the shear span (Δ/a). The deflection ratio can be considered approximately the rotation at the support, given that the concrete panel has a relatively small flexural deflection compared to the unbraced span.

It can be observed from Figure 3-46 that a certain level of the F.S. corresponds to a unique deflection ratio given a specified unbraced span length. For instance, when the F.S. equals 1.67, indicated as a redline in the charts, the deflection ratio for an electro-welded unbraced length of 30 in. is 1.54%, as shown in Figure 3-46(a). It should be noted that the F.S. value of 1.67 was selected per AASHTO LRFD. AASHTO LRFD requires construction loads to be amplified by a factor of 1.5 to account for dynamic effects. With a resistance factor of 0.9 for flexural behavior, the equivalent factor of safety is then 1.5/0.9=1.67. This F.S. level of 1.67 can be standard because the relationship between the F.S. and the deflection ratio is linear when F.S. is under 1.67 for all tested unbraced span lengths.

The two observations mentioned above facilitated the formulation of the F.S. with respect to the deflection ratio given an unbraced length. The deflection ratio at an F.S. of 1.67 was extracted and

plotted versus the unbraced length, as shown in Figure 3-47. The figure shows that electro-welded and hand-welded unbraced spans yielded approximately the same deflection ratios at a certain F.S. In other words, only one formula was needed to describe the relationship among the F.S, the deflection ratio, and the unbraced length, whether electro-welded or hand-welded wire trusses were considered. This result echoes that the two types of wire trusses had similar flexural rigidity, which is independent of the yield strength of the steel.

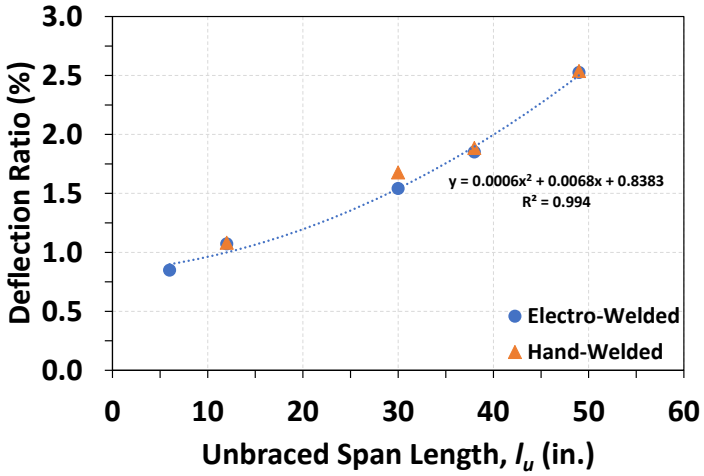

Figure 3-47 Deflection ratio at F.S. equal to1.67 of each specimen

Here, the series of electro-welded wire trusses were taken as representing the deflection ratio level. A trendline of the deflection ratio regarding the unbraced span length at F.S equal to 1.67 was generated and shown in Figure 3-47. It was found that a polynomial with a power of two closely represents the trend, which echoes the fact that flexural rotation is proportional to the length with a power of two given a certain rigidity. Through using the trendline equation shown in Figure 3-47 and the linear relationship between the F.S. and the deflection ratio, one can determine the deflection ratio by

$$\text{Deflection ratio (\%)} = (0.0006l_u^2 + 0.0068l_u + 0.8383)(\frac{1.67}{\text{F.S.}}) \qquad (3\text{-}36)$$

where the deflection ratio is in percentage; F.S. is the target factor of safety, which should be greater than 1.67.

Eq. (3-36) gives designers an approach to determining a reasonable factor of safety given a target deflection ratio. For instance, when the designer targets a deflection ratio of 1% for a hand-welded unbraced span length of 38 in., the F.S., generated by Eq. (3-36), is 3.28. In other words, the allowable construction moment should be limited to M_y/3.28 = (158 kip-in.)/3.28=48.2 kip-in. In addition, Eq. (3-36) can be used to determine the reserve capacity during construction. For example, if a deflection ratio of 2% is detected for an electro-welded unbraced span of 49 in., the bending moment is 81.6 kip-in., corresponding to 45.8% of the yield moment.

3.5. Summary

PCP with Wire Truss Testing was performed as part of TxDOT Project 0-7041: *Develop NextGen Texas Bridge Decks* in order to develop a full-width partial-depth precast panel (PCP) bridge deck. This load-testing investigated the strength and performance of 24 wire truss partial-depth (WTPD) PCPs with no cast-in-place concrete topping to evaluate the NextGen Bridge Deck's performance during the construction phase of a bridge deck, when the wire trusses will be exposed and unbraced by concrete. Two types of wire trusses were tested: electro-welded and hand-welded; several unbraced lengths suitable for TX girders were selected. Flexural behavior under four-point bending and shear behavior under cantilever loading were experimentally investigated. Based on the test results, the following conclusions can be drawn:

- The NextGen Bridge Deck WTPD PCPs exhibited an overall ductile load response that was primarily controlled by the plastic moment of the truss. Specimens tested in flexure developed load plateaus, indicating yielding of the top chords. After a load plateau developed, some specimens experienced global buckling of the bottom truss chords. Specimens with longer (30 in., 38 in., and 49 in.) unbraced truss spans had a higher propensity for bottom chord buckling.

- The bundling of additional No. 4 or No. 5 reinforcing bars to the bottom chords proved to completely eliminate global buckling in all of the specimens tested. Specimens with additional bundled bars generally reached slightly higher moment capacities as well, although not in every case.

- The yield strengths and geometries of the truss members played an important role in determining the post-yield response of WTPD PCPs. The electro-welded trusses had a higher yield strength in the chords, with more slender web members. Specimens with these trusses tended to experience global buckling of bottom truss chords sometime after reaching a load plateau if the unbraced truss length was large (30 in., 38 in., and 49 in.). This led to sudden load drops sometime after the load plateau developed. In contrast, the hand-welded wire trusses had lower yield strength in the chords and more stout web members. Although individual trusses were shown to occasionally buckle for the larger unbraced truss lengths, these specimens did not exhibit significant buckling-type behavior in their load-deformation curves, nor any sudden load drops.

- The moment capacity of the WTPD PCPs can be estimated as the bending moment that yields the top chords of the wire trusses. The baseline can be the onset of yielding of the top chords (the yield moment) or the yielding of the entire top chords (the plastic moment). The WTPD PCPs developed load plateaus after extreme top chord yielding, so this procedure produced results that were reasonably accurate and marginally conservative on average.

- The shear response of the wire trusses was determined by the properties of the web members. The electro-welded trusses had more slender web members, and therefore exhibited buckling of individual web members when loaded in high shear, resulting in a rapid drop in load-carrying capacity. It was determined that an effective length factor of $K = 1.1$ was appropriate for the web members of the electro-welded trusses. In contrast, the hand-welded truss web members were less slender and did not buckle. Instead, they held up under shear testing until the specimen experienced largely load plateauing.

- Specimens III-E-U6-SC and VI-H-U6-SW-C experienced premature failures related to the inadequate embedment of the wire trusses into the concrete panels. Specimen III-E-U6-SC failed via slippage of the wire truss out of one of the panels, and Specimen VI-H-U6-SW-C failed via flexural and shear cracking of the concrete panel. In the case of Specimen III-E-U6-SC, the wire trusses were not well-developed in the concrete which led to delamination and pull-out of the chord bars, causing extreme deflections of the panel. For Specimen VI-H-U6-SW-C, shear and flexural effects were not properly transferred to the wire trusses, causing the concrete panel to flex and crack. The lack of wire truss embedment led to a lack of reinforcement to arrest the crack formation, causing rapid load dropping, and thus failure.

- An analytical method for the buckling behavior of wire trusses was developed. It was shown that the lateral stiffness of web members is important to achieve the yield strength or the plastic strength before the occurrence of buckling. More studies are needed to accurately verify the analytical method for estimating the buckling load of wire trusses under flexural bending or shear force.

- The factor of safety during construction can be determined with design yield strength, specified unbraced span, and desired deflection ratio using the developed method. A factor of safety of 1.67 was recommended per AASHTO LRFD.

Chapter 4. Full-Scale Bridge Deck Structural Test

This chapter reviews the experimental program for structure performance of NextGen Texas bridge decks. Following the introduction of the experimental program, test results and discussion are also presented.

4.1. Overview of Test Plan

The primary purpose of the experimental program was to investigate the behavior of full-scale wire truss bridge decks subjected to AASHTO LRFD design loads. The viability of such bridge decks was to be evaluated by comparing the test results to those of the experimental program of Project 0-4418, where current partial depth precast prestressed panel decks in Texas were introduced. To achieve the objectives, full-scale wire-trussed bridge decks were fabricated and tested as schematically shown in Figure 4-1.

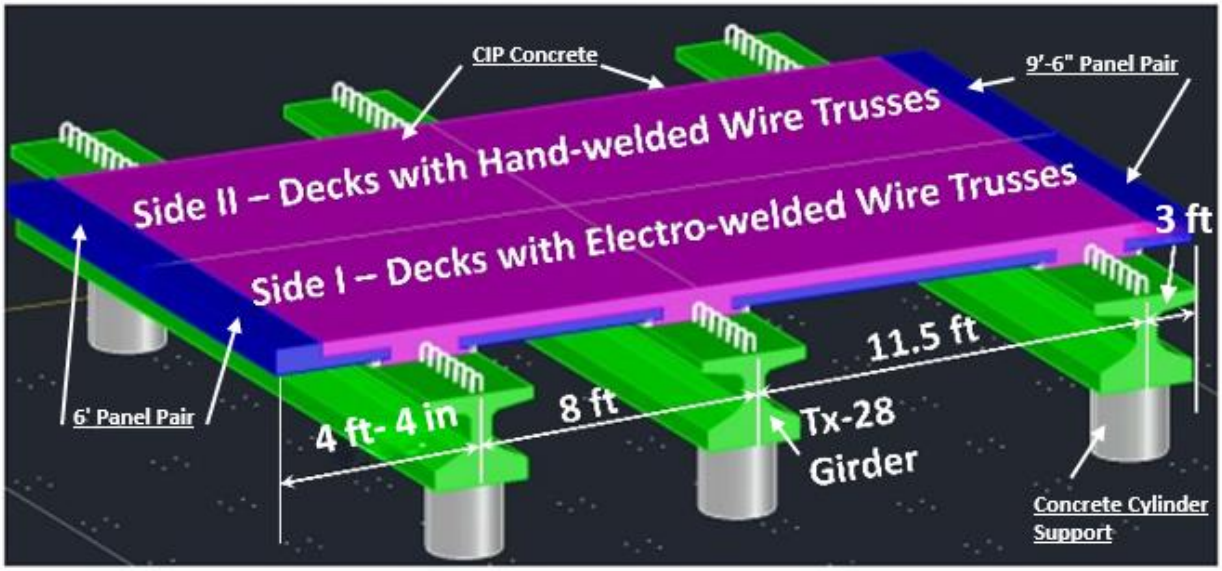

Figure 4-1 Schematic Full-scale bridge deck structural test

To simulate real-world configurations, the test specimen, as shown in Figure 4-1, was designed to be supported by three 25-ft-long Tx-28 girders. The Tx-28 girders were chosen to accommodate the TxDOT typical top flange width of 36 in. and typical R-bar spacings. This flange width was selected as a majority of the Tx Girders, which have 36-in.-wide top flanges, resulting in the representation of behavior in real-world as-built conditions. The three girders were spaced at 8 ft and 11.5 ft, simulating common deck spans in the field. To accommodate the girder spaces, two different panel pair widths (perpendicular to the girders), 6 ft and 9ft-6in. were used.

The overhang lengths from the exterior girders' centerline had lengths of 3 ft. and 4 ft-4 in.; the former represented common overhang length in Texas, and the latter represented the maximum

length encountered in the field according to AASHTO for a 36-in. top flange. The girders were placed onto cylindrical reinforced concrete supports.

The test specimen consisted of four WPTD panel pairs, denoted in Figure 4-1, which are described in detail in later sections. Two of the WPTD panel pairs were fabricated with electro-welded trusses, and the other two panel pairs were fabricated with hand-welded trusses. Each of the panel pairs was designed to have a length of 8 ft, making the total length of the specimen 16 ft. No reinforcement was across the transverse joint to avoid affecting the other side when testing. After the placement of the panel pairs, CIP concrete topping, denoted in Figure 4-1, was to be cast on top of the panel pairs to form a full-depth bridge deck. Loading was to be applied through rams and tensioning rods on the top of the bridge deck specimen, which is described in later sections.

4.2. Specimen Design and Schedule

The full-scale bridge deck specimen consisted of four separate WTPD panel pairs. Each panel pair was fabricated by connecting a PCP and an overhang with continuous wire trusses throughout both concrete elements. The overhang had an end curb through its length, serving as a side form for later CIP concrete topping. An example fabricated panel pair can be seen in Figure 4-2.

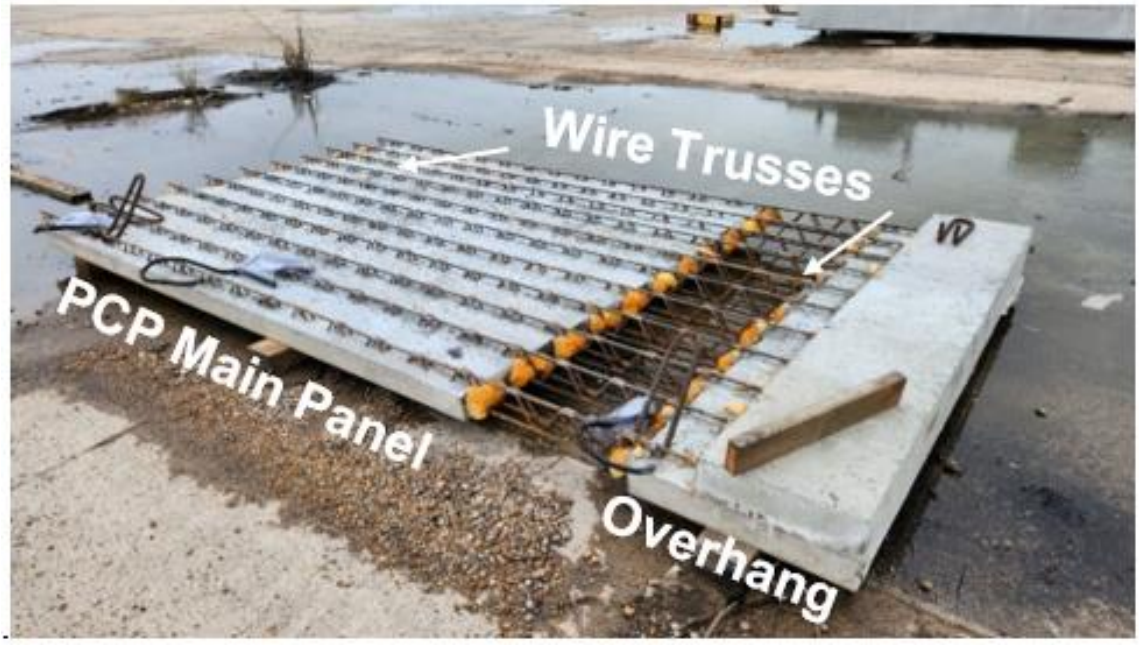

Figure 4-2 Fabricated panel pair

The four panel pairs, as mentioned previously, were designed to have differences in the panel widths, overhang panel widths, and truss type for the purpose of accommodating the design of the full-scale deck specimen, as summarized in Table 4-1. Regarding the truss type, the type of hand-welded wire trusses was made with Grade 60 steel, while the electro-welded wire trusses were Grade 75. For simplicity, the following panels will be named by the following rules: WTPD type

- PCP Panel Widths. For example, Panel 1 and Panel 4 will be referenced in this chapter as “HW – 9’-6”“ and “EW – 6’” respectively.

Table 4-1: Panel Pair schedule

Panel Pair Number	Truss Type	PCP Main Panel Width	Overhang Width *
1	HW: Hand-Welded	9'-6"	3'
2	HW: Hand-Welded	6'	4'-4"
3	EW: Electro-Welded	9'-6"	3'
4	EW: Electro-Welded	6'	4'-4"

* Distance measured from girder centerline to free edge

The varying PCP panel widths, overhang panel widths, and truss types were scheduled to experimentally capture a larger range of representative cases that are expected to be utilized in real-world structures. The PCP panel width 9’-6” was according to the maximum width prescribed in TxDOT Miscellaneous Detail Sheets – PCP-FAB - Prestressed Concrete Panel Fabrication Details. PCP Panel Widths of 9’-6” and 6’ were selected to capture the maximum PCP Panel Width as well as a reasonable middle ground PCP panel width. The panel length of all Panel Pairs was selected to be 8 ft according to TxDOT standard practice and the maximum shipping size for a truck without special permits.

Further, the maximum overhang width for a 36-in-wide flange is 4 ft-4 in. from the Tx-28 girder centerline as prescribed from TxDOT BDM LRFD Chapter 3 Section 2, which then references AASHTO LRFD Article 4.6.2.1.6. An overhang panel width of 3 ft-4 in. corresponded to an overhang width of 4 ft-4 in. from the girder centerline, which captured the maximum prescribed overhang width for a 36-in.-wide flange. An overhang panel width of 2 ft corresponded to an overhang width of 3 ft from the girder centerline, which captured the typical TxDOT overhang design for 36-in-wide flanges.

The reinforcement of the PCP panel pairs were detailed according to the reinforcement details of a typical PCP per TxDOT Miscellaneous Detail Sheets – PCP-FAB - Prestressed Concrete Panel Fabrication Details. Similar reinforcement details were prescribed for the purpose of minimizing unnecessary changes to typical designs, avoiding fabrication challenges at precast plants, as well as maintaining typical TxDOT details that have already been extensively used in the field. In particular, the wire trusses were spaced at 9 in., as proven effective in resisting construction loading in Chapter 3. A 3-in truss projection was provided at the edge of the PCP panel, comparable to the strand projection in typical PCP panels. In the direction transverse to the wire trusses, No. 3 bars spaced at 6 in. were provided under the wire trusses as bottom mat reinforcement. The reinforcement details in the plan view for the 9 ft-6 in. and 6 ft panel pairs are provided in Figure 4-3 and Figure 4-4, respectively. It should be noted that only the top chord of the transverse WTPD is shown, as well as only the bottom mat reinforcement is shown in the plan views.

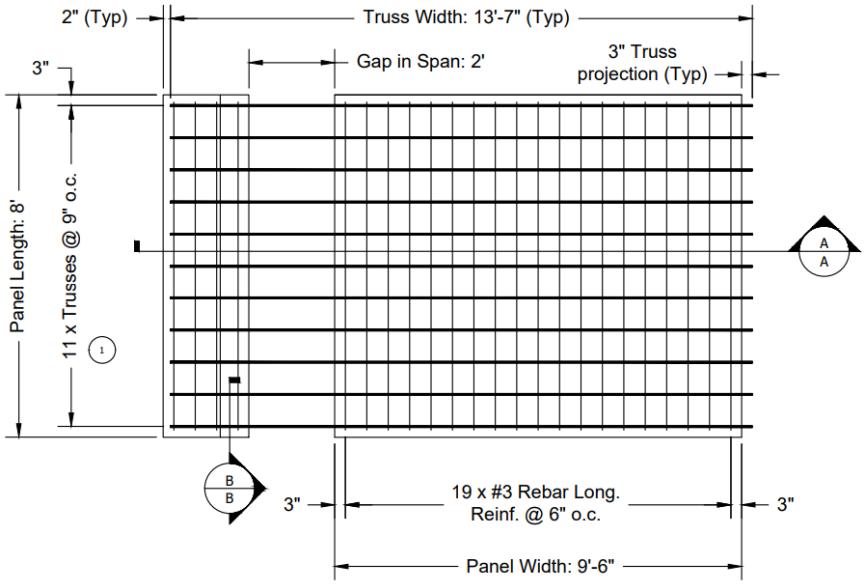

(a) Plan View

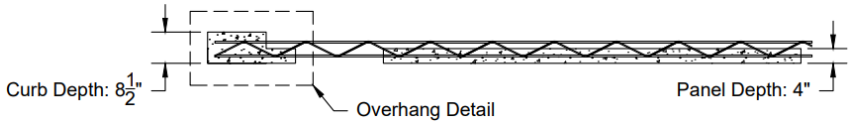

(b) Section A-A

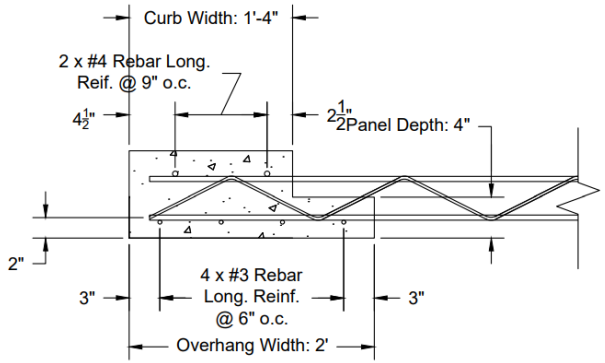

(c) Overhang Detail

Figure 4-3 9'-6" Panel Pair Details

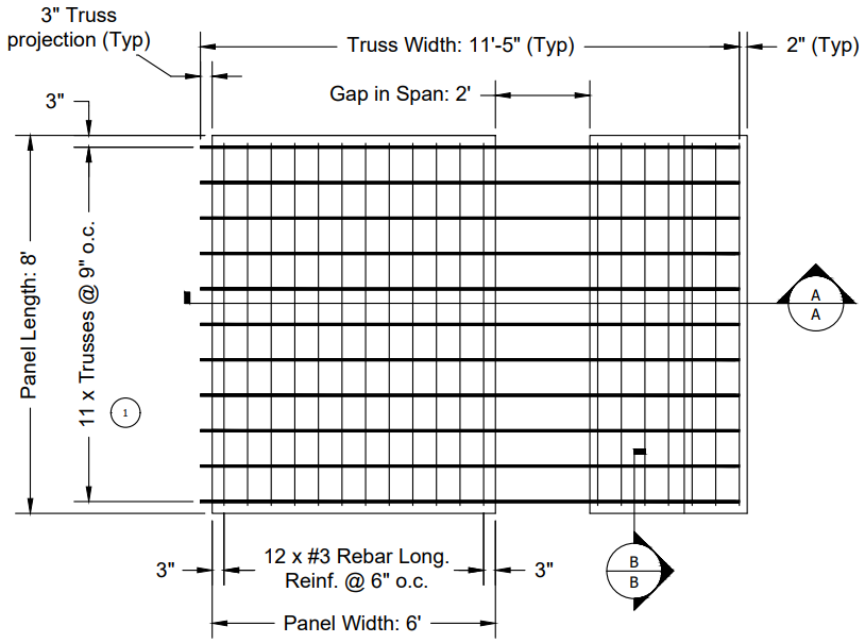

(a) Plan View

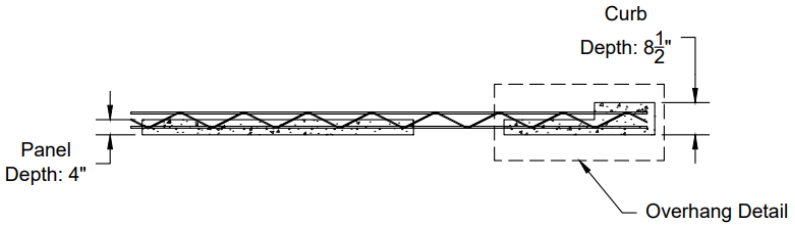

(b) Section A-A

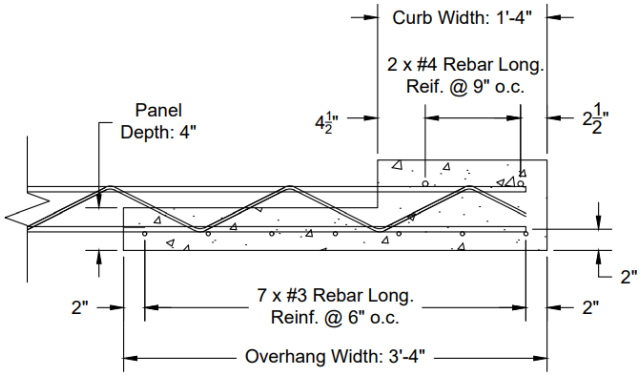

(c) Overhang Detail

Figure 4-4 6' Panel Pair Details

Since the objective of the panel pairs was to speed up construction by eliminating the need for overhang formwork, a precast full-depth curb was included in the panel pair designs to retain the cast-in-place top layer concrete. The details of the precast full-depth curb were modeled to be as similar as possible to previously designed TxDOT precast concrete overhang designs; in particular, the design was modeled after TxDOT Detail Sheet - PCP(O)-FAB – Precast Concrete Panels for Overhangs Fabrication Details. Section and overhang details can be found in Figure 4-3(b) and Figure 4-3(c) for the 9 ft -6 in. panel pairs, as well as Figure 4-4(b) and Figure 4-4(c) for the 6' panel pairs. The curb width was designed as 1 ft-4 in. to accommodate screed railing in the field. It should be noted that screed railing was not used in the lab fabrication.

4.3. Precast Panel Pair Specimen Fabrication

Since the designs of the panel pairs were unique, careful collaboration and considerations were taken to ensure that WTPD panel pairs are feasible to fabricate. This section dives into the challenges faced with fabricating the panel pairs and specifically highlights the solutions to these challenges to ensure proper fabrication.

As mentioned previously, four panel pairs were to be used in the full-scale bridge deck specimens. Each of the four panel pairs had its particular width and therefore required a specific length of the wire trusses. In this regard, the wire trusses were fabricated and shipped to the FSEL, where the research team then cut the trusses to specified lengths and stacked them for shipment to a local precast plant, as shown in Figure 4-5.

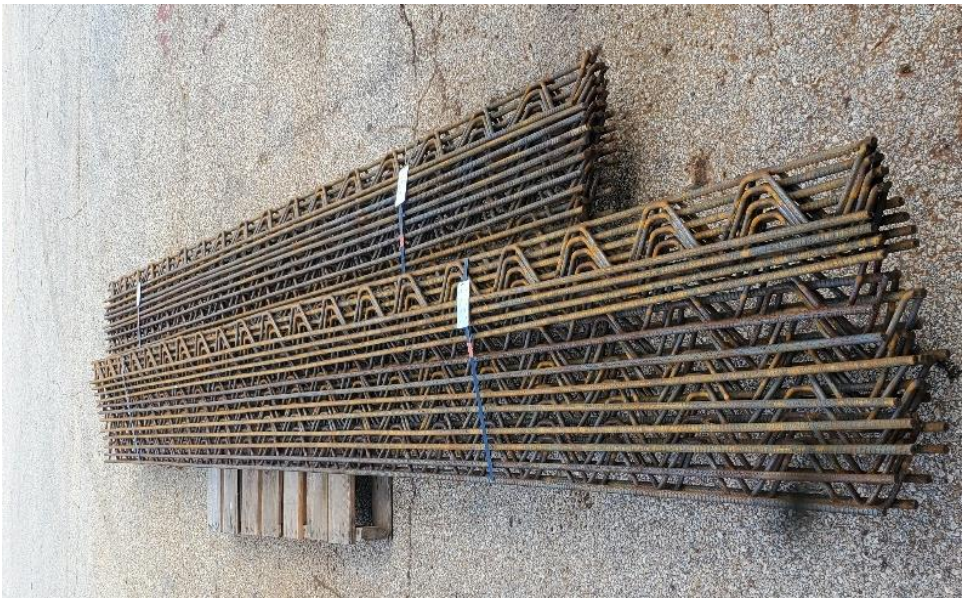

Figure 4-5 Cut and Bundled Trusses

At the precast plant, the wire trusses were placed into steel bed formwork, as shown in Figure 4-6. Typical 8 ft steel side forms were utilized along with lumber end forms to make the PCP main panel have the desired length and width. Special lumber formwork was needed to allow for the

casting of the end curb as well as create the gap between the main PCP panel and the overhang, which can be seen in Figure 4-7. The lumber formwork was cut with slots to allow the wire trusses to pass through without conflicts. Spray foam was used to seal the gaps between the slots and wire trusses to prevent concrete from flowing out.

Figure 4-6: Trusses and Lumber Formwork in Standard Precast Bed

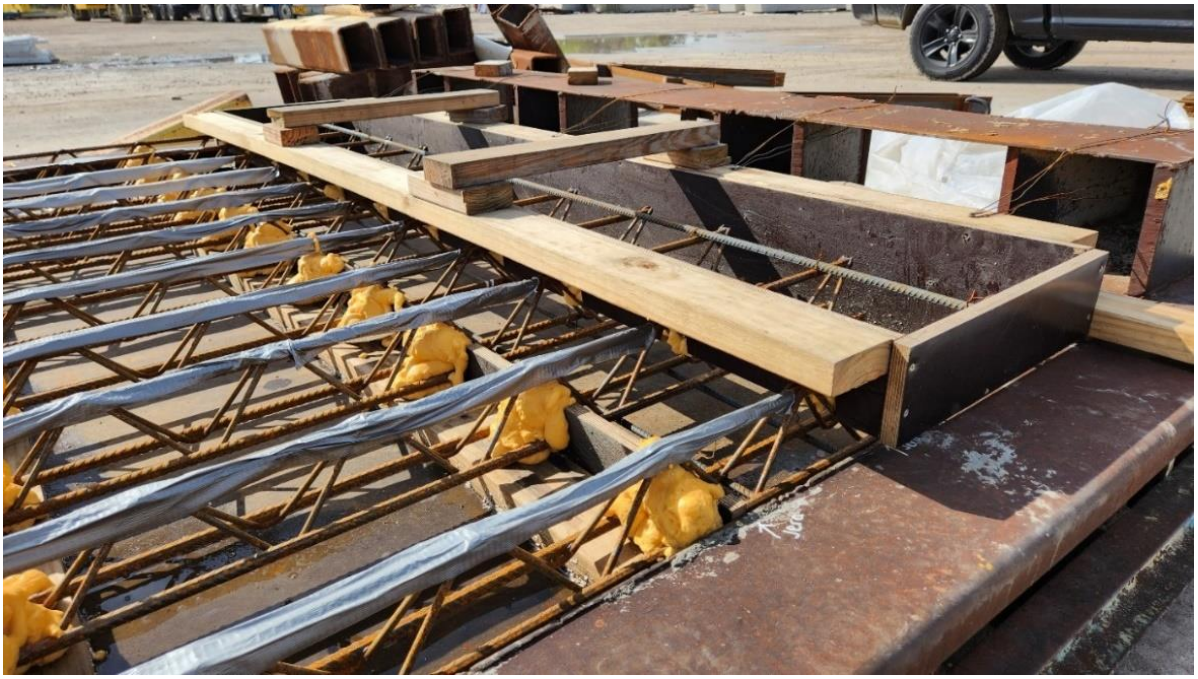

Figure 4-7: Full-Depth Curb Lumber Formwork

Regular fabrication equipment and typical concrete pouring practices were used for the panel pairs, as shown in Figure 4-8. Before casting, duct tape was used to keep the top chord of the trusses clean of concrete. The concrete type was a typical mix for precast members (Type H) in Texas. While casting, typical vibrating techniques were used for concrete consolidation, as seen in Figure 4-9. Vibrating was performed with extra care as not to vibrate the trusses out of their formwork. The top surfaces of the panel pairs were finished with a hand float, but no special roughening techniques were used. Regular moist curing techniques were used, as shown in Figure 4-10. After casting, moist burlap was used to cover the finished surface, preventing water evaporation. It should be noted that the EW – 9'-6" panel pair had a delay in casting due to unexpected early concrete setting that seemingly caused a slight cold joint near the testing region. Nevertheless, the impact of the cold joint on the structural behavior of the side with EW – 9'-6" panel pair was deemed to have little to no effect to the structural capacity of the bridge deck, which will be introduced in later sections.

Figure 4-8: Panel pair concrete pouring

Figure 4-9: Panel pair concrete vibrating

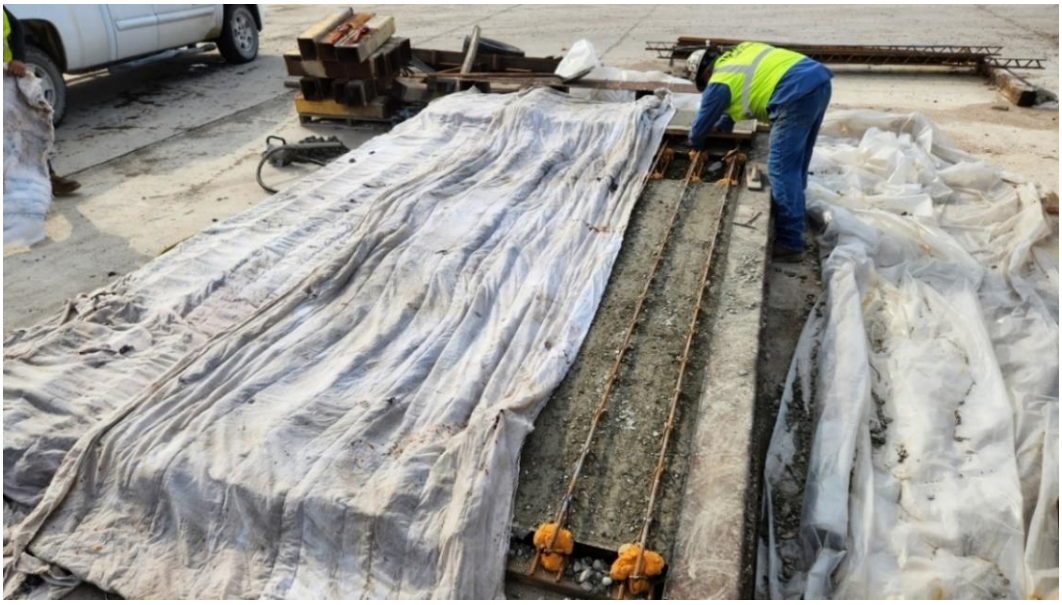

Figure 4-10: Moist burlap covering panel pairs

Shipping the finished panel pairs entailed little to no extra difficulty compared to standard PCPs. The panel pairs were stacked on top of each other to ship compactly, as shown in Figure 4-11. In the design of the panel pairs for the current task, rail anchorage bars were not included; nevertheless, similar shipping practices are expected to be effective.

Figure 4-11: Stacked panel pairs shipped to FSEL

Collaborating and working with a local precast plant helped accelerated fabrication immensely. It was evident that fabricating WTPD PCP panel pairs has little to no extra difficulties compared to fabricating traditional PCPs.

4.4. Lab Fabrication

Lab fabrication of the full-scale WTPD bridge deck specimen included five major steps, including: 1) the placement of the steel loading frame, 2) the placement of supports and Tx-28 girders, 3) the placement of WTPD PCP panel pairs, 4) the placement of top mat reinforcement and lap-splices, and 5) forming and casting of the CIP concrete topping.

Firstly, the steel formwork was placed and tensioned on the FSEL strong floor. Then, six cylindrical concrete supports with a height of 24 in. were placed onto the strong floor, serving to level and support the Tx-28 girders to ensure sufficient clearance for the loading system and instrumentation. After the supports were positioned, three Tx-28 girders with pre-embedded R-bars were craned onto the supports at the planned girder spacings. The Tx-28 girders were 9 ft longer than the total length of the designed deck specimen for later forming and fencing. Bedding strips with cross-sectional dimensions of 2 in. by 2 in. were then glued and placed on the edges of the Tx28-girder flanges, where the fabricated panel pairs were later placed. The completed supporting system is shown in Figure 4-12.

Figure 4-12: Supports and Tx28-girders

Upon the completion of the supporting system, the panel pairs were craned into place by resting them on top of the bedding strips secured to the Tx-28 girders, as seen in Figure 4-13. It should be noted that at times, it was difficult to place the panel pairs onto the girders due to conflicts between the R-bars and wire trusses, which would not occur when placing traditional PCPs. When positioning the panel pairs, a sledgehammer was used to bend some of the R-bars out of the way of wire trusses. For real-world construction, it is recommended to carefully detail R-bars or shear studs on the top flange of the girders to avoid clashes, or the contractor can cut and/or bend the problem R-bars.

Figure 4-13: Placement of panel pairs

After placing the panel pairs, the top mat longitudinal reinforcement was tied into place. Since the top chords of the wire trusses already provide the top mat transverse rebar, only the longitudinal top mat rebar was placed, as shown in Figure 4-14. It should be noted that the top mat longitudinal rebar did not require rebar chairs, as the longitudinal reinforcement could be tied directly to the

top chord of the trusses. The longitudinal top mat reinforcement consisted of No. 4 bars spaced at 9 in., following common practice for TxDOT bridges. Between two panel pairs of different spans, a gap formed above the middle Tx-28 girder where the trusses terminate. To ensure moment transmission, lap-splices were provided to the top chords, as shown in Figure 4-14. The lap-splice length was 39 in. on each side of the girder centerline, making the total length of the lap splice bar 6 ft- 6 in.

Figure 4-14: Reinforcement and lap-splice

Lumber side forms and safety railings were constructed and anchored to the Tx-28 girders before pouring the cast-in-place concrete topping. Only the two transverse sides of the deck needed to be closed with formwork, as the overhangs had end curbs to contain the wet concrete. A concrete hopper lifted by an overhead crane transported the fresh concrete from the ready-mix concrete truck to the bridge deck for casting. Standard concrete vibration and screeding were conducted while casting. Casting and finished bridge deck specimen can be seen in Figure 4-15

Figure 4-15: Casting and finished WTPD deck specimen

4.5. Test Setup

4.5.1. Test Plan and Schedule

The research team planned ten loading patterns at different load levels on the WTPD bridge deck to capture the performance at service and ultimate loading conditions. A summary of the location of all planned tests can be found in Figure 4-16. The ten tests consisted of five unique tests on the two different truss types. For example, Tests 1 and 2 are the same as Tests 3 and 4, except for the tests being performed on different truss types. This gives the research team the ability to directly compare the impact of truss type on the structural behavior of the WTPD bridge deck for each of the five unique test types.

The five unique test types consisted of the following: 1) negative moment over the second girder, 2) positive moment over the short span, 3) positive moment over the long span, 4) short overhang, and 5) long overhang. It should be noted that the negative moment over the second girder and positive moment over the short span tests were only to be brought up to service loads, whereas the positive moment over the long span, short overhang, and long overhang tests were all brought to their respective ultimate capacities. Table 4-2 details a summary of the testing schedule matrix.

Table 4-2: Testing Schedule Matrix

Test #	Test Type	Truss Type	Loading
1	Negative moment over second girder	Electro-welded	Service
2	Positive moment short span	Electro-welded	Service
3	Negative moment over second girder	Hand-welded	Service
4	Positive moment short span	Hand-welded	Service
5	Positive moment long span	Hand-welded	Ultimate
6	Short overhang	Hand-welded	Ultimate
7	Short overhang	Electro-welded	Ultimate
8	Positive moment long span	Electro-welded	Ultimate
9	Long overhang	Hand-welded	Ultimate
10	Long overhang	Electro-welded	Ultimate

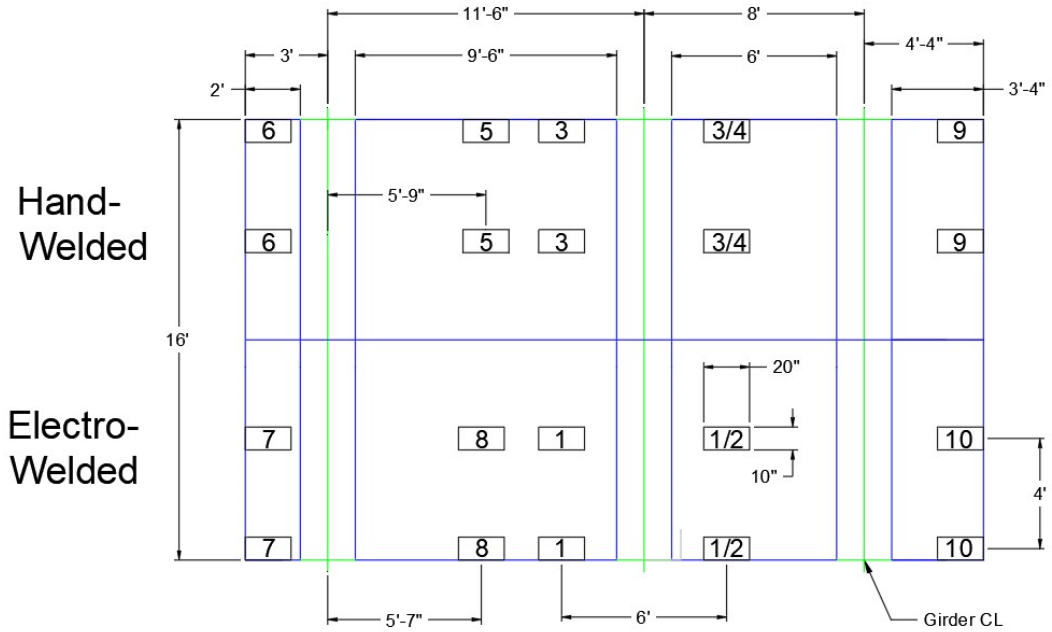

Figure 4-16: Testing Schedule

All tests have at least a pair of load points, which are separated by 4 ft in the longitudinal direction to simulate the design tandem loads. In the case of the negative moment over the second girder, two sets of these pairs spaced 6 ft apart in the transverse direction are utilized to simulate a tandem axel straddling the second girder. The research team designed the loading patterns so that the loading plates were all located in positions to maximize stresses in the bridge deck. All load-bearing plates were 10 in. by 20 in. by 2 in., simulating the footprint of tandem loads according to AASHTO LRFD. It should be noted that the test numbers represent the order in which the bridge was tested.

The negative moment over the second girder and positive moment over the short span tests were only tested up to service loads and not to ultimate failure loads. The research team decided to test only these regions to service loads to preserve the structural integrity of the bridge for later tests. The positive moment over the long span and the two overhang tests were tested to ultimate failure loads to evaluate the deck overall capacity and if the wire trusses' webs would add additional capacity to the decks. The wire trusses' webs could have the ability to behave similarly to stirrups in beams, and thus provide additional shear capacity.

4.5.2. Loading System

The loading system for the full-sized specimen is shown in Figure 4-17. The loading system consisted of floor beams, reaction channels, tensioning rods, and rams. The floor beams were post-tensioned to the strong floor in FSEL to serve as part of the reaction system. Back-to-back C-channels were installed on top of the floor beam, allowing for the loading rods to be adjusted and matched with desired loading points. The 1-1/4-in. diameter-150 ksi loading rods, 200-kip rams, 10 in. by 20 in. by 2 in. steel loading plate, and load cells were used to apply the load on the deck. The loading rods went through the full depth of the deck, which required 2 in. diameter holes to be cored through the precast and cast in place concrete layers.

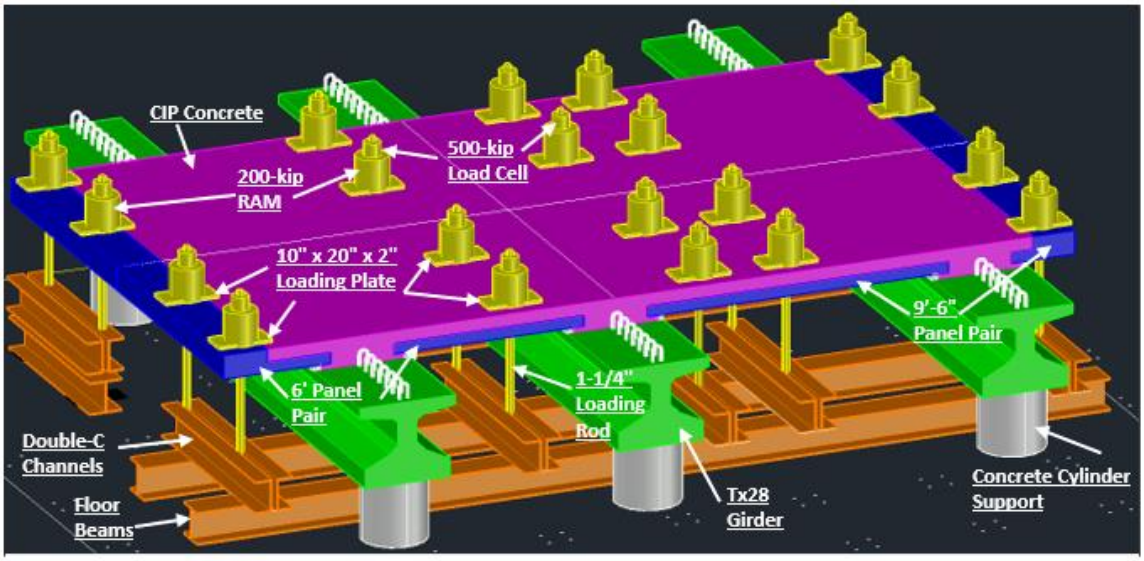

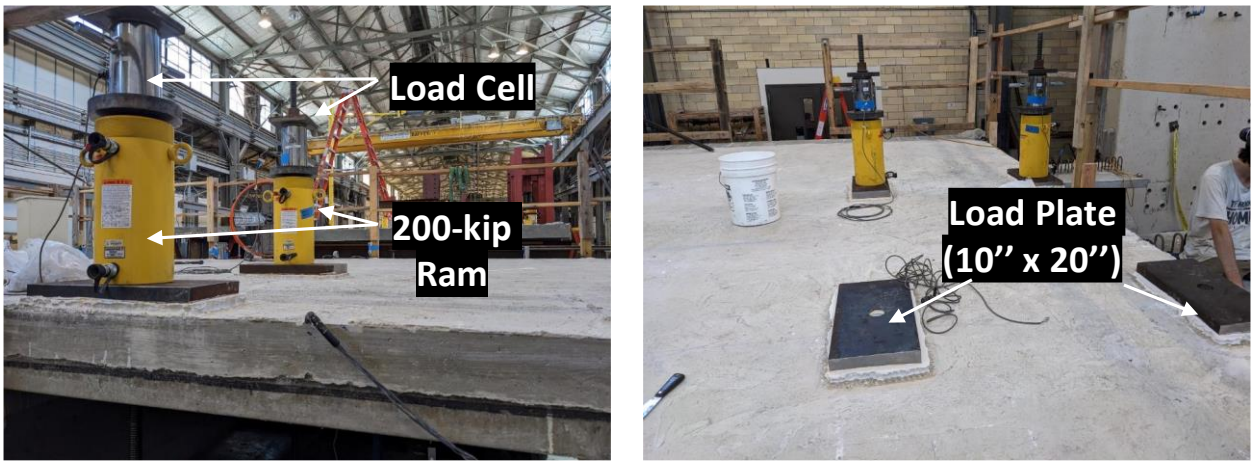

Figure 4-17: Loading System

4.5.3. Instrumentation

Strain gauges and linear potentiometers (L-Pots) were used to measure strains in the chords and web of the wire trusses as well as deck deflections, respectively. Strain gauges were distributed along top chords and bottom chords and on selected web members of the wire truss passing through the potential cracked zones due to the loading points. L-Pots were typically mounted underneath the load points. Load cells were also utilized to accurately measure the applied load. A summary of the location of these gauges can be found in Figure 4-18 for Tests 1 and 2, Figure 4-19 for Tests 5 and 8, and Figure 4-20 for Tests 6 and 7. Tests 3 and 4 utilized the same instruments as Tests 1 and 2. Tests 9 and 10 used an identical instrumentation plan as Tests 6 and 7, but on the longer overhang span. The photo of a positioned L-Pot on a stand under one of the exterior load points is shown in Figure 4-21.

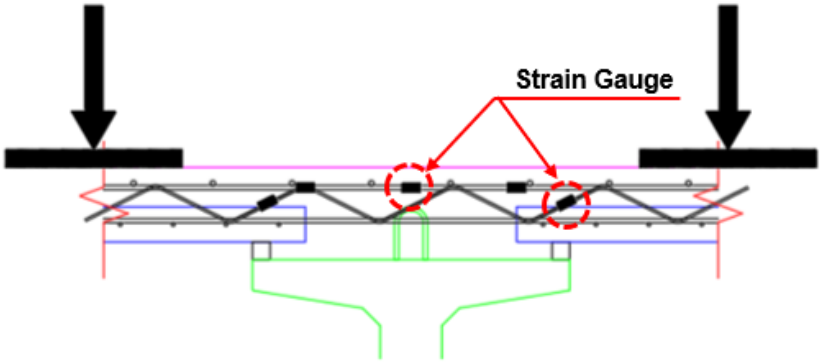

Figure 4-18: Tests 1 & 2 – Negative moment on second girder

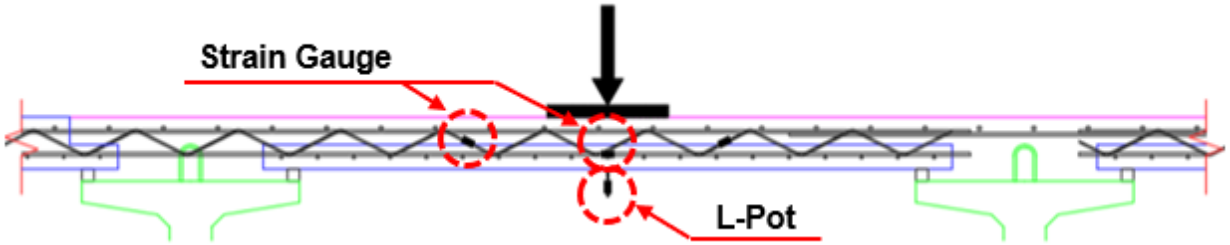

Figure 4-19: Tests 5 & 8 – Positive moment on long span

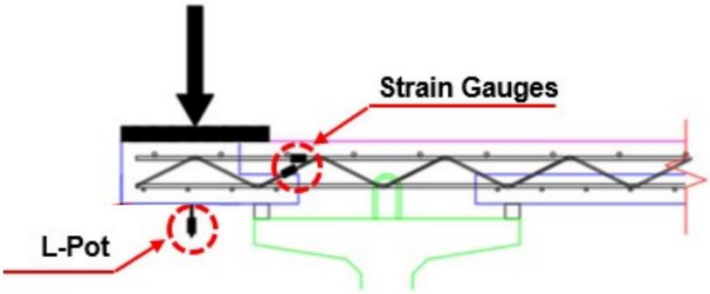

Figure 4-20: Tests 6 & 7 –Short Overhang test

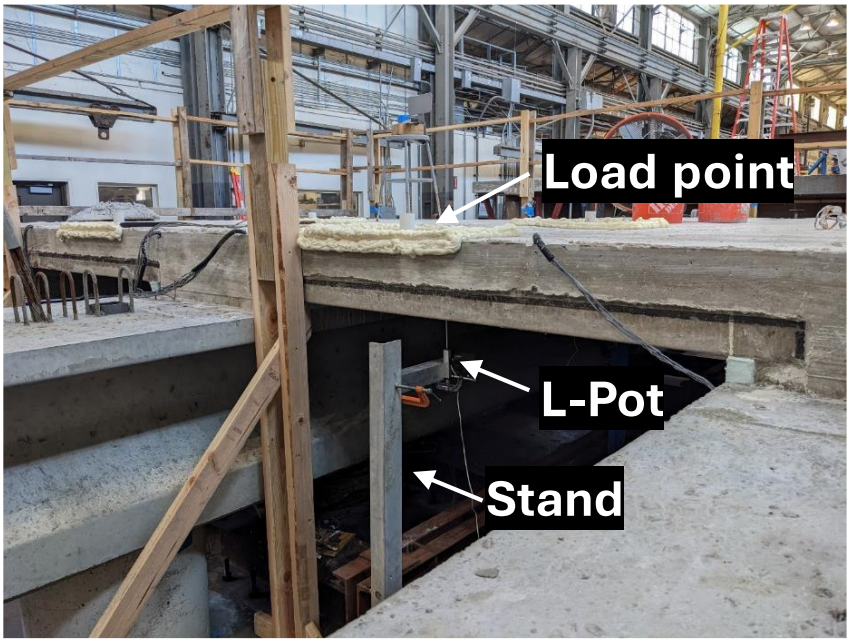

Figure 4-21: Installed L-Pot

4.5.4. Test Procedure

Each of the tests was conducted by applying loads onto the deck monotonically. Load increments were either 2, 5, or 10 kips; between load increments, crack propagation was inspected and marked, and the maximum observed crack width was measured and documented. A load increment of 2

and 5 kips was used for tests performed inside or near the service load limit, whereas a load increment of 10 kips was used for the tests that brought the bridge deck to its ultimate load. Loads were applied until the specified load level for tests reaching service loads and until ultimate failure (load drop in excess of 20% of peak load reached) or excessive deflections occurred for the tests reaching ultimate loads. The safety of the research team and the equipment was also taken into consideration, as well as when to stop loading the bridge deck.

4.6. Test Results and Discussion

The research team conducted a series of ten distinct tests, consisting of five assessments on electro-welded panel pairs and an equivalent number of evaluations on hand-welded panel pairs. These tests covered a range of conditions including negative moment over the second girder, positive moment in both short and long spans, as well as short and long overhang scenarios. All directly comparable data from these tests pertaining to the two wire truss types are meticulously presented in this section.

The subsequent section outlines the test results in a systematic manner, following the sequence of negative moment over the second girder, positive moment in the short span, positive moment in the long span, short overhang, and long overhang. Each figure within this section juxtaposes data from both electro-welded and hand-welded trusses, allowing for a direct comparison of their respective performance. Additionally, crack maps accompanying the figures depict current test cracks in black, while previous test cracks are represented in grey. These maps offer contextual insights into variations observed between the data collected for each truss type. Notably, tests reaching their ultimate capacity may lack crack card width data near this limit due to safety considerations.

For each test type, the presentation includes five plots: load versus displacement, load versus transverse strain, load versus web strain, and load versus crack card width. The load depicted in these plots represents the average load per ram active during the test. Specifically, if multiple rams were utilized, such as in the case of negative moment over the second girder tests, the average load across all rams was considered for each respective metric. This approach was adopted to account for slight variations in force measurements across load cells during the loading process. The displacement, strain readings, and crack width values correspond to the maximum recorded among all sensors or crack meters employed in each test.

4.6.1. Negative Moment over the Middle Girder

The first and third tests performed on the bridge deck specimen were the negative moment over the middle girder at the service load. A total of four rams were used to perform the tests. Two rams were located on either side of the middle girder, 3 ft from either side of the middle girder center line. The two rams on the same side of the girder were spaced 4 ft apart, parallel to the girder. This spacing was utilized as it represents a typical design tandem axel spacing according to AASHTO

LRFD, and the spacing is consistent with Project 0-4418. The four loading points were butted against the free edge of the panel pair, as this loading formation resulted in the worst-case scenario loading pattern. Figure 4-22 shows the loading pattern for the electro-welded panel pairs (Test 1) and the hand-welded panel pairs (Test 3).

The loading over the middle girder was stopped at 36 kips per ram to ensure that no severe damage occurred, which could affect future test results for other tests. Considering the AASHTO LRFD service design tandem loading is 12.5 kips, data was collected to nearly three times the expected service loads to capture more data.

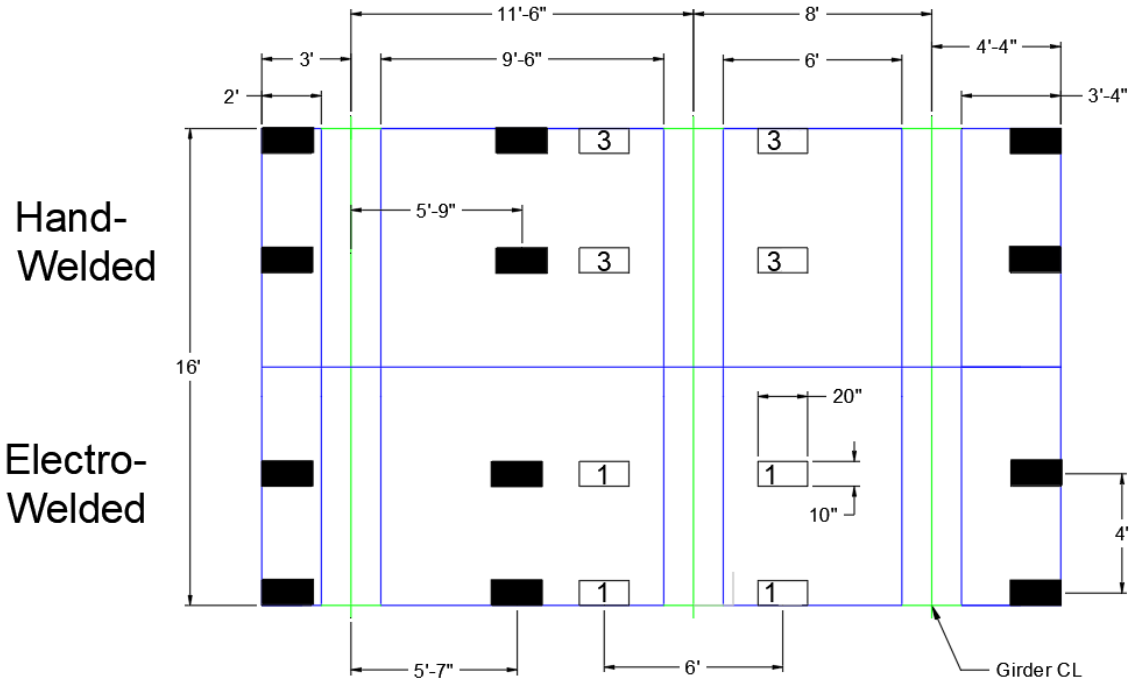

Figure 4-22: Negative Moment over Middle Girder Loading Schedule

4.6.1.1. Visual Observations and Cracks

During loading, cracks were carefully marked and measured on the specimen. Following each loading increment, cracks were traced, and photographs were taken. Figure 4-23 and Figure 4-24 present a summary of observed cracks on the top surface of the deck for Test 1 and Test 3, respectively. While no significant damage occurred during load tests, cracking was observed at the end of test. The cracks observed on the electro-welded deck (Test 1), located above the termination of the top flange, which was considered critical section for flexural capacity, propagated longitudinally along the girder and did not enter the other test region. However, the cracks observed on the hand-welded deck (Test 3) similarly propagated, but the cracks did appear to enter the electro-welded deck specimen region. This observation was unexpected as the top mat longitudinal rebar was severed to prevent the transfer of stresses between the hand-welded and electro-welded test regions. This phenomenon implies that the 4.5-in. CIP concrete topping was

solely able to transfer stresses. It should be noted that Test 3 had pre-existing cracks induced from Tests 1 and 2, and it was believed that the loading from Test 1 and Test 2 would have slightly affected the structural behavior of Test 3, which is introduced in later sections.

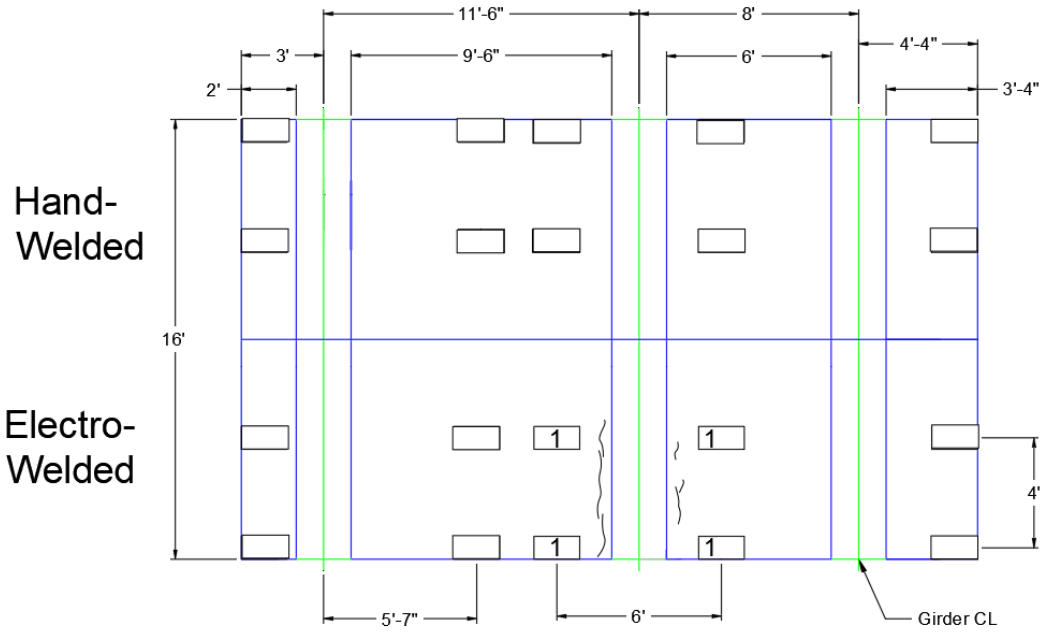

Figure 4-23: Crack Map - Test 1, Electro-Welded - Negative Moment over Middle Girder

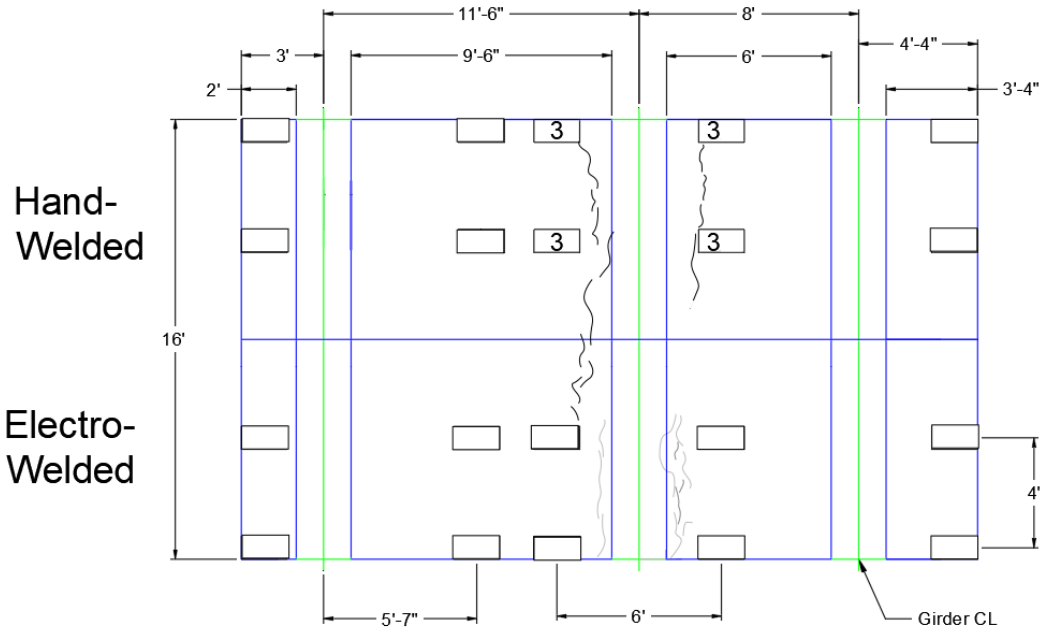

Figure 4-24: Crack Map - Test 3, Hand-Welded - Negative Moment over Middle Girder Load vs. Displacement

4.6.1.2. Load vs Displacement

The average load-max displacement relationships of Tests 1 and 3 were plotted together as shown in Figure 4-25, in which electro-welded panel pairs (Test 1) is presented in a dotted line and the hand-welded panel pairs (Test 3) in a solid line. Typically, this maximum displacement was observed from the loading points on the free edge of the panel pair. Both tests were stopped at a load level of 36 kips, which was approximately three times the design tandem load. Under this load level, both specimens remained linear without noticeable softening. However, the electro-welded panel pairs (Test 1) behaved stiffer that the hand-welded panel pairs (Test 3) did; at 36 kips per ram, Test ended up with a max displacement of 0.056 in., and Test 3 with 0.107 in.

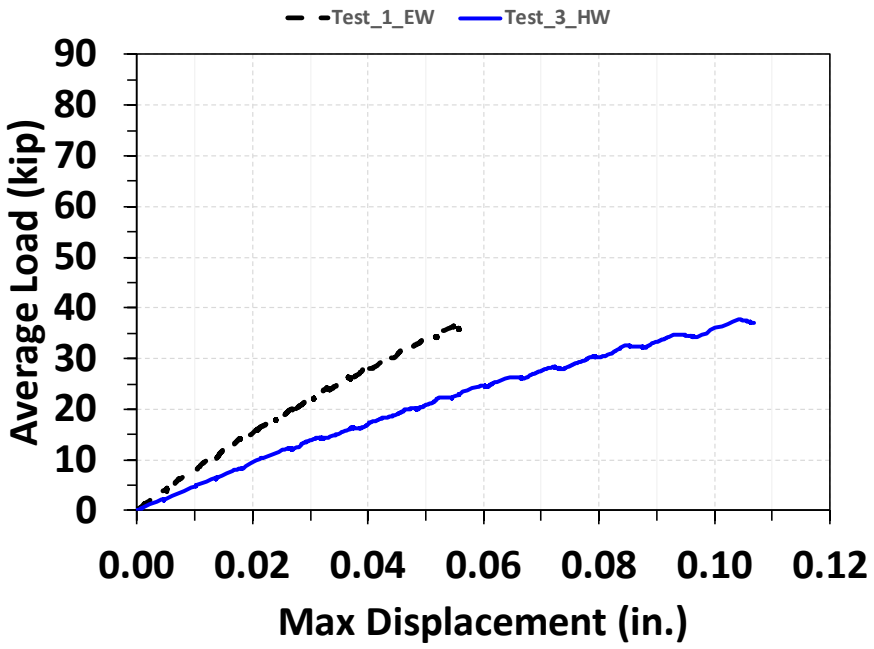

Figure 4-25: Load vs Displacement - Test 1 & 3 Compared - Negative Moment over Middle Girder

The discrepancy in stiffnesses and deflections could be due to cracking from Tests 1 and 2 contaminating Test 3, leading to Test 3 measuring post-cracking behavior and Test 1 measuring uncracked concrete behavior. The existing cracks in Test 3 did not open until 14 kips per ram was loaded onto the deck. That being said, the cracked moment of inertia of the concrete deck could be less than the uncracked moment of inertia.

4.6.1.3. Load vs. Transverse Strain

Figure 4-26 shows the collected load-transverse strain data for the electro-welded panel pairs (Test 1) in a dotted line and the hand-welded panel pairs (Test 3) in a solid line until a load of 36 kips per ram. The reported maximum transverse strain was the maximum of all strain values collected on the transverse reinforcement in the test region. The maximum transverse strains were typically observed on the top mat lap splice over the second girder nearer the free edge.

It can be seen from Figure 4-26 that the transverse strain developments were comparable until approximately the design tandem load. After that, an abrupt softening occurred at a load of around 22 kips for Test 1, corresponding to noticeable crack opening. However, Test 3 did not exhibit such abrupt softening but had a relative gradual softening. The peak load achieved was, resulting in a maximum transverse strain of 190 and 140 microstrain for the electro-welded panel pairs (Test 1) and the hand-welded panel pairs (Test 3), respectively. Although there was a difference in the max strain readings between the two tests after a load of 30 kips, corresponding to state of stress 4 ksi and 5.5 ksi, both tests were still in too early stages to attribute to the types of wire trusses causing differences. In addition, this discrepancy in softening behavior could be due to the previously mentioned possibility of pre-cracking caused by Tests 1 and 2 transverse crack propagating into Test 3's testing region.

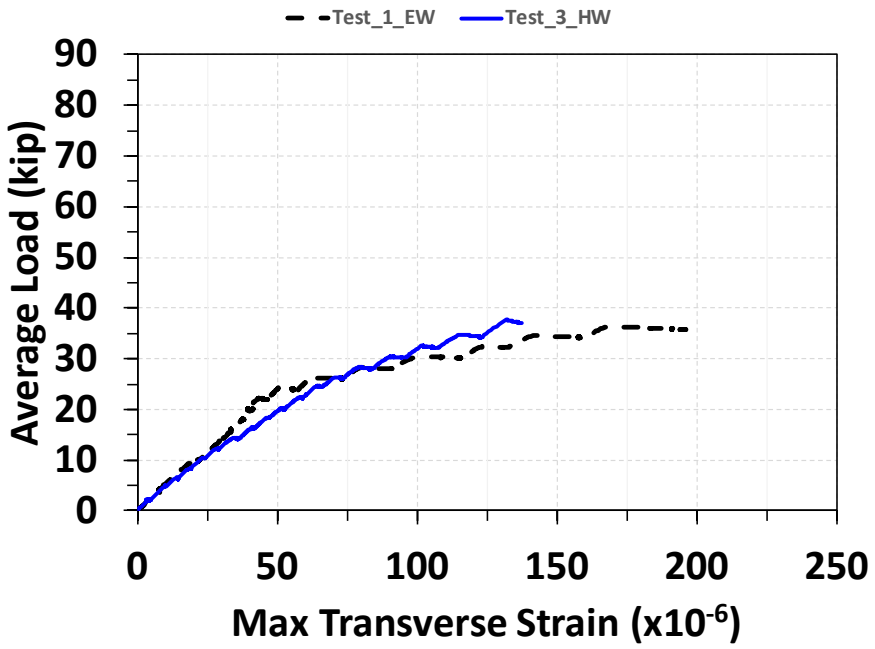

Figure 4-26: Load vs Transverse Strain - Test 1 & 3 Compared - Negative Moment over Middle Girder

4.6.1.4. Load vs Web Strain

Figure 4-27 illustrates the load-max web strain relationships for Tests 1 and 3, up to 36 kips per ram, the stopping point for the tests. The reported maximum web strain represents the highest value among all strain measurements collected on web reinforcement within the test region. Typically, the greatest web strains were observed in the web members closest to the second girder on the free edge. In the figure, electro-welded panel pairs (Test 1) are denoted by a dotted line, while hand-welded panel pairs (Test 3) are represented by a solid line.

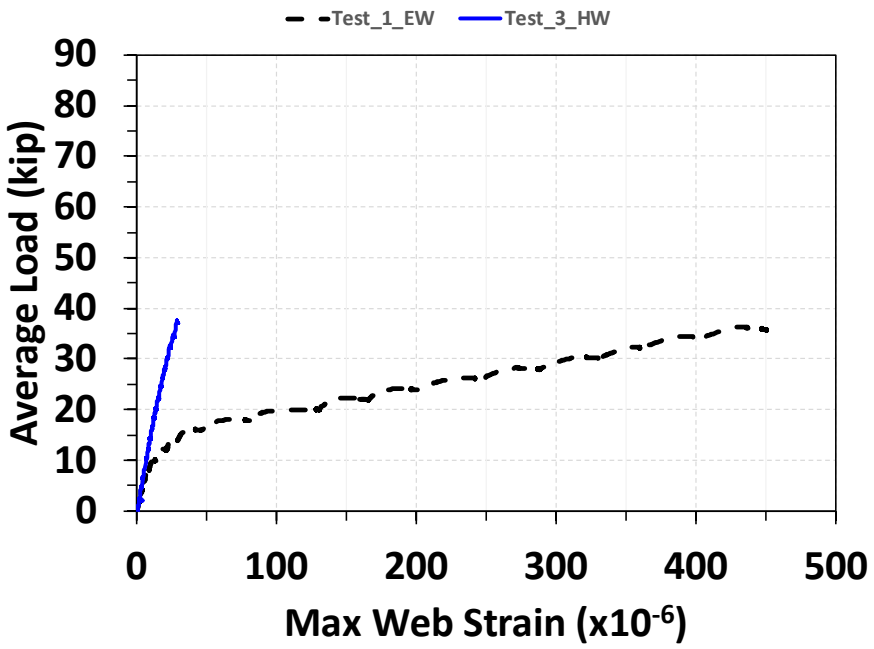

Figure 4-27: Load vs Web Strain - Test 1 & 3 Compared - Negative Moment over Middle Girder

A notable discrepancy is evident in the figure regarding strain development and the peak strain achieved at a load of 36 kips. Specifically, Test 1 exhibited significant growth in web strain, while Test 3 remained at a low level. At the conclusion of the tests, a maximum web strain of 450 microstrain was recorded for the electro-welded panel pairs (Test 1), whereas only 30 microstrain was achieved for the hand-welded panel pairs (Test 3).

This observation may indicate difficulties encountered in placing strain gauges on the web reinforcement, given the alternating direction of the web reinforcement in the wire truss. This made it challenging to position the strain gauge in the anticipated critical zone, as the orientation of the web reinforcement in that zone may not have contributed to the bridge deck's shear capacity. Consequently, strain gauges were consistently placed on the nearest web member oriented correctly to the anticipated critical zone for shear. The critical zone for web members was determined to lie along a projected 45-degree line from the edge of the loading plate.

While it is acknowledged that the webs of the hand-welded trusses were larger in diameter compared to the electro-welded trusses, the difference in size would not explain the vast disparity in web strain. Instead, the placement of the deck and the wire truss configuration are more likely contributors, leading to strain gauges being positioned away from the proper orientation and location within the critical zone.

4.6.1.5. Load vs Crack Card Width

Figure 4-28 shows the load-max crack width relationship of Tests 1 and 3 until the tests were stopped at a load of 36 kips. In the figure electro-welded panel pairs (Test 1) is presented using

triangles at each load step connected with a dotted line and the hand-welded panel pairs (Test 3) using squares at each load step connected in a solid line. Typically, the maximum crack card widths were observed at the expected critical section which was located on the top of the deck at the vertical projection of the top flange edge.

It can be seen from Figure 4-28 that Test 1 cracked at an average load of 20 kips per ram, and Test 3 cracks reopened at 14 kips per ram. Before the load levels, crack widths remained zero. The discrepancy in the cracking loads was not necessarily caused by the types of wire trusses; instead, the pre-cracks due to loading of Tests 1 and 2 on Test 3 were more likely the explanation. After cracking or reopening, both tests had a jump in crack width to 0.005 in. and no more growth was observed along with the load increased. The level of crack width was lower than the serviceability requirement on deck per AASHTO LRFD, which is 0.013 in.

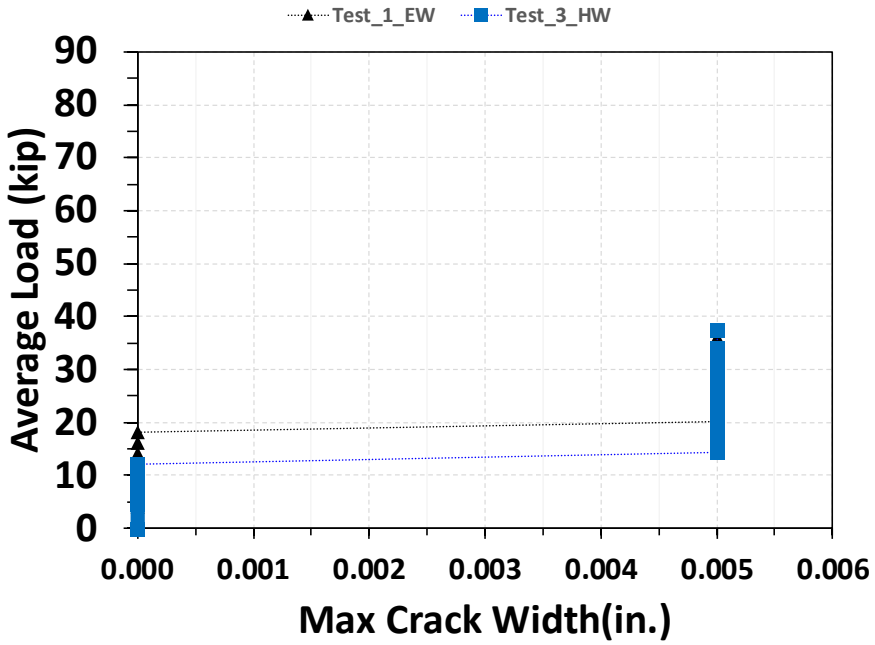

Figure 4-28: Load vs Crack Card Width - Test 1 & 3 Compared - Negative Moment over Middle Girder

4.6.2. Positive Moment over the Short Span

The second and fourth tests performed on the bridge were the positive moment over the short span tested to service loads. After the negative moment over the second girder tests were performed (Test 1 and Test 3), the rams located in the long span of the bridge were disconnected, and the rams in the short span were left in place. In the tests, the positive moment arm in the short span was located 3 ft from the second girder center line. Figure 4-29 shows the loading pattern for the electro-welded panel pairs (Test 2) and the hand-welded panel pairs (Test 4). All of the instrumentation was kept in the same location between the tests for the same panel pair type (Test 1 and Test 2 as well as Test 3 and Test 4). After reaching the planned service level, the research

team decided to continue the tests as not much cracking nor damages could be observed. Consequently, the tests were brought up to 60 kips per ram

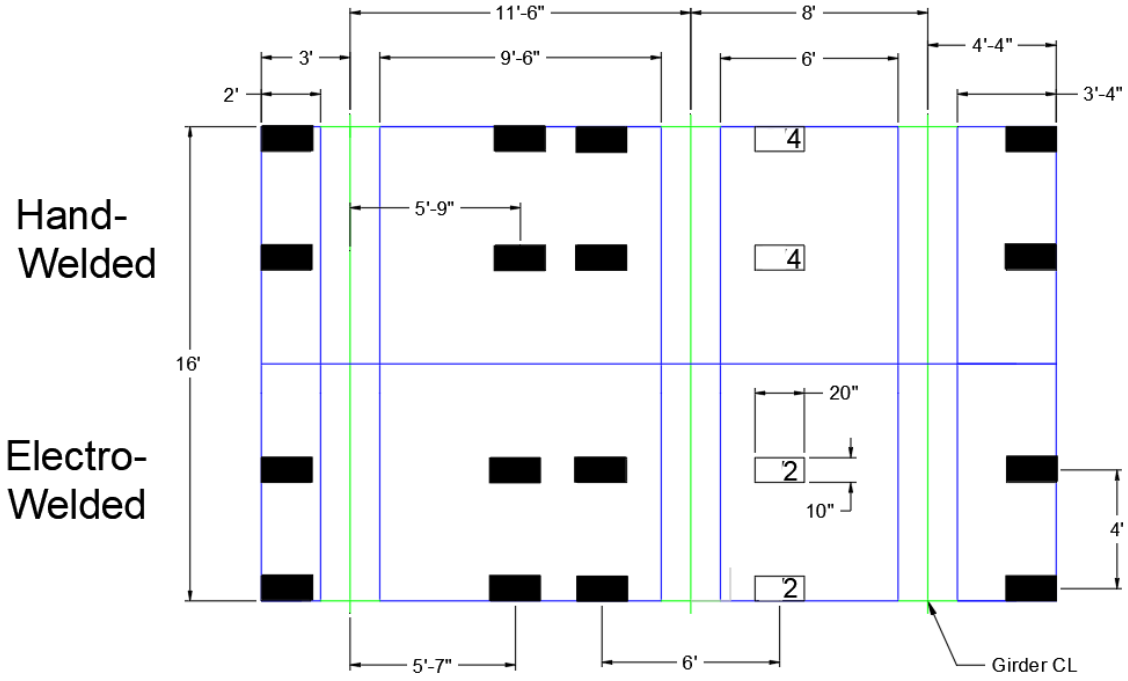

Figure 4-29: Positive Moment over the Short Span Loading Schedule

Careful consideration was made to ensure that no severe cracking or damage occurred in the long span or overhang region, which could potentially affect later test results. Considering the AASHTO service design tandem loading is 12.5 kips, data was collected to nearly five times the expected service loads. No significant damage to other regions of the bridge occurred during these service load tests, but it should be noted that more extensive cracking did occur compared to the negative moment over the second girder; all cracking was localized to the test region, which is discussed in later sections.

4.6.2.1. Visual Observations and Cracks

Cracks were marked and measured during loading of the specimen. In between each loading increment, the cracks were traced, and photos were taken of the cracks. A summary of the observed cracks on the top surface of the deck for Test 2 and 4 are shown below in Figure 4-30 and Figure 4-31 respectively. All previous tests' cracking is shown in grey to acknowledge their presence but distinguish them from the cracking caused from the current test of interest. Some cracks from previous tests reopened in subsequent tests, but careful consideration of the existing cracks was taken when comparing test results between differing existing deck conditions. Efforts were made by the research team to prevent excessive cracking from entering other future test regions.

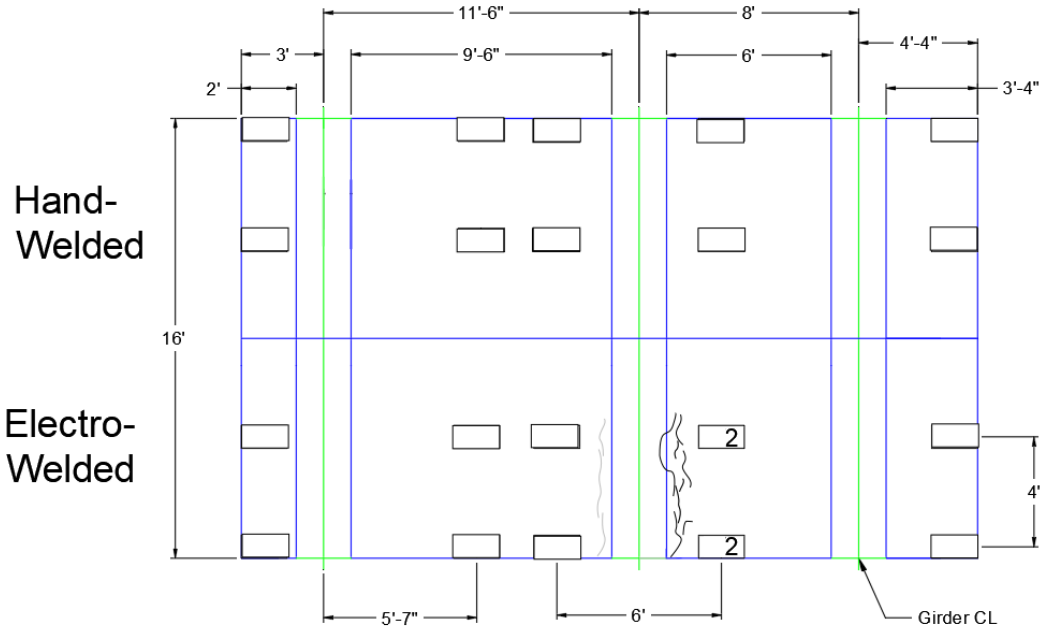

Figure 4-30: Crack Map - Test 2, Electro-Welded - Positive Moment over Short Span

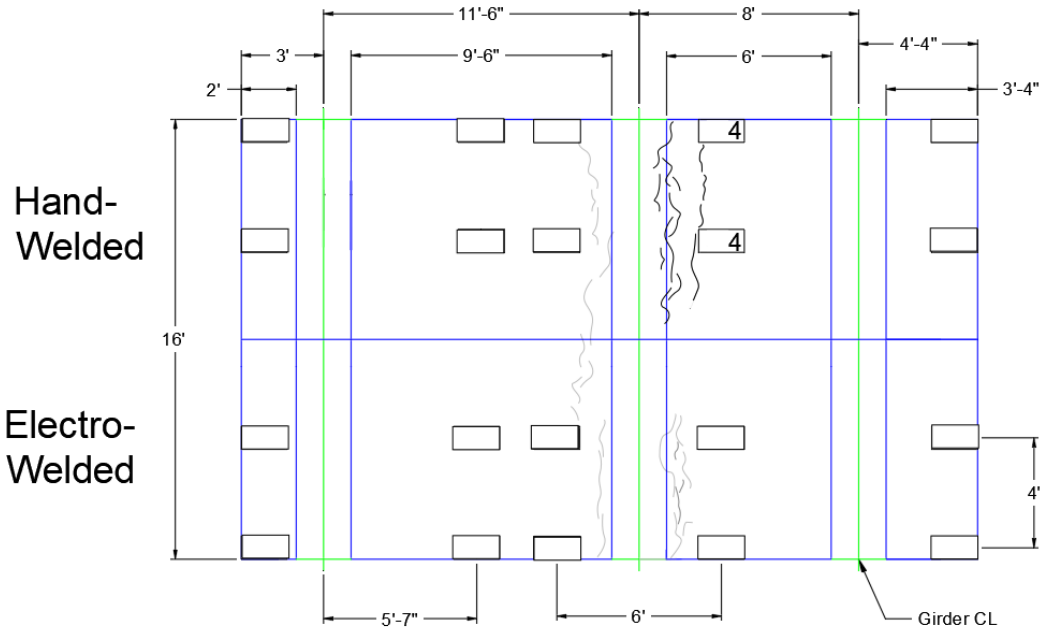

Figure 4-31: Crack Map - Test 4, Hand-Welded - Positive Moment over Short Span

The observed cracks were expected for service positive moment over the short span. The cracks observed on the electro-welded deck (Test 2) and the hand-welded deck (Test 4) were very typical and did not enter other test regions. Most cracks from Test 1 and 3 in test regions 2 and 4 respectively reopened during loading over the short span. Negative moment cracking at the supports, or the girders, was expected as negative moment stresses were maximized at the edge of

the girder flange. Not much differences in terms of crack patterns were observed except one additional crack forming nearly along the edge of the loading plate of Test 4.

4.6.2.2. Load vs Displacement

Figure 4-32 shows the load-max displacement relationships for Test 2 and Test 4. In the figure, electro-welded panel pairs (Test 2) are presented in a dotted line and the hand-welded panel pairs (Test 4) in a solid line. Typically, this maximum displacement was observed from the loading points on the free edge of the panel pair. Both tests were stopped at a load level of 60 kips, which was higher than five times the design tandem load.

The positive moment over the short span electro-welded and hand-welded panel pairs had a nearly identical load to displacement charts. There were no noticeable differences in the stiffnesses between the two tests. At the end of the tests, a maximum displacement of 0.103 in. for the electro-welded panel pairs was achieved (Test 2), and 0.099 in. for the hand-welded panel pairs (Test 4) was achieved. It can be inferred that when both tests were conducted on a pre-cracked specimen, the types of the wire trusses did not cause changes in load-displacement behavior up to five times the design tandem load. The observation could strengthen the reasoning that the discrepancies between Tests 1 and 3 were caused by pre-cracking.

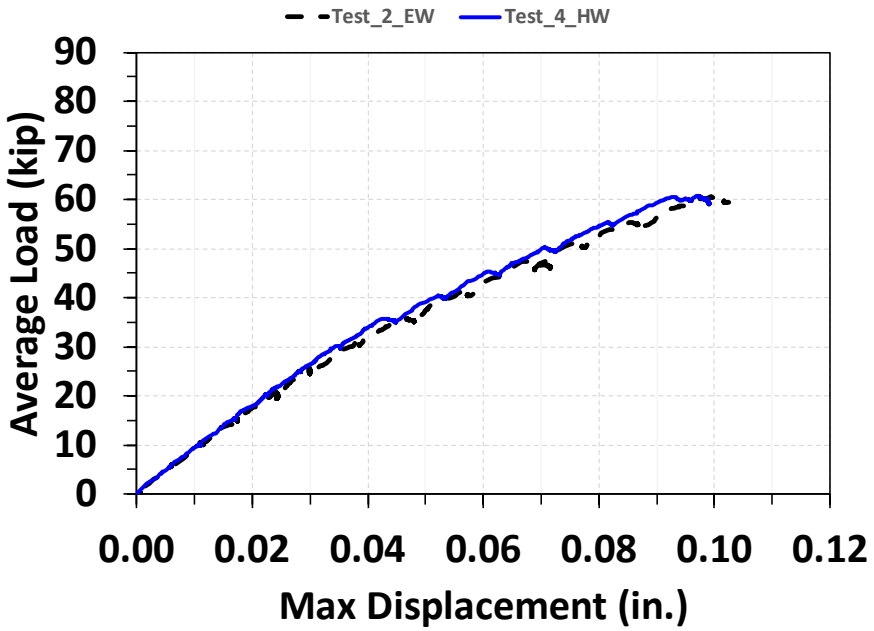

Figure 4-32: Load vs Displacement - Test 2 & 4 Compared – Positive Moment over Short Span

4.6.2.3. Load vs. Transverse Strain

Figure 4-33 shows the load vs max transverse strain relationships for the positive moment over the short span for Test 2 and Test 4. In the figure, the electro-welded panel pairs (Test 1) display in a dotted line and the hand-welded panel pairs (Test 3) in a solid line until a load of 60 kips per ram.

The reported values are of strain gauges on the top mat lap splice over the second girder. Typically, this maximum transverse strain was observed from the lap splices nearest the free edge of the panel pair. It can be seen that the electro-welded and hand-welded panel pairs have a nearly identical load to transverse strain response in most portion of the curves. Slight difference in the development of the transverse strain was observed after 36 kips. In addition, the peak load of 60 kips per ram resulted in a maximum transverse strain of 200 microstrain for the electro-welded panel pairs (Test 2), and 240 microstrain for the hand-welded panel pairs (Test 4). These differences did not have significance in structural implication.

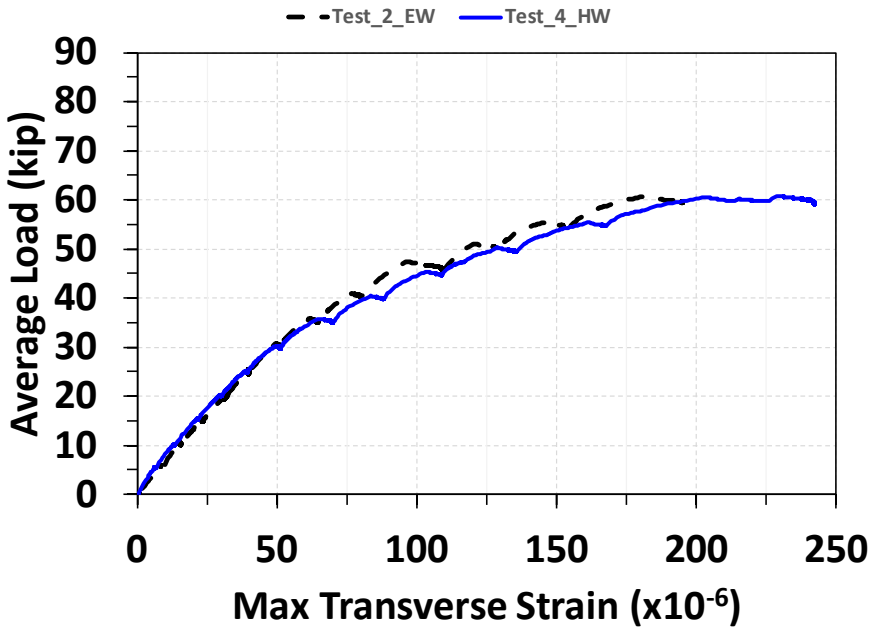

Figure 4-33: Load vs Transverse Strain - Test 2 & 4 Compared – Positive Moment over Short Span

4.6.2.4. Load vs. Web Strain

Figure 4-34 shows the collected load vs max web Strain data for the positive moment over the short span for Test 2 and Test 4. Similarly, the electro-welded panel pairs (Test 1) display in a dotted line and the hand-welded panel pairs (Test 3) in a solid line until a load of 60 kips per ram. Typically, the maximum web strains were observed in the web members nearest to the second girder flange edge.

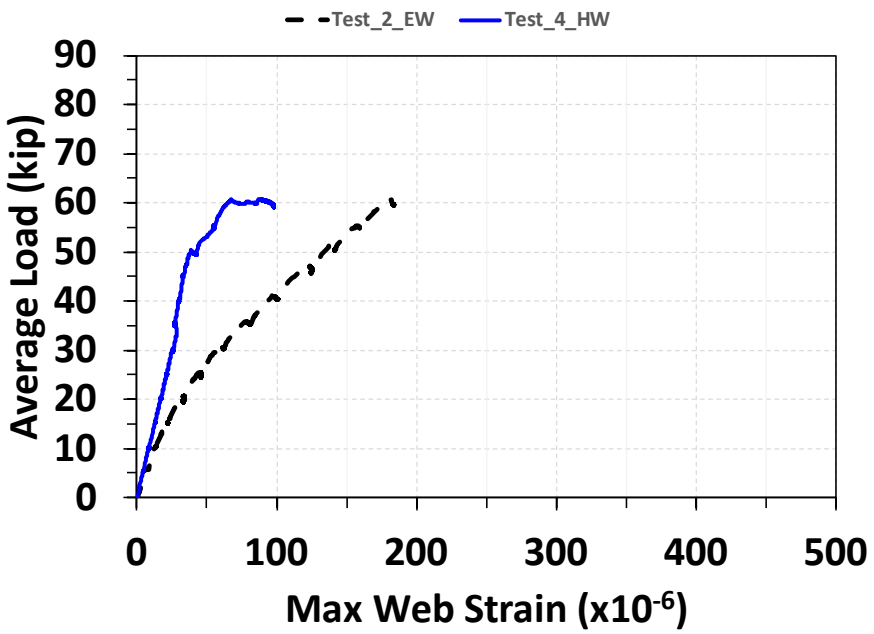

Figure 4-34: Load vs Web Strain - Test 2 & 4 Compared – Positive Moment over Short Span

Comparing the development of web strains between Tests 2 and 4 obtains that the strain reading of the electro-welded truss web was approximately 2.3 times that of the hand-welded truss web before 25 kips in general. The phenomenon was expected because the web members of the hand-welded wire trusses had a diameter larger than that of the electro-welded wire trusses. After the load level, an irregular but stiffer growth was observed in Test 4 but not in Test 3. At this level more cracks were spotted that connected other cracks from previous test and a new crack along the edge of the loading plates formed. On the other hand, Test 3 did not exhibit new cracking; instead, previous cracks reopened. Because of the phenomenon, it is inferred that shear strain redistribution happened at this load level that involve more web members' contribution. At the end of the tests, maximum web strains of 180 and 100 microstrain were achieved for the electro-welded panel pairs (Test 2) and the hand-welded panel pairs (Test 4), respectively.

4.6.2.5. Load vs Crack Card Width

Figure 4-35 shows the collected load vs crack card width data for the positive moment over the short span for Tests 2 and 4. The reported maximum crack card width was the maximum observed crack width in the test region. Typically, the maximum crack card widths were observed at the expected critical section which was located on the bottom of the deck underneath the point of loading.

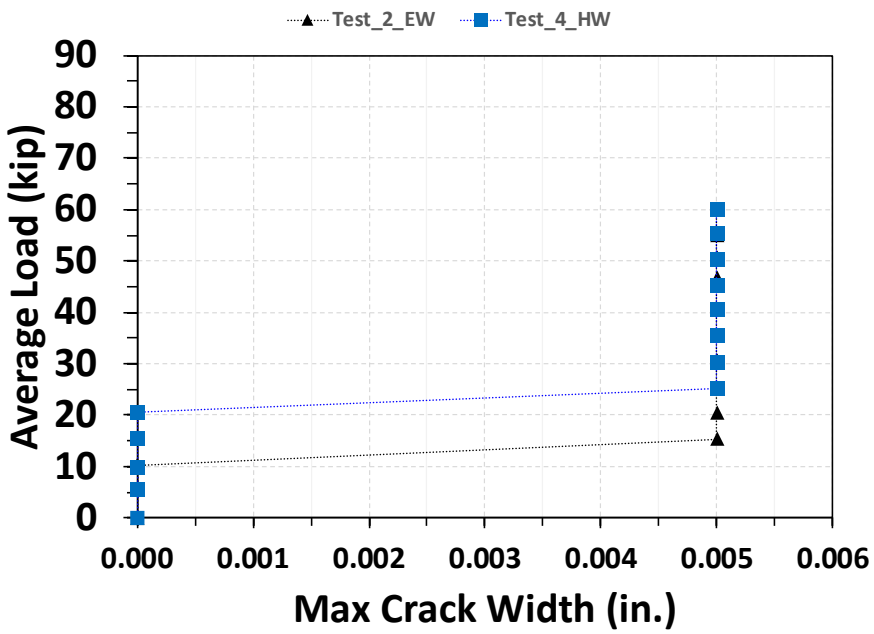

Figure 4-35: Load vs Crack Card Width - Test 2 & 4 Compared – Positive Moment over Short Span

Both tests occurred on pre-cracked specimens, since Tests 1 and 3 were done before the positive moment short-span test. The cracks in the electro-welded panel pairs were observed to have opened up again at 15 kips, whereas the hand-welded panel pairs opened up at 25 kips. at the cracking loads of both specimens, the crack widths jumped to the same width, 0.005 in., and the crack width remined until the peak load 60 kips. The measured peak crack width was lower than the serviceability requirement, 0.013 in., per AASTHO LRFD.

4.6.3. Positive Moment over the Long Span

The fifth and eighth tests conducted on the bridge involved subjecting it to positive moments over the long span until reaching ultimate loads. For Test 5, the two load points were positioned directly in the middle of the long span. However, for Test 8, adjustments were necessary due to the discovery, after concrete casting, that the strain gauge wires embedded in the electro-welded panel pair precast concrete interfered with the planned load points. To address this issue, the research team opted to shift the loading points 2 in. closer to the short overhang, ensuring no wires were severed. Given that these tests were expected to fail via punching shear, the adjustment in loading points was deemed not to affect the ultimate capacity, as elaborated in later sections. Figure 4-36 illustrates the loading pattern for the electro-welded (Test 8) and hand-welded panel pairs (Test 5).

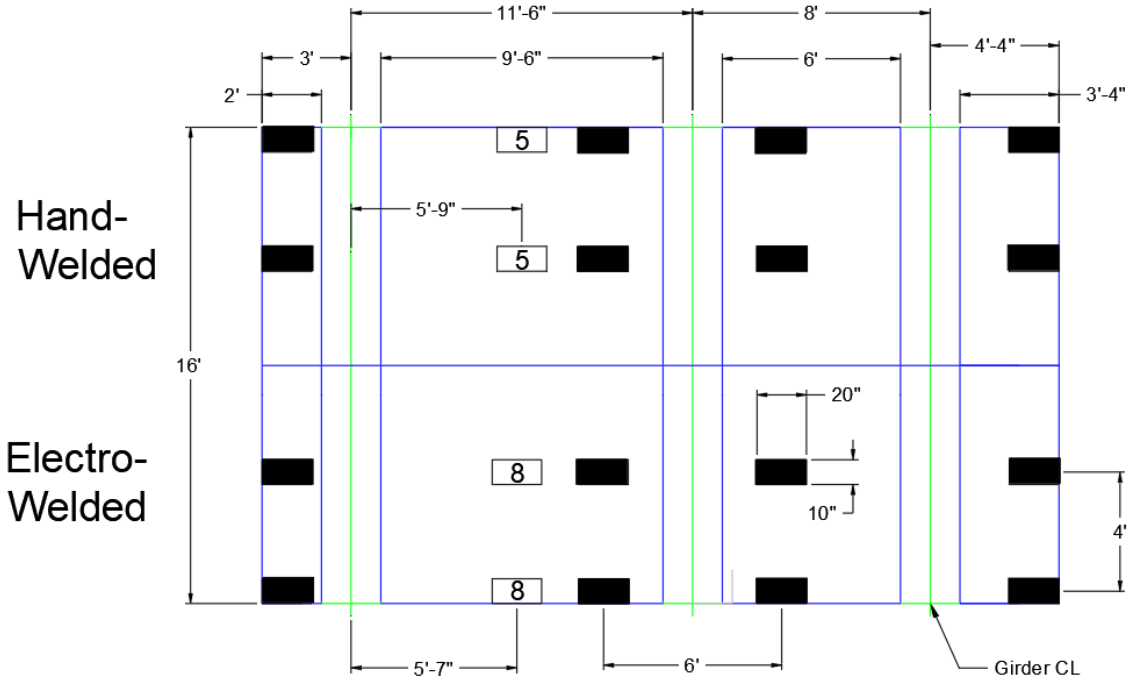

Figure 4-36: Positive Moment over the Long Span Loading Schedule

The objective of subjecting the bridge to positive moments over the long span was to bring both panels to their ultimate capacities, with the aim of investigating whether the wire trusses could enhance the deck's ultimate capacity compared to a standard PCP. The hypothesis was that the web members in the trusses could contribute sufficiently to the shear capacity to increase punching shear capacity or prevent a brittle punching shear failure, favoring a more ductile flexural failure instead.

4.6.3.1. Visual Observation, Cracks, and Failure Mechanism

Cracks were marked and measured during loading of the specimen. In between each loading increment, the cracks were traced, and photos were taken of the cracks. A summary of the observed cracks on the top surface of the deck for Tests 5 and 8 are shown below in Figure 4-37 and Figure 4-38, respectively. All previous tests' cracking is shown in grey to acknowledge their presence but distinguish them from the cracking caused from the current test of interest. Some cracks from previous tests reopened in subsequent tests, but careful consideration of the existing cracks was taken when comparing test results between differing existing deck conditions.

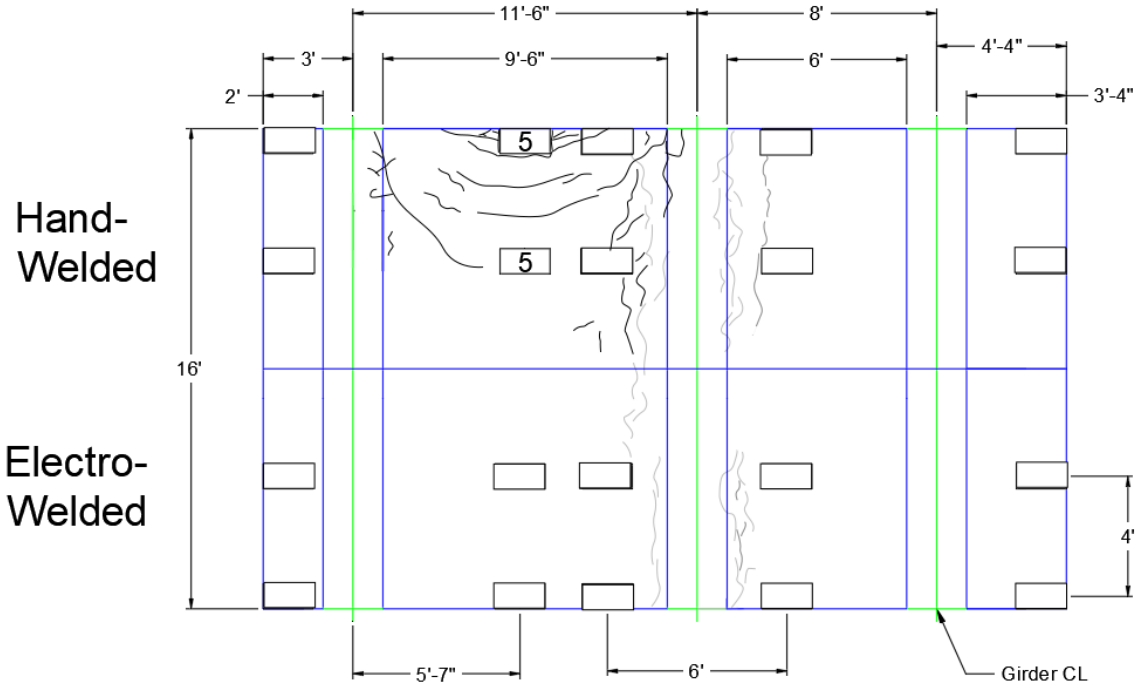

Figure 4-37: Crack Map - Test 5, Hand-Welded - Positive Moment over Long Span

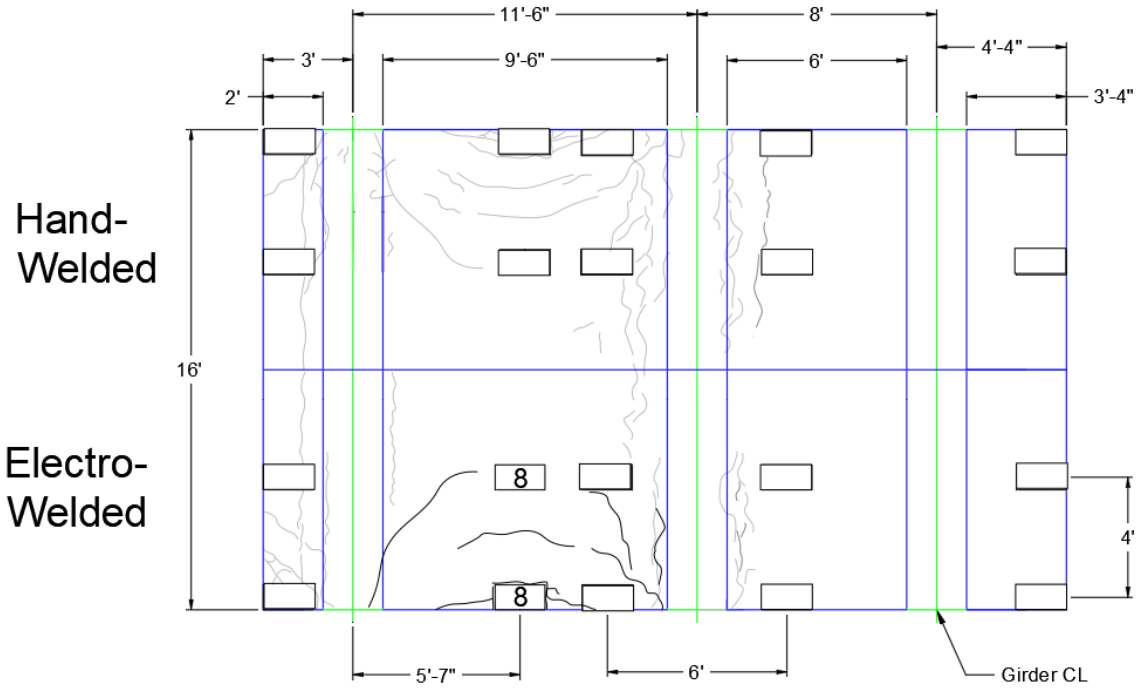

Figure 4-38: Crack Map - Test 8, Electro-Welded - Positive Moment over Long Span

The crack patterns observed on both the electro-welded deck (Test 8) and the hand-welded deck (Test 5) exhibited similarities, with several cracks forming around the edge loading plate. These cracks, nearly half-oval in shape, were confined within the two adjacent girders and the middle loading plate. Additionally, during loading over the long span, some cracks from Test 1 and Test 3 in test regions 2 and 4, respectively, reopened.

A selection of photos depicting the positive moment over the long span at ultimate capacity is provided to characterize the failure mechanism, as shown in Figure 4-39 and Figure 4-40 for Tests 5 and 8, respectively. Notably, both specimens displayed punching shear failures at the edge loading plate; the failing cracks originated from the sides of the edge loading plate, forming a cone-shaped failing surface and propagating to the bottom surface in a sudden, brittle manner. The inclination of the failing surface was less than 45 degrees, and the crack changed direction upon reaching the interface. Some delamination was also observed at the interface. The failure mode was consistent between the two specimens, indicating that both types of wire trusses were unable to prevent the brittle, instantaneous punching shear failure, instead of favoring a ductile flexural failure.

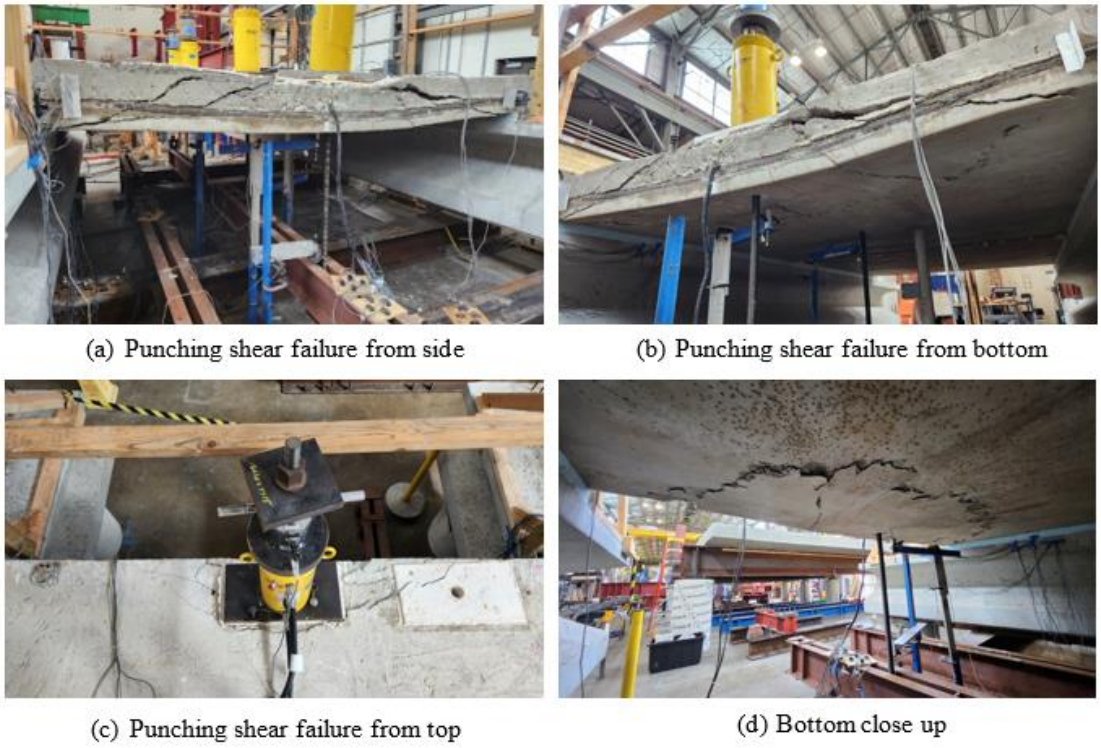

Figure 4-39: Test 5 – Hand-Welded Panel Pair Positive Moment Long Span – Punching Shear at Ultimate Load

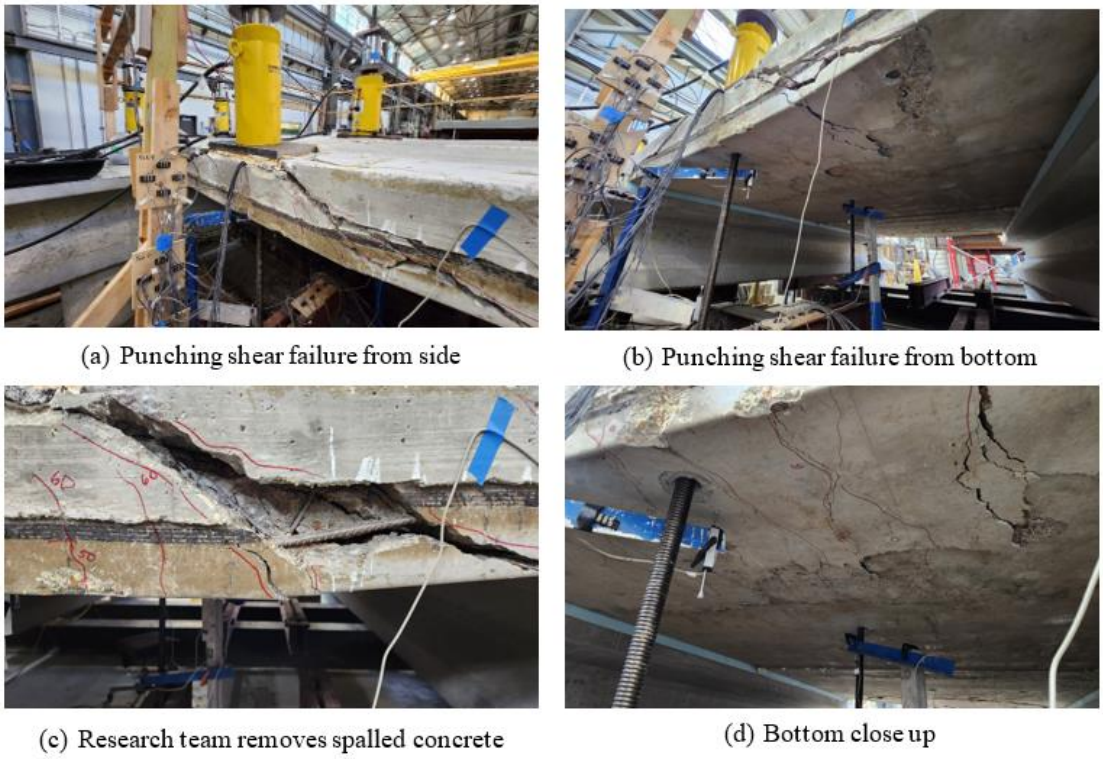

Figure 4-40: Test 8 – Electro-Welded Panel Pair Positive Moment Long Span – Punching Shear at Ultimate Load

It should be noted that a transverse cold joint in the electro-welded panel pair formed during fabrication because the concrete unexpectedly started to set rapidly, resulting in a cold joint on the 9 ft-6 in. electro-welded panel pair, as mentioned in Section 4.3. Nevertheless, this cold joint does not seem to have affected the failure mode or cracking pattern.

4.6.3.2. Load vs Displacement

Figure 4-41 shows the collected load-max displacement data for Test 5 and Test 8 for the positive moment long span. The reported maximum displacement was the maximum of the two displacements measured under each load point. Typically, this maximum displacement was observed from the loading points on the free edge of the deck slab.

The electro-welded and hand-welded panel pair decks responded similarly with respect to load-displacement behavior. They both had a softening behavior: higher stiffness in the beginning but gradually softening. Nevertheless, some discrepancies can be observed from Figure 4-41; the hand-welded WTPD panel deck specimen had a higher stiffness but the softening was quicker than the electro-welded WTPD panel deck specimen. At a load approximately between 50 kips and 60 kips, the stiffness of the hand-welded WTPD panel deck specimen became lower.

Both specimens achieved an ultimate peak load of 85 kips per ram, corresponding to a displacement of 1.14 in. for the electro-welded panel pair overhang (Test 8), and 1.23 in. for the

hand-welded panel pair overhang (Test 5). It can be inferred that the truss type also did not appear to have impact on ultimate capacity The increased yield strength of the electro-welded trusses also did not appear to increase the ultimate capacity of the bridge deck.

Despite Test 5 having more pre-cracking in the region compared to Test 8, the ultimate capacity of the long span deck was similar as punching shear failure is controlled by the concrete perimeter length and deck depth. The cracks from Test 6 and the concrete cold joint appear to have little to no effect on the punching shear capacity of the electro-welded long span deck (Test 8).

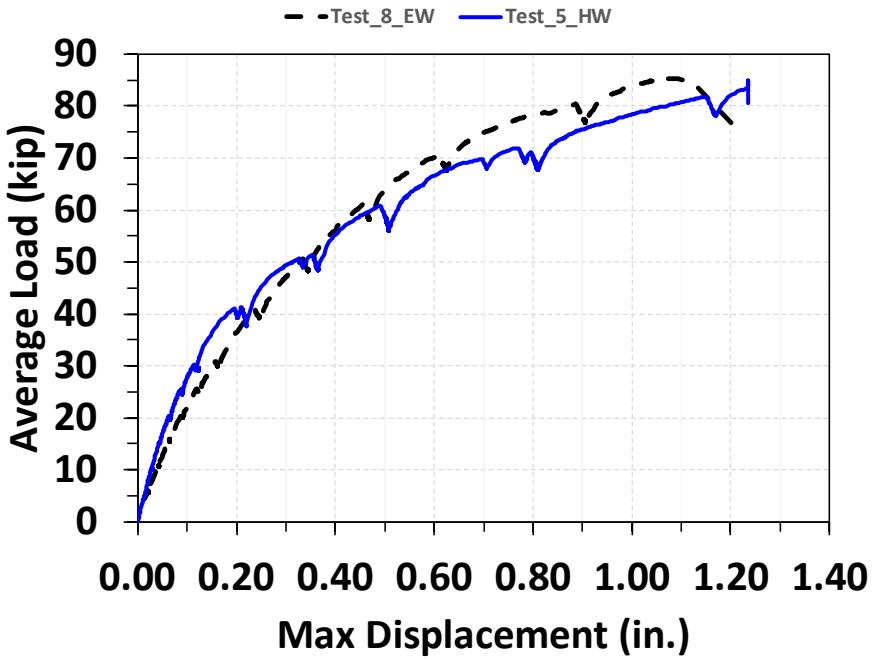

Figure 4-41: Load vs Displacement - Test 5 & 8 Compared – Positive Moment over Long Span

4.6.3.3. Load vs. Transverse Strain

Figure 4-42 shows the load-transverse strain data for the positive moment over the long span for Test 5 and Test 8. The reported maximum transverse strain was the maximum of all transverse reinforcement on the top mat reinforcement. Bottom mat transverse strain gauges were located directly under the loading plate on the bottom chord of the trusses in the test region. The reported values are of strain gauges on the bottom chord of the truss directly below the load point. Typically, the maximum transverse strain was observed from the bottom chord on the truss nearest to the free edge.

The hand-welded panel pair deck appears to have yielded before the electro-welded panel pair but was similar until about ~60 kips per ram was applied to the deck, while the electro-welded panel pair deck reached the yield strain approximately at a load of 68 kips, as its wire trusses had a higher yield strength. The load level 60 kips was also when the hand-welded panel pair deck started to have a lower stiffness, as mentioned in the previous section. After yielding, the hand-welded panel

pair deck seems to have undergone significant stress redistribution in the final load steps before failure, indicated by jumpy strain readings. On the other hand, the electro-welded panel pair deck maintained a stable growth in strain data. The results imply that the electro-welded wire trusses, with a higher yield strength, might have provided a more stable post-yield behavior in flexure.

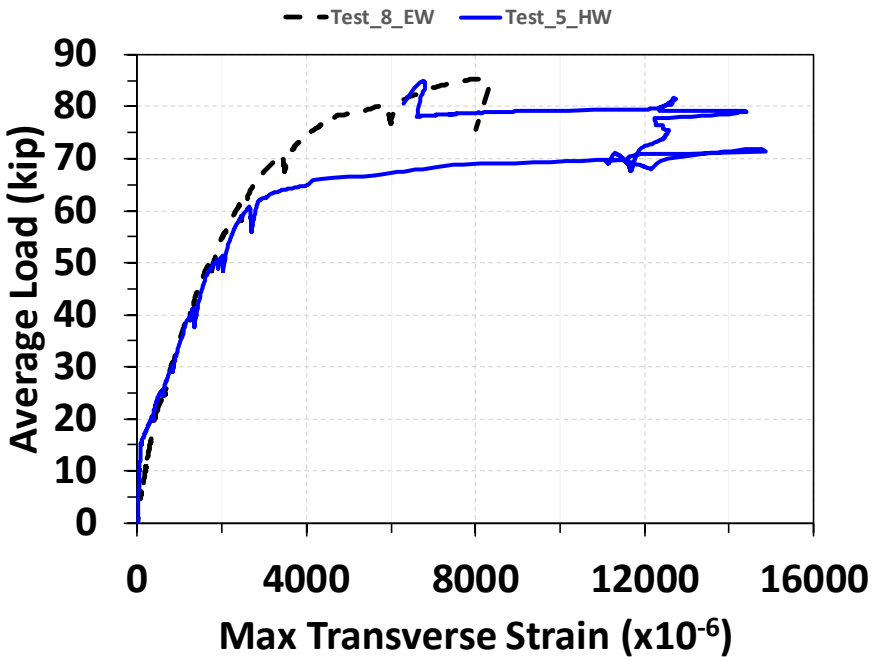

Figure 4-42: Load vs Transverse Strain - Test 5 & 8 Compared – Positive Moment over Long Span

4.6.3.4. Load vs. Web Strain

Figure 4-43 shows the collected load-max web strain data for the positive moment over the long span for Test 5 and Test 8. The reported maximum web strain was the maximum of all strain values collected on web reinforcement in the test region. Typically, the maximum web strains were observed in the web members nearest to the point of loading and the free edge.

It can be seen from Figure 4-43 that the web strain of the hand-welded wire truss maintained a similar development pattern. Both specimens started to have a quicker growth in the web strain approximately between 40 kips and 50 kips. However, the former specimen was in general lower than that of the electro-welded wire trusses, which can be attributed to the fact the hand-welded wire trusses had stiffer web members. Before the end of the tests, the web members of both specimens had reached their yield strength; however, the hand-welded wire truss specimen reached the peak load before yielding of the web members occurred. The observations indicate that the web members did contribute to the strength but did not change the ultimate punching shear capacity. This is because the complexity of the interaction between two different concretes, web members, and the interface. Further study is required to quantify the contribution at various load stages of each element.

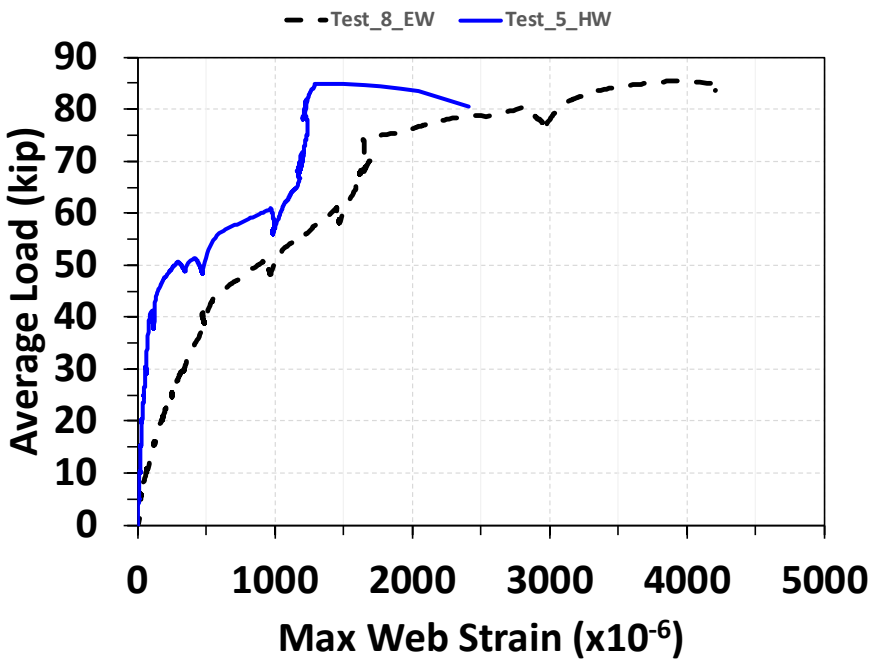

Figure 4-43: Load vs Web Strain - Test 5 & 8 Compared – Positive Moment over Long Span

4.6.3.5. Load vs Crack Card Width

Figure 4-44 shows the relationship Load vs. Crack Card Width for the positive moment long span. The hand-welded panel pair specimen seems to have smaller crack widths compared to the electro-welded panel pairs. The reported maximum crack card width was the maximum observed crack width in the test region. Typically, the maximum crack card widths were observed on the bottom of the deck below the point of loading. Due to safety, crack widths were only measured until 70 kips for both tests.

It can be seen that the hand-welded panel pair specimen's crack formed (reopened) at a load of 25 kips with a width of 0.005 in. while the electro-welded panel pair specimen's crack formed at a load of 15 kips also with a width of 0.005 in. These load levels had passed the design tandem load but the crack width still satisfied the AASHTO LRFD's serviceability requirements. Before reaching the end of crack marking, the specimens had different rate of crack width growing, but both specimens ended up with a crack width of 0.040 in.

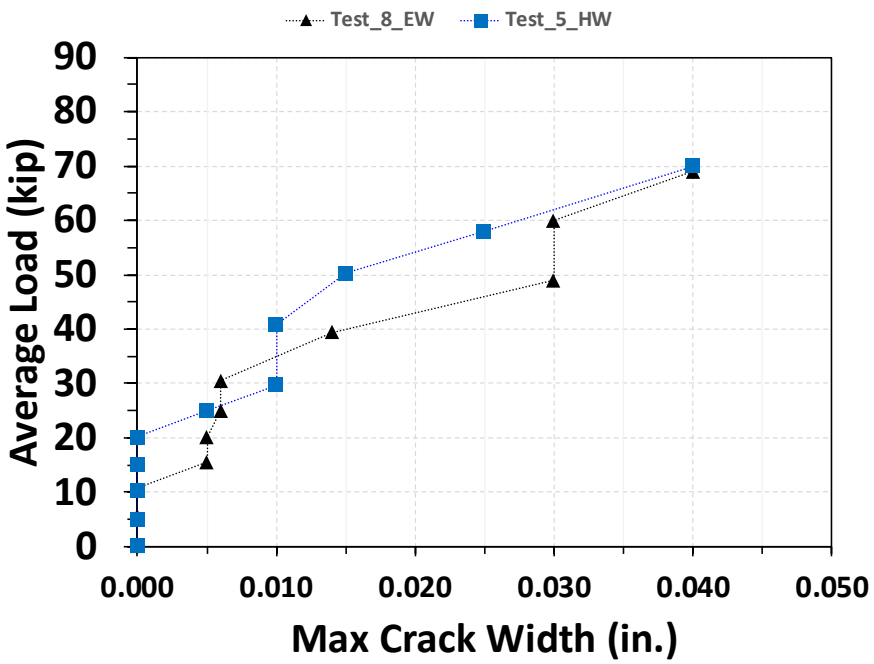

Figure 4-44: Load vs Crack Card Width - Test 5 & 8 Compared – Positive Moment over Long Span

4.6.4. Short Overhang

The sixth and seventh tests performed on the bridge were the short overhang tested to ultimate capacity. One loading plate was butted against the extreme edge of the overhang so that the loading plate was flush on two free edges of the overhang. The other loading plate was located 4 ft away parallel to the girder, which also was flush with one free edge. Figure 4-45 shows the loading pattern for the electro-welded and hand-welded panel pairs.

The short overhang test aimed to bring both specimens to their ultimate capacities in hopes of seeing the failure mode and capacity of the short overhang and to see if the truss type impacted the structural behavior of the short overhang.

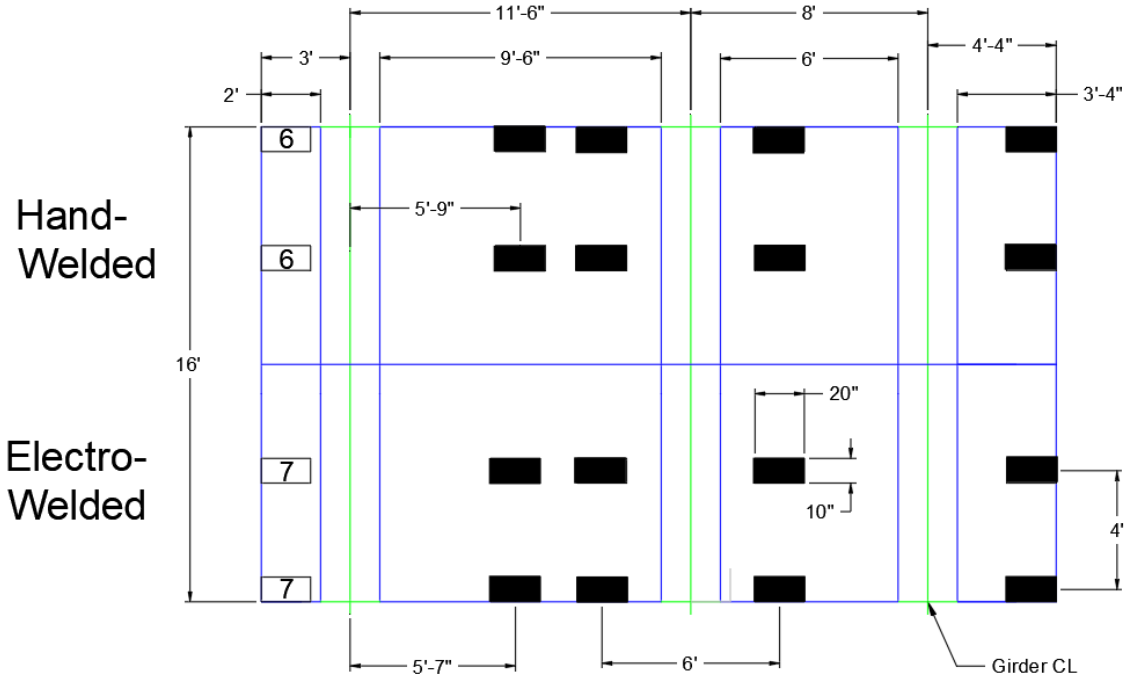

Figure 4-45: Short Overhang Loading Schedule

4.6.4.1. Visual Observation, Cracks, and Failure Mechanism

During the loading of the specimen, cracks were meticulously marked and measured. Following each loading increment, cracks were traced, and photographs were taken for documentation. A summary of the observed cracks on the top surface of the deck for Tests 6 and 7 is provided in Figure 4-46 and Figure 4-47, respectively. All previous test cracks were depicted in grey to distinguish them from those caused by the current test. Although some cracks from prior tests reopened during subsequent tests, careful consideration was given to existing cracks when comparing results between differing deck conditions.

The electro-welded and hand-welded short overhangs exhibited very similar crack patterns, as illustrated in Figure 4-46 and Figure 4-47. Initially, the short overhangs displayed typical flexural cantilever deflection. Despite the research team severing the top mat longitudinal rebar at the transverse joint to prevent stress transfer between Tests 6 and 7, during the structural testing of the hand-welded short overhang (Test 6), a crack was noted above the electro-welded interior flange tip of the facia girder. The mentioned crack appeared on the opposite side of loading in the electro-welded panel pair region while loading the hand-welded region.

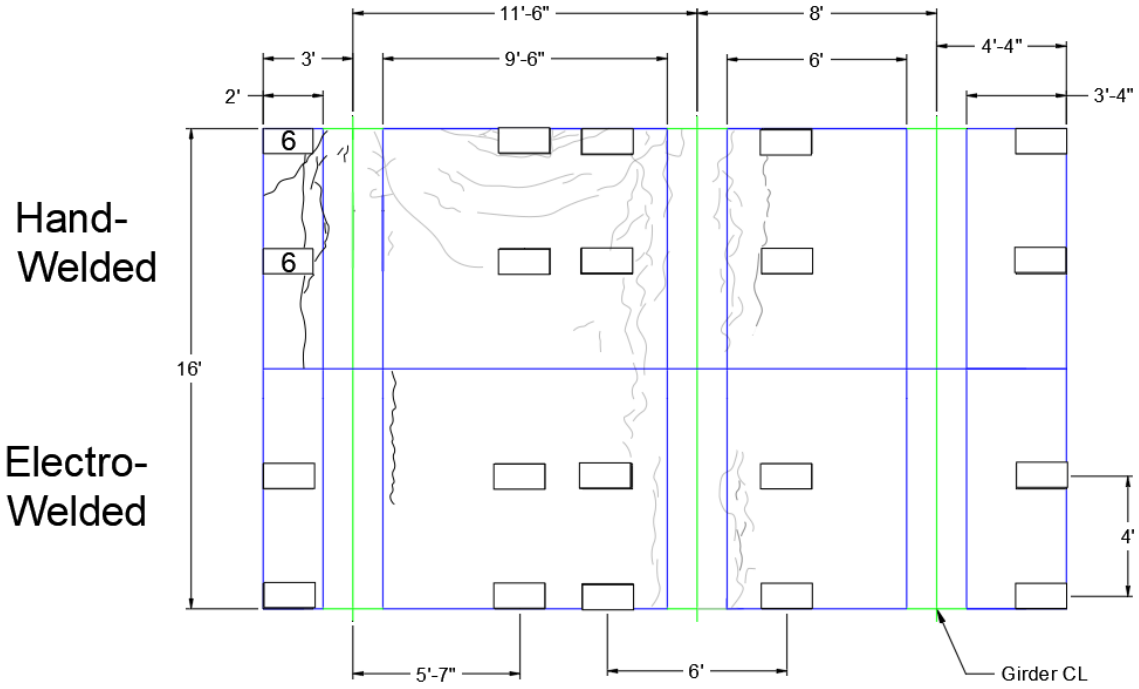

Figure 4-46: Crack Map - Test 6 - Hand-Welded - Short Overhang

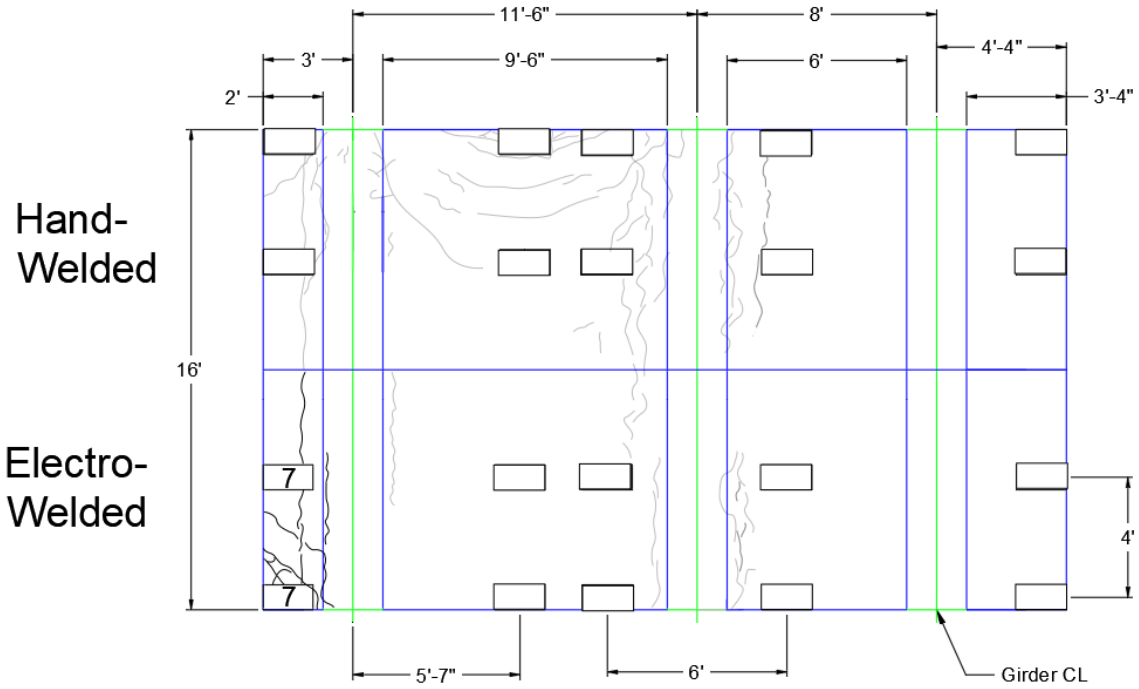

Figure 4-47: Crack Map - Test 7 - Electro-Welded - Short Overhang

In both Tests 6 and 7, flexural cracks appeared first, followed by the development of shear cracks. Once the shear cracks fully developed, the long overhang exhibited excessive deflection, signaling a loss of stiffness. A selection of figures of the overhang at ultimate capacity is provided to

contextualize the data at failure, as shown in Figure 4-48 and Figure 4-49. Similar failure modes were characterized as combined flexural failure and shear failure at the girder flange tip. The shear crack being in almost the same position and width for both the electro-welded and hand-welded panel pair overhangs. Both failures were ductile flexural failures after a large shear crack had developed. The electro-welded overhang test was stopped as the overhang began to lose capacity as the loading increased, whereas the hand-welded overhang test was stopped due to excessive deflections. The hand-welded overhangs seem to have more ductility compared to the electro-welded overhangs.

(a) Shear crack from free edge

(b) Shear crack from transverse joint

(c) Shear crack from top view

Figure 4-48: Test 6 – Hand-Welded Panel Pair Short Overhang – Shear Crack at Ultimate Load

Moreover, the overhang on the electro-welded panel pair had a major concrete spall at the ultimate load. It should be noted that once the shear crack formed on both overhangs, the structure started to deflect without taking more load. Once the electro-welded overhang began to excessively deflect, the load started to drop, and the large concrete piece spalled off. The hand-welded panel pair overhang did not have a large concrete piece spall off and had slightly more ductility compared to the electro-welded counterpart.

Figure 4-49: Test 7 – Electro-Welded Panel Pair Short Overhang – Shear Crack at Ultimate Load

4.6.4.2. Load vs Displacement

Figure 4-50 shows the collected load-max displacement data for Tests 6 and 7 for the short overhang. The reported maximum displacement was the maximum of the two displacements measured under each load point. Typically, this maximum displacement was observed from the loading points on the free edge of the panel pair. The average ultimate load of 60 kips and 59 kips per ram was achieved by both the test specimens, which corresponds to a displacement of 0.84 in. for the hand-welded wire truss panel pair overhang (Test 6), and 0.4 in. for the electro-welded wire truss panel pair overhang (Test 7).

The load- max displacement relationships were different in terms of shapes. For the hand-welded wire truss panel pair overhang (Test 6), the relationship was a seemingly bilinear behavior, reaching its peak load-carrying capacity after a longer plateauing. On the other hand, for the electro-welded wire truss panel pair overhang (Test 7), the specimen reached its peak not long after its proportional limit and started to lose its load-carrying capacity early. The observation can be attributed to different top chord material. Test 6 had Grade 60 steel for its top chords that was more ductile and better deformability than Test 7, which consisted of higher strength steel for its top chords. It should be noted that the actual behavior could be more complex as the load points

overlapped a portion of the girder flange and the flexural and shear stress interacted on the region. Also, the pre-cracking on the opposite side of the girder before Test 7 might have influenced the behavior of the overhang. More study is needed to better understand and analytically describe the behavior.

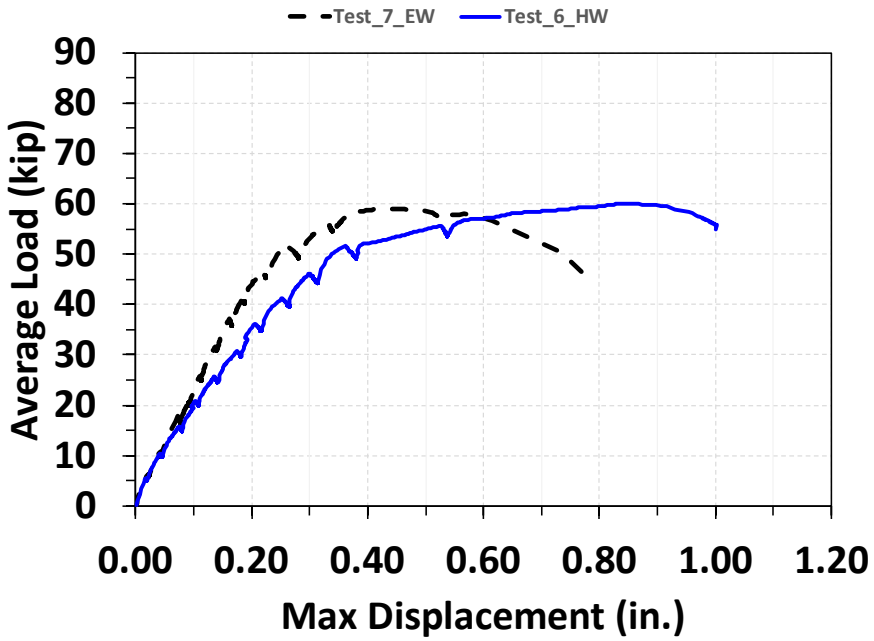

Figure 4-50: Load vs Displacement - Test 6 & 7 Compared – Short Overhang

4.6.4.3. Load vs Transverse Strain

Figure 4-51 shows the load-transverse strain data for the short overhang for the hand-welded wire truss panel pair overhang (Test 6) and the electro-welded wire truss panel pair overhang (Test 7). The reported transverse strain was the maximum of all transverse reinforcement on the top mat reinforcement. The reported values are of strain gauges on the top chord of the truss directly above the termination of the top flange. Typically, the maximum transverse strain was observed from the top chord on the truss nearest to the free edge.

It can be seen from Figure 4-51 that both tests had the top chord yield before the end of the test, indicating a flexural type of failure along the termination of the top flange, echoing the observed cracking along the same line. For Test 6, when reaching the peak load, a sudden jump in the strain reading happened, followed by a load drop, while Test 7 did not have the same phenomenon. In general, the top chord strain in the hand-welded wire trusses was growing slower than that in the electro-welded wire trusses. As mentioned in the previous section, the structural implication requires more comparative and analytical study to confirm, as various stresses interacted within the test area.

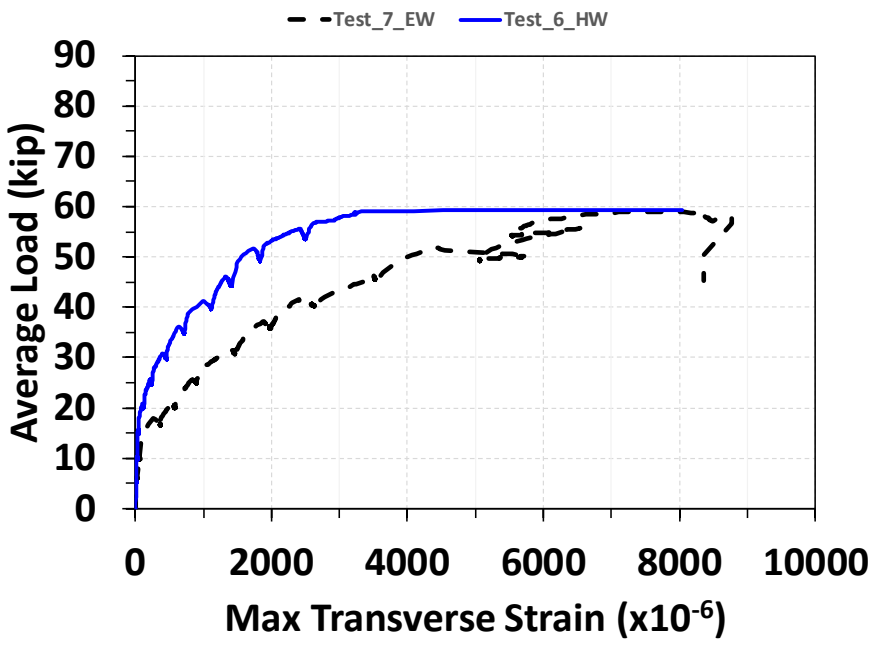

Figure 4-51: Load vs Transverse Strain - Test 6 & 7 Compared – Short Overhang

4.6.4.4. Load vs. Web Strain

Figure 4-52 shows the collected Load vs Web Strain data for the short overhang for Test 6 and Test 7. The reported maximum web strain was the maximum of all strain values collected on web reinforcement in the test region. Typically, the maximum web strains were observed in the web members nearest to the facia girder and the free edge.

In general, the hand-welded panel pairs (Test 6) had its web strain growing slower than the electro-welded panel pairs (Test 7) did between approximately 20 kip and 46 kip. After 46 kip, both specimens showed anomalies in terms of strain development along with the load increasing. The load level also corresponded to the formation of the punching shear type of cracks. Before 20 kips, both specimens did not have obvious web strain.

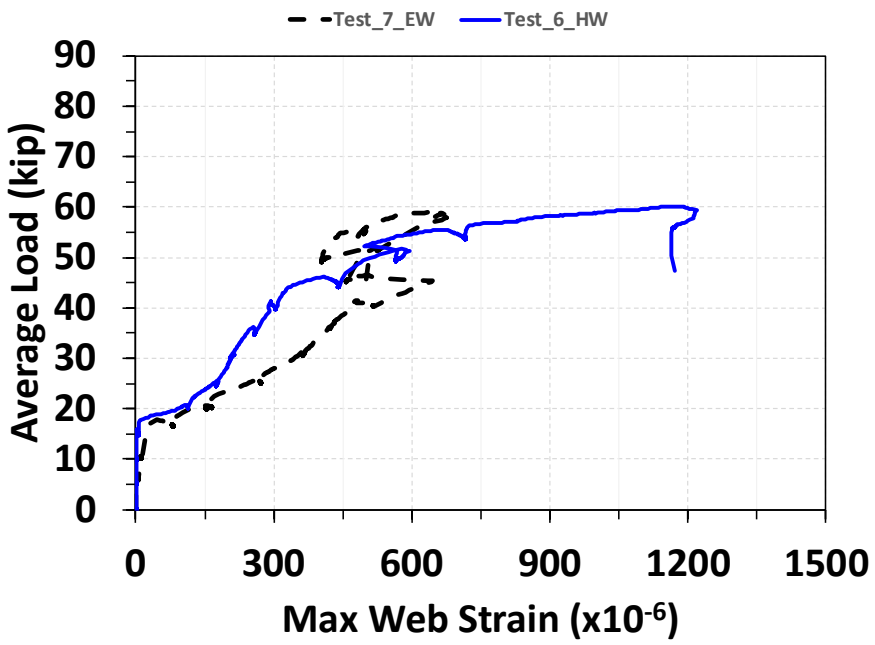

Figure 4-52: Load vs Web Strain - Test 6 & 7 Compared – Short Overhang

4.6.4.5. Load vs Crack Card Width

Figure 4-53 shows the collected data for load-crack card width for the short overhang. The reported maximum crack card width was the maximum observed crack width in the test region. Typically, the maximum crack card widths were observed at the expected critical section which was located on the top of the deck above the termination of the flange along the shear crack. After about 50 kips, the crack width of the edge punching shear type crack became the widest.

Both tests had similar patterns of crack width growth until the specimen started to approach the ultimate capacity, where the electro-welded panel pair started to open up more than the hand-welded panel pair. Nevertheless, the difference was not significant and hardly can this phenomenon be attributed to the types of the wire trusses.

The ultimate load of 60 kips per ram was reached, but due to safety, crack widths were only measured until 55 kips for the electro-welded panel pair short overhang (Test 7), resulting in a maximum observed crack width of 0.07 in. The maximum load where a crack was measured for the hand-welded panel pair short overhang (Test 6) was 50 kips, which corresponds to a 0.075-in.-wide crack.

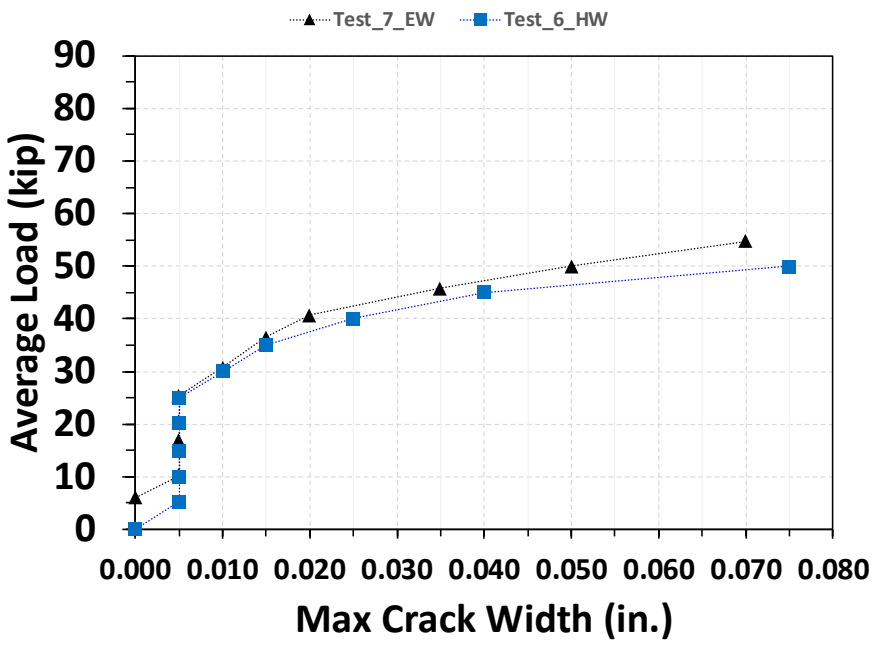

Figure 4-53: Load vs Crack Card Width - Test 6 & 7 Compared – Short Overhang

4.6.5. Long Overhang

The ninth and tenth tests performed on the bridge were the long overhang tested to ultimate capacity. One loading plate was butted against the extreme edge of the overhang so that the loading plate was flush on two free edges of the overhang. The other loading plate was located 4 ft away parallel to the girder, which also was flush with one free edge. The ultimate capacity of each long overhang is comparable, as both the electro-welded and hand-welded panel pairs failed at approximately 34 kips per ram. Figure 4-54 shows the loading pattern for the electro-welded and hand-welded panel pairs.

The long overhang test aimed to bring both specimens to their ultimate capacities in hopes of seeing the failure mode and capacity of the long overhang and to see if the truss type impacted the structural behavior of the long overhang. The displacements, transverse strain, web strain, crack card widths and observed cracks are discussed in the following sections.

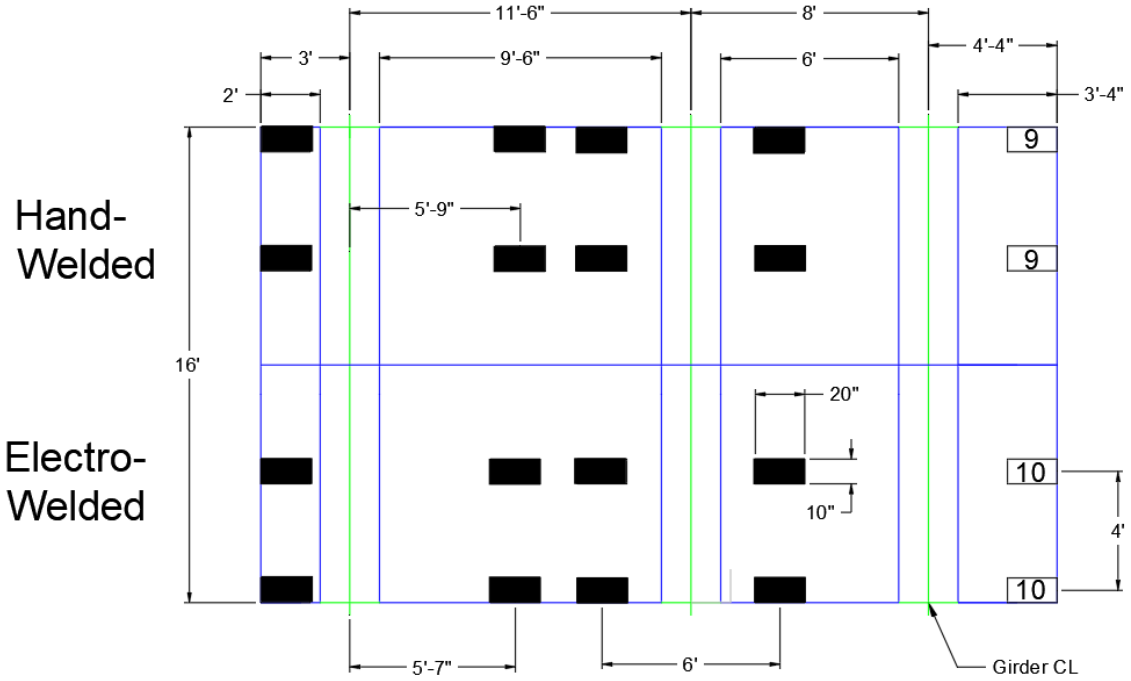

Figure 4-54: Long Overhang Loading Schedule

4.6.5.1. Visual Observation, Cracks, and Failure Mechanism

Cracks were meticulously marked and measured during specimen loading, with photos taken between each loading increment to document their progression. A summary of observed cracks on the top surface of the deck for Tests 9 and 10 is provided in Figure 4-55 and Figure 4-56, respectively. Previous test cracks are depicted in grey to differentiate them from those caused by the current test. While some cracks from prior tests reopened during subsequent tests, careful consideration was given to existing cracks when comparing results between different deck conditions.

Similar crack patterns were noted on both the electro-welded and hand-welded long overhangs, as evident in Figure 4-55 for Test 9 and Figure 4-56 for Test 10. Initially, the long overhangs displayed typical flexural cantilever deflection. These cracks propagated towards the interface of the two sides and did not enter the other side.

Following these flexural cracks, the development of shear cracks appeared near the load plates. Once the shear cracks fully developed, the long overhangs exhibited excessive deflection, signaling a loss of stiffness. Testing was halted upon reaching the ultimate load of 34 kips per ram for both the electro-welded and hand-welded overhangs to prevent damage to the testing equipment. It is important to highlight that many more flexural cracks were observed at the ultimate capacity of both the electro-welded and hand-welded long overhangs, as expected due to the extended overhang moment arm.

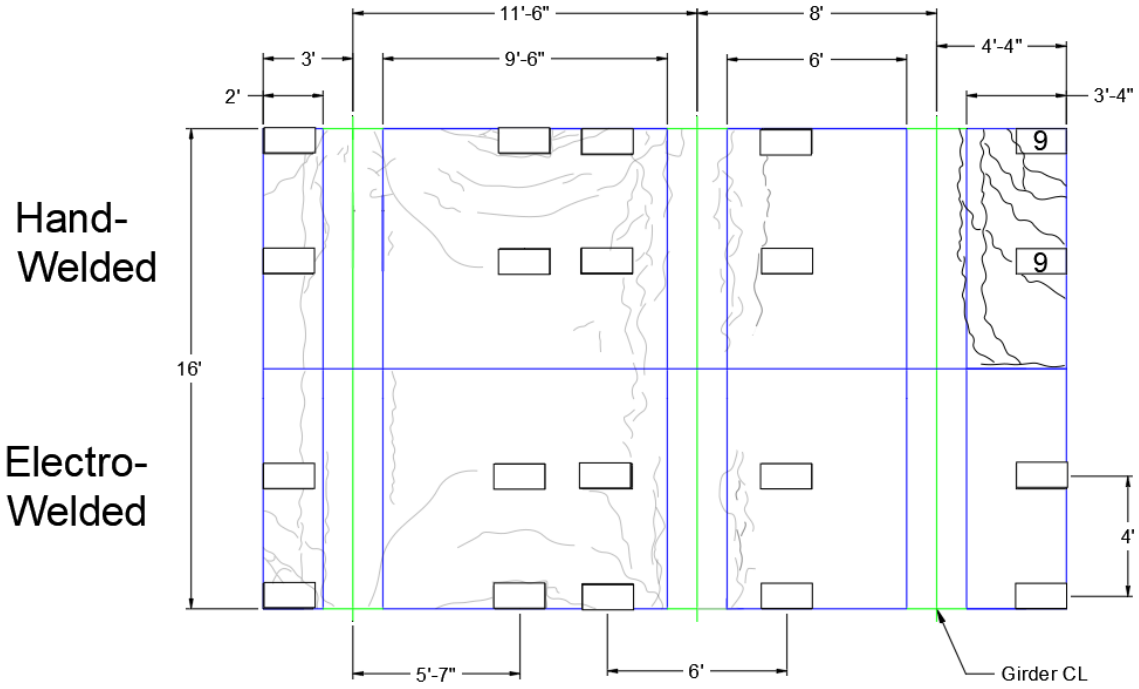

Figure 4-55: Crack Map - Test 9 - Hand-Welded - Long Overhang

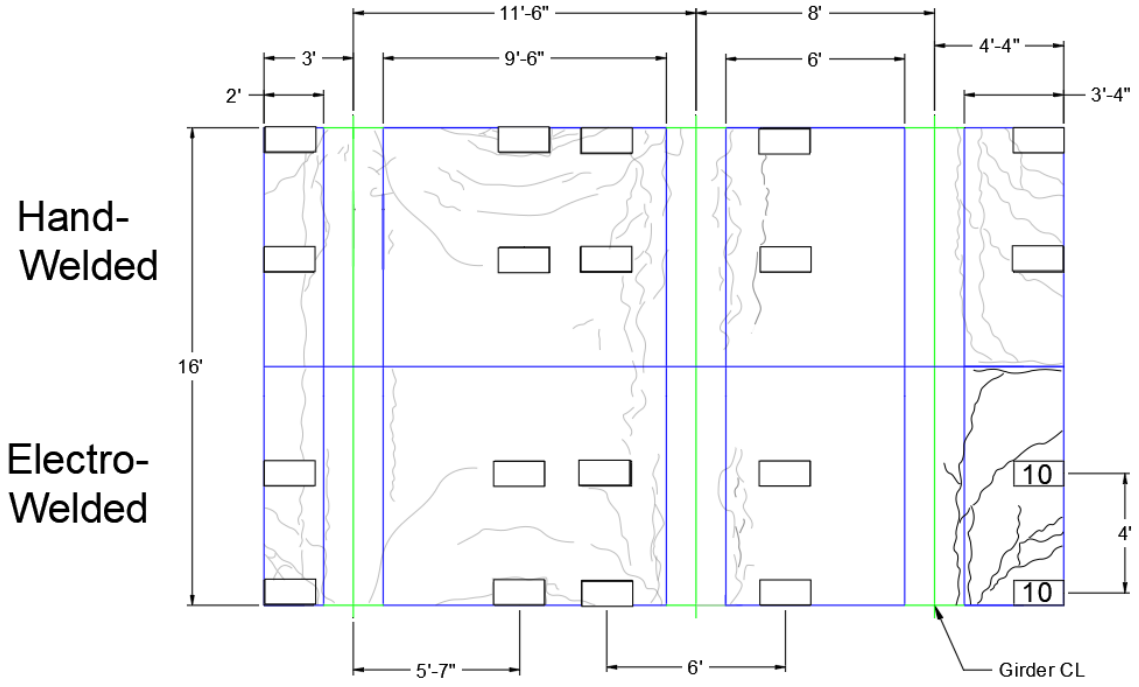

Figure 4-56: Crack Map - Test 10 - Electro-Welded - Long Overhang

To provide context for the failure mechanism, Figure 4-57 and Figure 4-58 showcase the overhangs at ultimate capacity. Figure 4-57(a) and Figure 4-58(a) present similar forms, underscoring the consistency in failure patterns between the two types of overhangs. Both figures illustrate the shear and flexural cracks previously discussed. Notably, the failures exhibit similarity, with shear and flexural cracks appearing almost identically in position and width for both the electro-welded and hand-welded panel pair overhangs. Both overhangs exhibited very large crack widths at ultimate capacity, as depicted in Figures Figure 4-57 (c) and Figure 4-58 (d).

Following the development of large shear cracks, both failures transitioned into ductile flexural failures, mirroring the behavior observed in the short overhang. However, the long overhang exhibited greater deflection and maintained at a lower loading per ram, as expected due to its longer moment arm. In addition, the load points did not overlap the girder flange, making it behave in flexure more. It is important to highlight that once the shear cracks fully formed on both overhangs, the structures began to deflect without bearing additional load. Ultimately, testing for both the electro-welded and hand-welded overhangs was halted as they began to deflect excessively.

(a) Shear crack from free edge

(b) Shear crack from transverse joint

(c) Shear crack from top view

Figure 4-57: Test 9 – Hand Welded Panel Pair Long Overhang – Shear Crack at Ultimate Load

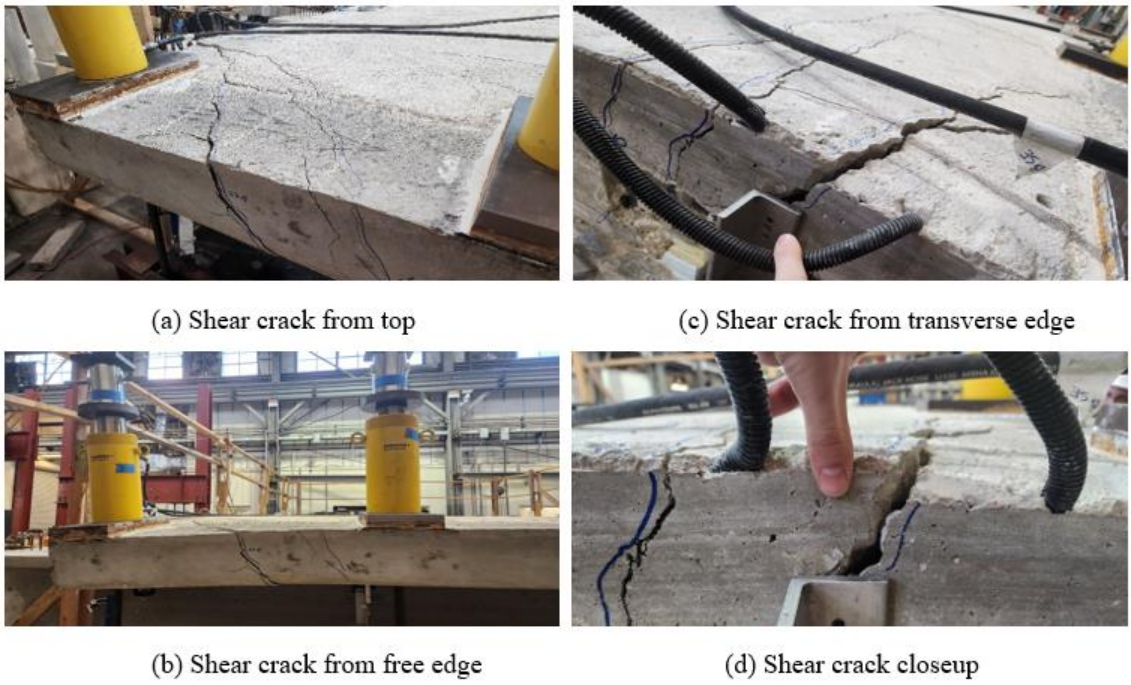

Figure 4-58: Test 10 – Electro-Welded Panel Pair Long Overhang – Shear Crack at Ultimate Load

4.6.5.2. Load vs Displacement

Figure 4-59 shows the collected load-max displacement data for Test 9 and Test 10 for the long overhang. The reported maximum displacement was the maximum of the two displacements measured under each load point. Typically, this maximum displacement was observed from the loading points on the free edge of the panel pair.

It can be seen from the figure that both specimens exhibited almost identical load-displacement relationships. Both specimens had an initial linear behavior, followed by a gradual softening and then gradually reaching a load of 34 kips per ram. Before the tests were stopped for safety issue, a maximum displacement of 1.69 in. was reached for the electro-welded panel pair overhang (Test 9), and 1.76 in. was attained for the hand-welded panel pair overhang (Test 10). In other words, both the electro-welded and hand-welded overhangs had a great level of ductility.

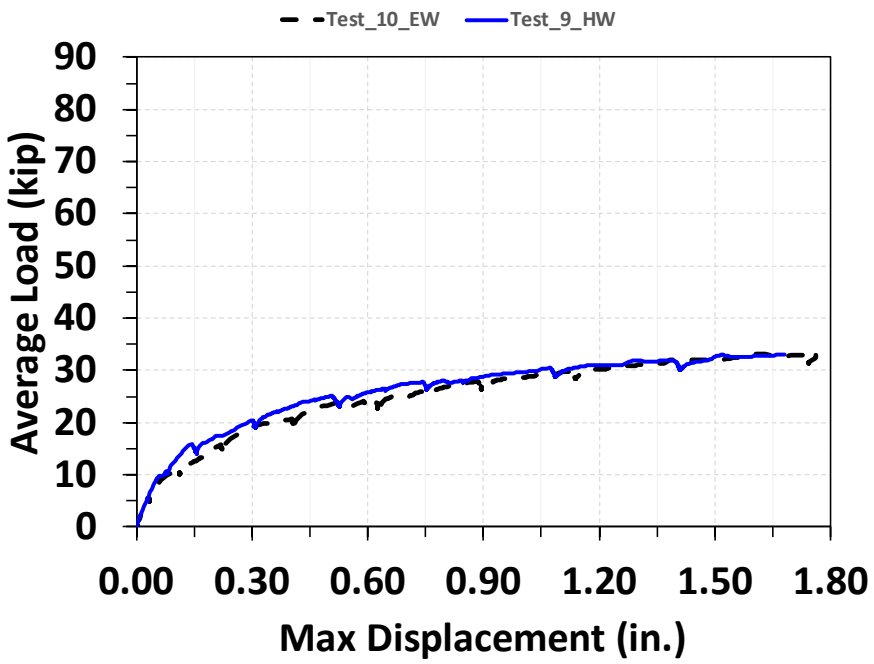

Figure 4-59: Load vs Displacement – Test 9 & 10 Compared – Long Overhang

4.6.5.3. Load vs Transverse Strain

Figure 4-60 shows the load vs transverse strain data for the long overhang for Test 9 and Test 10. The reported maximum transverse strain was the maximum of all transverse reinforcement on the top mat reinforcement. No bottom mat transverse strain gauges were located in the test region, only on the top mat. The reported values are of strain gauges on the top chord of the truss directly above the termination of the top flange. Typically, the maximum transverse strain was observed from the top chord on the truss nearest to the free edge.

From Figure 4-60, it can be observed that the electro-welded panel pair overhang and the hand-welded panel pair overhang exhibited similar trend of growing transverse strain along with the increasing load. The electro-welded panel pair overhang appeared to be slightly more stiff but not obvious. Both specimens had the reached the yield strength of the top chords; at the end of the tests, Test 9 reached a maximum transverse strain of 4600 microstrain for the hand-welded panel pair overhang, and Test 10 reached a maximum transverse strain of 4200 microstrain for the electro-welded panel pair overhang.

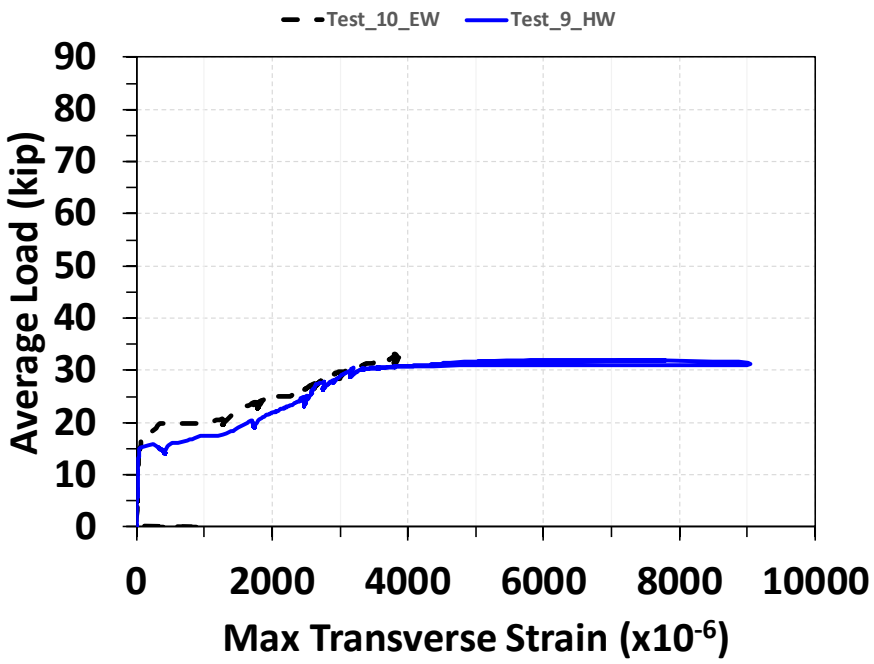

Figure 4-60: Load vs Transverse Strain – Test 10 & 9 Compared – Long Overhang

4.6.5.4. Load vs Web Strain

Figure 4-61 shows the collected Load vs Web Strain data for the long overhang for Test 10 and Test 9. Typically, the maximum web strains were observed in the web members nearest to the facia girder and the free edge. The reported maximum web strain was the maximum of all strain values collected on web reinforcement in the test region.

It can be seen from Figure 4-61 that the two specimens behaved differently in terms of web strains. Although both specimens had reached their yield strength before the end of the tests, the electro-welded panel pair overhang attained a maximum web strain of 7900 microstrain, which is significantly higher than the hand-welded panel pair overhang, which ended up with 2300 microstrain. It should be noted that difficulty placing the strain gauges on the web reinforcement occurred since the direction of the web reinforcement in the wire truss alternates. In addition, complicated stress distribution might have happened at the level of deflection. More study is required to understand the structural implications.

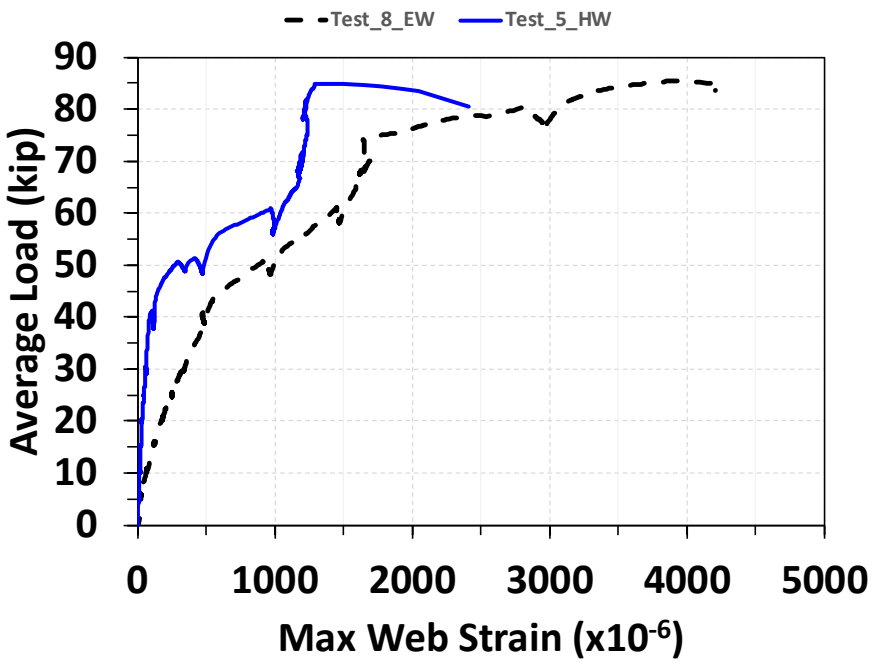

Figure 4-61: Load vs Web Strain – Test 10 & 9 Compared – Long Overhang

4.6.5.5. Load vs Crack Card Width

Figure 4-62 shows the collected data for load-crack card width for the long overhang. Both tests had very similar crack widths throughout the entire test, including at ultimate capacity. The reported maximum crack card width was the maximum observed crack width in the test region. Typically, the maximum crack card widths were observed at the expected critical section which was located on the top of the deck above the termination of the flange along the shear crack.

The ultimate load of 34 kips per ram was reached, but due to safety, crack widths were only measured up to 27.5 kips for the electro-welded panel pair long overhang (Test 10), resulting in a maximum observed crack width of 0.12 inch. The maximum load where a crack was measured for the hand-welded panel pair long overhang (Test 9) was 29 kips, which corresponds to a 0.13-in.-wide crack. At the ultimate capacity of the long overhang 34 kips, the shear crack width became around half an inch wide, as shown in Figure 4-58(c) and Figure 4-58(d).

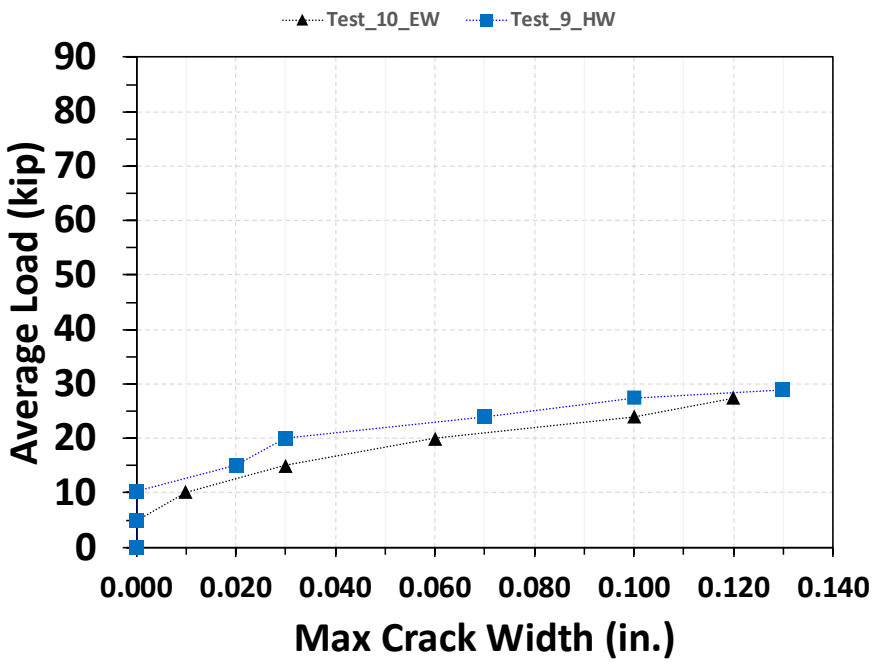

Figure 4-62: Load vs Crack Card Width – Test 10 & 9 Compared – Long Overhang

4.7. Evaluation of Strength and Serviceability

In this section, the average applied loads on different specimens at various loading stages are compared for the purpose of evaluating the strength and the serviceability of WTPD panel decks with different wire truss types. Applicable test results from Project 0-4418, which developed the traditional prestressed precast partial depth panel deck system, were extracted and presented together to have a direct comparison.

The evaluation includes three loading stages: 1) V_{test}, representing the average load at the end of test or the ultimate load, 2) V_{crack}, representing the average load that caused the first crack, and 3) V_{Δ}, representing the average load that caused a deflection-to-span ratio of 1/800, which is the AASHTO LRFD deflection limitation. The average load in this section is presented in terms of the ratio of the average load to the design tandem load (DT, or 12.5 kips).

4.7.1. Interior Long Span under Positive Moment

Figure 4-63 demonstrates a comparison among specimens loaded at the interior long span under positive moment from the current project and available specimens in Project 0-4418. For the specimens from Project 0-4418, the specimen ID SEJ, 6 in.-TS PCPE represents panel decks reinforced with top mat reinforcement of 6 in. and sealed expansion joints; the other specimen had the same top reinforcement pattern but had no expansion joints. In the current comparison, all test average loads are the ultimate loads, and it should be noted that the specimens from 0-4418 had a span of 10 ft, which is somewhat lower than that of the current project.

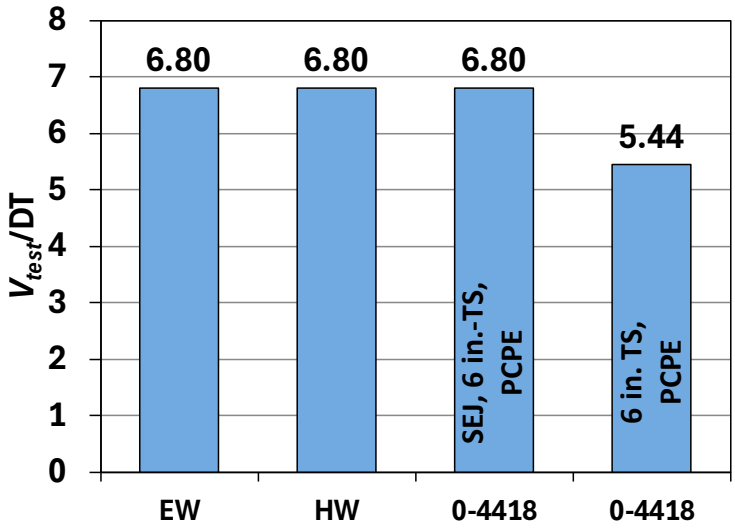

Figure 4-63 Comparison of Ultimate Load Carrying Capacity in Long Span under Positive Moment

It can be seen from Figure 4-63 that the electro-welded and the hand-welded WTPD panel deck specimens had the same ultimate capacity as SEJ 6 in.-TS PCPE, reaching a load-carrying capacity of 6.8DT. In addition, they surpassed the load-carrying capacity of 6 in.-TS PCP. It is evident that WTPD panel decks, regardless of the wire truss type, had comparable or better load carrying capacity when the span is under 11.5 ft.

Other than the load-carrying capacity, the average load that caused the first crack was also available for this test, as shown in Figure 4-64. It can be seen from the figure that specimens from the current project had cracking loads slightly lower than their counterparts in Project 0-4418. The electro-welded WTPD panel decks cracked at a load of 1.24DT while the hand-welded ones at 2.00 DT; both of their counterparts had a cracking load of 2.20DT. Nevertheless, cracks all occurred at loads higher than the DT, indicating the serviceability is satisfactory. In addition, as the test conditions did not perfectly match Project 0-4418, the specimens from the current project were not considered inferior in terms of serviceability.

Moreover, serviceability was evaluated using the load that caused deflections surpassing the AASHTO LRFD limitation. In this case, the deflection limitation was 0.17 in. As shown in Figure 4-65, when reaching a deflection of 0.17 in., the electro-welded WTPD panel decks required 1.22 DT while the hand-welded ones required 2.01, implying the domestically made product might have a better serviceability, echoing the results of cracking loads shown in Figure 4-64.

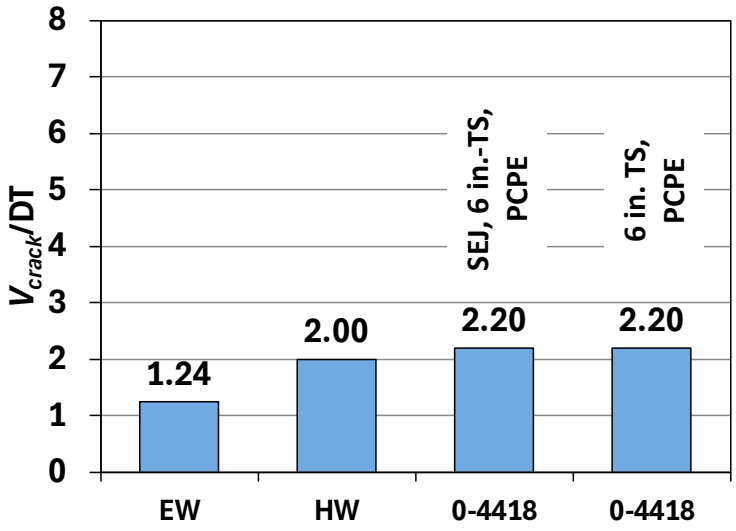

Figure 4-64 Comparison of Cracking loads in Long Span under Positive Moment

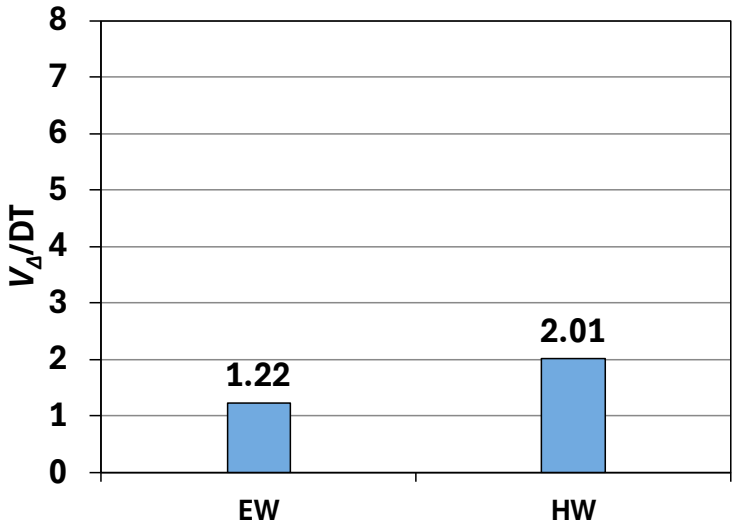

Figure 4-65 Comparison of loads causing deflection limit in Long Span under Positive Moment

4.7.2. Interior Short Span under Positive Moment

Figure 4-66 shows a comparison between the electro-welded WTPD panel deck test and the hand-welded one under positive moment in the interior short span. In these tests, the specimens were not brought to failure so that the V_{test} value in the figure represents the load at the end of the test. In can be seen that both specimens reached a load of 4.8DT without any sign of failure, meaning the capacities of both specimens were considerably higher than the design tandem load.

Moreover, the V_{crack} values of the two specimens were also higher than DT, requiring 1.22DT and 2.01DT to cause the first crack for the electro-welded WTPD panel deck test and the hand-welded one, respectively. It is evident once again that the domestically made product might have a better serviceability.

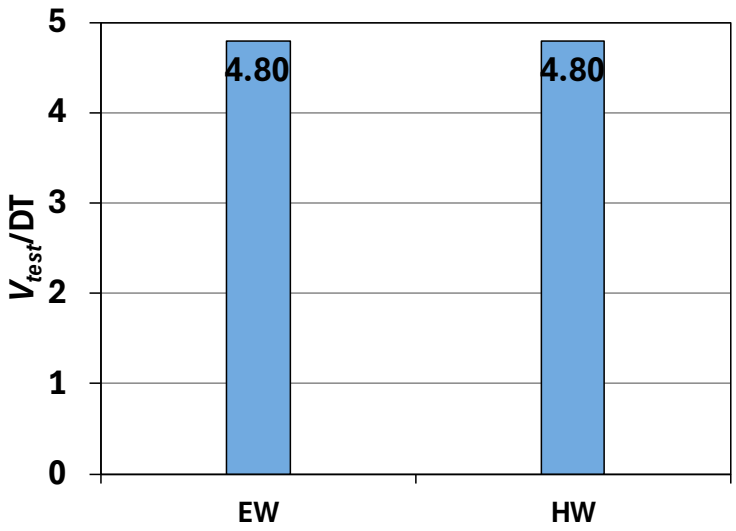

Figure 4-66 Comparison of Loads at the End of Test in Short Span under Positive Moment

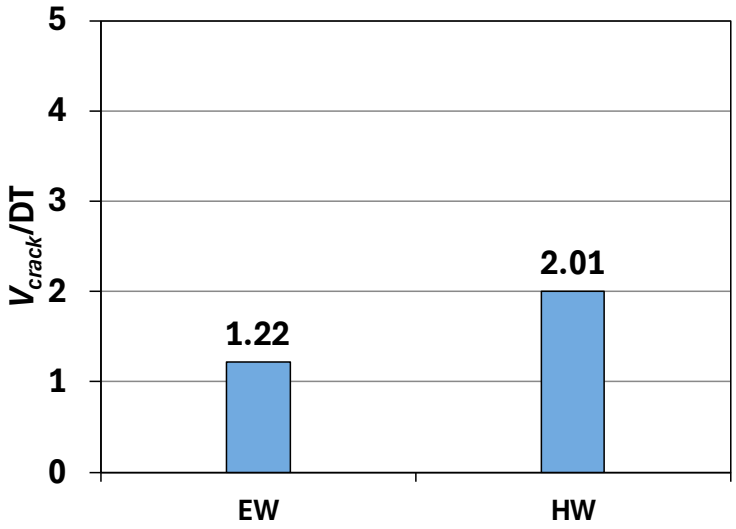

Figure 4-67 Comparison of Cracking Loads in Short Span under Positive Moment

In these two tests, none of the specimens reached the deflection limitation, 0.12 in. under the applied load at the end of the tests. This observation indicates that the deflection remained low although a load of 4.8DT was applied. Both specimens exhibited great serviceability in terms of deflection.

4.7.3. Interior Spans under Negative Moments

Figure 4-68 shows a comparison between the electro-welded WTPD panel deck test and the hand-welded one under negative moment in the interior short span. In these tests, the specimens were not brought to failure so that the V_{test} value in the figure represents the load at the end of the test. In can be seen that the specimens reached loads of 2.88DT and 3.04DT without any sign of failure, meaning the capacities of both specimens were considerably higher than the design tandem load.

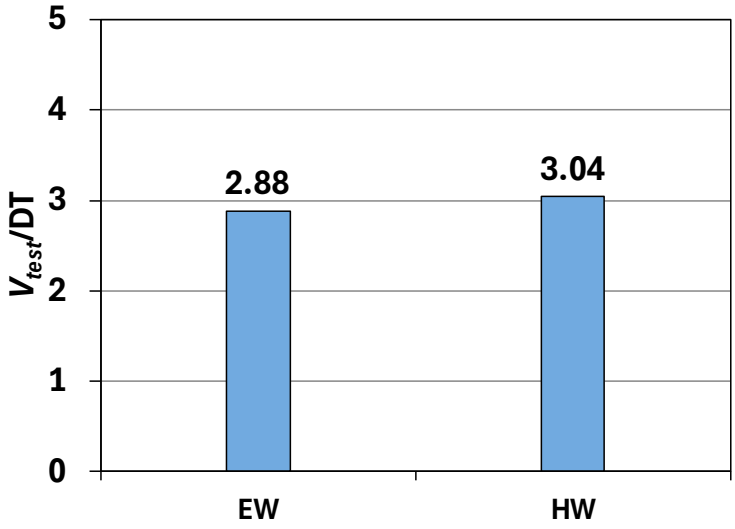

Figure 4-68 Comparison of Loads at the End of Test in Interior Span under Negative Moment

Moreover, the V_{crack} values of the two specimens were also higher than DT, requiring 1.62DT and 1.15DT to cause the first crack for the electro-welded WTPD panel deck test and the hand-welded one, respectively. In this case, the electro-welded one had a higher cracking load; therefore, it is not decisive which product led to better serviceability. Similarly, both specimens did not reach the deflection limitation during the tests.

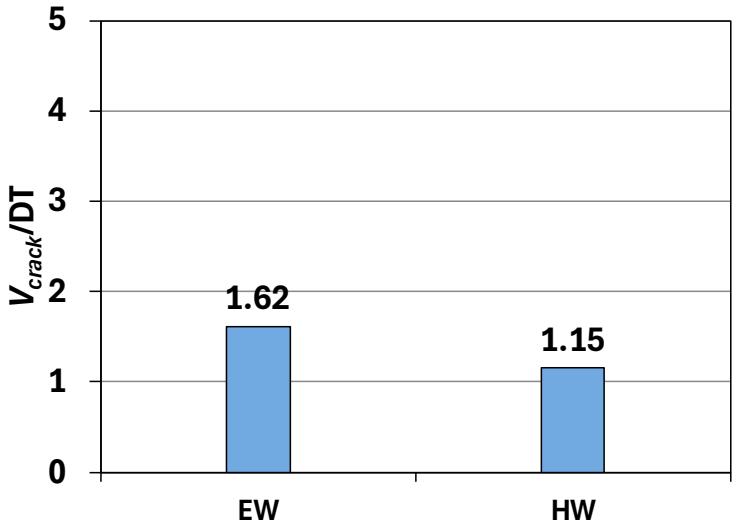

Figure 4-69 Comparison of Cracking Loads in Interior Span under Negative Moment

4.7.4. Short Overhang

Figure 4-70 shows a comparison among specimens loaded at the short span from the current project and available specimens in Project 0-4418. In the current comparison, all test average loads are the ultimate loads. It can be seen from the figure, the two specimens from the current project reached

loads of 4.72DT for the electro-welded one and 4.80DT for the hand-welded one, comparable to 6 in TS, PCPE from Project 0-4418. Specimen SEJ, 6 in.-TS PCPE was much higher than any other presented specimens, which can be attributed to the existence of the SEJ. It should be noted that for overhangs, rail impact load should be considered but the shown tests did not reach the level. Nevertheless, the WTPD panel decks, regardless of wire truss types, can at least match the capacity of the traditional panel deck system.

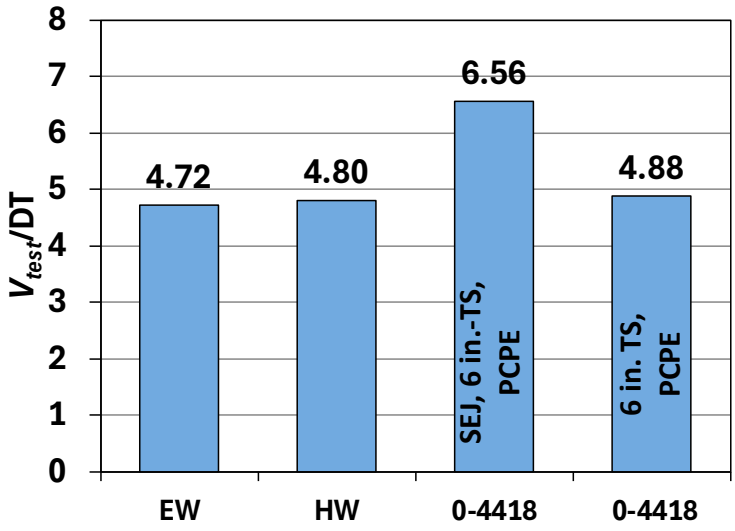

Figure 4-70 Comparison of Ultimate Load Carrying Capacity in Short Overhang Test

It should also be noted that cracking loads and deflection limit were not evaluated here because none of the tests was tested under rail impact load, and there was no companion evaluation in Project 0-4418.

4.7.5. Long Overhang

Figure 4-71 demonstrates a comparison between the electro-welded WTPD panel deck test and the hand-welded one at the long overhang. In these tests, the specimens were brought to failure so that the V_{test} value in the figure represents the ultimate load-carrying capacity. It should be noted that there are no companion specimens in Project 0-4418. It can be seen from the figure that the specimens had identical ultimate capacities, reaching a load of 2.64DT. It should also be noted that the tests did not reach the level of rail impact; nevertheless, the capacity information provided in the figure provides insight into the long overhang capacities, which were still higher than twice the design tandem load.

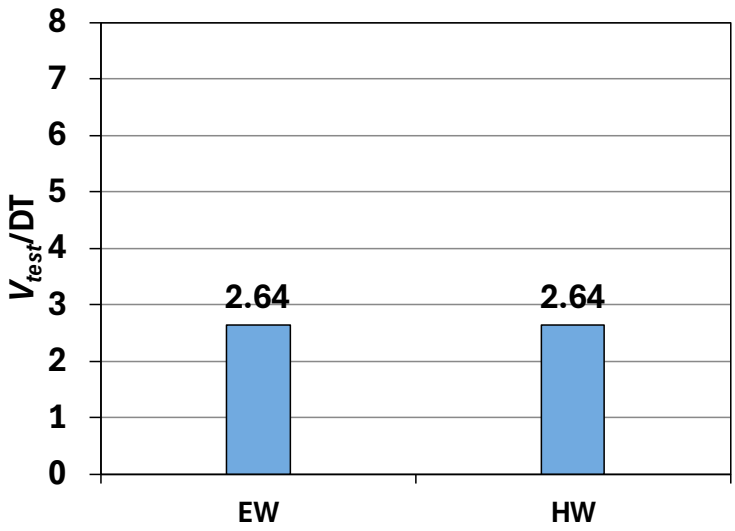

Figure 4-71 Comparison of Ultimate Load Carrying Capacity in Long Overhang Test

4.8. Finite Element Modeling

This section presents applying non-linear finite element analysis on the full-scale bridge deck. Modeling techniques, analytical results, and verification against the test results are included.

4.8.1. FEM Software and Modeling Approach

The research team used ATENA 3D from Červenka Consulting for the FEM analysis. This software was chosen due to its focus on reinforced concrete modeling. Due to the size of the specimen, modeling all loading cases in one model was impossible to do computer memory and time constraints. Therefore, the specimen was divided into four separate, smaller models. Each model focused on a different test location in the specimen (positive moment on short span, positive moment on long span, short overhang, and long overhang). Negative moment across the interior girder was not included due to constraint of computational resources.

The models were made with 3D elements as opposed to shell elements. The tests were expected to fail in punching shear, so shell elements were not expected to capture this result as well as the 3D elements would. The following paragraphs detail how the modeling was approached by outlining the process using pictures from Test 5.

4.8.1.1. Material Parameters

The material properties of the steel loading plates, CIP concrete, precast concrete, reinforcement, and bond for reinforcement were defined. Firstly, the steel loading plates used a 3D Elastic Isotropic template and all others parameters were kept at default settings. Secondly, the precast and CIP concrete material properties were based on the 3D Nonlinear Cementitious 2 template. This was a direct definition using a cubic compressive strength. The cubic compressive strength

was calculated from the cylinder compressive strength testing that had been completed; the cylinder compressive strength was multiplied by 1.176 to get the cubic compressive strength. The elastic modulus parameter was replaced by cylinder modulus testing if it had been completed. All other parameters were kept at default settings. Lastly, bond for reinforcement was defined as shown in Figure 4-72, which was based on the default settings for good confinement and the bar size of the wire truss' chords.

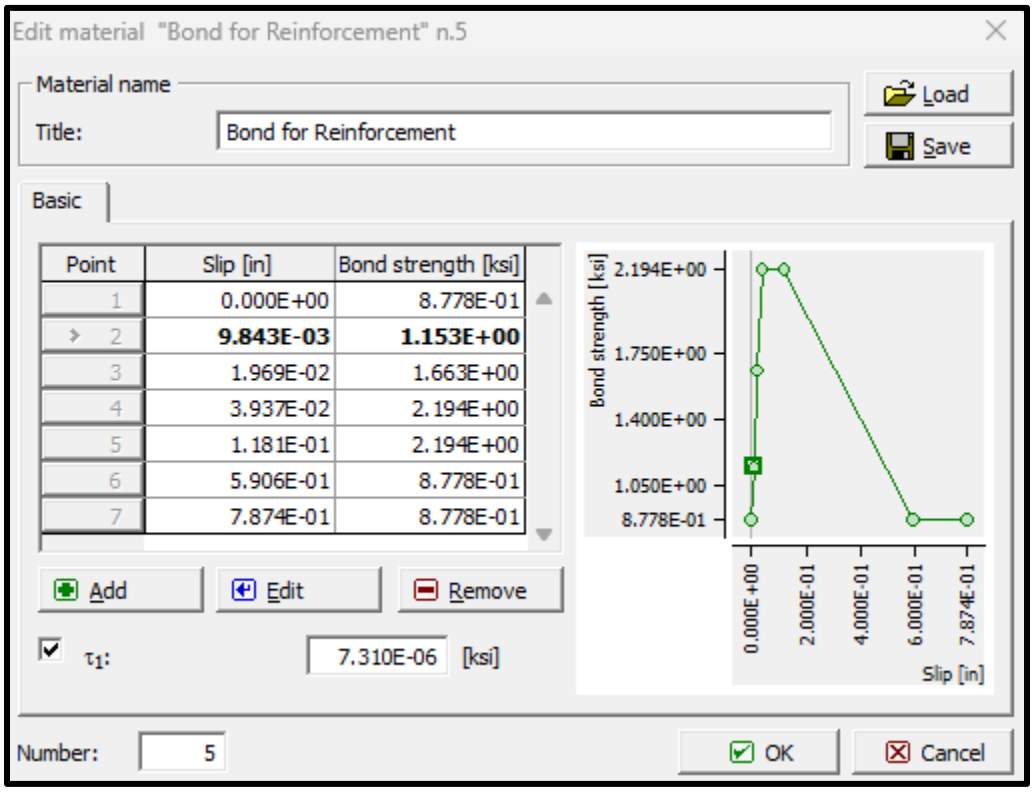

Figure 4-72: Bond for Reinforcement Properties

4.8.1.2. Modeling Elements

Macroelements are used in the software for solid elements in the real-world. The macroelements of test specimens were created per relative locations of the test program. These included steel loading plates, CIP concrete, and precast concrete. These macroelements extended to where the centerline of the Tx-28 girders would be.

The CIP and precast macroelements included smear reinforcement in the vertical direction. This smear reinforcement represented the web members of the steel trusses. The reinforcement ratio was the same for both the precast and CIP and was a ratio of the area of all web members that intersected a horizontal plane between the chords divided by the total area of concrete the intersected that same plane. The layout of the macroelements can be seen in Figure 4-73.

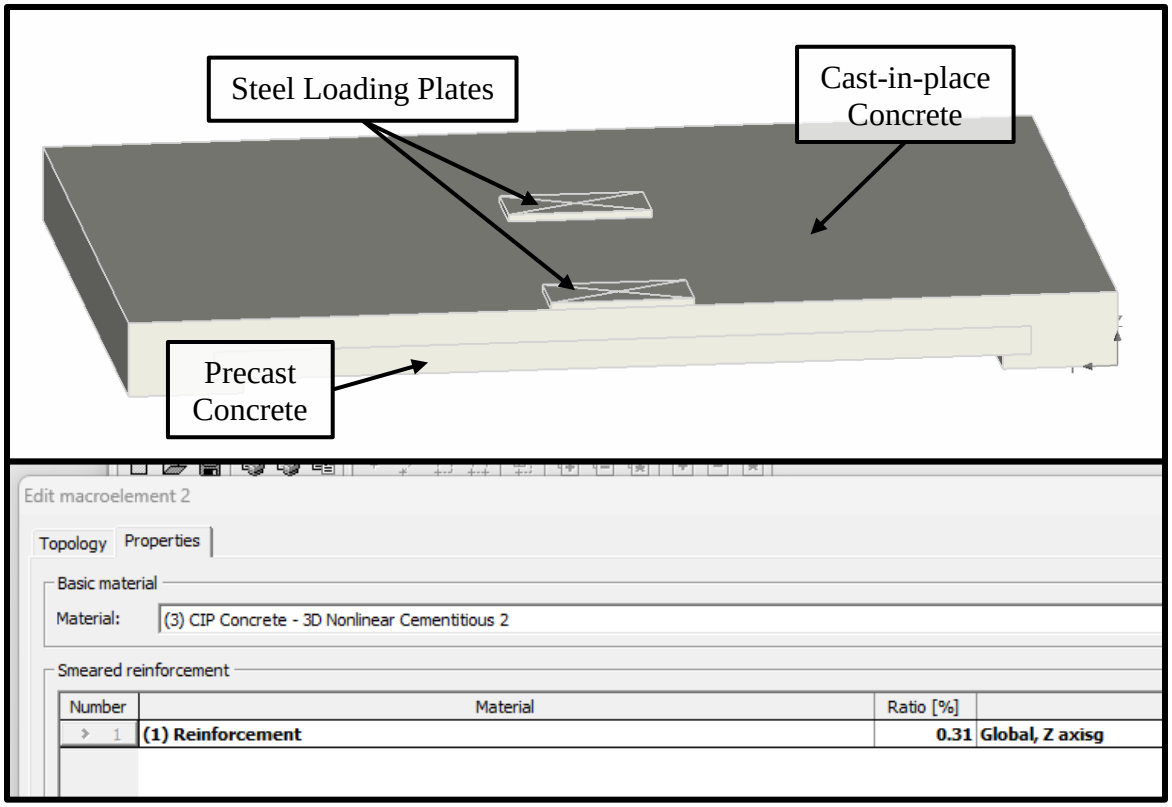

Figure 4-73: Macroelement Layout and Properties

The top and bottom chords of the trusses were made from discrete reinforcement as shown in Figure 4-74. Each chord had dimensions of a No. 4 rebar and had bonding properties as shown before in Figure 4-72. Additionally, the R-bars that extended from the girders were also modeled. Reinforcement that would have extended further in the experimental specimen was not allowed slip in the FEM.

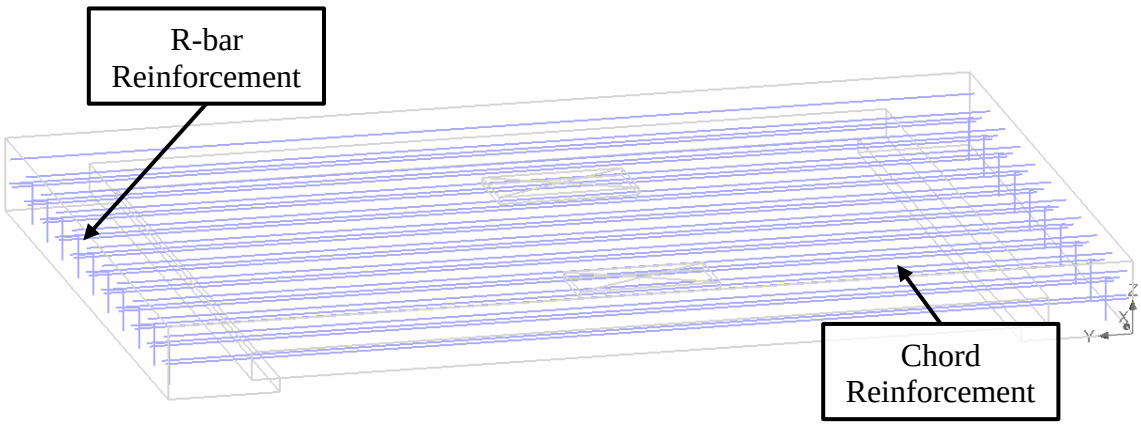

Figure 4-74: Reinforcement Layout

4.8.1.3. Boundary Conditions

The boundary conditions of the model consisted of restricting the edge faces from moving out-of-plane. The edge faces include the faces above the girders, the faces that form the separation between panels, and the faces that neighbor the girders. It should be noted that the Tx-28 girders were not actually modeled; instead, fixity as the boundary condition was assigned as the support. These can be seen in Figure 4-75.

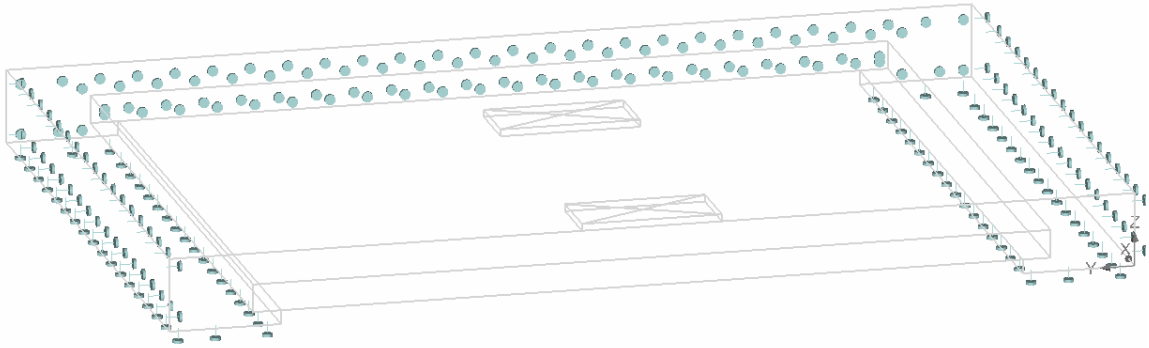

Figure 4-75: Boundary Conditions

Load was applied at the center of each loading plate. The loading was stepped at one kip, to give significant resolution to the model. The deflection of each loading plate was monitored with monitoring points during each load step. The model used the standard Newton-Raphson for the solution parameters. The model was run until the model failed, where the model could no longer converge on a solution.

4.8.1.4. Mesh

Both the CIP and precast concrete macroelements used an extruded finite element mesh while the steel plates used a tetra finite element mesh. The model had a depth of four elements. Due to limitations of the computer memory, the fineness of the mesh could not be increased further. This mesh is shown in Figure 4-76.

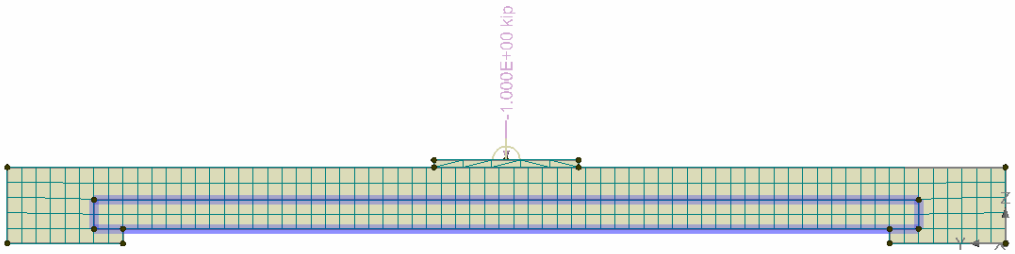

Figure 4-76: Finite Element Mesh

4.8.1.5. Analysis

The research team started with Test 5 as it was the most straightforward of all the cases and would serve as a prototype to refine the material properties and boundary conditions. After these the research team was satisfied with the results of this model, all other models were made. Each of these and their results compared with the experimental results can be found in the following sections.

4.8.2. Modeling Results and Verification

4.8.2.1. Test 5 – Positive Moment Long Span

This case was the first location to be modeled in FEM. This was selected because this was the only test that sought for ultimate punching shear capacity in the interior span, making the test the most representative of the real-world setup. Therefore, the research team used this case as the benchmark and then applied the technique, including the material properties and boundary conditions to all other cases. Figure 4-77 shows an overview of the FE mesh and discrete reinforcement. As mentioned in Section 4.8.1, the top and bottom chords are modeled as discrete reinforcement. Additionally, the longitudinal and R-bars are modeled as well for completeness.

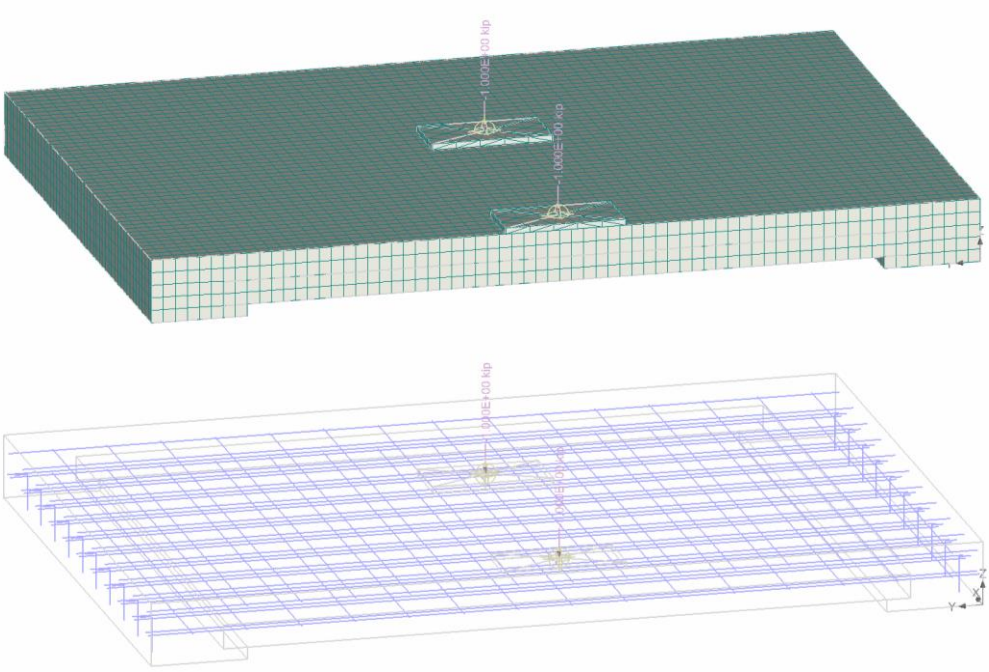

Figure 4-77: Finite Element Model for Test 5

As shown in Figure 4-78, the FEM correctly aligns with the strength capacity of the experimental results. The research team took the liberty of removing the last data point of the FEM – Ext. Plate series. This data point approached 8 in. in deflection, which made the other series difficult to view. As a deflection of 8 in. is an unobtainable deflection, this point was considered divergent and removed.

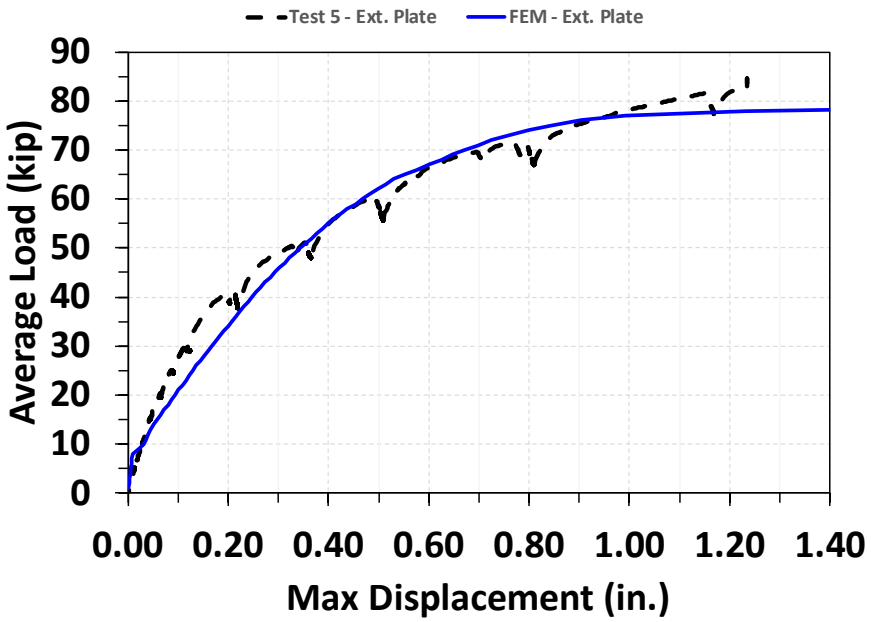

Figure 4-78: Test 5 Load Deflection Comparison

4.8.2.2. Test 4 – Positive Moment Short Span

This case was one of the last sections modeled in FEM. The model was made using the same techniques used in the FEM for Test 5. The model was contained the portion of the deck being loaded and was bound by the centerlines of the girders as shown in Figure 4-79. The maximum load was not reached in the experimental test, and so the results achieved by the FEM exceed experimental results in Figure 4-80. The loading surpassed 90 kips without failure as it was deemed to be diverging from expectations. It can be seen from the figure that the analytical results are not well matching the experimental results. The cause can be due to the improper boundary conditions and intact model. In the test program, these two tests were started with pre-cracking. In addition, the test specimen was placed on Tx-28 girders instead of fixed supports. On the short span, the girders might have taken higher loads than that on the long span (Test 5), which may have caused more deflection in the real-world setup. Further study is needed to gain more insights.

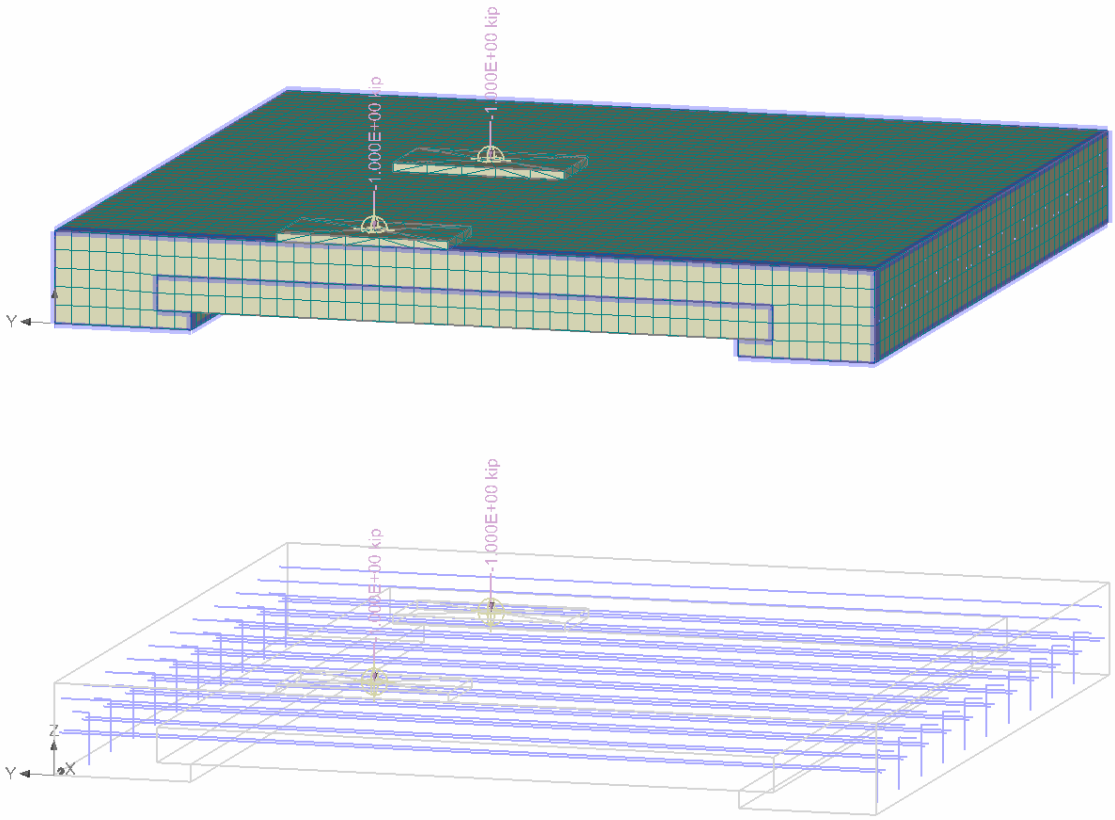

Figure 4-79: Finite Element Model for Test 4

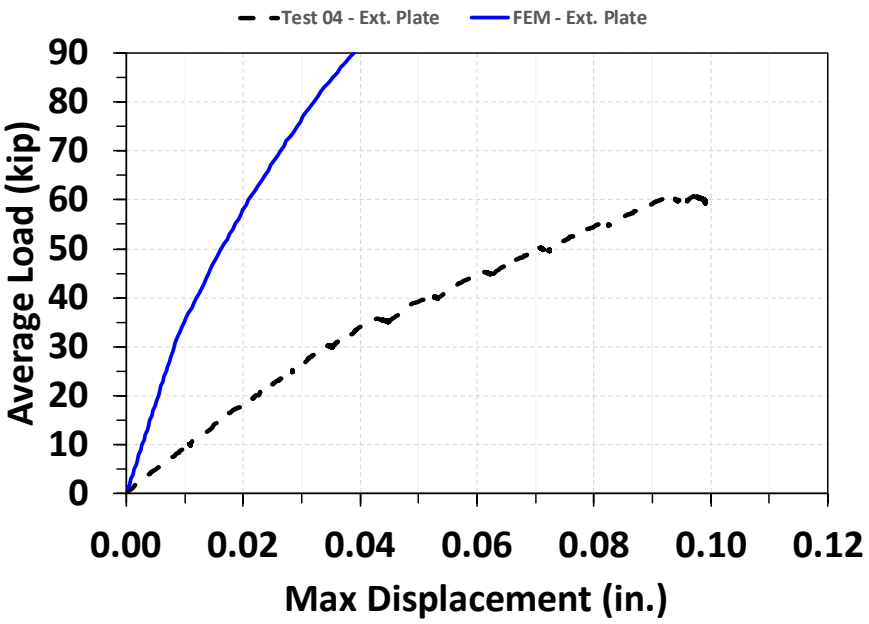

Figure 4-80: Test 4 Load Deflection Comparison

4.8.2.3. Test 06 – Short Overhang

The model for this overhang consisting of the precast panel and CIP layers of the overhang stretches to the centerline of the fascia girder, shown in the fixed condition of the girder did not allow any rotation from the back span. Figure 4-81 shows that the precast panel includes the curb that prevents the CIP concrete from spilling over the end of the panel during casting.

As shown in Figure 4-82, this case showed significantly more stiffness in the FEM results when compared to the experimental results. This can partially be attributed to existing cracking that would have occurred from pervious experimental testing that propagated into these tests' regions. Improper assigned boundary conditions would have contributed to the difference in the stiffness. In addition, the maximum load of the FEM exceeded the load in Test 6. The research team believes this to be due to the fineness of the mesh. Shear behavior can be easily influenced by the mesh. This explains why the long overhang and long span positive moment tests align more closely with the FEM results. However, the maximum load of the FEM is still close enough to provide a suitable approximation.

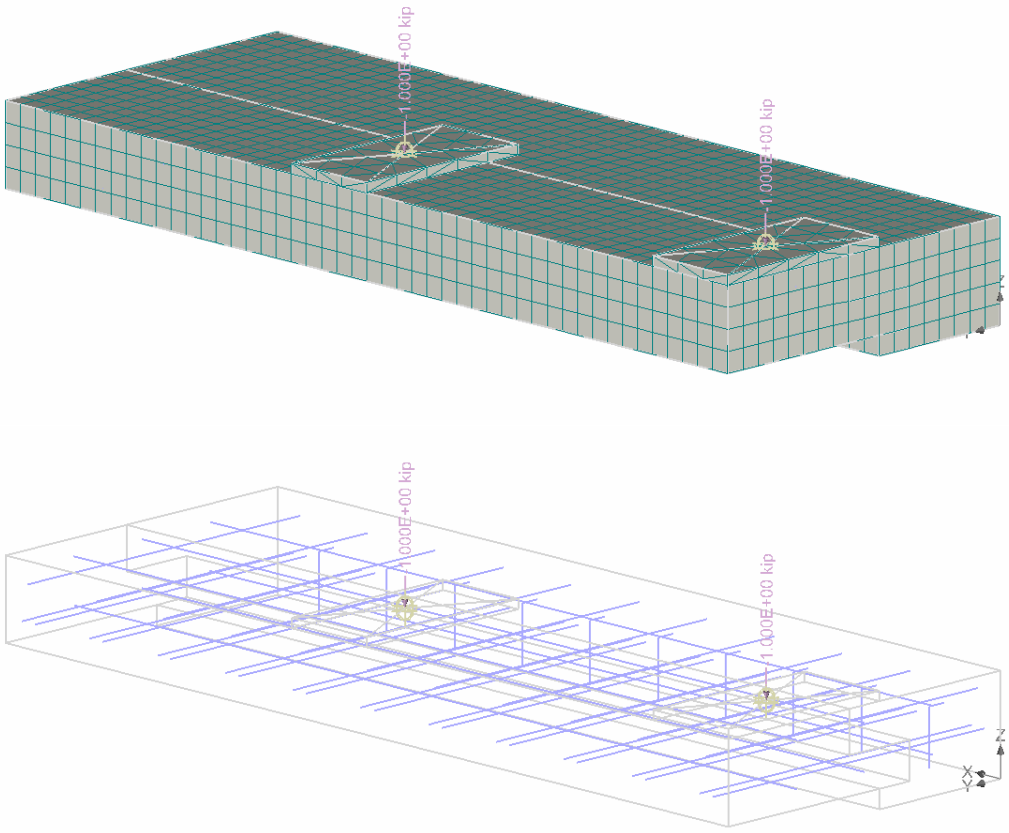

Figure 4-81: Finite Element Model for Test 6

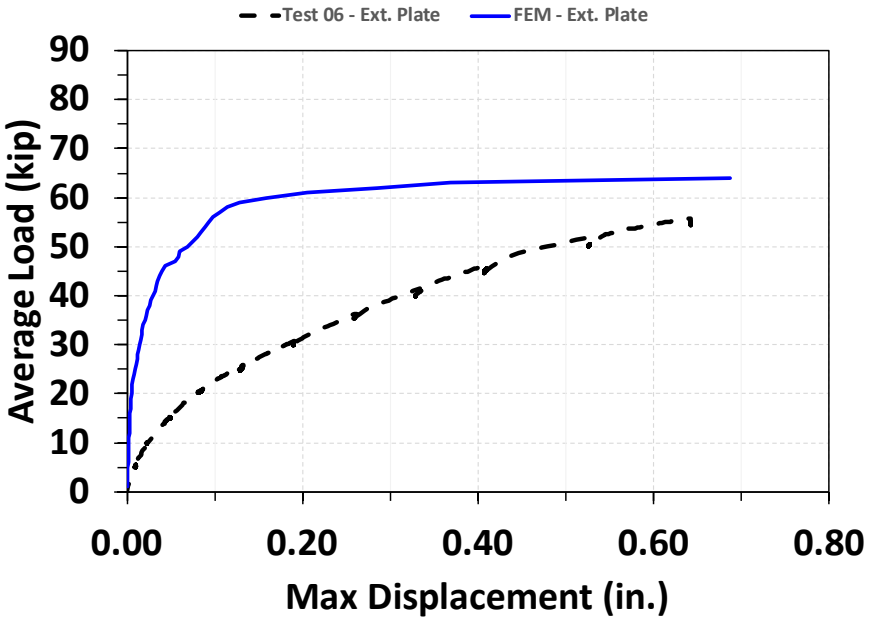

Figure 4-82: Test 6 Load Deflection Comparison

4.8.2.4. Test 10 – Long Overhang

Like the model for the short overhang, this model consisted of the precast panel and CIP layers of the up to the centerline of the fascia girder, which was defined to be a fixed boundary. Load was applied on steel plates to prevent any local cracking that ended the test early. These plates can be seen in Figure 4-83. The maximum load of the FEM results closely aligned with that of Test 10. Both the model and the experimental results failed around 32 kips. The load deflection plot comparing the FEM and experimental results can be found in Figure 4-84.

In this case, the discrepancies between the analytical and experimental results were smaller than the case of short overhang. It is, again, believed that the behavior of long overhangs tends to have more flexural instead of shear deformation, which was not as sensitive to mesh size.

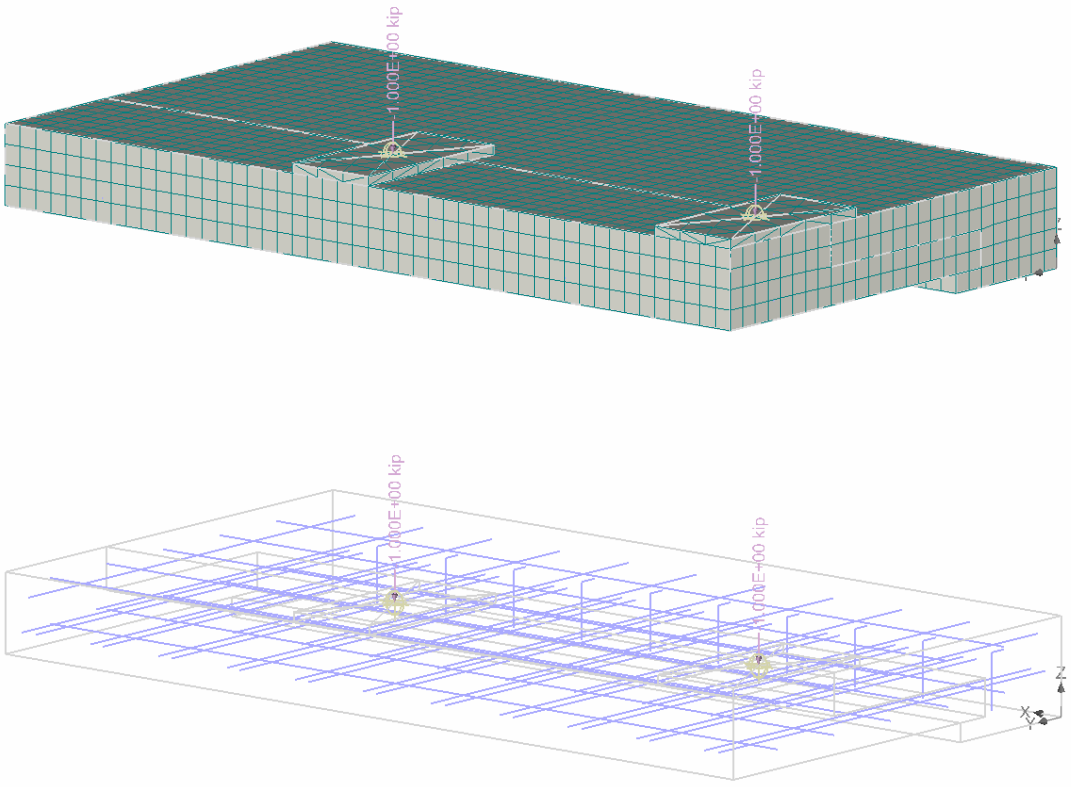

Figure 4-83: Finite Element Model for Test 10

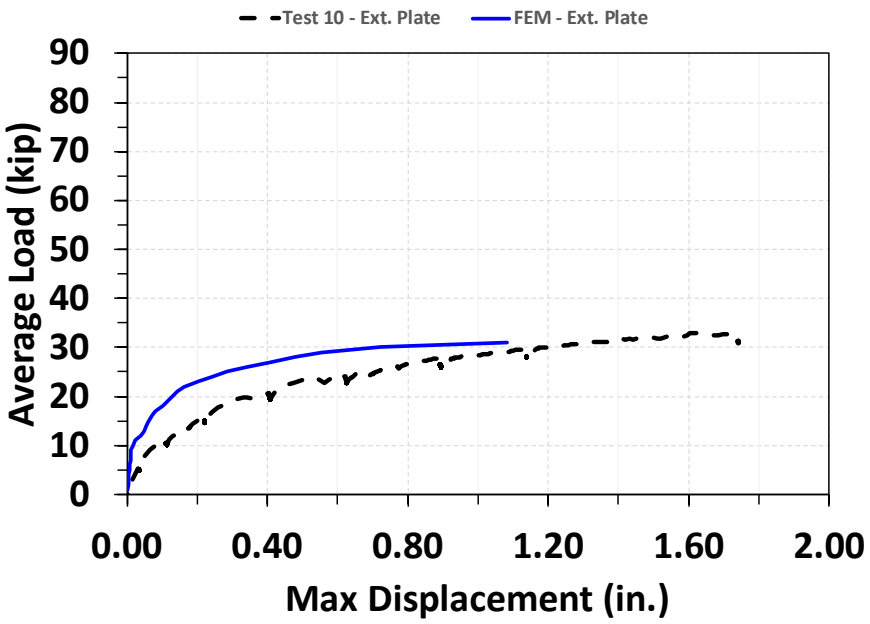

Figure 4-84: Test 10 Load Deflection Comparison

4.9. Summary

TxDOT Project 0-7041: Develop NextGen Texas Bridge Decks aims to develop a full-width partial-depth precast concrete panel (PCP) deck for Texas bridges. Ten tests were conducted on the full-scale bridge deck specimen. The full-scale deck specimen was divided into two sides; one side was reinforced with hand-welded wire trusses while the other side was reinforced with electro-welded wire trusses. Each side consisted of five different tests: applying design tandem load through loading steel plates that created 1) negative moments near the interior girder, 2) positive moment on the long span, 3) positive moment on the short span, 4) loads on the short overhang, and 5) loads on the long overhang. The span and overhang lengths were based on those commonly used in Texas. After completing the tests and data analysis, conclusions can be drawn as follows:

- Both of the hand-welded and the electro-welded panel pair decks failed in punching shear at the same load level during the positive moment over the long span test. During the short overhang test, both hand-welded and electro-welded panel pairs failed in combined flexure and shear at a similar load level. Therefore, wire truss type does not appear to alter the ultimate capacities.

- Both of the hand-welded and the electro-welded panel pairs deflected similarly at service loads; at ultimate loads, the hand-welded panel pairs demonstrated greater ductility than their electro-welded counterparts at the short overhang test mainly due to the difference in the mechanical properties of the two different trusses; both specimens sustained similar deflection at the long overhang test until the test was halted for safety.

- The ultimate capacity of the positive moment over the long span was 6.8 times larger than the service design tandem for both truss types. The ultimate capacity was comparable to the traditional partial depth panel deck system developed in Project 0-4418, implying that the wire trusses, regardless of types, did not notably enhance WTPD bridge decks' punching shear performance, which can be attributed to the fact that the placement of the wire trusses may not effectively have web member oriented correctly to arrest punching shear cracks.

- The measured crack widths of both tests under the design tandem load (12.5 kips) were satisfactorily under the AASTHO LRFD's requirement.

- The FEM approach successfully approximated the capacity of these overhang panels for the majority of load cases. For some cases, the deflection and stiffness were not appropriately captured, which can be attributed to improperly assigned boundary conditions and mesh size limitations. Nevertheless, this approach could be used in the field for determining the strength of the overhang sections and punching shear capacity of bridge decks.

Chapter 5. Investigation into Fatigue Behavior

The research project was split into different tasks that were carried out by members of the research team. The first task, found above in Chapter 3, centered on testing the exposed trusses under construction conditions, before the CIP deck is cast. Specimens were placed under 4-point bending to confirm the failure mode (buckling, pullout, and yielding) of the trusses met the minimum load requirements and so the trusses could be modified if needed to present a more favorable failure mode in later tasks. The second task, found above in Chapter 4, centered on load testing full-size overhang panels in a full-scale bridge deck after the top CIP deck was cast. The loading matrix included positive moment and negative moment test cases, as well as a long overhang and short overhang test case. Finally, the last task investigated the behavior of specimens under fatigue loading. These specimens were subjected to cyclic loading until failure or adequate life were achieved.

This chapter will center on the fatigue testing and fabrication process for the fatigue panel design. It will cover the design and fabrication of the fatigue specimens, the experimental testing, and experimental results.

5.1. Experimental Program

5.1.1. Test Plan

The fatigue test was to apply cyclic load onto a WTPD panel deck strip that simulated decks supported with a 36-in. flange, as shown in Figure 5-1. Loads were applied simultaneously on both ends, creating negative moment in the deck.

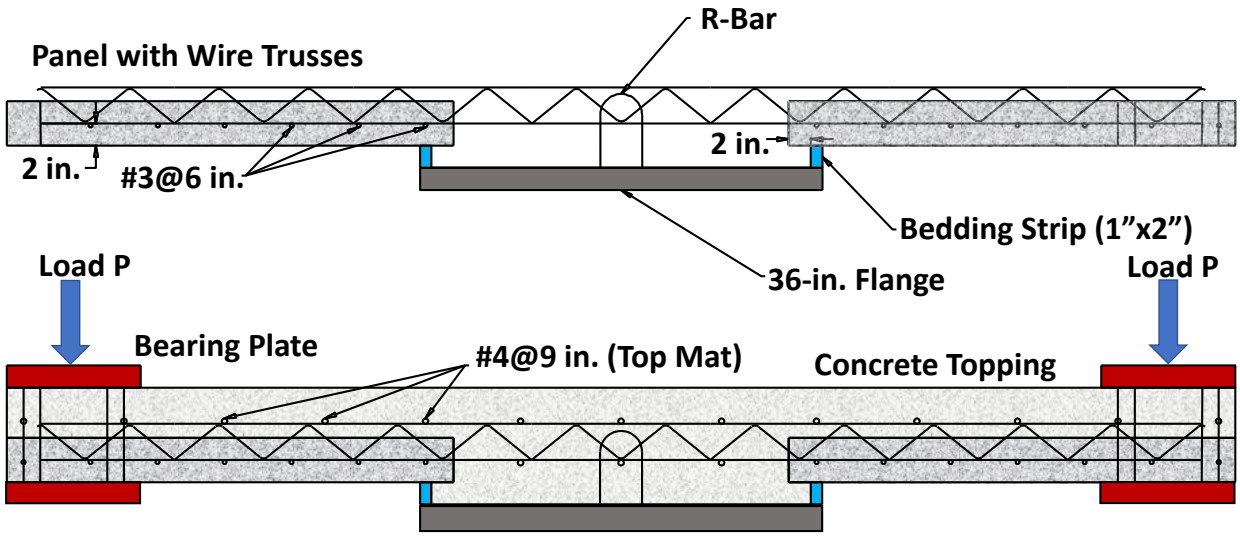

Figure 5-1 Schematic Test Specimen

Two types of wire trusses, hand-welded and electro-welded, were embedded in the deck strip and tested. In addition, two different stress ranges were applied. The first stress range was per AASHTO LRFD, targeting at infinite life [Eq. (2-3)], while the second stress range was planned to be near yield stress, verifying S-N curved prediction for typical rebar [Eq. (2-1)]. Consequently, four individual fatigue tests were included. In addition, for specimens under low stress range, after five million cycles, which is considered infinite life, the specimen was moved to another test frame and tested under monotonic loading for the purpose of determining the residual static capacity.

5.1.2. Specimen Design

As shown in Figure 5-2, the fatigue specimens, simulating decks under cyclic negative moment, were designed to be placed on the footprint of a Tx-28 girder, which has a standard width of 36 in. Instead of using a full-size Tx-28 girder for each specimen, the girder was substituted for a steel plate that would have the same footprint as the girder. Using a steel plate dramatically decreased the overall height and allowed the specimens to be transferred about the lab with a forklift which made placement and installation of the specimens significantly easier. This steel plate could also be more securely bolted down than a concrete girder could be anchored. This substituted steel plate had bent rebar welded to it to replicate the R-bars that would connect the deck to the bridge girders. This was completed using a stud welder. The rebar was welded at 9 in. on center to avoid complication with the trusses. This spacing was not in compliance with TxDOT Bridge Standard for prestressed concrete I-girder details for R-bar spacing in the first 23 ft of girders but served to keep the steel plate attached to the specimen during transportation. The top chords had the nominal diameter of No. 4 rebar, and so were spaced at a max 9 in. on center as set by TxDOT Bridge Standards for slabs cast on I-girders. With this spacing, four trusses were selected to fit into a 36-inch-wide specimen. The top chords were crossed with additional No. 4 bars spaced at 9 in. on center to complete the top reinforcement mat. Each of these bars were tied to the top chords of the first and last truss. Similar reinforcement was not tied to the bottom chords of the trusses above the substitute steel plate. Each precast panel sat on 2-in. by 2-in. foam bedding strips as instructed by TxDOT Bridge Standards for PCP. The total length of all specimens was 110 in. A breakdown of the length into curb, precast, and open elements can be found in the next section on the design of the precast panel. After the precast panel was placed on the steel plate and formwork attached, a 4.5-in. CIP layer is placed on top of the precast panel and over the girder line. This provides a 3-in. cover from the top chords of the truss. Prior to testing, steel loading plates are placed at either end of the specimen. These plates each measured 12 in. by 36 in. An overview of the fabrication and casting of the specimens can be found in Section 5.1.5. The layout of the components that make up the specimen can be found below in Figure 5-2.

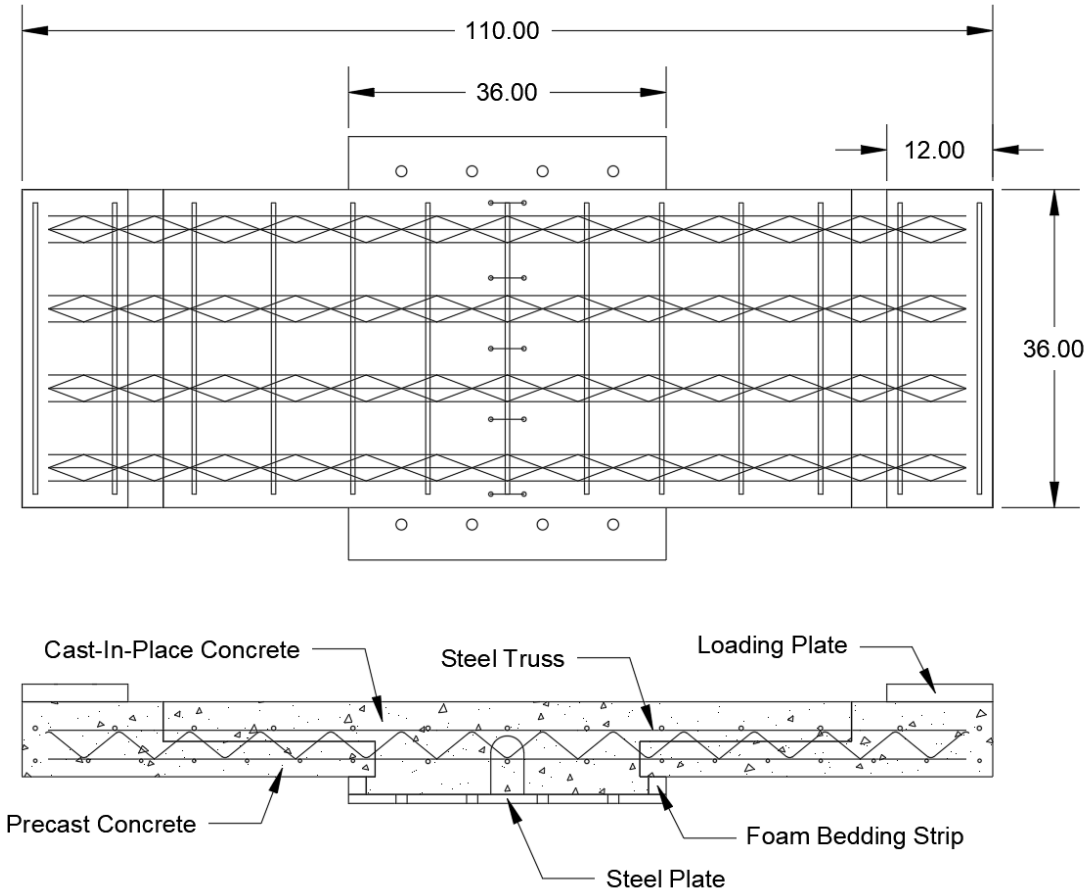

Figure 5-2: Specimen Drawing

5.1.3. Precast Panel Design

The design of the precast panels was designed to align as closely with TxDOT Bridge Standards as possible. This would allow for simple implementation of the full-scale panels as many of the same forms and fabrication practices for standard PCP could be used for these panels as well. Additional dimensions of the overhang panels are fixed for the reasons described in the specimen design found above. The depth of the slab was set at 4 in. in line with TxDOT Bridge Standard PCP Fab drawings. The panels have the same width of the specimens of 36 in. The panels have the same length of the specimens of 110 in. Each of the overhang slabs had a length of 40 in. This left 30 in. of exposed truss between the slabs. Four trusses were placed at 9 in. on center to parallel typical TxDOT Bridge Standards slab details. The bottom chords of the trusses had a 2-inch depth to the bottom soffit. No. 3 rebar was placed at 6 in. on center underneath the bottom chords as typical of standard PCP. A full-depth, 16-inch curb was cast at each end of the panel. This removed the need for formwork at those ends and would allow minimal formwork to be required in full-size panels in the field. Many of these dimensions can be seen below in Figure 5-3. The concrete was required to have a minimum 28-day compressive strength of 5,000 psi. However, the precast plant was asked to use their typical mix if it exceeded this value.

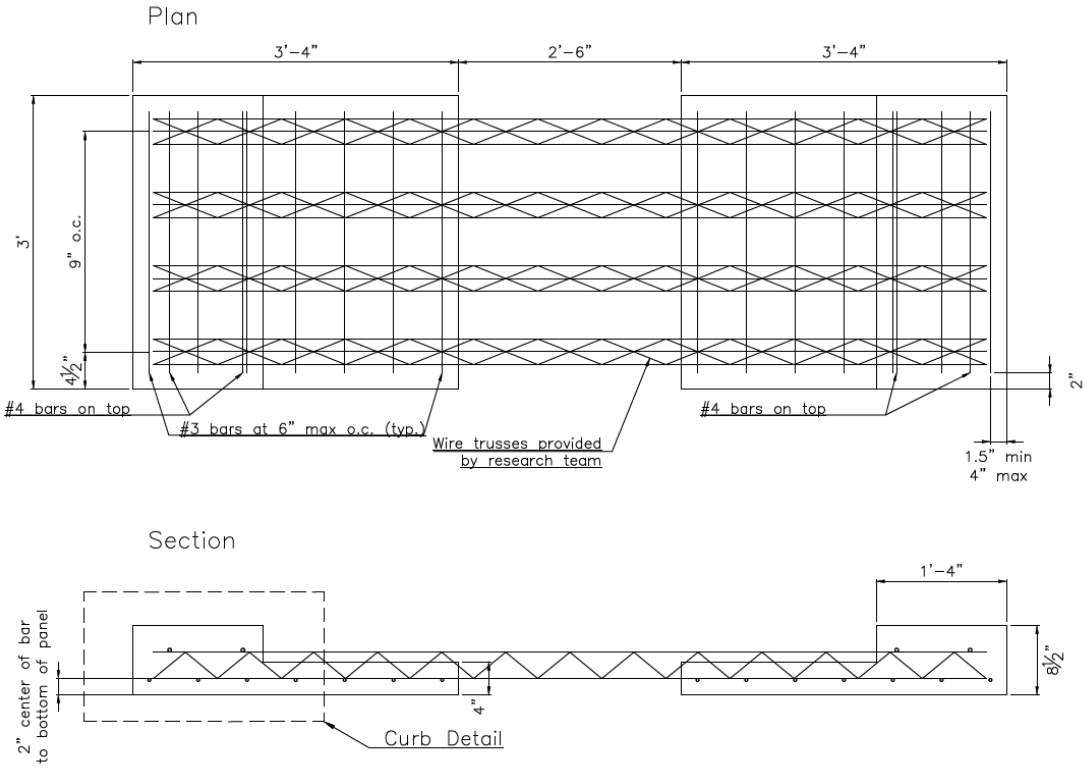

Figure 5-3: Precast Panel Drawing

5.1.4. Panel Fabrication in Precast Plant

The precast sections with wire trusses installed were set to be fabricated at local precast plant. The research team provided the plant with design drawings from which wooden formwork could be assembled from laminated plywood. The dimensions of the fatigue specimens were very similar to those of the construction testing's specimens and therefore existing formwork existed and could be reused. This formwork consisted of laminated plywood that was screwed together. The fatigue specimens required additional curbs to be cast at each end of the panels, which did not exist for the construction testing specimens. Design drawings of the fatigue specimen panels and the construction testing specimen panels can be found in the Appendix. The specimen shape did not facilitate the use of the steel prestressing beds of which the full-size panels typically use.

Figure 5-4: Construction of Formwork for Testing Specimen

A total of four specimens were cast, two including electro-welded trusses and two including hand-welded trusses. The specimens were cast in two sets. The first set was cast in early December 2022, while the second was cast in late December 2022.

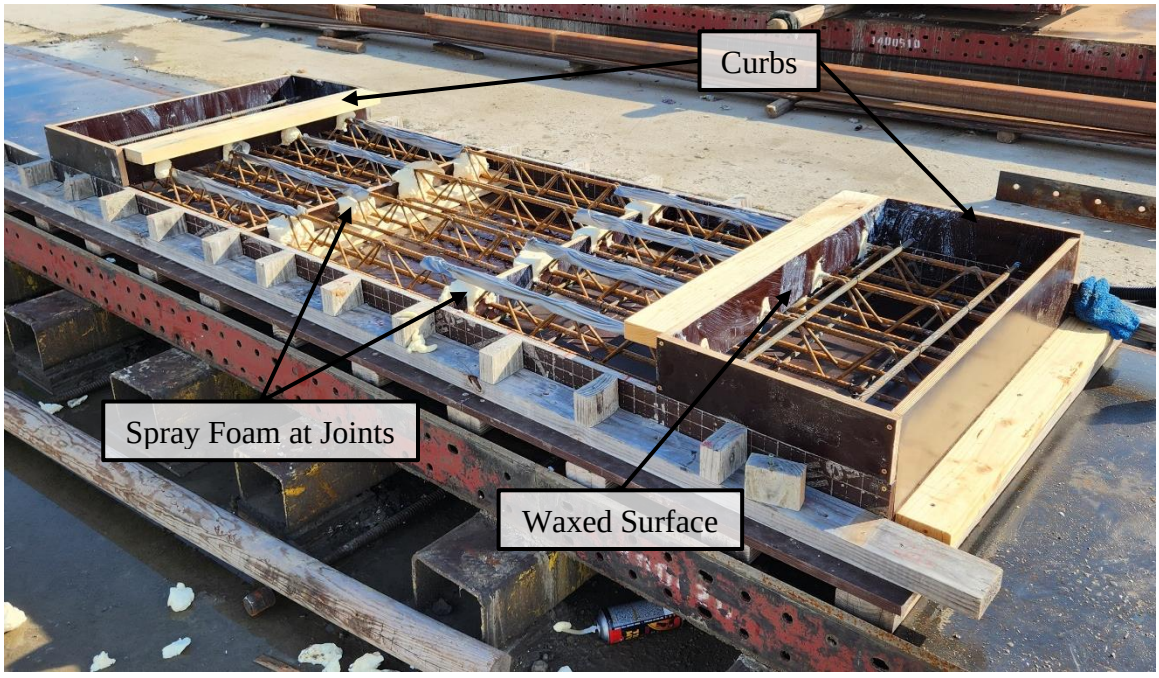

Figure 5-5: Precast Panel Formwork

As shown in Figure 5-6, spray foam was used to seal the vertical faces of the panels where the trusses protruded. Tape was placed on the top chords of all trusses to prevent concrete from setting on them after casting and reducing the bond strength between the CIP concrete and the steel trusses. All laminated surfaces on the inside of forms were waxed beforehand to make the panel removal easier. The panels were vibrated with needle vibrators to ensure compaction and finished with hand floats. The research team was present at all casts to oversee completion and provide quality control as needed. After casting, the panels were covered with impermeable tarp to cure. The panels were transported to the laboratory alongside the full-size panels roughly one month after casting.

Figure 5-6: Precast Panel Cast

5.1.5. Specimen Fabrication in Lab

The specimens' fabrication consisted of four components: wooden formwork, precast panels, steel substitute plate, and CIP concrete. The purpose and fabrication of these components will be explained in the following paragraphs.

The wooden formwork was made of plywood and 2x4s for support, as shown in Figure 5-7. The forms were placed on both open edges of the precast panels. This formwork provided siding to enclose the CIP layer during casting. The formwork was designed to be as deep as the deck depth plus the two-inch-deep bedding strips under the panels. Alongside the precast curbs, this formwork enclosed all sides of the specimens.

Figure 5-7: Wooden Formwork

Instead of using a TxDOT standard Tx-28 concrete girder to place the precast panels on, a steel plate with the same overhead dimensions was used. This drastically decreased the total thickness of the specimen, making it easier to install and secure into the test setup. This plate was cut from a one-inch steel sheet to be 36 in. by 48 in. The 36-in. dimension kept the same width as a standard Tx-28 so the overhang distance and restraint conditions would match that of a concrete girder. The 48-in. dimension extends the plate beyond the surfaces of the concrete, which allows bolt holes to be used to attach the specimen to the test setup. All bolt holes were made with a magnetic drill (steel slugger).

Additionally, curved rebar was welded to the centerline of the plate to act as a proxy for the R-bars that would be extending out of a concrete I-girder, as shown in Figure 5-8. The size of rebar was matched to that of the R-bars present in the girders used for the full-sized tests. However, the spacing of the rebar was selected to ease fabrication and did not perfectly follow TxDOT standard. The rebar was attached with use of stud welding equipment at the lab. Standard No. 4 rebar settings for amperage, time, lift, and plunge settings were used.

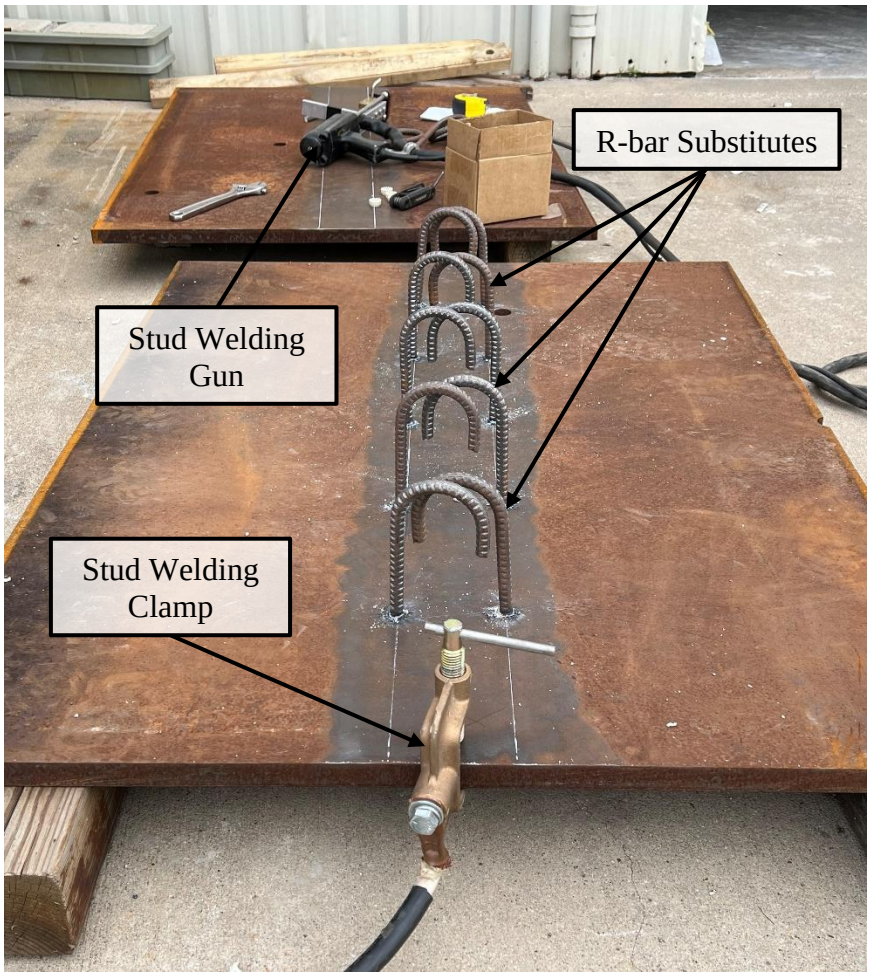

Figure 5-8: Welded R-bars on Substitute Steel Plate

The specimens were assembled once the formwork, precast panels, and steel plates were fabricated. As shown in Figure 5-9, the plates were placed in a wooden jig with the foam bedding strips in place. The precast panels were then positioned on top. Meanwhile, window weather stripping was attached to the edges of the formwork that would be in contact with the formwork. This provided a consistent waterproof seal to keep concrete from escaping when the formwork did not smoothly contour the precast panel. The formwork received several coats of form oil in areas that would be in contact with the CIP concrete to make its removal easier after casting. Ratchet straps then attached the formwork to the precast panels at the curb ends. Rebar was tied transversely to the top chords of the exposed trusses. Finally, the vibrating wire gauges were placed on the top chord at the base of each overhang, ready to be cast as shown in Figure 5-10.

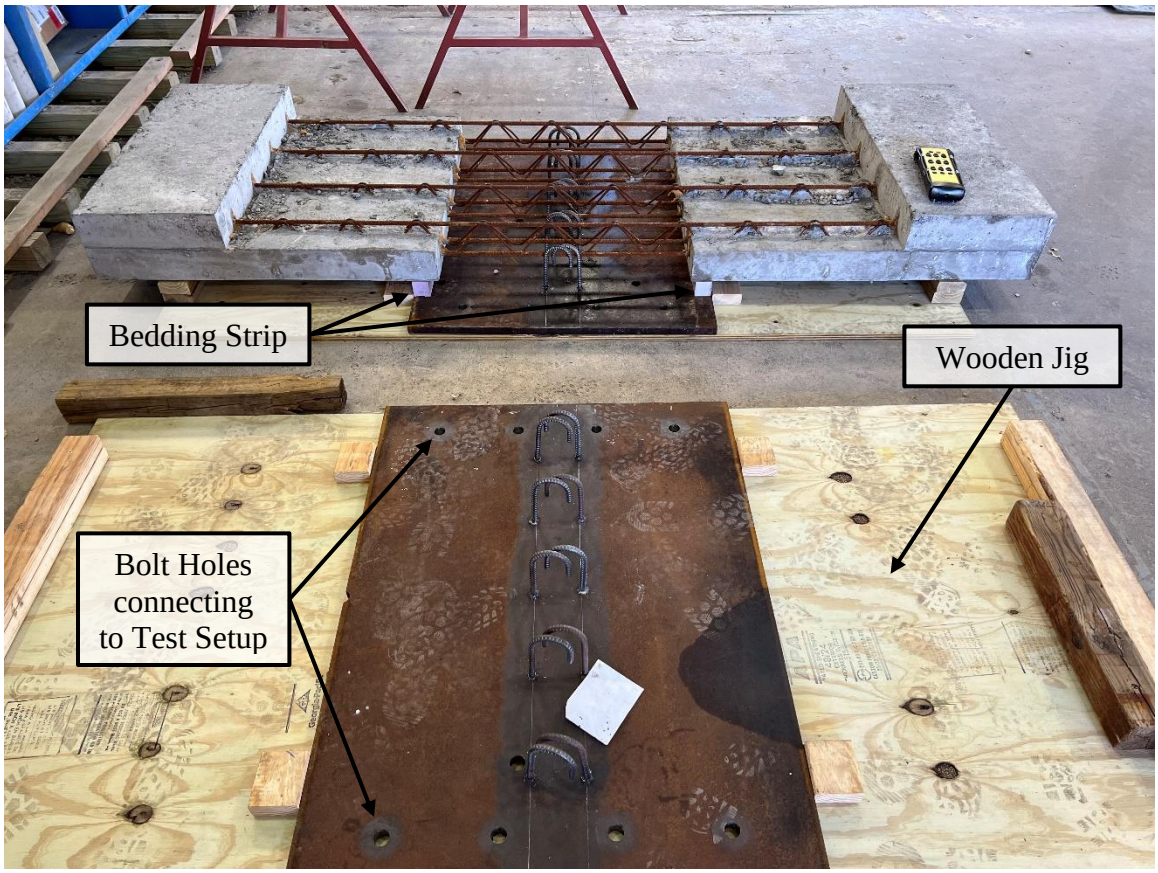

Figure 5-9: Casting Setup Steps

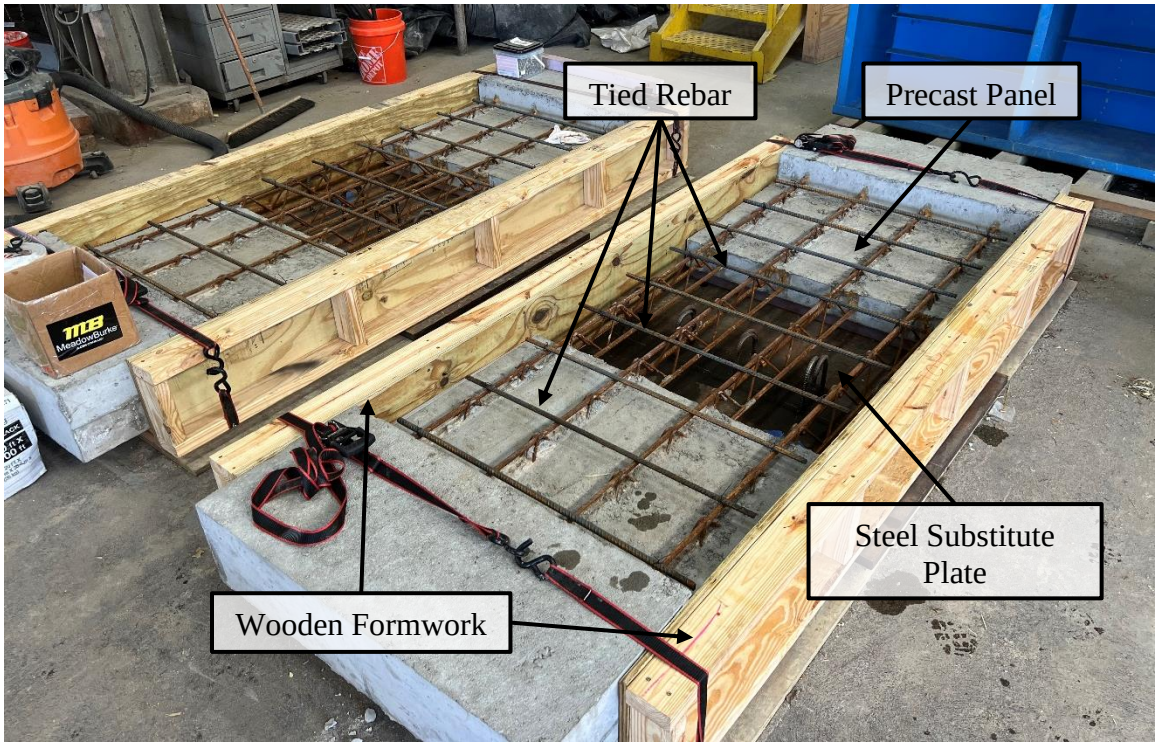

Figure 5-10: Assembled Casting Setup

As shown in Figure 5-11, after the CIP concrete had been placed and finished, but before it set, four steel pickup points were inserted into the concrete so that the specimens could be moved to the test setup elsewhere in the laboratory. After curing, steel loading plates were placed at the ends of the specimen onto a layer of gypsum cement above the curbs. This cement ensured an equal loading across the bottom of the plates.

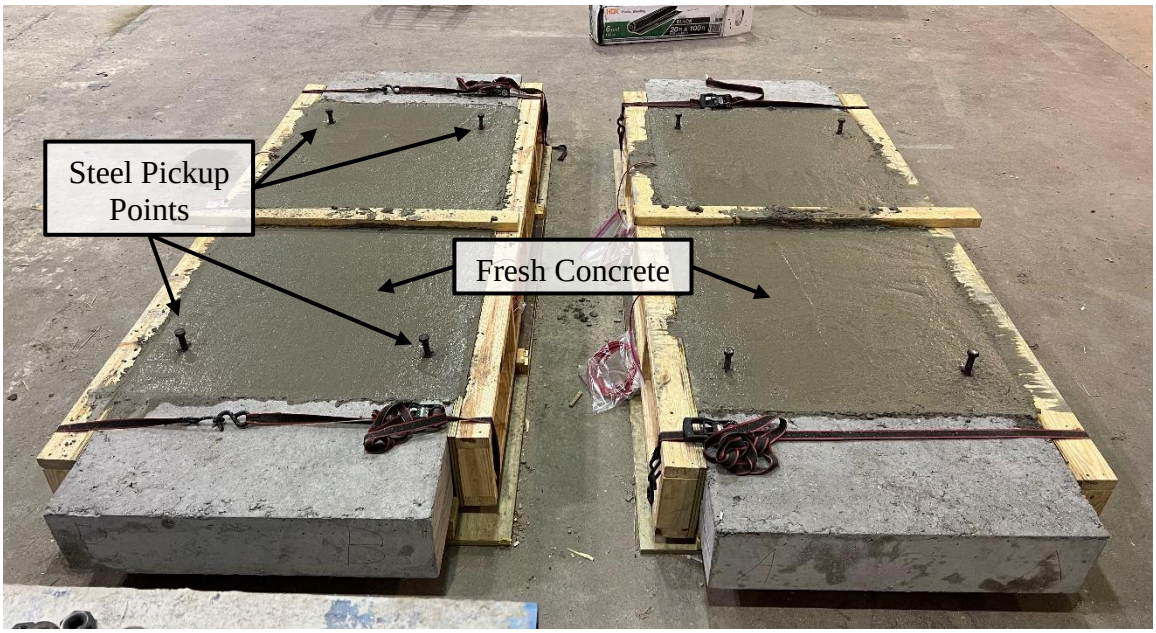

Figure 5-11: Finished Specimens after Casting

Four total specimens were fabricated. Like the precast panels, the CIP concrete was added to the specimens in two sets of casts. The first cast was finished in early April 2023. This cast consisted of the panels with electro-welded trusses. The second cast was finished in early June 2023. This cast consisted of the panels with hand-welded trusses.

5.1.6. Test Setup Design

The test setup was designed to support a hydraulic actuator that would provide the load cycles to the specimens. The test setup was designed for the use of a hydraulic actuator which provided the load cycles into the specimens. This actuator was centered above the specimen as shown in Figure 5-12 where its load would be directed to either end of the specimen with use of a steel spreader beam. A set of portal frames and crossbeam were fabricated for the actuator to react against. Beneath the specimens a steel “table” was built out of steel HSS and I-beams. This “table” allowed for quick retrieval and insertion of specimens. All elements of the test setup were oversized for the expected loads as any deflections in the supporting elements would be caught by the specimen and ac displacement sensors. Specific details of the loading system and layout of the test setup will be explored in the following paragraphs.

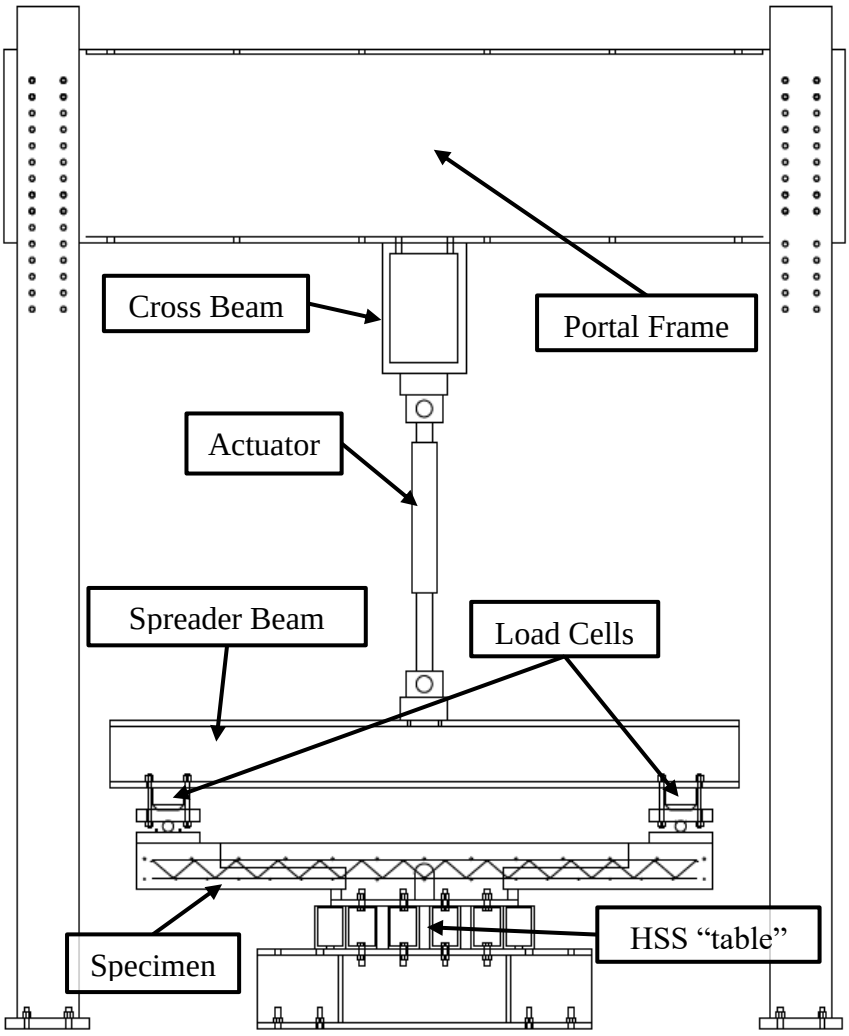

Figure 5-12: Test Setup Diagram

The loading and control systems consisted of several different MTS units to provide and regulate pressure, control flow direction, and monitor behavior. An MTS Model 244.22 hydraulic actuator (Figure 5-13) was used to load the specimens. It had a capacity of 22 kips and a stroke of 10 in. This actuator was selected because it met the loading requirements, but did not have significant excess capacity.

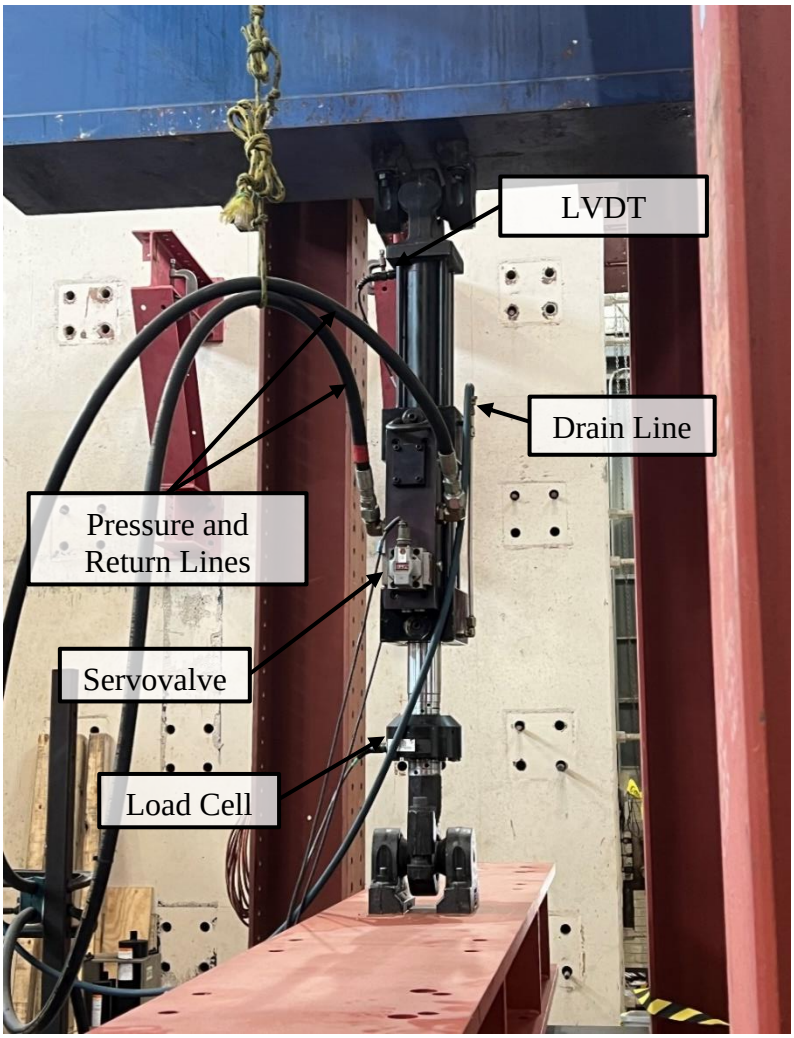

Figure 5-13: Hydraulic Actuator Overview

The hydraulic actuator was connected to an MTS Series 293 Hydraulic Service Manifold or HSM (Figure 5-14). This unit allows for multiple hydraulic systems to connect to the same pump, allowing for different projects to run in parallel without interaction between them. Additionally, the unit smooths jumps in hydraulic pressure during changes. This may happen if the pump shuts off, or there is a sudden pressure loss during a failure.

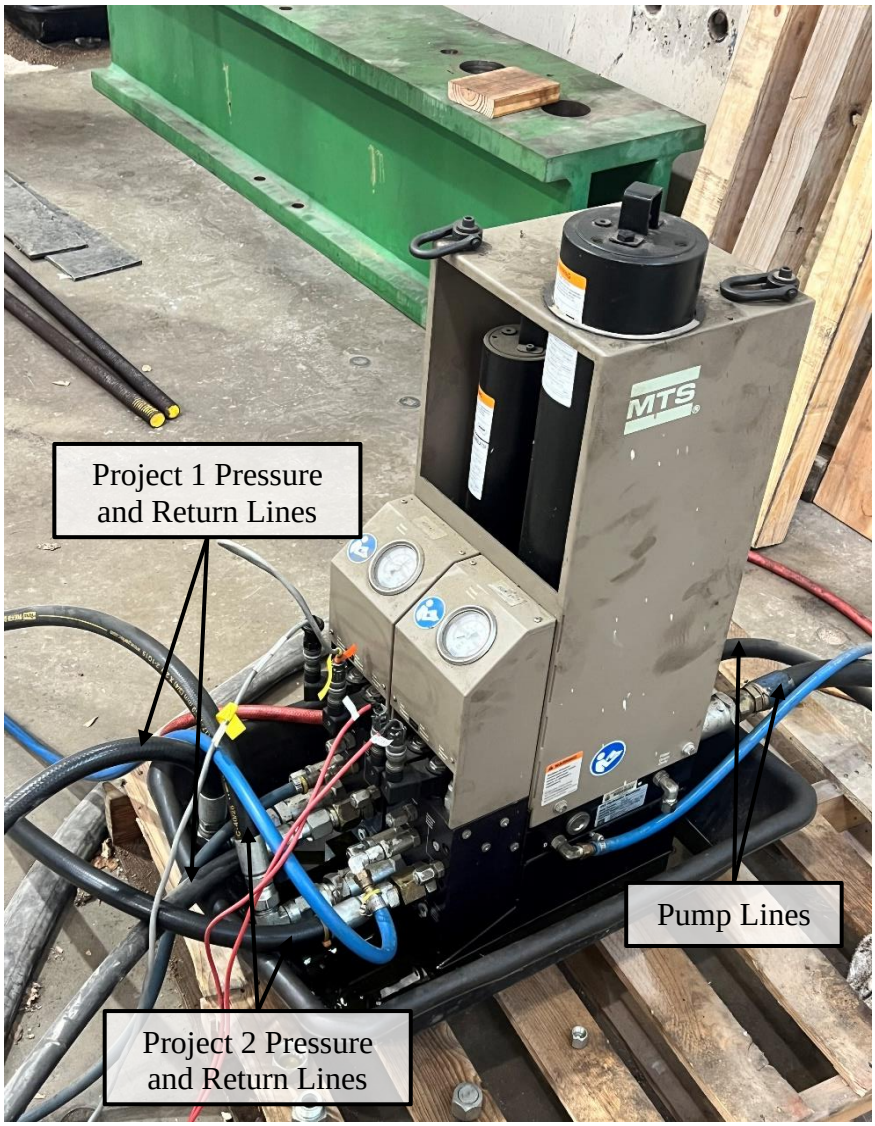

Figure 5-14: Hydraulic Service Manifold Overview

The HSM was pressurized using an MTS Silent Flo™ Model 515.30 Hydraulic Power Unit or HPU (Figure 5-15). This pump supplied the pressure to continuously run the test setup for all tests. The pump was water cooled to keep its internal temperature within the operational limits. Should the temperature have exceeded these limits, the pump would automatically shut off to protect itself and the rest of the test setup.

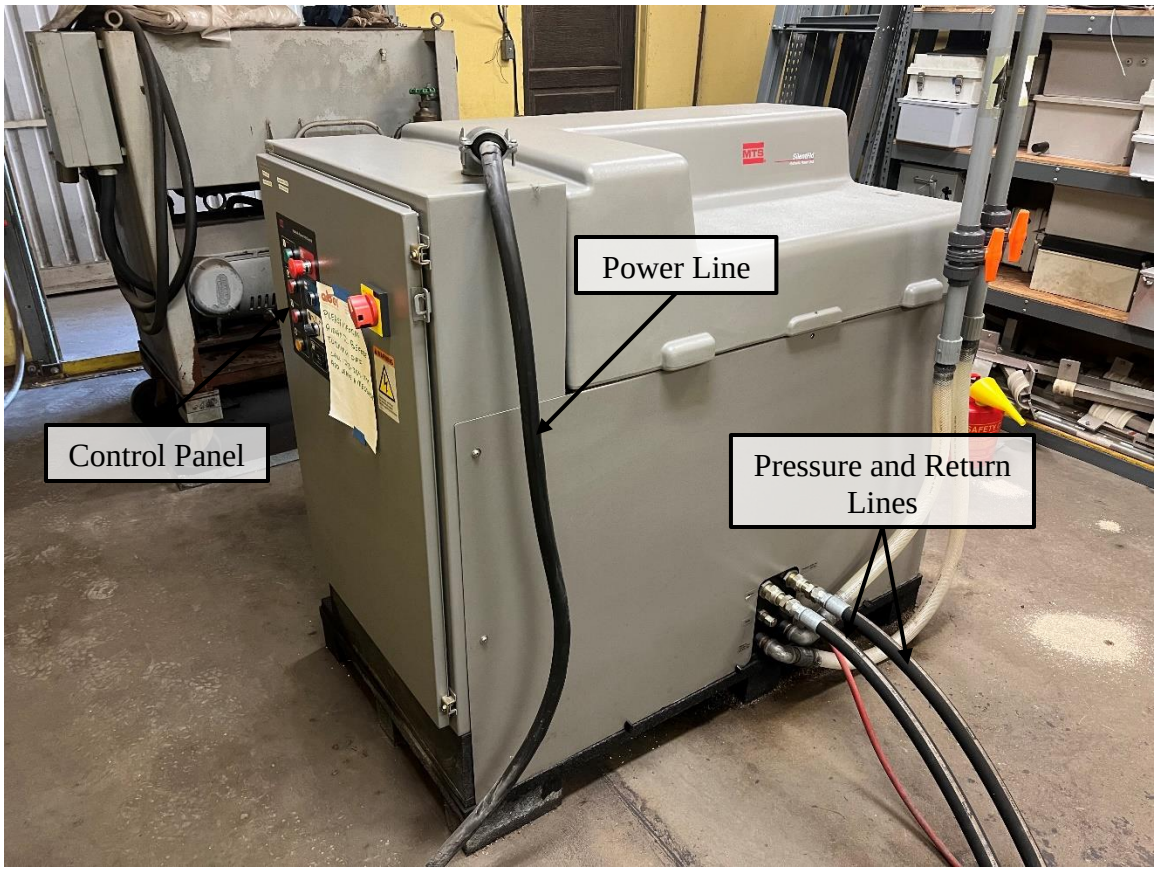

Figure 5-15: Hydraulic Power Unit

Finally, all MTS units were controlled from an MTS FlexTest 60 controller (Figure 5-16). This controller sends commands to the HSM and actuator to set the loading frequency and magnitude. MTS MultiPurpose TestWare was the software used to monitor the cycle count, run the loading procedure, and halt at the desired cycle count.

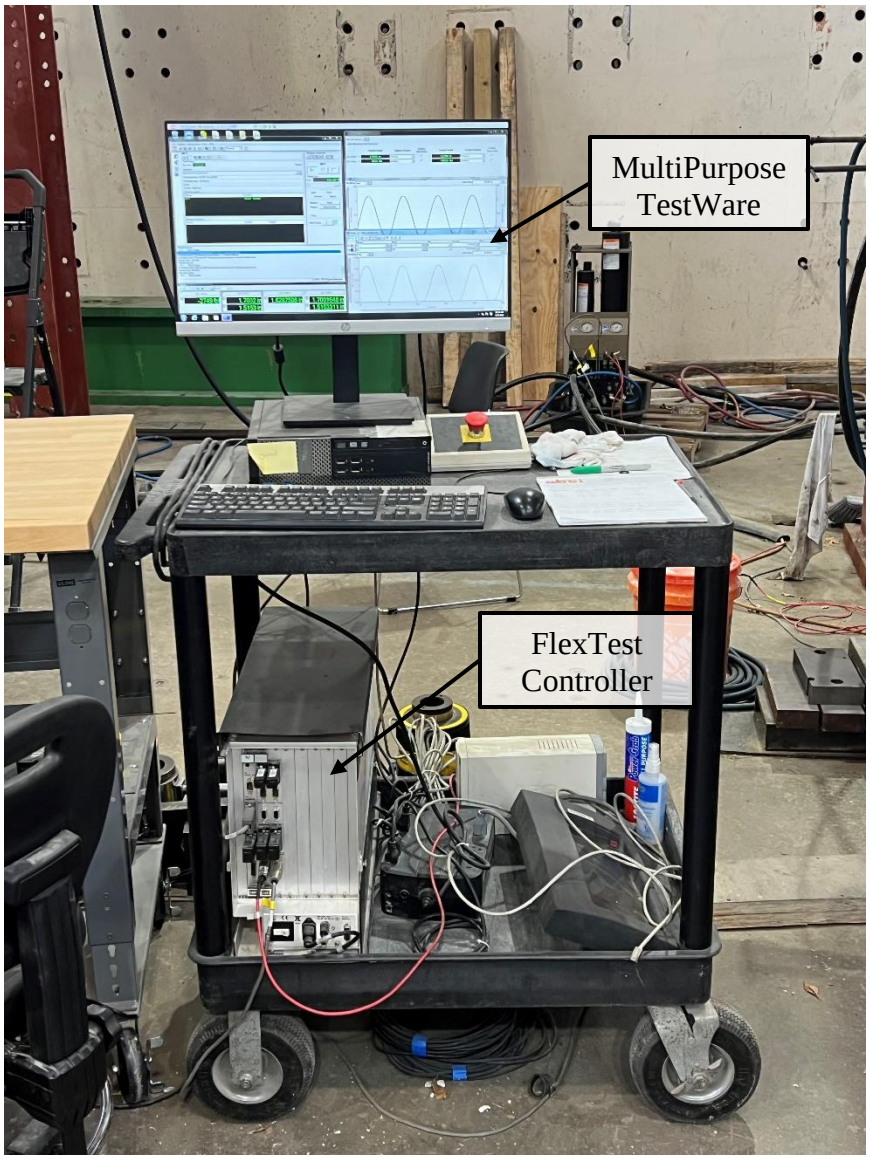

Figure 5-16: FlexTest Controller and Software Overview

5.1.7. Instrumentation

As this experimental program pertained to fatigue behavior, the most important metric was the number of cycles the specimens could achieve before failure. This was recorded using MTS MultiPurpose TestWare which recorded cycle count, load from the actuator's internal load cell, and distance the actuator travels from the actuator's internal LVDT. Additional external load cells were also used to corroborate the MTS load readings and verify that each overhang was receiving equal load. These external load cells were situated between the spreader beam and pin/roller plates. Surface concrete strain gauges were placed on the top and bottom surfaces at the base of the overhangs. These were set to create a strain profile through the section to indirectly measure strains in the trusses. Vibrating wire gauges were used for a similar purpose. These were cast into the specimen next to the top chords. These would measure the strain in the concrete at a location just

adjacent to the trusses. See Figure 5-17 for a layout of the vibrating wire and surface strain gauge layout. Unfortunately, due to where cracks would occur in the specimen, the strain readings of these sensors did not give accurate results.

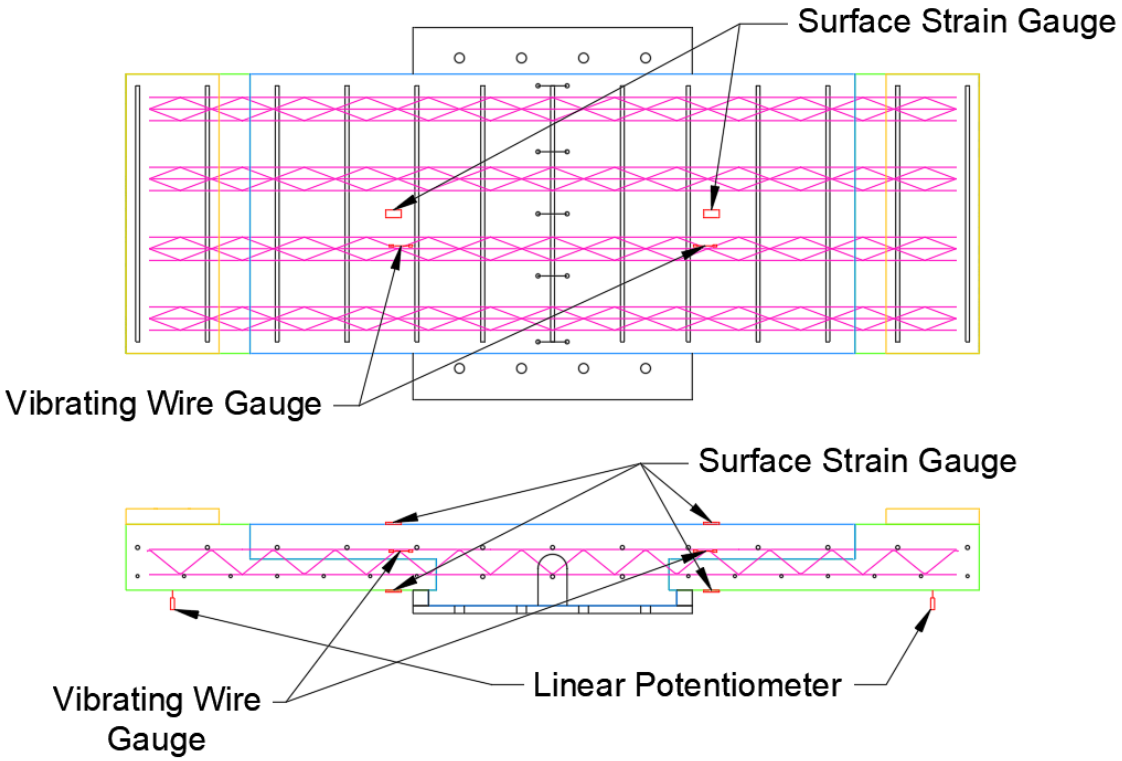

Figure 5-17: Surface Strain & Vibrating Wire Gauge Sensor Layout (Delamination Sensors Not Shown)

Linear potentiometers (L-pots) were placed at the ends of the overhangs, directly underneath each loading point. Additional l-pots were used to measure any delamination that would occur between the precast and CIP layers of concrete. These were placed horizontally at the locations of highest moment and shear. See Figure 5-18 for their layout.

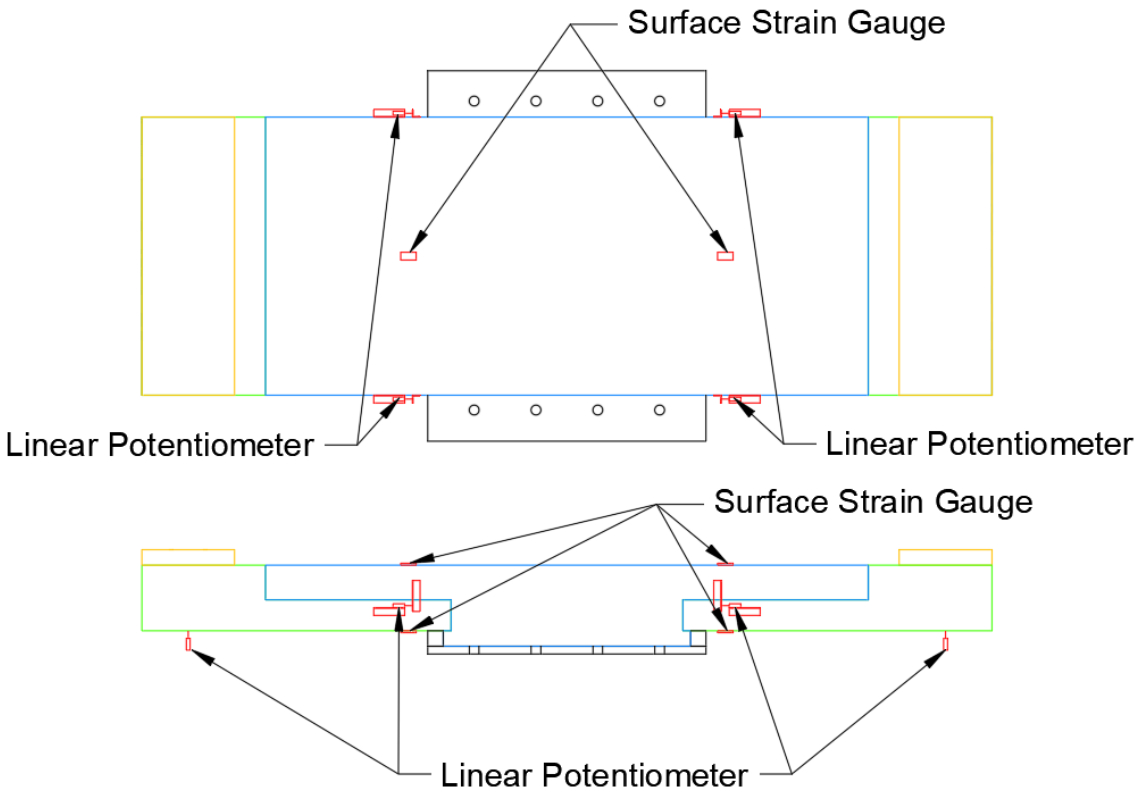

Figure 5-18: Surface Strain Gauge and L-Pot Sensor Layout

5.1.8. Testing Procedure

Four specimens were fabricated for the fatigue testing and the full test matrix is shown in Table 5-1. Two included hand-welded trusses and two included electro-welded trusses. One of each type of truss were subjected to cyclic loading that induced either a high stress into the reinforcement or a low stress into the reinforcement. The high stress testing was meant to induce a stress range between zero and yielding (60 ksi for hand-welded trusses and 75 ksi for electro-welded trusses). This would demonstrate the minimum number of cycles to failure and the behavior of trusses if they were to approach failure. The loading frequency was set at 0.25 Hz. This allowed instrumentation to gather enough data to plot the load and deflection history throughout the test. An example of this data is shown in Figure 5-19. Using Eq. (2-1) from Chapter 2, the hand-welded trusses should have failed between 20,000 and 100,000 cycles and the electro-welded trusses should have failed between 5,500 and 30,000 cycles.

The low stress testing was meant to induce a stress between 0 ksi and 18 ksi. Stress of 18 ksi was selected as it aligns with the maximum stress that allowed in reinforcement before finite life as predicted by Eq. (2-3) (AASHTO Equation 5.5.3.2-2). This would demonstrate whether the panels would achieve infinite life under the worst-case conditions. When a cycle count of 5,000,000 is reached, the panels were considered to have infinite life and testing would conclude. The loading frequency was set at 1.5 Hz. This higher loading frequency was used to reduce the test time.

Table 5-1: Loading Test Matrix

Test No.	Specimen No.	Truss Type	Limit State	Loading	Range
Test 1	Specimen 1	Electro-welded	Fatigue	High Stress	0 – 75 ksi
Test 2	Specimen 2	Electro-welded	Fatigue	Low Stress	0 – 60 ksi
Test 3	Specimen 3	Hand-welded	Fatigue	Low Stress	0 – 18 ksi
Test 4	Specimen 4	Hand-welded	Fatigue	High Stress	0 – 18 ksi
Test 5	Specimen 3	Hand-welded	Strength	Static	-
Test 6	Specimen 2	Electro-welded	Strength	Static	-

Before each fatigue test was conducted, each specimen was loaded enough to crease an initial crack in the concrete surface. This crack was meant to engage the reinforcement in the load-carrying mechanism. Without this initial loading, the low stress specimens would not crack, and the reinforcement would not take any significant stress during the tests. The size and depth of this initial crack could not be easily controlled between tests. Therefore, the magnitude of deflections between tests and north/south overhangs were not consistent.

After the specimens achieved infinite life with the low stress testing, they were tested to failure under monotonically increasing load to determine whether loss of capacity occurred due to cycling at low stress. Their maximum strengths would then be compared to calculated theoretical maximum strengths before cycling. These calculations can be found in the Appendix. This testing was done in a separate loading frame that had a similar design to the fatigue loading setup. This loading frame can be seen in Figure 5-20. A hydraulic ram was used instead of the actuator to achieve the higher loads that were necessary to fail the specimens.

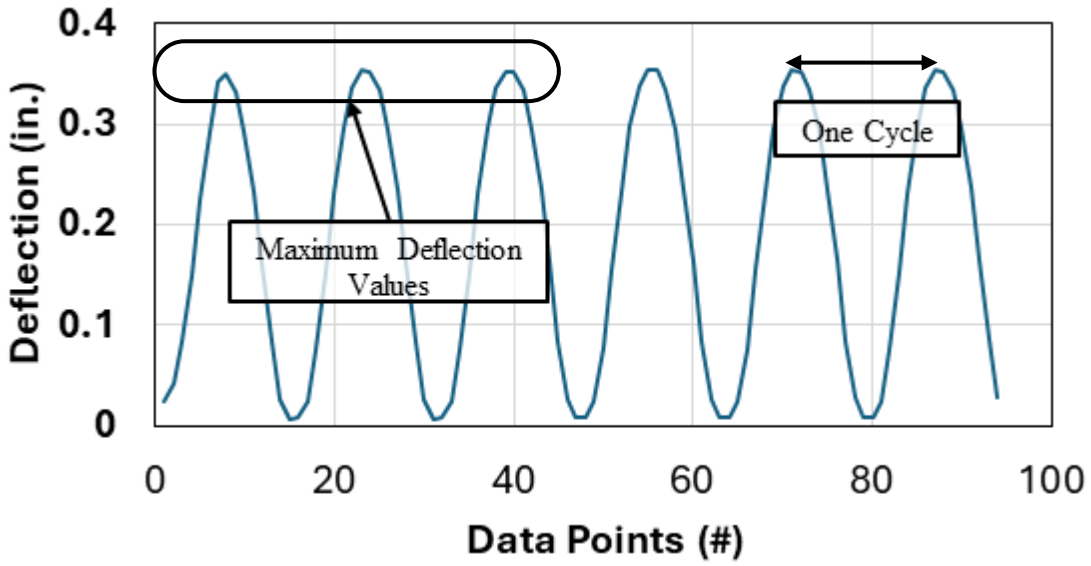

Figure 5-19: Test 1 - Stress Example Deflection Data

Figure 5-20: Test Setup for Monotonic Loading

5.2. Experimental Results and Discussion

5.2.1. Test 1 – High Stress, Electro-Welded Wire Truss

The first test completed was the high stress testing of the electro-welded wire truss specimens. This occurred during early November 2023. The applied load induced a yielding of the top chords of the trusses. The specimen was then cycled to this load until failure. The maximum load for each cycle is shown in Figure 5-21. Due to an instrumentation collection issue and a failure in the actuator's seals, the first 10,000 cycles of data were not captured. However, the research team is confident that this missing data would mirror the consistent data that followed it.

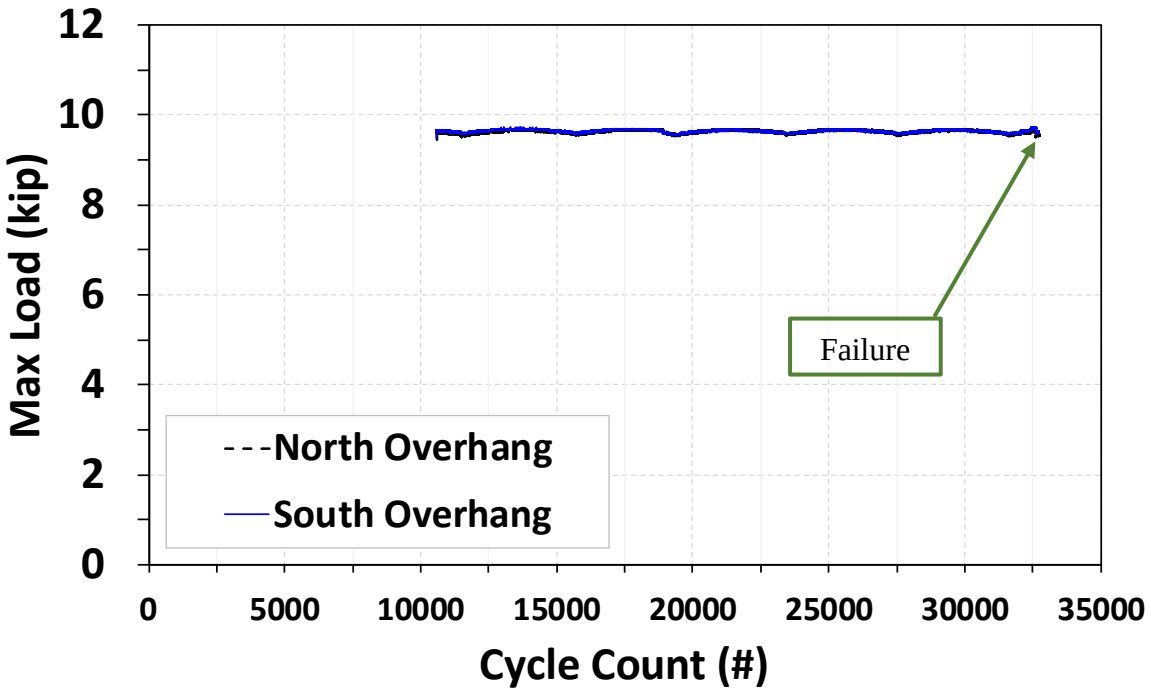

Figure 5-21: Test 1 – Maximum Load versus Cycle Count

Figure 5-22 shows that the north overhang failed at approximately 32,756 cycles and was characterized by a constant deflection followed by a sudden runaway increase. The delamination sensors and visual inspection showed that no delamination had occurred. Cycling was halted before the reinforcement ruptured as control over the actuator would become difficult when the stiffness of the specimen reached zero. For this reason, pictures of the top chords post-testing are not available. Along with the increasing cycles, the deflection on the North overhang had a tendency to increase on both ends but it was not obvious. The deflection began with 0.35 in. and became 0.377 in. right before the runaway failure.

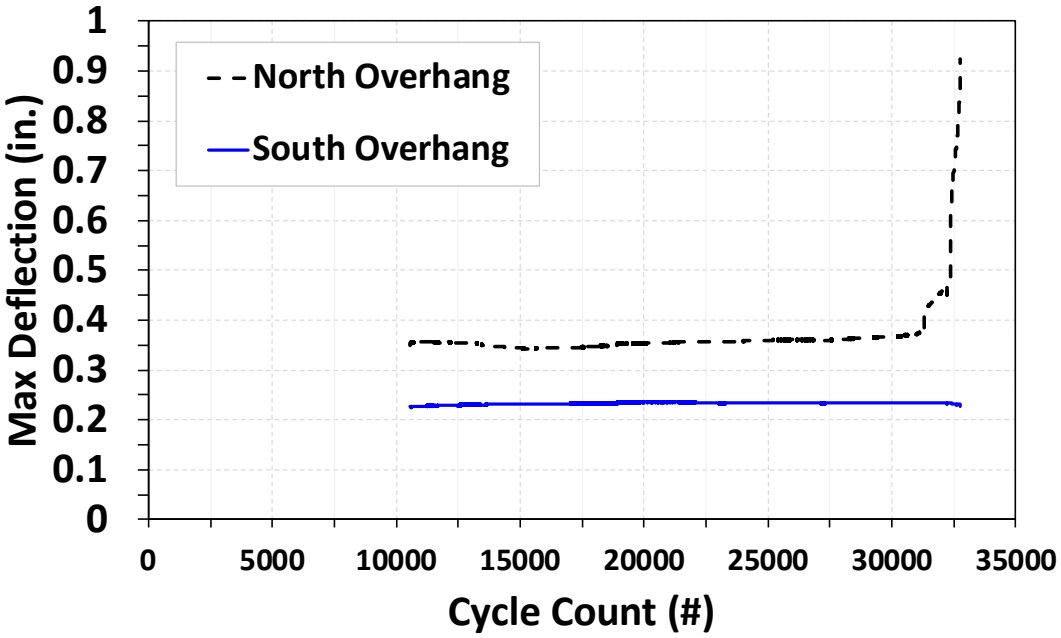

Figure 5-22: Test 1 – Maximum Deflection versus Cycle Count

5.2.2. Test 2 – Low Stress, Electro-Welded Wire Truss

The second test completed was the low stress testing of the electro-welded trusses. This test was finished in late January 2024. The applied load induced a stress of 18 ksi in the top chords of the trusses. The specimen was then run to 5,000,000 cycles, which was considered infinite life for this research program. Crack widths started at 0.014 in. and did not significantly increase throughout the test. As shown by the trendlines in Figure 5-24, the trusses appear to soften slightly over the course of the test. The initial deflection of the South overhang was 0.066 in. and that of the North overhang was 0.061 in, but in the end of the test the South overhang became 0.071 in. and the North overhang became 0.063 in. Due to the amount of data produced over the course of this test, it is not possible to show a continuous recording of it. Therefore, each data point shown in Figure 5-23 and Figure 5-24 are1,000 data point extracts of the overall data set. The specimen did not delaminate anywhere during the test.

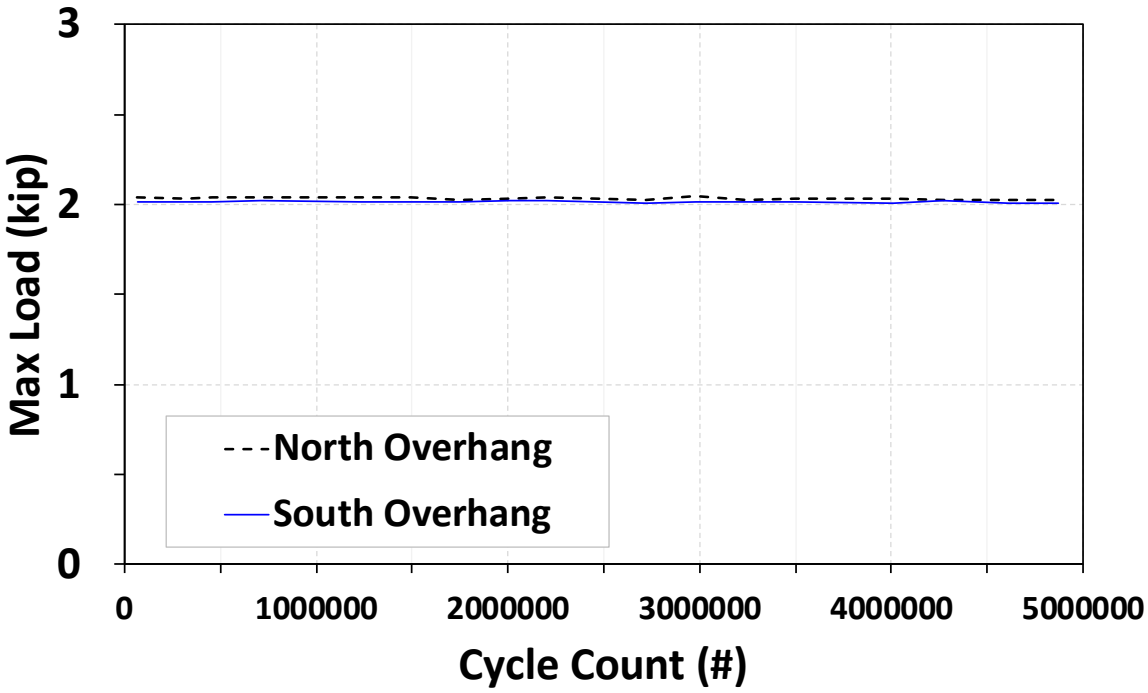

Figure 5-23: Test 2 – Maximum Load versus Cycle Count

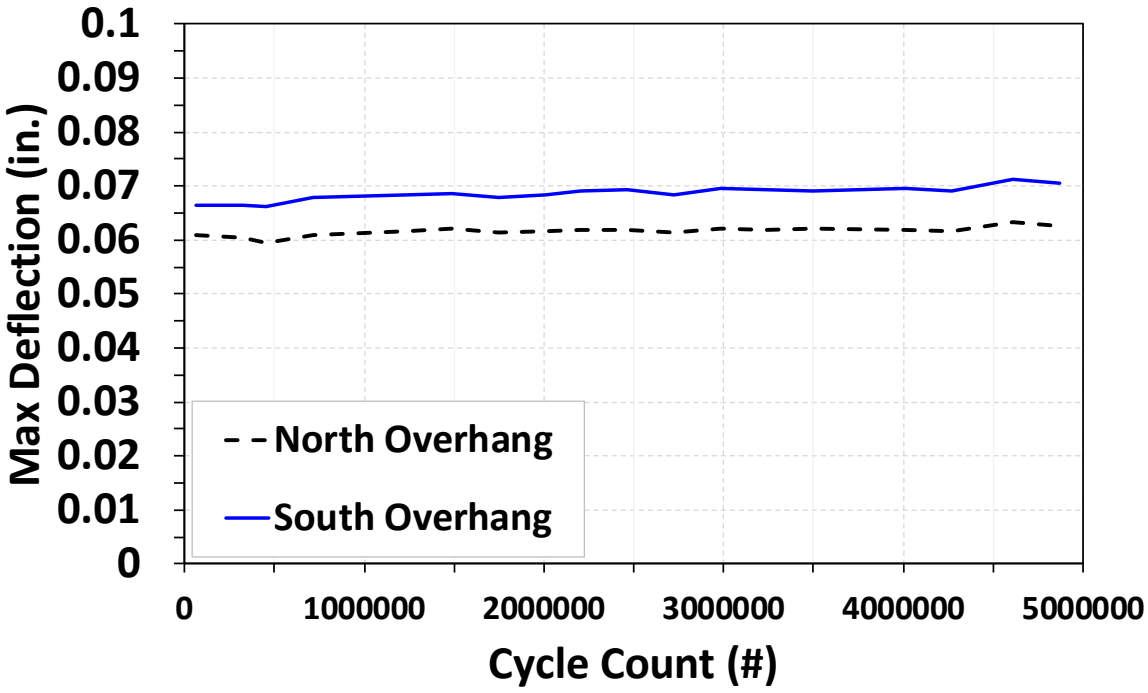

Figure 5-24: Test 2 – Maximum Deflection versus Cycle Count

5.2.3. Test 3 – Low Stress, Hand-Welded Wire Truss

The third test completed was the low stress testing of the hand-welded wire trusses. This test was run from early February 2024 through early March 2024. The applied load induced a stress of 18 ksi in the top chords of the trusses. The specimen was then run to 5,000,000 cycles, which was considered infinite life for this research program. Cracks started as hairline (0.005 in.) and did not significantly increase throughout the test. Due to the amount of data produced over the course of this test, it is not possible to show a continuous recording of it. Therefore, each data point shown in Figure 5-25 and Figure 5-26 are 1,000 data point extracts of the overall data set. It can be seen from Figure 5-25 that the applied load was maintained constant. The specimen did not delaminate anywhere during the test.

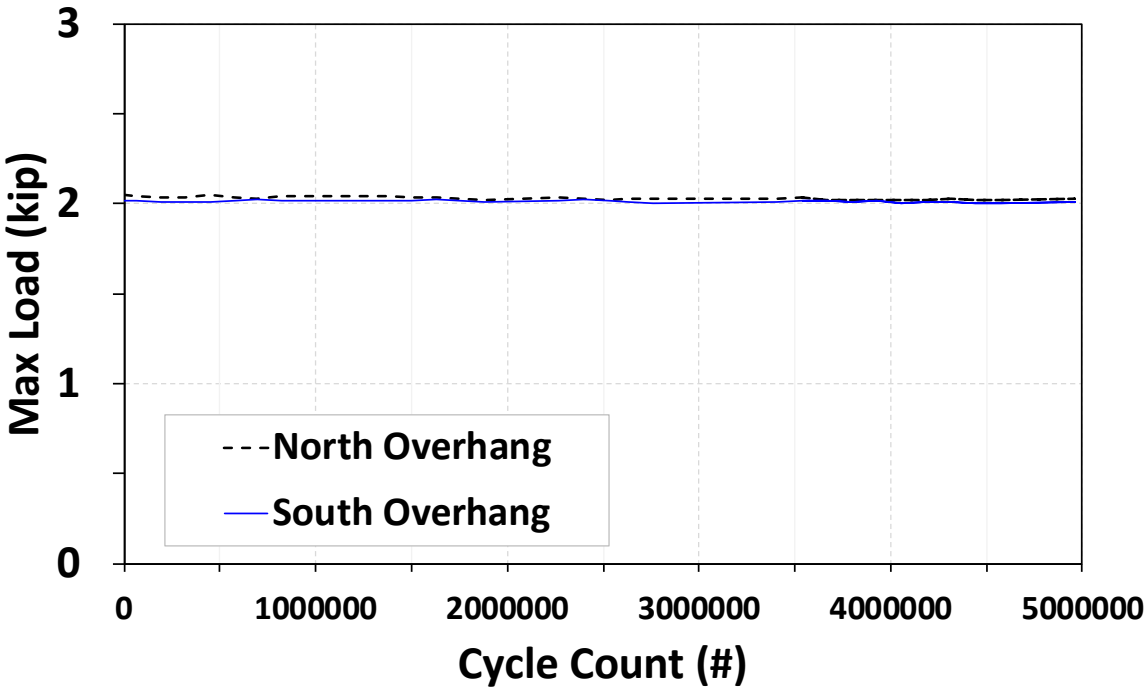

Figure 5-25: Test 3 – Maximum Load versus Cycle Count

Deflection data shown in Figure 5-26 indicate a somewhat unstable deflection through the course of testing. The general trend was that the deflection decreased along with the cycle counts increasing with a few jumps in between. It is unknown what might have caused this unexpected phenomenon. More data analysis would be needed; nevertheless, the specimen sustained 5 million cycles and could be considered having infinite life.

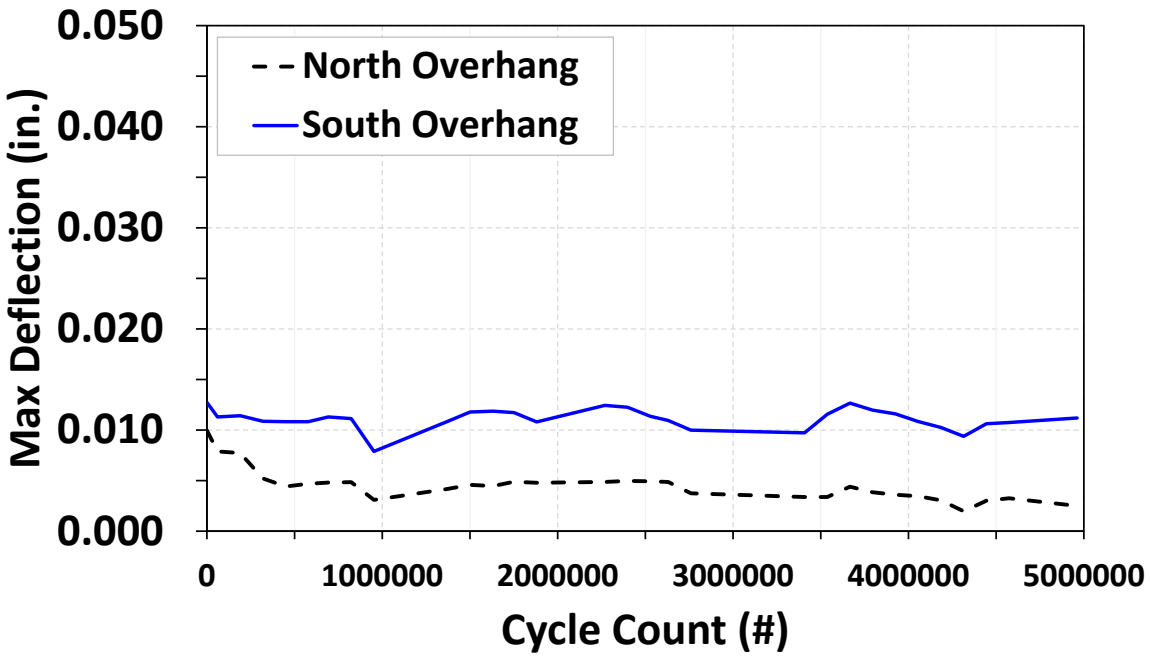

Figure 5-26: Test 3 – Maximum Deflection versus Cycle Count

During installation of the specimen, a crack formed over the substitute steel plate that extended horizontally between the overhangs. The research team believes this cracking occurred when the bolts connecting the specimen to the test setup were tensioned. During casting, fresh concrete leaked through holes in the substitute steel plate and formed a small ring around the perimeter of the hole on the bottom side of the plate. When the bolts were tensioned for the test, this concrete ring caused a prying action that put the concrete above the plate into tension, causing the cracking. However, due to the crack's location and orientation, it is expected to have had little to no influence on the test results.

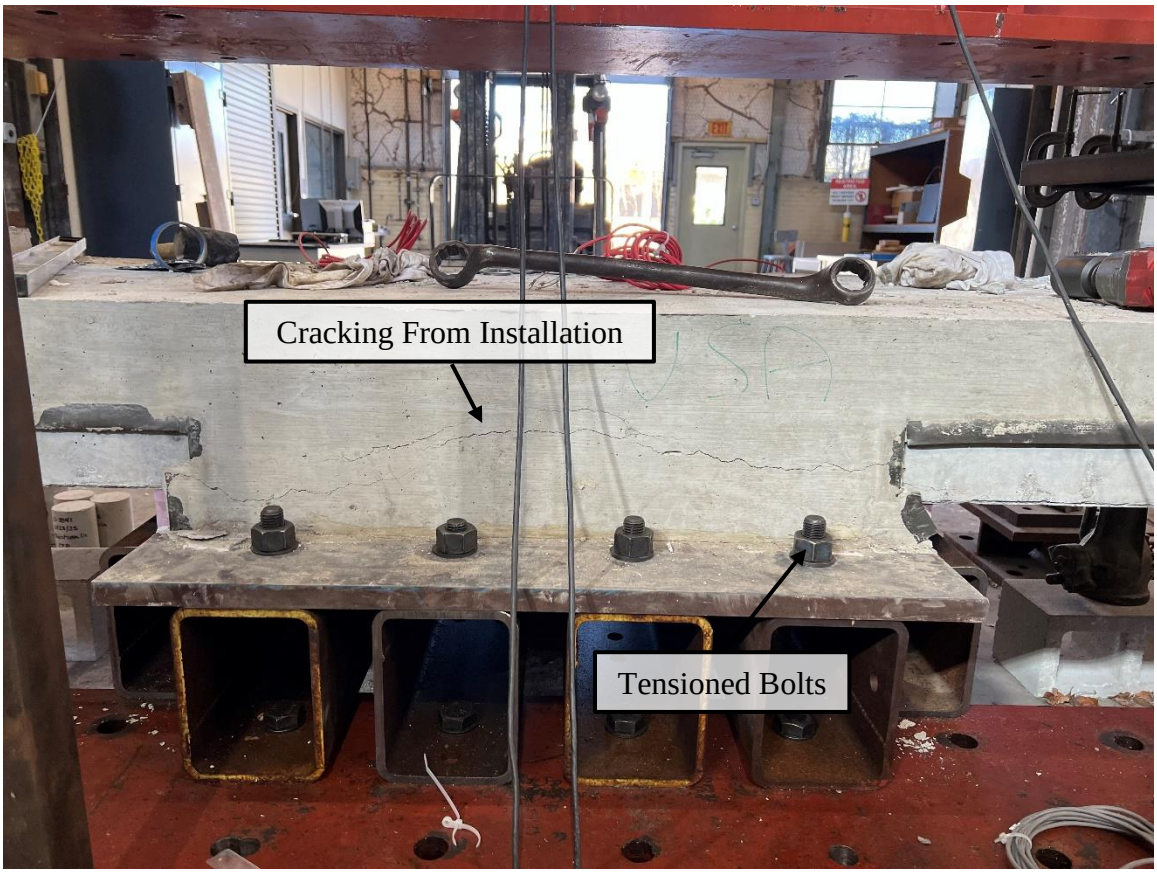

Figure 5-27: Test 3 – Installation-Induced Cracking

5.2.4. Test 4 – High Stress, Hand-Welded Wire Truss

The fourth test completed was the high stress testing of the hand-welded truss specimens. This test was finished in mid-March 2024. The applied load induced yielding in the top chords of the trusses. The specimen was then cycled with this load until failure. The maximum load in the load cells for each cycle is shown in Figure 5-28. Due to an instrumentation collection issue, the first 13,000 cycles were not captured. However, the research team is confident that this missing data would mirror the consistent data that followed it. Figure 5-29 shows that the south overhang failed at approximately 67,647 cycles and was characterized by a constant deflection followed by a sudden runaway increase. This failure method was also seen in the electro-welded trusses in Test 1. Cycling was halted before the reinforcement rupture as control over the actuator would become difficult when the stiffness of the specimen reached zero. For this reason, pictures of the top chords post-testing are not available. The research team did not observe any delamination from the sensors at failure.

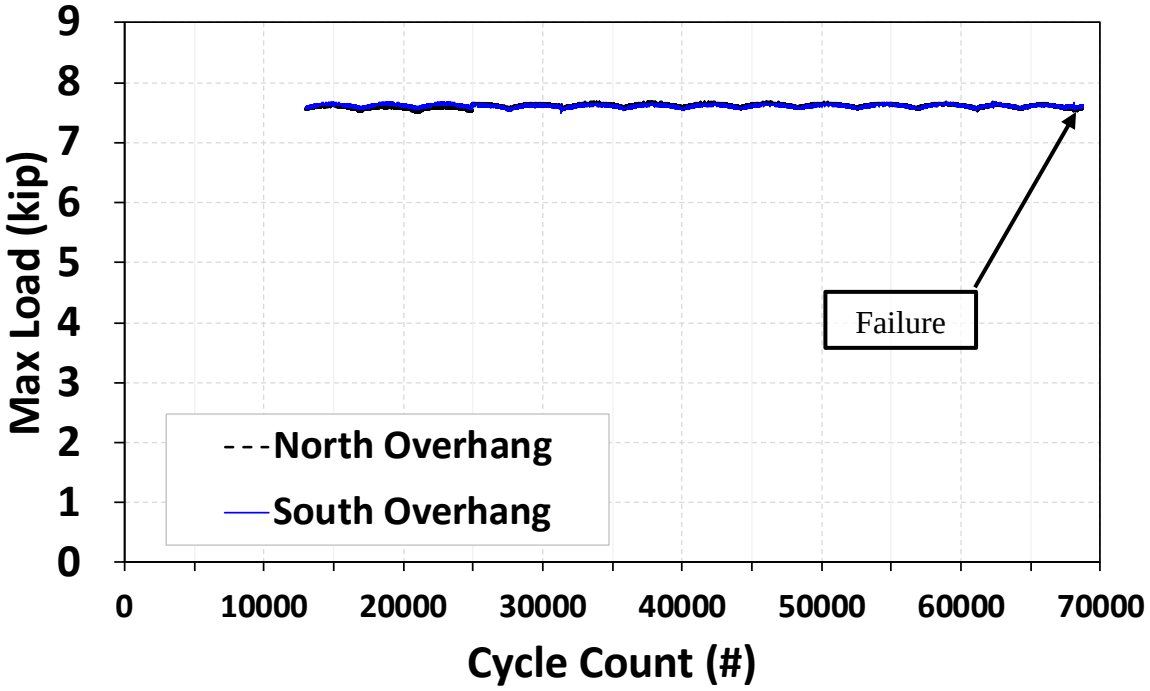

Figure 5-28: Test 4 – Maximum Load versus Cycle Count

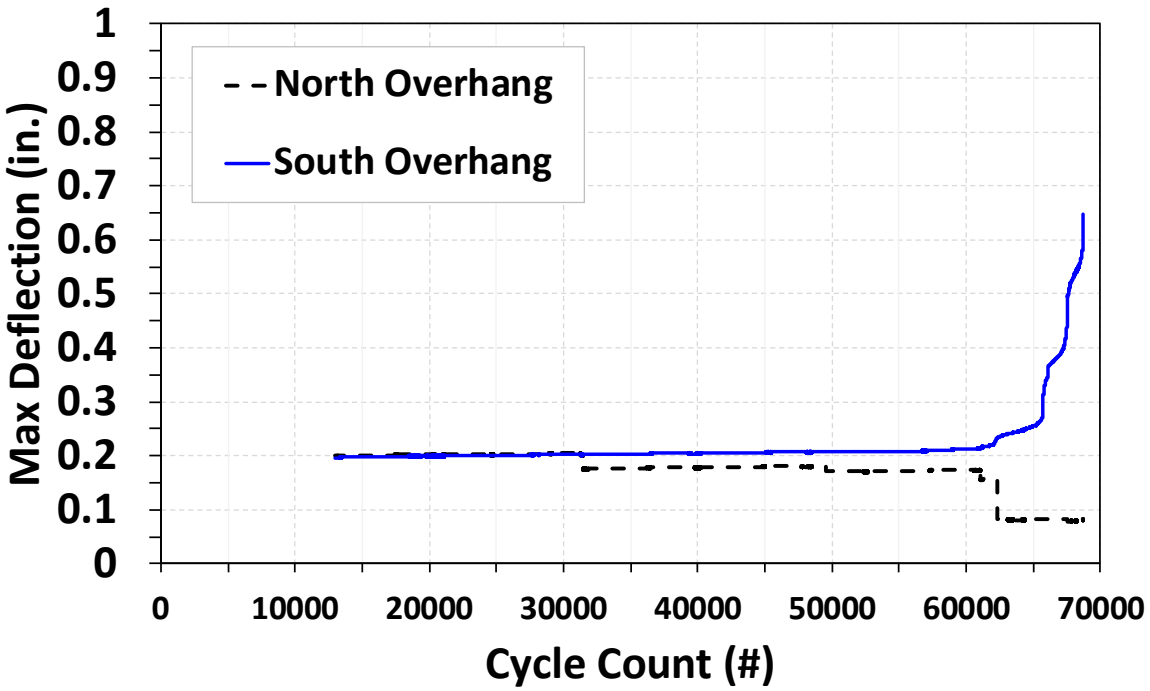

Figure 5-29: Test 4 – Maximum Deflection versus Cycle Count

5.2.5. Test 5 – Static, Hand-Welded Wire Truss

The fifth test completed was the static loading with hand-welded wire trusses. The specimen from Test 3 was used to show the effect that that the cycles would have on strength capacity. Sectional analysis calculations showed that the theoretical strength of the specimen should be 29 kips. As shown in Figure 5-30, there was not any loss in strength due to the low stress cycling. The specimen was able to endure 30 kips of applied load without failing. Crack widths grew to a maximum size of 0.5 in. before loading was stopped. The research team did not see any crushing of the precast panel. The test was concluded when adding additional hydraulic oil to the ram no longer saw an increase in load. Furthermore, with the ability to still reach the theoretical capacity of a fresh specimen, more loading was not required to avoid excessive deflection and damage to equipment.

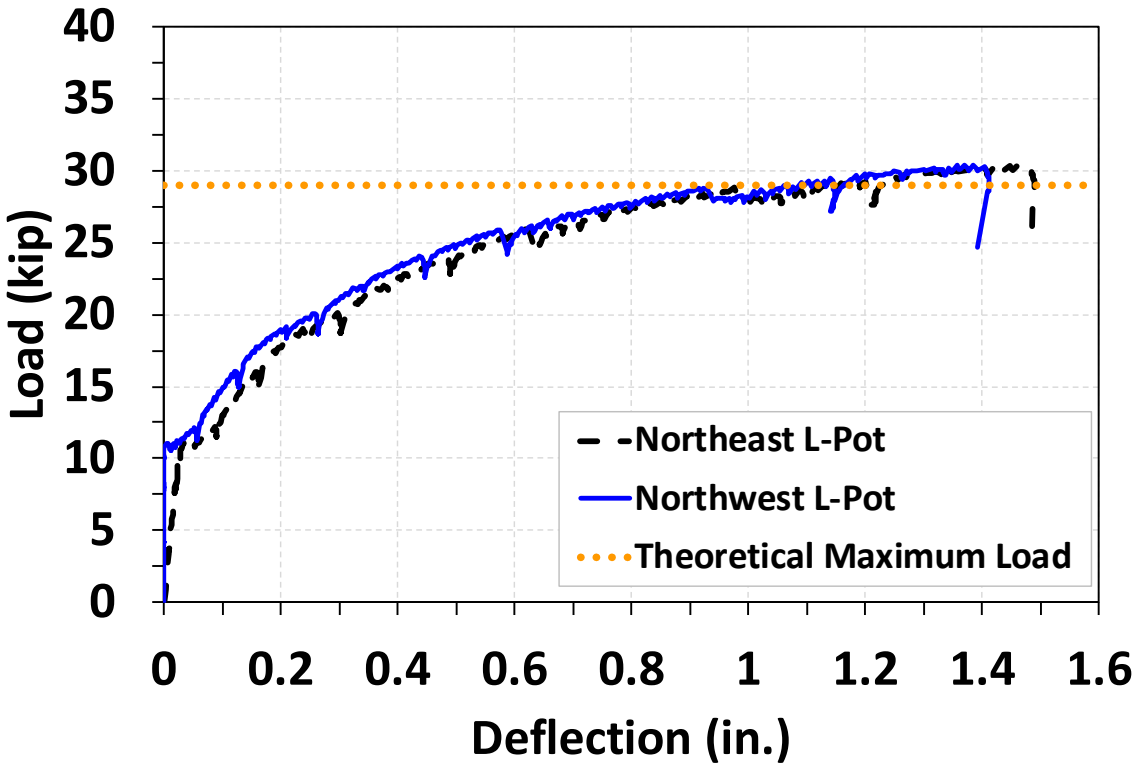

Figure 5-30: Test 5 - Load versus Deflection

Figure 5-31: Test 5 - Cracking Under Max Loading

5.2.6. Test 6 – Static, Electro-Welded Wire Truss

The sixth test completed was the static loading with electro-welded trusses. The specimen from Test 2 was used to show the effect that the cycles would have on strength capacity. Sectional analysis calculations showed that the theoretical strength of the specimen should be 33 kips. As shown in Figure 5-32, the test showed that there was not any loss in strength due to the low stress cycling. The specimen was able to endure 35 kips of applied load without failing. Crack widths grew to a maximum size of 0.5 in. before loading was stopped. The research team did not see any crushing of the precast panel during the test. The test was concluded when adding additional hydraulic oil to the ram no longer saw an increase in load. Furthermore, with the ability to still reach the theoretical capacity of a fresh specimen, more loading was not required to avoid excessive deflection and damage to equipment.

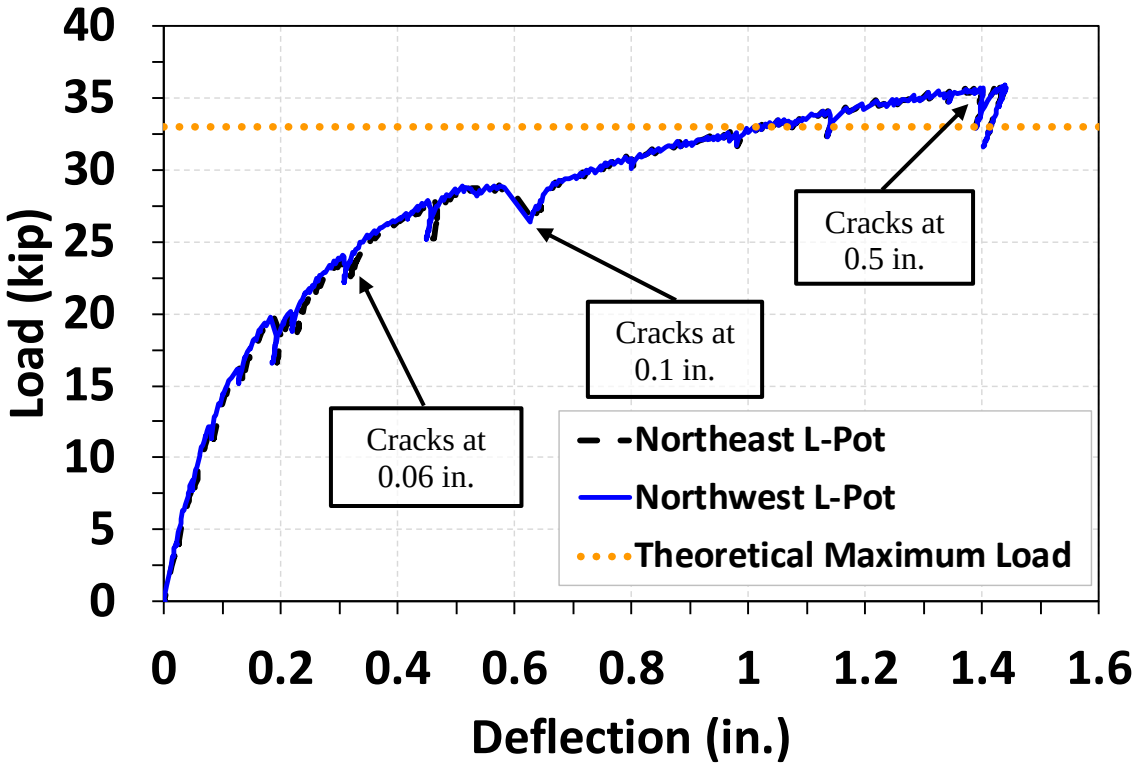

Figure 5-32: Test 5 - Load versus Deflection

Figure 5-33: Test 5 - Maximum Crack Width at End of Loading

5.3. Discussion

The fatigue testing of Test 1 and Test 4 showed how both truss types resulted in a failure mode where there would be a sudden loss in strength of the top chords, should heavy loads be applied that stress them beyond 18 ksi. They did not show an apparent softening; should the loads be similar to those applied during the tests. Increased deflections will develop very close to failure. The hand-welded trusses were able to undergo 67,647 cycles while the electro-welded trusses were only able to last until 32,756 cycles. This difference in fatigue strength may be, in part, attributed to the difference in ductility between the hand-welded wire trusses and electro-welded wire trusses. The material testing shown showed that the electro-welded wire trusses would rupture early in their life, while the hand-welded wire trusses could withstand a substantial amount of plastic deformation. However, since the yield strength of the electro-welded trusses was higher, the increased loading that they experienced could also be a factor in the difference. While the hand-welded wire trusses failed within their expected lifespan, the electro-welded wire trusses last slightly longer than what Eq. (2-1) predicted. The fatigue testing of Test 2 and Test 3 showed that the overhang specimens passed the 18 ksi AASHTO LRFD stress limit that comes from Eq. (2-3) for the amount of stress that can be supported in an element while maintaining infinite fatigue life. Furthermore, the low stress specimens performed optimally in the strength testing that followed.

The strength testing showed expected differences in strength between the hand-welded wire trusses and electro-welded wire trusses, as shown in Figure 5-34. With higher grade steel, the electro-welded wire trusses were able to withstand a higher applied load than the hand-welded trusses. Since both specimens still reached their expected theoretical capacities, sectional analysis can still be used to assess the ultimate capacity of the overhang even after a fatigue load of 5 million cycles.

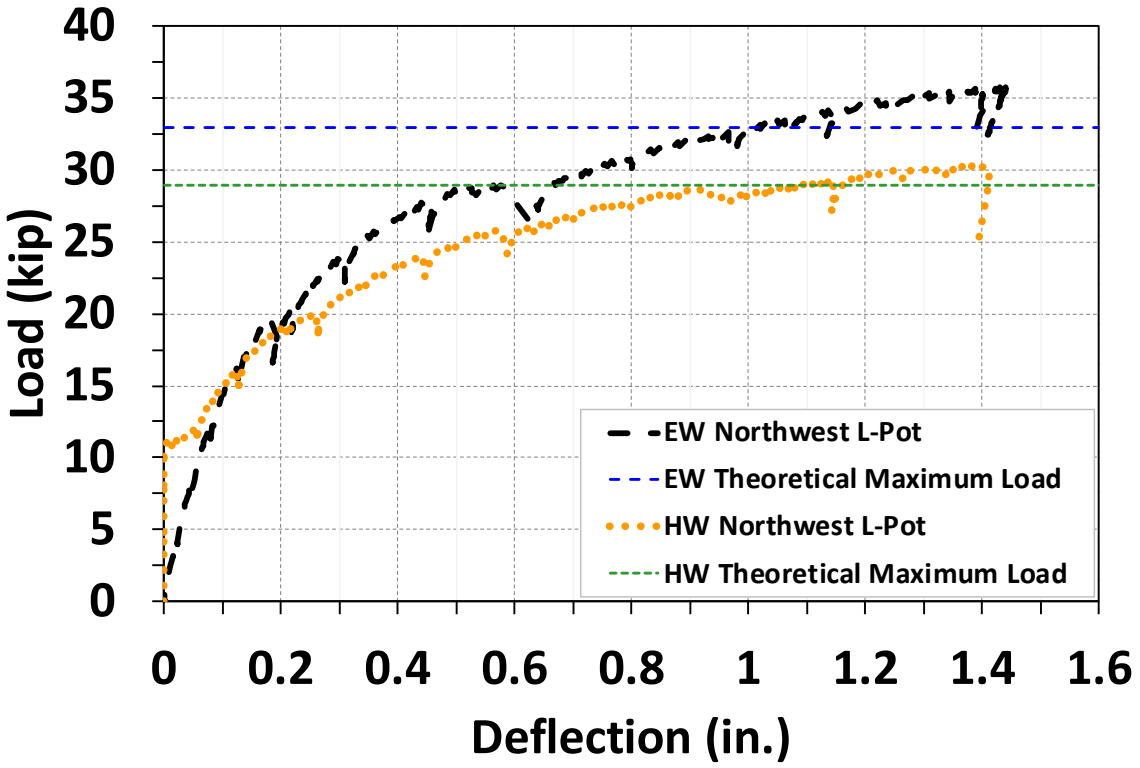

Figure 5-34: Static Test Strength Comparison

5.4. Summary

5.4.1. Summary of Fatigue Program

This experimental testing focused on testing bridge deck specimens that were made with precast panels with partially embedded trusses for fatigue capacity. Two sets of two specimens were made. One set used hand-welded trusses and the other used electro-welded trusses. One of each set was cycled while inducing a yielding stress in the top chords of the trusses. The other of each set were cycled while inducing a low stress in the top chords of the trusses. While the specimens that experienced a yielding stress failed, the low stress specimens reached a cycle count that constituted infinite life. These specimens were later strength tested to see if they had lost any strength due to the cycles they had experienced in relation to their theoretical fresh state. These specimens did not show any loss in strength due to their previous cycling. Both specimens also showed significant deflections and cracking to indicate a failure was approaching.

5.4.2. Suggested Implementation for Overhang panels

There are two suggestions for implementation of these panels that arose from the results of the experimental fatigue tests and finite element models:

- First, fatigue damaging is more likely in bridge areas subject to heavy loading, such as those frequently used by large trucks or oversized vehicles. These vehicles should avoid loading the edges of the overhangs, as their weight can cause high stress cycles that increase the risk of fatigue failure with little warning.
- Second, reinforcement that is made from more ductile steel is preferred to steel that is a higher grade. Both trusses performed the strength tests well, and so their major differentiation is the maximum cycle counts under high stress loading. Since the hand-welded trusses had twice the maximum cycle count as the electro-welded, the US A706 rebar is the preferred material choice.

Chapter 6. Design Recommendations

This chapter outlines design recommendations for NextGen Texas bridge decks, which include appropriate wire truss shop drawings, wire truss spacings and reinforcement layouts, WTPD Panel Pair fabrication drawings, overhang length guidance, and essential considerations for the construction of the precast panel pairs and WTPD precast overhangs, based on findings from the experimental programs in this project.

6.1. Summary of Key Findings

6.1.1. WTPD Precast Panel Pair Strip Tests

The overall findings from the testing show that WTPD precast overhangs, without a cured CIP deck, can sustain expected construction loads. The WTPD precast overhang specimens were designed with typical TxDOT bridge deck reinforcement layouts in conjunction with typical Tx Girder top flange widths, 36 in. to 42 in. In addition, this test program provided a wide range of wire truss unbraced span that fit various commonly used flange widths.

The typical deck reinforcement layouts utilized in the testing were comprised of spacing the wire trusses at 9 in. on center to ensure similar construction practices used in typical TxDOT bridge decks. The wire trusses consisted of No. 4 rebar used as the top and bottom chords. The WTPD bridge decks provided the required capacity for construction and screed loading before the CIP layer was been cast.

Although extra reinforcement bundled with the bottom chords to prevent premature buckling were explored in the structural tests, it was determined that extra reinforcement is unnecessary for typical TxDOT bridge overhang applications during construction.

The relationship between overhang deflection ratio and top chord stress was established for designers' reference. The proven results of the 9-inch spacing from this testing would be implemented for the full-scale structural testing.

6.1.2. Full-Scale WTPD Panel Pair Fabrication

The WTPD Panel Pair specimens were fabricated by a local precast plant experienced in typical PCP fabrication practices. They were fabricated in a typical 8-ft-wide prestressing bed commonly used for typical PCP fabrication. The required fabrication techniques and practices for the WTPD Panel Pairs were similar and added little difficulty to the already implemented techniques and practices with typical PCP fabrication.

Important challenges and considerations encountered during the fabrication and casting of the WTPD panel pairs are summarized below:

- **Covering exposed top chord rebar**: Since the wire trusses were partially embedded into the precast panel pair, the top chord of the truss remained exposed during the casting process. The research team used duct tape to cover the top chord during the fabrication of all precast specimens as shown in Figure 6-1. The top chord is recommended to remain free of cured concrete as its presence could prevent proper bonding between the CIP concrete and the top chord rebar, which serves as the top mat transverse rebar. Appropriate methods of preventing the precast concrete from curing onto the top chord rebar should be applied. For example, the research team considered using a reusable and temporary angle iron or hot rolled L sections during full scale production of the WTPD Panel Pair.

Figure 6-1: Duct tape covering top chord rebar

- **Finishing and Troweling**: During construction of the WTPD panel pair specimens, the precast concrete was troweled with typical finishing practices; a broom or tine drag finish was not utilized. Finishing took extra time and care as only hand trowels were used, due to the protruding top chord rebar of the wire truss, as shown in Figure 6-2. Specialized equipment could be developed in the future to expedite the process of finishing the precast concrete as the trusses are spaced at a repeating 9 in. on center.

Figure 6-2: Finishing and troweling

- **Specialized Forms**: As previously mentioned, the WTPD panel pair specimens were cast in a typical steel prestressing bed. Given the unique cross section of the wire trusses compared to typical 0.6-inch prestressing strands, specialized steel end forms and steel overhang curb forms would help expedite the casting process. In the casting process, all WTPD Panel Pair specimens were fabricated using lumber end forms and overhang curb forms as shown in Figure 6-3, which, although easy to fabricate for small batches, required extra fabrication techniques to prevent precast concrete from leaking out of the end forms. In particular, special considerations must be made where the wire truss rests on the end forms. In these regions, spray foam was used to seal and close the gaps, as shown in Figure 6-4. Proper sealing and fitting of the overhang curb formwork should also be considered, as a visible seam was apparent on the interface of the steel prestressing bed and the lumber overhang curb formwork. It should be noted that minimal difficulty was encountered when applying the form release agent to the steel prestressing bed formwork to prevent bonding between the steel formwork and the precast concrete.

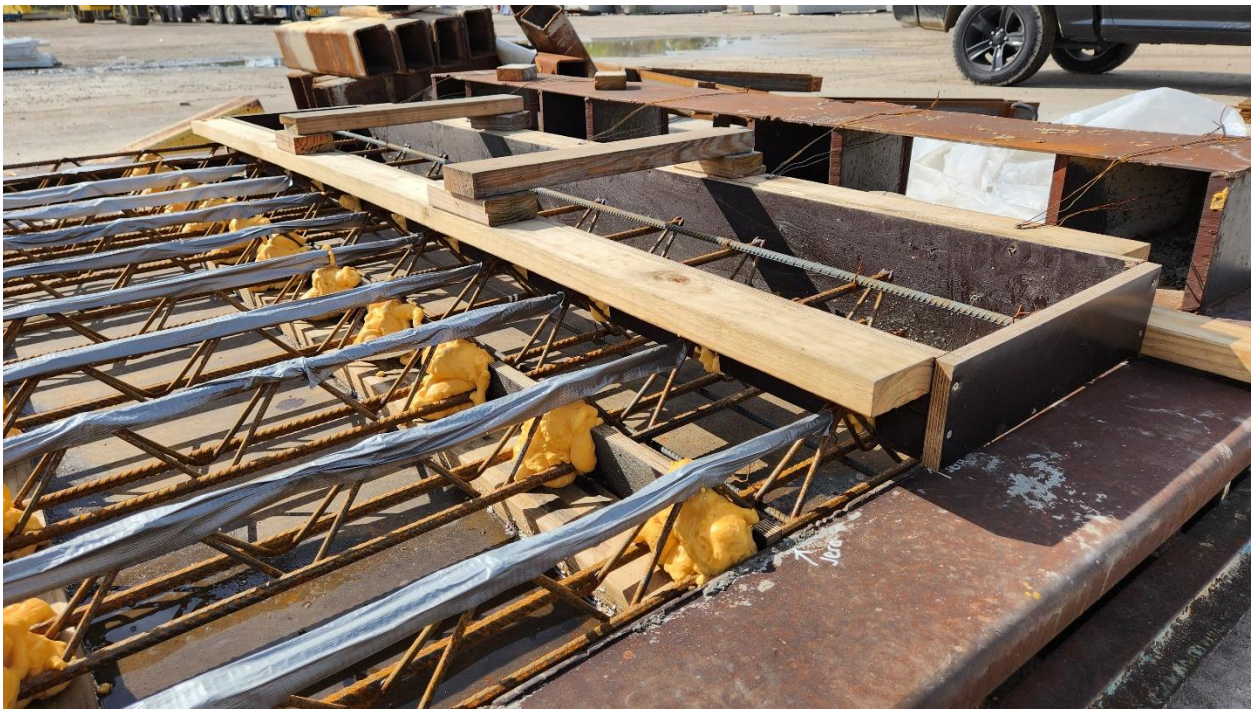

Figure 6-3: Lumber overhang curb formwork

Figure 6-4: Lumber end form and spray foam

6.1.3. Casting Full-Scale Deck

The research team designed and constructed a full-scale deck onto a typical 36-inch top flange prestressed Tx-28 girder superstructure that followed typical TxDOT bridge deck details and fabrication techniques. During placement of the WTPD Panel Pairs onto the Tx-28 prestressed girder's bedding strips, the research team encountered one complication beyond the typical PCP placement: conflicts arose between the R-bars and bottom chord rebar of the wire trusses, as shown in Figure 6-5. The conflict occurred between the R-bars and the bottom chord of the wire trusses directly over the centerline of the facia girder. The challenge was overcome by bending the R-bars out of the way using a sledgehammer. However, other methods could also be implemented during full scale production. These include either applying special consideration during the detailing and placement of R-bars on the prestressed girders or simply bending and/or cutting the conflicting R-Bars to mitigate the conflict. The research team recommends deferring the decision of mitigating the R bar conflicts to the engineer of record or field engineer.

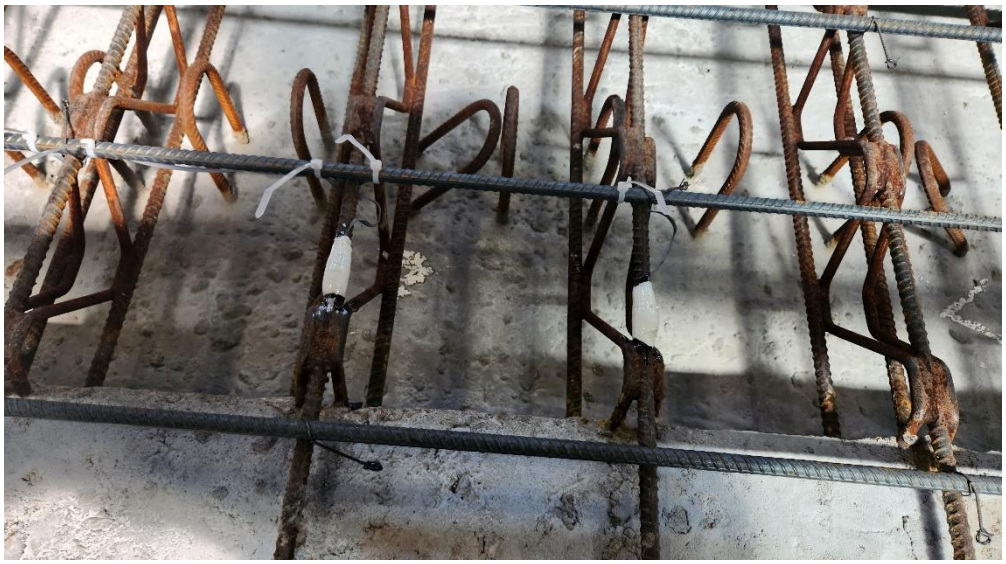

Figure 6-5: Conflict Between R-Bars and Wire Trusses

After the WTPD panel pairs were placed, the research team applied spray foam to seal the gaps and cracks between the transverse butt joints between the WTPD panel pairs with minimal difficulty compared to typical PCPs. The full depth bridge deck was cast at 8.5 in., adhering to typical TxDOT bridge deck construction practices without encountering any extra difficulty casting, screeding, and finishing the deck. It should be noted that the CIP concrete was hand screeded and finished, without the use of a Bidwell Screed used in typical TxDOT CIP bridge deck fabrication.

Although a Bidwell Screed was not used to fabricate the CIP bridge deck, calculations and test results from the WTPD precast overhang testing indicate no anticipated issues with the screed load or screed rail placement on the precast overhang curb. The screed rail would be placed on the curb

of the precast overhang as close to the facia girder centerline as possible, providing room and accommodating the protruding rebar for the CIP rail anchorage. The precast overhang curb width of 1'-4" was used as precedent from the precast overhang curb width detail used in the archived TxDOT Bridge Standard Detail Sheet PCP(O). It should also be noted that protruding rebar for the CIP rail anchorage was not utilized in the full-scale deck specimen, but little difficulty is expected with providing rail anchorage.

The use of F bars, to prevent overturning of the WTPD Panel Pair during construction loads, as detailed in the archived TxDOT Bridge Standard Detail Sheet PCP(O), were not utilized in the full-scale deck specimen. Calculations were performed which showed that in extreme cases, with an extended overhang (4 ft-4 in. from girder centerline) and short interior PCP panel back span (6 ft), extra precautions may need to be considered for high construction live loads.

6.1.4. Full-Scale Deck Structural Testing

Key findings from the full-scale deck structural testing that are relevant to the design recommendations are summarized as follows:

- **WTPD Deck Structural Capacity Compared to DT Loads:** The ultimate capacity of the positive moment over the long span (Tests 5/8) was 6.8 times the service design tandem for both truss types. The ultimate capacity of the short overhang (Tests 6/7) was 4.8 comparable to that of traditional precast prestressed panel decks for both truss types. The ultimate capacity of the long overhang (Tests 9/10) demonstrated lower capacity and combined failure mechanism for both truss types.

- **Wire Truss Type and Deck Stiffness:** Both of the hand-welded and the electro-welded WTPD decks deflected similarly at service loads and at ultimate loads. The hand-welded WTPD decks demonstrated greater ductility than their electro-welded counterparts for the short overhang (Tests 6/7), but both truss types reached similar ductility for the long overhang (Tests 9/10) before the tests were stopped for safety reasons. Crack propagations and width growths in the tests on hand-welded WT panel pair decks were similar to electro-welded WT panel pair decks, and the cracks widths satisfied serviceability requirements.

- **Comparable Performance to Existing Deck System:** The NextGen Deck performance had similar or better performance compared to the test results reported in Project 0-4418, warranting the implementation of the NextGen bridge deck system. Regardless of truss type, WTPD decks provide adequate capacity for TxDOT bridges.

- **Contribution of Wire Trusses:** Test results showed that adding wire trusses does not necessarily increase the punching shear capacity, which may be attributed to wire truss webs' orientation and location being difficult to locate to be effective. It would be

conservative to ignore the presence of webs for punching shear capacity. Further data analysis and research could better explain the structural behavior of WTPD bridge decks.

6.1.5. Fatigue Testing

The research team verified that the WTPD Decks perform satisfactory under fatigue conditions as described by AASHTO LRFD Bridge Design Specifications Eq. 5.5.3.2-2. In particular, WTPD deck specimens with either truss type sustained 5,000,000 cycles under a stress range between 0 ksi and 18 ksi, which is considered infinite life per AASHTO LRFD. For WTPD decks for low-stress-range fatigue loads, since no significant softening or cracking was observed over these cycles, no special guidance is required.

Specimens which were cycled between 0 ksi and yield showed that the overhangs failed as the top chord of the trusses in the top mat lose its stiffness and fatigues. This failure can occur under cycle counts less than 50,000. This is similar to current standard CIP overhangs and likewise should be avoided.

6.2. Design Recommendations

The main goal of Project 0-7041 was to demonstrate the feasibility of WTPD Decks in typical TxDOT bridge construction. After multiple structural tests on representative structures of typical TxDOT bridge deck and overhang construction, the research team arrived at the following design recommendations:

1. **WTPD Panel Pair Wire Truss Spacing Details:** Fabricate WTPD panel pairs with 9-inch wire truss spacing to maintain typical top mat reinforcement ratios found in TxDOT deck and overhang designs. Further research into bundling an additional No. 4 rebar on the top chord is recommended for cases requiring extra overhang capacity.

2. **Reinforcement Along the Traffic Direction:** For bottom mat reinforcement in precast panel pairs, distribute No. 3 bars at 6 in. Longitudinal top mat reinforcement should consist of No. 4 bars spaced at 9 in., following common practice for TxDOT bridges.

3. **Main Panel Dimensions:** Use a maximum width (transverse to traffic) of 9 ft-6 in. and a maximum length (longitudinal to traffic) of 8 ft for main panels, with a thickness of 4 in. These dimensions align with current TxDOT practice and shipment limitations.

4. **Typical Overhang Lengths:** Maintain the TxDOT typical 3-ft overhang from the girder centerline for standard specifications to ensure adequate stiffness, structural capacity, and crack width control. Avoid overhang lengths longer than 3 ft from the girder centerline, as they may not provide sufficient stiffness and capacity. Extra reinforcing bars might be distributed or bundled with top chords to have higher stiffness and capacity if longer overhangs are to be

used. However, the test program did not provide supporting experimental data for the strengthening.

5. **R-Bars:** Conflicts between R-bars and bottom chord wire trusses may occur during placement of WTPD Panel Pairs. Mitigation decisions should be deferred to the engineer of record, who should provide guidelines and constructability notes for the contractor.

6. **F-Bars for Stability:** Consider specifying F-bars to prevent overturning if extra stability is desired. Field welding F-bars to R-bars as detailed in the Archived TxDOT PCP(O) Standard Detail Sheet can provide counter moment resistance to the overturning moment produced by the screed rail.

7. **Lap Splices:** Recommend a lap splice length of at least 39 in. on each side of the girder centerline over interior girders, following AASHTO LRFD standards.

8. **End Curb and Screed Rails:** Install a full-depth end curb with a back span of 16 in. for the placement of screed rails and as end forms. This facilitates the use of Bidwell screeds in typical TxDOT bridge construction.

Chapter 7. Conclusion

The Texas Department of Transportation (TxDOT) has been exploring innovative solutions to streamline bridge construction processes and enhance safety. Traditional methods, relying on precast partial-depth panels, face challenges with deck overhangs, necessitating additional forming and bracing. Drawing inspiration from successful practices in Spain, TxDOT introduced the NextGen Texas bridge deck system. By utilizing full-width precast partial-depth panels connected with wire trusses spanning the entire width of the bridge deck, this system eliminates the need for extra forming and bracing, potentially reducing costs and accelerating project delivery. Under Project 0-7041, a comprehensive research initiative was orchestrated to develop and validate this innovative system. Through rigorous experimental investigation and advanced nonlinear finite element analysis, the behavior and performance of the full-width partial-depth panels were evaluated. The project also established design guidelines for widespread adoption of the NextGen Texas bridge deck system, promising more efficient, cost-effective, and accelerated bridge construction in Texas. Conclusions drawn from completing each of the major tasks of this project are as follows:

In Chapter 2, the literature review examined the current state of partial-depth precast concrete panel bridge deck construction in Texas, focusing on the challenges of extending such a system to a full-width design. Inspired by Spanish bridge design, which incorporates steel lattice girders embedded into the panels, a novel design technique was proposed. The review identified that while partial-depth bridge deck design and behavior are well understood within the fascia girders, challenges arise in achieving a uniform full-width design, particularly regarding moment transfer and composite action with the girder. Despite attempts to address these challenges, logistical issues remained unresolved. However, there was substantial potential for safety improvement, cost savings, and enhanced design efficiency with full-width partial-depth precast concrete overhangs. Concrete sections with lattice girder reinforcement demonstrated greater stiffness and resilience, although challenges such as compression buckling during construction and accurate stiffness prediction persisted. Differences between the Texas and Spanish systems were also noted, warranting further investigation. Additionally, existing methods for predicting fatigue cycles might not be directly applicable to wire truss configurations, necessitating further research in this area. Based on these findings, the research team initiated three large-scale experimental programs that addressed wire trussed partial-depth panel bridge deck under different stages: construction (Chapter 3: Partial-Depth Precast Panel Pairs), service (Chapter 4: Full-Scale Bridge Deck Structural Test), and long-term behavior (Chapter 5: Investigation into Fatigue Behavior).

In Chapter 3, load-testing was conducted on 24 wire truss partial-depth (WTPD) precast concrete panels (PCPs) to assess the feasibility of the NextGen Bridge Deck system during construction. The experiments evaluated flexural and shear behavior under various conditions, revealing several significant findings. The WTPD PCPs demonstrated ductile load responses primarily governed by the yield moment, with longer unbraced spans leading to bottom chord buckling. Additional

reinforcement effectively mitigated buckling and increased moment capacities. Variations in yield strengths and truss member geometries influenced post-yield responses, with electro-welded trusses exhibiting more sudden load drops than hand-welded ones. The shear response depended on web member properties, with electro-welded trusses exhibiting buckling and rapid load drops, while hand-welded trusses maintained load plateauing. Premature failures highlighted issues with wire truss embedment and concrete panel reinforcement. Analytical methods for buckling behavior were developed, but require further verification. These findings contribute to establishing construction safety factors and design guidelines, advancing the development of the NextGen Bridge Deck system.

In Chapter 4, ten tests were conducted on a full-scale bridge deck specimen, each side reinforced with either hand-welded or electro-welded wire trusses. These tests subjected the deck to various loading conditions simulating common scenarios in Texas bridges, including negative and positive moments on both short and long spans, as well as loads on the overhangs. The results revealed that both wire truss types failed similarly in punching shear during positive moment tests over the long span and in combined flexure and shear during short overhang tests. While wire truss type did not significantly affect ultimate capacities, hand-welded panel pairs exhibited greater ductility at the short overhang test. Ultimate capacities were comparable to traditional deck systems, suggesting limited enhancement by wire trusses. Crack widths met AASTHO LRFD requirements under design tandem loads. Finite Element Method (FEM) analysis approximated panel capacities well, but encountered limitations in capturing deflection and stiffness due to boundary condition and mesh size constraints. This still offered potential for field use in strength and punching shear capacity determinations.

Experimental fatigue testing introduced in Chapter 5 focused on precast panel bridge deck specimens with partially embedded trusses under cyclic loading that created negative moment near the support, aiming to verify the applicability of current AASTHO LRFD's fatigue stress limitation on the system. While specimens subjected to yielding stress in the top chords failed earlier, those under low stress reached infinite life cycles. Strength testing post-fatigue showed no strength loss. Suggestions for implementation include caution against high stress loading on overhang edges, particularly from heavy vehicles, and preference for ductile steel reinforcement, such as US A706 rebar, for improved fatigue resistance.

Chapter 6 provided design recommendations. The design recommendations included maintaining 9-inch wire truss spacing in WTPD panel pairs to match typical reinforcement ratios and crack widths of cast-in-place overhangs. Additional No. 4 rebar on the top chord or different web member patterns could enhance overhang capacity. Bottom mat reinforcement should consist of No.3 bars at 6 in. spacing, and the longitudinal top mat reinforcement should be No. 4 bars at 9-in. spacing. Panel dimensions should align with TxDOT standards, with suggested maximum widths of 9 ft-6 in., lengths of 8 ft, and thicknesses of 4 in. Keeping overhang lengths at 3 ft from the girder centerline was recommended for adequate stiffness and capacity. The recommendations also addressed conflicts with R-bars and suggested using F-bars for stability. Lap splice lengths

over interior girders should be at least 39 in. on each side, and full-depth end curbs with back spans of 16 in. were advised for screed rail placement.

In conclusion, Project 0-7041 has made significant strides in advancing the feasibility of WTPD Decks for Texas bridge construction. Through comprehensive structural tests and analyses, valuable insights have been gained regarding design optimizations, reinforcement strategies, and construction considerations. The successful demonstration of WTPD panel pairs with wire trusses showcases a promising alternative to traditional bridge deck systems, with potential benefits in terms of construction efficiency, cost-effectiveness, and long-term durability. Moving forward, the recommendations derived from this project will inform future bridge construction practices, offering engineers practical guidelines for implementing WTPD Decks in accordance with TxDOT standards. With continued research and refinement, the NextGen Texas Bridge Deck system has the potential to revolutionize bridge construction in Texas, paving the way for safer, more efficient, and resilient infrastructure networks.

Chapter 8. Value of Research

8.1. Introduction

The following chapter reviews the value gained from this research, and the selected benefit area is shown in Table 8.1. The research team believes that these panels can have a meaningful improvement on engineering to enhance current construction practices. This project introduces a new system for overhang bridge decks that does not have similar kind in the United States. This project therefore has contributions to knowledge about the use of embedded trusses in bridge decks. Finally, this research is expected to have substantial cost-savings for construction and design by removing the need for falsework and other labor-intensive steps.

Table 8.1 Selected Benefit Area

Benefit	Qualitative	Economic	Both	TxDOT	State	Both
Contribution to knowledge	X					X
Improvement on Engineering Design	X					X
Cost-effectiveness			X			X

8.2. Improvement on Engineering

Multiple approaches, such as the NUDECK panel, have been made to introduce an overhang panel to improve or supplement the standard prestressed concrete panel (PCP) which sees prevalent use in states such as Texas, Missouri, and Colorado. Project 0-7041 introduces the use of lattice trusses for overhang panels to the United States (US). This technology sees application in Spain and Australia where it is used to connect a system of panels that span the width of the bridge instead of the separated PCP that the US has historically used. The outcomes of this research are anticipated to establish the behavior of WTPD PCP and provide a basis for their implementation into Texas standards. This includes design details for the WTPD PCP reinforcement and lattice truss geometry. This research also gives suggestions for construction practices for fabrication of the panels and placement on-site. As the full-scale specimens did not see a significant increase in strength due to the use of these panels, engineers using these panels should continue to use common equations for the shear strength of concrete decks with conventional mild reinforcement.

8.3. Contributions to Knowledge

As these panels and trusses are new to the US, previous research using them has not been carried out. Therefore, the results from this research program serve as the basis for the behavior of trusses employing US grade rebar and wire until subsequent research is carried out to verify these results.

Full-scale testing has shown that the use of trusses results in comparable or superior strength to the traditional panel deck system. The fatigue testing does not show any deviation from expectations of performance, supporting the validity of current relevant provisions for fatigue design in AASHTO LRFD.

8.4. Cost-effectiveness

Cost-effectiveness is one of the primary benefits for WTPD PCP and so the research team endeavored to make the design as efficient for industry as possible. The implementation of WTPD PCP allows costs to be saved in a number of areas in construction, design, and fabrication.

First among these cost savings is eliminating the need for installation and removal of falsework such as brackets, lumber, or metal forms. Time requirements can be quite significant if worker access to the falsework after casting is limited. This can occur in such cases as bridges over marine environments, areas of high traffic flow, or in highly elevated locations. For a single 100’ span, upwards of 70 brackets may be needed to support both overhangs during casting. This can be quite an investment when considering multi-span bridges that can have hundreds of brackets supporting more than a thousand square foot of falsework panels.

The second saving is from reducing the amount of reinforcement that needs to be tied. The WTPD PCP has the same benefits as standard PCP in that the bottom mat is set into the precast concrete, so it does not need to be placed and tied by workers. Additionally, the top chords of the lattice trusses serve as the transverse reinforcement in the top mat, so the longitudinal reinforcement can be placed on and tied directly to these chords instead of needing to be manually chaired and tied. Since additional precast concrete is being used in the deck, the amount of CIP concrete that needs to be poured is also reduced.

Third, fabrication in precast yards can be conducted in a more easily controlled environment. This generally leads to a higher quality concrete that has more consistent material properties and reinforcement that is more accurately placed. This increased quality has benefits in deck performance and durability. Additionally, the use of precast elements reduces the amount of concrete that needs to be cast on-site. Using the same 100’ span, the precast overhangs replace approximately a single truck’s capacity.

Finally, WTPD PCP can be easily standardized for simplifying designs and streamlining fabrication practices. This saves money for engineers and CAD technicians who can spend less time designing and making drawings. Fabricators will expect repeat designs, and so can make specialized formwork and/or develop techniques to improve their efficiency. Similarly, contractors can become knowledgeable with the panels’ implementation and can more accurately plan around them.

References

ACI Committee 209. (1999). "Prediction of Creep, Shrinkage, and Temperature Effects in Concrete Structures," ACI 209R-92, American Concrete Institute, Farmington Hills, Michigan.

ACI Committee 223. (1998). "Standard Practice for the Use of Shrinkage Compensating Concrete," ACI 223-98, American Concrete Institute, Farmington Hills, Michigan.

ACI Committee 318. (2008). "Building Code Requirements for Structural Concrete (ACI 318-08) and Commentary (318R-08)," American Concrete Institute, Farmington Hills, Mich., 465 pp.

ACI Committee 544. (2002). "State of the Art Report on Fiber Reinforced Concrete," Report 544-1R-96 (Reapproved 2002)," ACI Committee 544, Fiber Reinforced Concrete.

ASTM International. (2001). ASTM C39/C39M. Standard Test Method for Compressive Strength of Cylindrical Concrete Specimens, 04(March).

American Association of State Highway and Transportation Officials (1998), AASHTO LRFD Bridge Design Specifications, 2nd Edition.

American Association of State Highway and Transportation Officials (2020), *AASHTO* LRFD Bridge Design Specifications, 9th Edition.

American Association of State Highway and Transportation Officials. (1960). *The AASHO Road Test Summary Report Special Report 61G*.

Azad, A., Baluch, M., Abbasi, M. and Kareem, K. (1994), "Punching Capacity of Deck Slabs in Girder Slab Bridges," ACI Structural Journal, Vol. 91, No. 6, Nov.-Dec. pp. 656-661.

Azad, A., Baluch, M., Al-Mandil, M., Sharif, A., and Kareem, K. (1993), "Loss of Punching Capacity of Bridge Deck Slabs from Crack Damage," ACI Structural Journal, Vol. 90, No. 1, Jan.-Feb., pp. 37-41.

Banthia, N., and Bhargava, A. (2008). "Permeability of Concrete with Fiber Reinforcement and Service Life Predictions," Materials and Structures, 41, pp. 363-372.

Batchelor, B. and Hewitt, B. (1976), "Tests of Model Composite Bridge Decks," ACI Structural Journal, Vol. 73, No. 6, Jun., pp. 340-343.

Batchelor, B., Hewitt, B., Casgoly, P. and Holowka, M. (1978), "Investigation of the Ultimate Strength of Deck Slabs of Composite Steel/Concrete Bridges," Transportation Research Record, No. 664, p. 162-170.

Bayrak, O., Chao, S.-H., Jirsa, J. O., Klingner, R. E., Azimov, U., Foreman, J., Foster, S., Karki, N., Kwon, K. Y., and Woods, A. (2013). "Bridge Deck Reinforcement and PCP Cracking: Final Report."

Bazant, Z. and Cao, Z. (1987), "Size Effect in Punching Shear Failure of Slabs," ACI Structural Journal, Vol. 84, No. 1, Jan.-Feb., pp. 44-53.

Beal, David B. (1982), "Load Capacity of Concrete Bridge Decks," Proceedings, ASCE, No. ST4, Apr., pp. 814-831.

Bloom, R. and Bentur, A., "Free and Restrained Shrinkage of Normal and High-Strength Concretes," ACI Materials Journal, Vol. 92, No. 2, March–April 1995.

Bouzoubaâ, N., Zhang, M.H., Bilodeau, A. and Malhotra, V.M., "Mechanical Properties and Durability of Concrete Made with High Volume Fly Ash Blended Cements," Fly-Ash, Silica Fume, and Slag, CANMET, Vol. I, pp. 449–474, 1998 (ed.: V.M. Malhotra).

Brown, M. D., Smith, C. A., Sellers, J. G., Folliard, K. J., and Breen, J. E., "Use of Alternative Materials to Reduce Shrinkage Cracking in Bridge Decks," ACI Materials Journal, V. 104, No. 6, NovemberDecember, 2007, pp. 629-637.

Burrows, R.D., The Visible and Invisible Cracking of Concrete, American Concrete Institute Monograph No. 11, 1998.

Cao, L., Allen, J., Shing, P., and Woodham, D. (1996), "Behavior of RC Bridge Decks with Flexible Girders," Journal of Structural Engineering, Vol. 122, No. 1, Jan., pp. 11-19.

Chao, S.-H., Liao, W.-C., Wongtanakitcharoen, T., and Naaman, A. E., "Large Scale Tensile Tests of High Performance Fiber Reinforced Cement Composites," High Performance Fiber Reinforced Cement Composites: HPFRCC-5, International Workshop, Mainz, Germany, July 10-13, 2007.

Chao, S.-H., Naaman, A. E., and Parra-Montesinos, G. J., "Bond Behavior of Strands Embedded in Fiber Reinforced Cementitious Composites," PCI Journal, V. 51, No. 6, November-December, 2006, pp. 56-71.

Cheng, M.-Y, and Parra-Montesinos, G., "Punching Shear Resistance and Deformation Capacity of Fiber Reinforced Concrete Slab-Column Connections Subjected to Monotonic and Reversed Cyclic Displacements," High Performance Fiber Reinforced Cement Composites: HPFRCC-5, International Workshop, Mainz, Germany, July 10-13, 2007.

Christiansen, K. (1963), "The Effect of Membrane Stresses on the Ultimate Strength of the Interior Panel in a Reinforced Concrete Slab," The Structural Engineer, Vol. 41, No. 8, Aug., pp. 261-265.

Clifton, S. P. (2008). "Bridge deck overhang construction." Thesis MS in Engineering--University of Texas at Austin.

Coselli, C. J., Griffith, E. M., Ryan, J. L., Bayrak, O., Jirsa, J.O., Breen, J., and Klingner, R.E. (2004), "Bridge Slab Behavior at Expansion Joints", Technical Report 0-4418-1, CTR, Bureau of Engineering Research, The University of Texas at Austin.

Csagoly, P., Holowka, M. and Dorton, R., (1978), "The True Behavior of Thin Concrete Bridge Slabs," Transportation Research Record, No. 664, pp. 171-179.

Culmo, M. P. (2009). "Connection details for prefabricated bridge elements and systems" (No. FHWA-IF-09-010). < https://www.fhwa.dot.gov/bridge/ prefab/ if09010/index.cfm >

Dorton, R., Holowka,M. and King, J. (1977), "The Conestogo River Bridge – Design and Testing," Canadian Journal of Civil Engineering, Vol. 4, No. 1, pp. 18-39.

Ebeido, T. and Kennedy, J. (1996), "Punching Strength of Deck Slabs in Skew Composite Bridges," Journal of Bridge Engineering, Vol. 1, No. 2, May, pp. 59-65.

Fang, I., Lee, J., and Chen, C. (1994), "Behavior of Partially Restrained Slabs under Concentrated Load," ACI Structural Journal, Vol. 91, No. 2, Mar.-Apr., pp. 133-139.

Fang, I., Worley, J., Burns, N. and Klingner, R. (1990), "Behavior of Isotropic R/C Bridge Decks on Steel Girders," Journal of Structural Engineering, Vol. 116, No. 3, Mar., pp. 659-678.

Fenwick, R. and Dickson, A. (1989), "Slabs Subjected to Concentrated Loading," ACI Structural Journal, Vol. 86, No. 6, Nov.-Dec., pp. 672-678.

Foster, S. W. (2010). "Reducing top mat reinforcement in bridge decks." thesis.

Freeby, G., Flournoy, L., Watts, S., and Bettis, G. (2018). "Partial-Depth Precast Deck Panel Design and Construction in Texas." Accelerated Bridge Construction University Transportation Center. (Jun. 22, 2020).

Gamble, L., Sozen, M. and Siess, C. (1962), "Tests of a Modified Reinforced Concrete Two-Way Slab," Journal of the Structural Division, ASCE, Vol. 95, No. ST6, June, pp. 1097-1116.

Graddy, J., Kim, J., Whitt, J., Burns, N. and Klingner, R. (2002), "Punching-Shear Behavior of Bridge Decks under Fatigue Loading," ACI Structural Journal, Vol. 99, No. 3, May-Jun., pp. 257-266.

Grubb, J. A., Blunt, J., Ostertag, C.P., and Devine, T. M., "Effect of Steel Microfibers on Corrosion of Steel Reinforcing Bars," Cement and Concrete Research, 37, 2007, pp. 1115-1126.

Grzybowski, M. and Shah, S.P., "Shrinkage Cracking of Fiber-Reinforced Concrete," ACI Materials Journal, 138–147, March–April 1990.

Guo, X.H. and Gilbert, R.I., "The Effect of Specimen Size on the Fracture Energy and Softening Function of Concrete," Materials and Structures, Vol 33, pp. 309-316, 2000.

Helgason, T., Hanson, J. M., Somes, N. F., Corley, W. G., & Hognestad, E. (1976). Fatigue Strength of High Yield Reinforcing Bars. Natl Coop Highw Res Program Rep, 164.

Hewitt, B. and Batchelor, B. (1975), "Punching shear strength of restrained slabs," Journal of the Structural Division, ASCE, Vol. 101, No. ST9, Sept., pp. 1837-1850.

Jackson, P. (1990), "The Global and Local Behavior of Bridge Deck Slabs," The Structural Engineer, Vol. 68, No. 6, Mar., pp. 112-116.

Jiang, D. and Shen, J. (1986), "Strength of Concrete Slabs in Punching Shear," Journal of Structural Engineering, Vol. 112, No. 12, Dec., pp 2578-2591.

J.M. Calvo Rodriguez. (2007, September). Viaducto 23.5 Calzada Derecha Detalles (VI). [Engineering drawing].

Jorge Cascales F., Sergio Couto W. (2017, July). Puente Sobre Rio Definicion General. Plan No. 02. [Engineering drawing].

Jun, Z., and Stang, Henrik, "Fatigue Performance in Flexure of Fiber Reinforced Concrete," ACI Materials Journal, V. 95, No. 1, January-February, 1998, pp. 58-67.

Kosa, K., "Practical Structural Applications of Fiber Reinforced concrete in Japan," HPFRCC 4, RILEM Publications S.A.R.L., Proceedings PRO 6, France, 2003, 606 pages.

Kosmatka, S. H. and Panarese, W. C. (1988), "Design and Control of Concrete Mixtures," Portland Cement Association, Skokie, Illinois.

Kovler, K., Sikuler, J. and Bentur, A. (1993), "Restrained Shrinkage Tests of Fibre-Reinforced Concrete Ring Specimens: Effect of Core Thermal Expansion," Materials and Structures, Vol. 26, pp. 231–237.

Krauss, P.D. and Rogalla, E.A. (1996), "Transverse Cracking in Newly Constructed Bridge Decks," National Cooperative Highway Research Program (NCHRP) Report 380, Transportation Research Board.

Kuang, J. and Morley, C. (1992), "Punching Shear Behavior of Restrained Reinforced Concrete Slabs," ACI Structural Journal, Vol. 89, No. 1, Jan.-Feb., pp. 13-19.

Law, S., Ward, H., Shi, G., Chen, R., Waldron, P. and Taylor, C. (1995), "Dynamic Assessment of Bridge Load-Carrying Capacities," Journal of Structural Engineering, Vol. 121, No. 3, Mar., pp. 478- 495.

Löfgren, I. N. G. E. M. A. R. (2001). "Lattice Girder Elements in Four Point Bending–Pilot Experiment" (No. 01, p. 7). Report.

Mander, T. J., Mander, J. B., & Head, M. (2010). Strength Analysis of Precast Bridge Decks with Full-Depth Precast Overhang Panels. Transportation Research Record, 2202(1), 70-76. https://doi.org/10.3141/2202-09

McDonagh, M., Foden, A., & Beyer, A. (2022). Partial-Depth Precast Concrete Panels. https://www.fhwa.dot.gov/bridge/concrete/hif22031.pdf

Mehta, P.K. and Monteiro, P. (1993), Concrete – Structure, Properties, and Materials, The McGrawHill Companies, Inc., New York.

Miller, R., Aktan, A. and Shahrooz, B. (1994), "Destructive of Decommissioned Concrete Slab Bridge," Journal of Structural Engineering, Vol. 120, No. 7, Jul., pp. 2176-2197.

Moehle, J., Kreger, M. and Leon, R. (1988), "Background to Recommendations for Design of Reinforced Concrete Slab-Column Connections," ACI Structural Journal, Vol. 85, No. 6, pp. 636-644.

Naaman, A. E., Fischer, G., and Krstulovic-Opara, N., "Measurement of Tensile Properties of Fiber Reinforced Concrete: Draft Submitted to ACI Committee 544," High Performance Fiber Reinforced Cement Composites, HPFRCC 5, RILEM Publications S.A.R.L., Proceedings, Mainz, Germany, 2007, 518 pages.

Naaman, A. E., Likhitruangsilp, V., and Parra-Montesinos, G., "Punching Shear Response of High Performance Fiber-Reinforced Cementitious Composite Slabs," ACI Structural Journal, V. 104, No. 2, March-April, 2007, pp. 170-179.

Naaman, A. E., Wongtanakitcharoen, T., and Hauser, G., "Influence of Different Fibers on Plastic Shrinkage Cracking of Concrete," ACI Materials Journal, V. 102, No. 1, January-February, 2005, pp. 49-58.

Newell, S., and Goggins, J. (2016). "Real-time monitoring of concrete–lattice girder slabs during construction." Thomas Telford Ltd.

Newell, S., and Goggins, J. (2019). “Experimental study of hybrid precast concrete lattice girder floor at construction stage.” Structures, 20, 866–885.

Ockleston, A. J. (1955), “Load Tests on a Three Story Reinforced Concrete Building in Johannesburg,” The Structural Engineer, Oct., pp. 304-322.

Ockleston, A. J. (1958), “Arching Action In Reinforced Concrete Slabs,” The Structural Engineer, Jun., pp. 197-201.

Ostertag, C. P., Yi, C., and Monteiro, P. J. M., “Effect on Confinement on Properties and Characteristics of Alkali-Silica Reaction Gel,” ACI Materials Journal, V. 104, No. 3, May-June, 2007, pp. 276-282.

Paillere, M., Buil, M. and Serrano, J.J., “Effect of Fiber Addition on the Autogenous Shrinkage of Silica Fume Concrete,” ACI Materials Journal, Vol. 86, No. 2, March–April 1989.

Park, R., and Gamble, L. (2000), Reinforced Concrete Slabs, John Wiley and Sons, New York.

Parra-Montesinos, G., “Shear Strength of Beams with Deformed Steel Fibers,” Concrete International, V. 28, No. 11, Nov., 2006, pp. 57-66.

Paskova, T, and Meyer, C., “Low-cycle Fatigue of Plain and Fiber-Reinforced Concrete,” ACI Materials Journal, V. 94, No. 4, July-August, 1997, pp. 273-285.

Petrou, M. and Perdikaris, P. (1996), “Punching Shear Failure in Concrete Decks as Snap-Through Instability,” Journal of Structural Engineering, Vol. 122, No. 9, Sept., pp. 998-1005.

Petrou, M., Perdikaris, P. and Duan, M. (1996), “Static Behavior of Non composite Concrete Bridge Decks under Concentrated Loads,” Journal of Bridge Engineering, Vol. 1, No. 4, Nov., pp. 143-154.

Raithby, K. D. (1979). Flexural Fatigue Behavior of Plain Concrete. Fatigue & Fracture of Engineering Materials & Structures, 2(3). https://doi.org/10.1111/j.1460-2695.1979.tb01085.x

Ryan, J. (2003), “Zero-skew Bridge Deck Behavior at Expansion Joints,” Master’s Thesis, The University of Texas at Austin, Texas, Aug., 319 pp.

Tan, K. and Gjorv, O. (1996), “Performance of Concrete Under Different Curing Conditions,” Cement and Concrete Research, Vol. 26, No. 3, pp. 355–361.

Texas Department of Transportation. (n.d.). Item 421 Hydraulic Cement Concrete. Retrieved March 11, 2024, from https://ftp.txdot.gov/pub/txdot-info/cmd/cserve/specs/2014/standard/s421.pdf

Tilly, G. P. (1979). Fatigue of Steel Reinforcement Bars in Concrete: A Review. Fatigue & Fracture of Engineering Materials & Structures, 2(3). https://doi.org/10.1111/j.1460-2695.1979.tb01084.x

Trejo, D., Head, M. H., Mander, J., Mander, T., Henley, M., Scott, R., Ley, T., & Patil, S. (2011). Development of a Precast Bridge Deck Overhang System. http://www.ntis.gov

Turco, T. (2018). “TxDOT Preferred Practices for Steel Update.” Texas Department of Transportation, (June 27, 2020).

Weiss, W.J., Yang, W. and Shah, S.P. (1998), "Shrinkage Cracking – Can it be Prevented?" Concrete International, pp. 51–55, April.

Weiss, W.J., Yang, W. and Shah, S.P. (1998), "Shrinkage Cracking of Restrained Concrete Slabs," Journal of Engineering Mechanics, Vol. 124, pp. 7–12.

Whiting, D. and Detwiler, R. (1998), "Silica Fume Concrete for Bridge Decks," NCHRP Report 410, Transportation Research Board.

Wiegrink, K., Marikunte, S. and Shah, S. (1996), "Shrinkage Cracking of High-Strength Concrete," ACI Materials Journal, Vol. 93, No. 2, September–October.

Wood, S. L. (2008). "Recommendations for the use of precast deck panels at expansion joints." (Texas. Dept. of Transportation. Research and Technology Implementation Office and University of Texas at Austin. Center for Transportation Research, eds.), (FHWA/TX-09/0-5367-1).

Xunta de Galicia. (2011, June). Viaducto P.K. 4+560. Plan No. 0.6_10.4. [Engineering drawing].

Youn, S. and Chang, S. (1998), "Behavior of Composite Bridge Decks Subjected to Static and Fatigue Loading," ACI Structural Journal, Vol. 95, No. 3, May-Jun., pp. 249-258.

Appendix A. Specimen Drawings

1) Hand Welded Wire Truss Shop Drawing
2) Electro Welded Wire Truss Shop Drawing
3) 9’-6’’ WTPD PCP Panel Pair Drawing
4) 6’ WTPD PCP Panel Pair Drawing
5) Fatigue Test Specimen Panel

Hand-Welded Wire Truss Shop Drawing

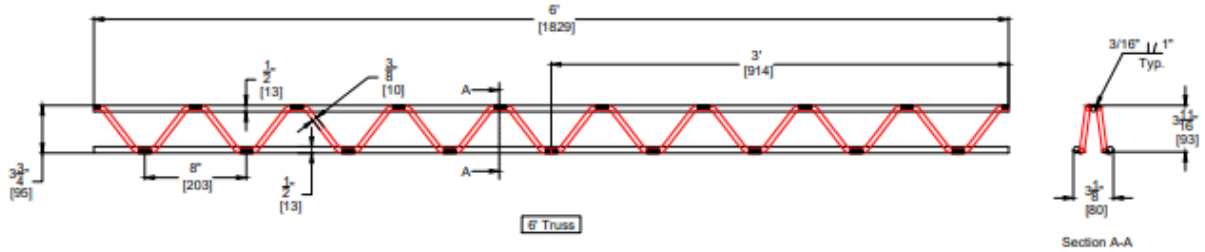

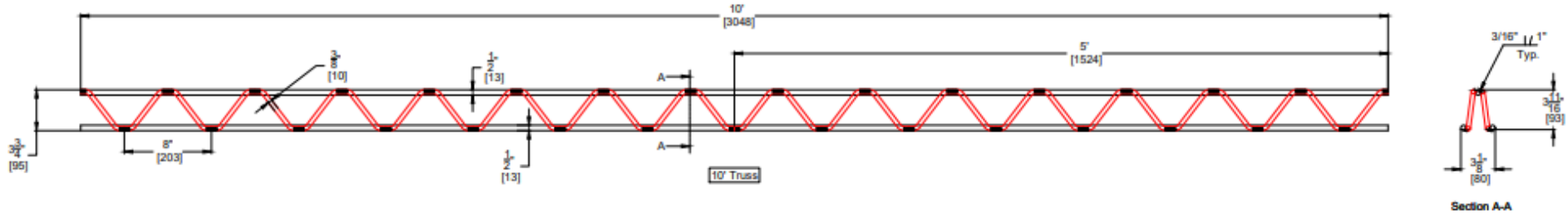

Electro-Welded Wire Truss Shop Drawing

Client : University of Texas at Austin
Type : Truss girder for bridge
Date of drawing : Dec. 21. 2021

Art no. : T130952600
Spec. : 13x7x13x2600L (H-95)
Q'ty : 36 pcs

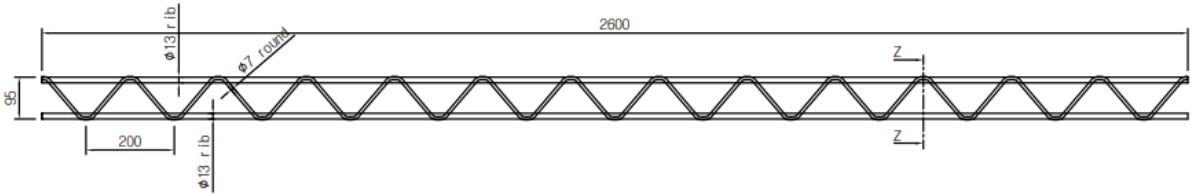

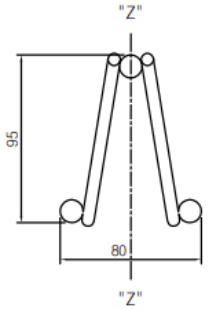

Art no. : T130953600
Spec. : 13x7x13x3600L (H-95)
Q'ty : 40 pcs

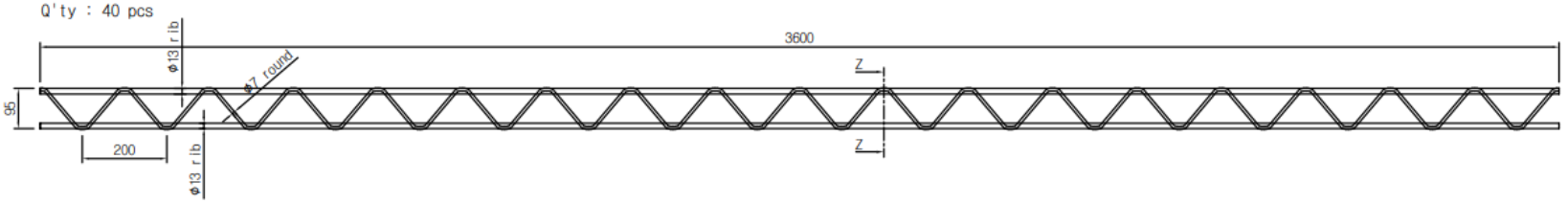

Art no. : T130954200
Spec. : 13x7x13x4200L (H-95)
Q'ty : 36 pcs

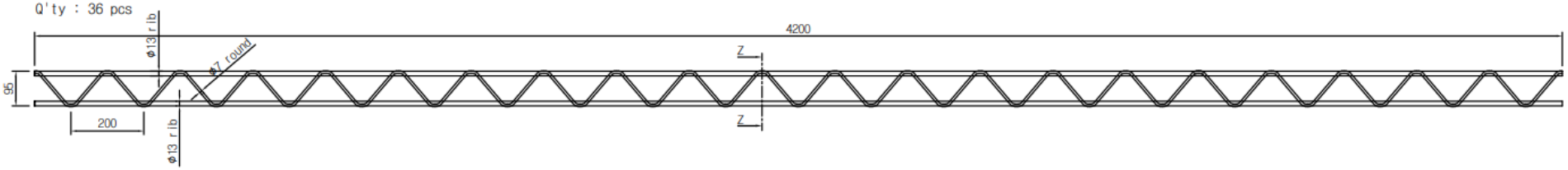

9’-6’’ WTPD PCP Panel Pair Drawing

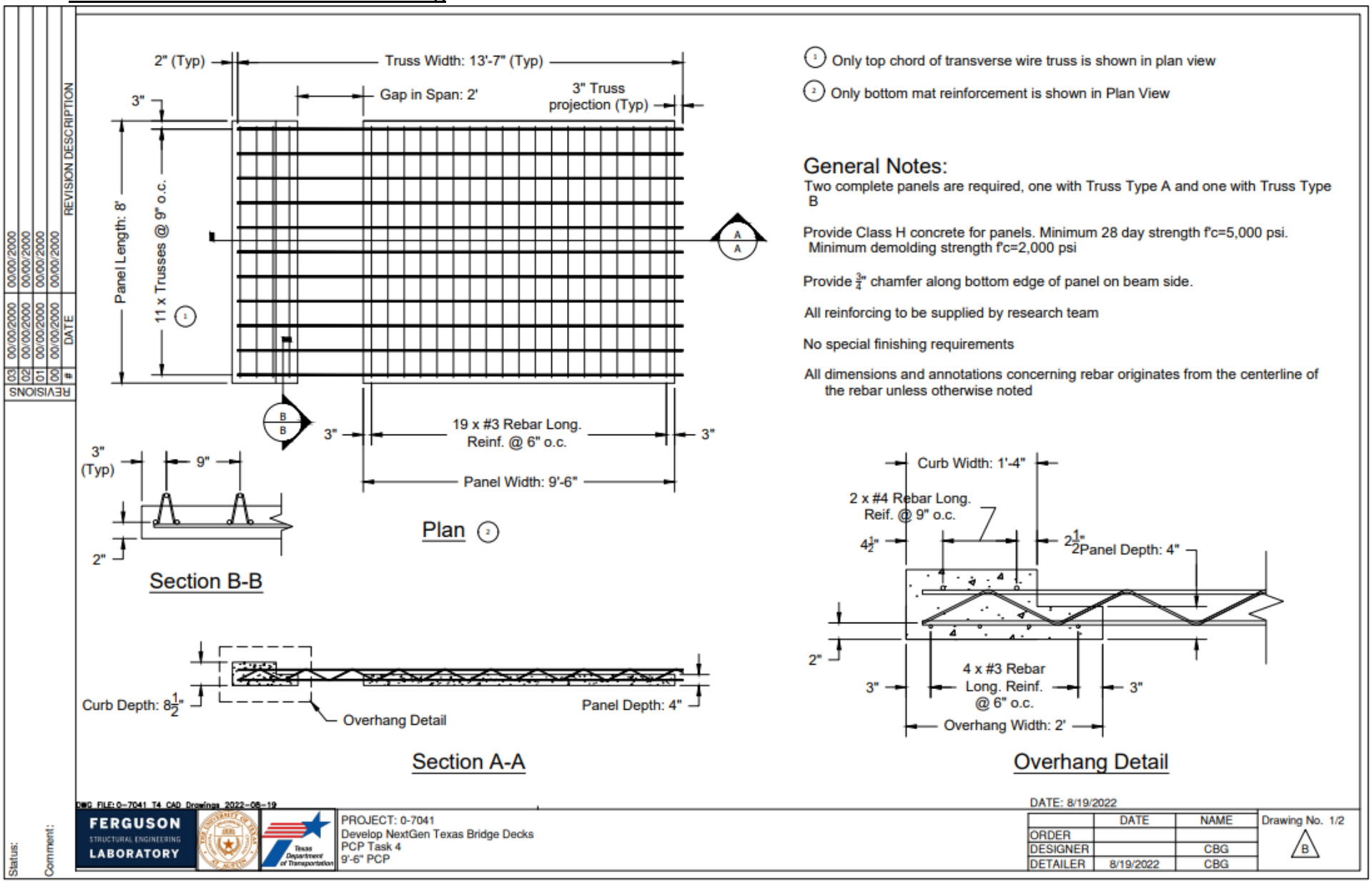

6’ WTPD PCP Panel Pair Drawing

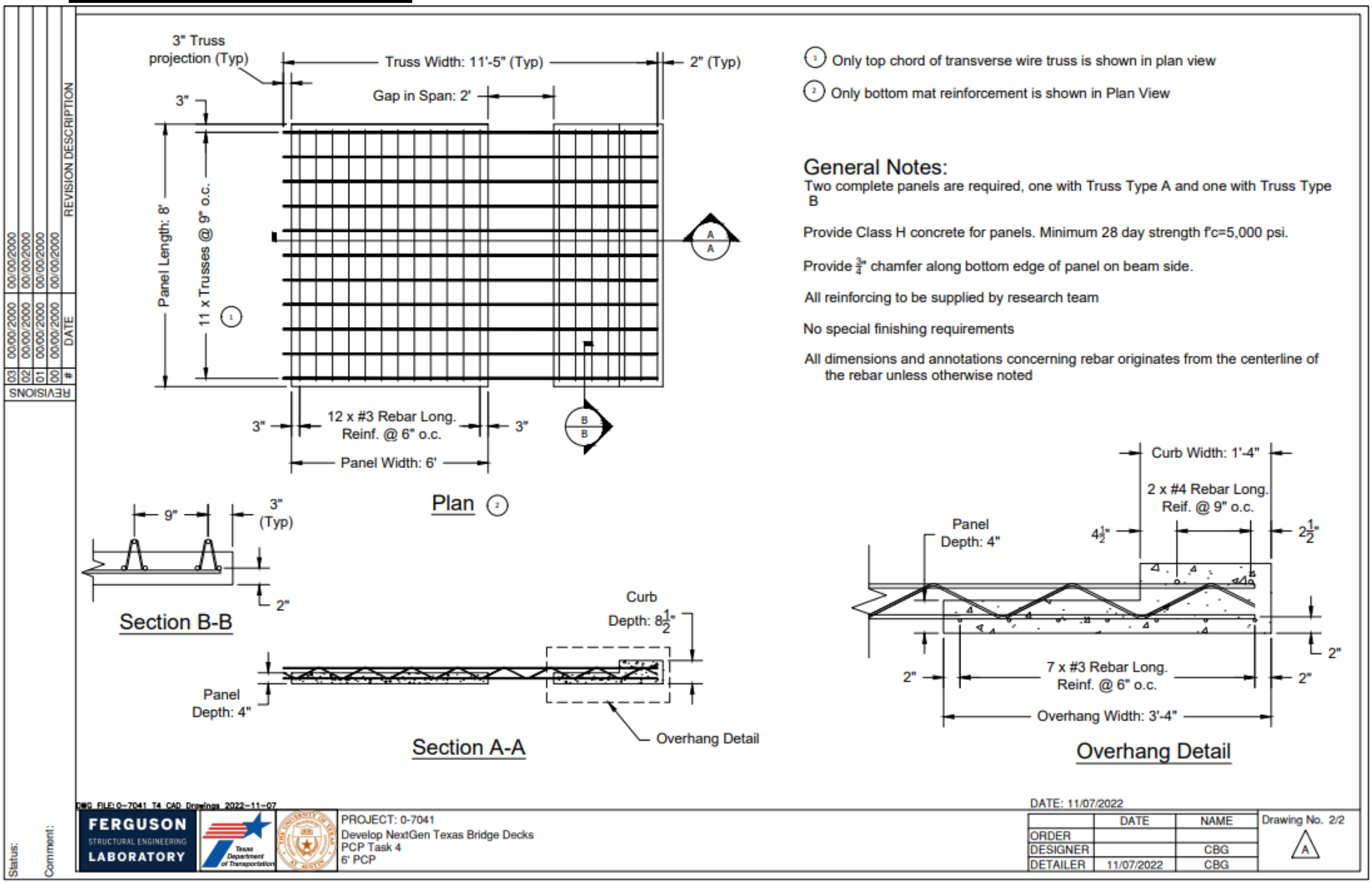

Fatigue Test Specimen Panel

General Notes:

Provide Class H concrete for panels. Minimum 28 day strength f'c = 5,000 psi.
Wire trusses are provided by the research team.
Four precast panel pairs (PCPPs) to be cast total. Two PCPPs will have the hand–welded wire trusses installed. The other two PCPPs will have the electro–welded trusses installed

Plan

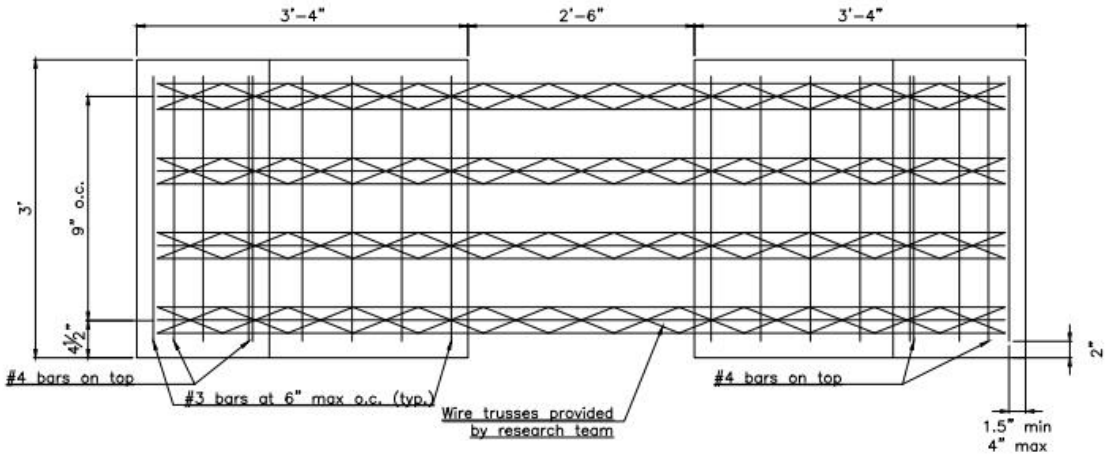

Section

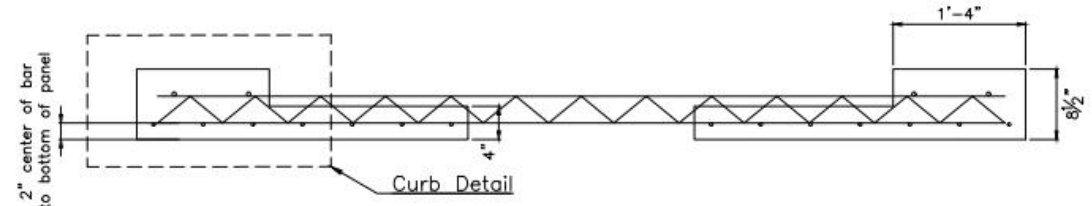

Wire trusses – for information only

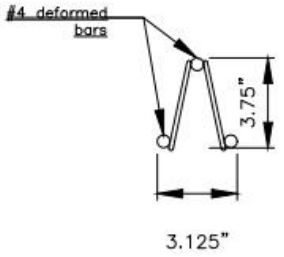

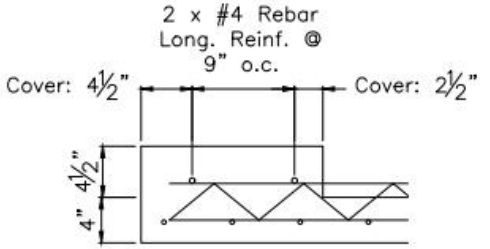

Curb Detail:

REVISIONS

#	DATE	REVISION DESCRIPTION
03		
02		
01		
00		

DWG FILE:

FERGUSON STRUCTURAL ENGINEERING LABORATORY

PROJECT: 0-7041
NextGen Texas Bridge Decks
Task 5 PCP Design

DATE: 11/09/2022

	DATE	NAME
ORDER		
DESIGNER		
DETAILER	11/09/2022	

Drawing No. A

Status:

Comment:

Appendix B. Theoretical Moment Capacity of Overhang Sections

c	=	Distance to Neutral Axis	inch
b_{slab}	=	Width of Slab	inch
E	=	Elastic Modulus of Reinforcement	ksi
L_{arm}	=	Moment Arm of Applied Load	inch
h	=	Height of Section	inch
y_{s1}	=	Depth to Top Chords from Top of Section	inch
y_{s2}	=	Depth to Bottom Chords from Top of Section	inch
A_{s1}	=	Combined Area of Top Chords	sq. inch
A_{s2}	=	Combined Area of Bottom Chords	sq. inch
f'_{pre}	=	Compressive Strength of Precast Concrete	ksi
C_C	=	Force in Concrete	kip
ε_{cc}	=	Concrete Strain at Bottom of Slab	-
ε'_c	=	Concrete Strain at Maximum Stress	-
F_y	=	Yielding Stress of Reinforcement	ksi
F_{s1}	=	Stress in Top Chord	ksi
F_{s2}	=	Stress in Bottom Chords	ksi
T_{s1}	=	Force in Top Chord	kip
T_{s2}	=	Force in Bottom Chord	kip
$M_{c,na}$	=	Moment from Concrete about Neutral Axis	k-in
$M_{c,ca}$	=	Moment from Concrete about Centroidal Axis	k-in
$M_{s1,ca}$	=	Moment from Top Chords about Centroidal Axis	k-in
$M_{s2,ca}$	=	Moment from Bottom Chords about Centroidal Axis	k-in
M_{ca}	=	Moment about Centroidal Axis	k-in
M_{self}	=	Moment due to Self-Weight, Spreader Beam, & Steel Plates	k-in
P_{act}	=	Required Load in Hydraulic Actuator	kip
P_{beam}	=	Weight of Spreader Beam	kip
P_{lcell}	=	Load in External Load Cell	kip

$$C_C = c \cdot b_{slab} \cdot f'_{pre}\left(\left(\frac{\varepsilon_{cc}}{\varepsilon'_c}\right) - \frac{1}{3} \cdot \left(\frac{\varepsilon_{cc}}{\varepsilon'_c}\right)^2\right)$$

$$\varepsilon_{s1} = \frac{\varepsilon_{cc} \cdot (y_{s1} - (h - c))}{c}$$

$$F_{s1} = E \cdot \varepsilon_{s1} \leq F_y$$

$$T_{s1} = F_{s1} \cdot A_{s1}$$

$$0 = C_C + T_{s1} + T_{s2}$$

$$M_{c,na} = c^2 \cdot b_{slab} \cdot f'_{pre}\left(\frac{2}{3} \times \left(\frac{\varepsilon_{cc}}{\varepsilon'_c}\right) - \frac{1}{4} \cdot \left(\frac{\varepsilon_{cc}}{\varepsilon'_c}\right)^2\right)$$

$$M_{c,ca} = M_{c,na} + C_C \cdot \left(\frac{h}{2} - c\right)$$

$$M_{s1,ca} = T_{s1} \cdot (\frac{h}{2} - y_{s1})$$
$$M_{ca} = M_{c,ca} + M_{s1,ca} + M_{s2,ca}$$
$$P_{act} = \frac{2 \cdot (M_{ca} - M_{self})}{L_{arm}}$$
$$P_{lcell} = \frac{P_{act} + P_{beam}}{2}$$

Required Load in Actuator:

The following calculations are the steps for finding the load required to achieve the desired stress in the reinforcement. Sectional analysis is performed to find the correct strain and depth to neutral axis. Once these values are known, moment is found around the centroidal axis. The lever arm from the spreader beam to the base of the cantilever is known, and so the load in the actuator is calculated. Finally, the predicted load in the external load cells is calculated to ensure proper loading. Example calculations taken for the high stress domestic test (Test 4). For this test, the desired stress was at yielding (60 ksi). The depth of the neutral axis has been given as 0.937 in.; this value is normally found by iteration, but this step has been omitted for conciseness.

$$C_C = c \cdot b_{slab} \cdot f'_{pre} \left(\left(\frac{\varepsilon_{cc}}{\varepsilon'_c} \right) - \frac{1}{3} \cdot \left(\frac{\varepsilon_{cc}}{\varepsilon'_c} \right)^2 \right)$$
$$C_C = 0.937 \cdot 36 \cdot 10 \left(\left(\frac{-0.000451}{-0.002} \right) - \frac{1}{3} \cdot \left(\frac{-0.000451}{-0.002} \right)^2 \right) = 70.4\ kip$$

$$\varepsilon_{s1} = \frac{\varepsilon_{cc} \cdot (y_{s1} - (h - c))}{c}$$
$$\varepsilon_{s1} = \frac{-0.000451 \cdot (3.27 - (8.5 - 0.937))}{0.937} = 0.002066$$

$$\varepsilon_{s2} = \frac{\varepsilon_{cc} \cdot (y_{s2} - (h - c))}{c}$$
$$\varepsilon_{s2} = \frac{-0.000451 \cdot (6.50 - (8.5 - 0.937))}{0.937} = 0.000512$$

$$F_{s1} = E \cdot \varepsilon_{s1} \leq F_y$$
$$F_{s1} = 29000 \cdot 0.002066 = 59.51\ ksi \leq 60\ ksi$$

$$F_{s2} = E \cdot \varepsilon_{s1} \leq F_y$$
$$F_{s2} = 29000 \cdot 0.000512 = 14.83\ ksi \leq 60\ ksi$$

Both trusses had the same elastic modulus of 29000 ksi. The yielding stress for the foreign trusses is 75 ksi.

$$T_{s1} = F_{s1} \cdot A_{s1}$$
$$T_{s1} = 59.51 \cdot 0.79 = 47.1\ kip$$

$$T_{s2} = F_{s2} \cdot A_{s2}$$
$$T_{s2} = 14.83 \cdot 1.57 = 23.3\ kip$$

$$0 = C_C + T_{s1} + T_{s2}$$
$$0 = -70.4 + 47.1 + 23.3 = 0 \text{ kip}$$

$$M_{c,na} = c^2 \cdot b_{slab} \cdot f'_{pre}\left(\frac{2}{3} \times \left(\frac{\varepsilon_{cc}}{\varepsilon'_c}\right) - \frac{1}{4} \cdot \left(\frac{\varepsilon_{cc}}{\varepsilon'_c}\right)^2\right)$$
$$M_{c,na} = 0.937^2 \cdot 36 \cdot 10\left(\frac{2}{3} \times \left(\frac{-0.000451}{-0.002}\right) - \frac{1}{4} \cdot \left(\frac{-0.000451}{-0.002}\right)^2\right) = 43.51\ k-in$$

$$M_{c,ca} = M_{c,na} + C_C \cdot \left(c - \frac{h}{2}\right)$$
$$M_{c,ca} = 43.51 + 70.4 \cdot \left(0.937 - \frac{8.5}{2}\right) = 276.59\ k-in$$

$$M_{s1,ca} = T_{s1} \cdot \left(\frac{h}{2} - y_{s1}\right)$$
$$M_{s1,ca} = 47.1 \cdot \left(\frac{8.5}{2} - 3.27\right) = 46.11\ k-in$$

$$M_{s2,ca} = T_{s2} \cdot \left(\frac{h}{2} - y_{s2}\right)$$
$$M_{s2,ca} = 23.3 \cdot \left(\frac{8.5}{2} - 6.50\right) = -52.43\ k-in$$

$$M_{ca} = M_{c,ca} + M_{s1,ca} + M_{s2,ca}$$
$$M_{ca} = 276.6 + 46.1 - 52.43 = 270.28\ k-in$$

$$P_{act} = \frac{2 \cdot (M_{ca} - M_{self})}{L_{arm}}$$
$$P_{act} = \frac{2 \cdot (270.28 - 65.80)}{32} = 12.78\ kip$$

The calculation for the moment due to self-weight, beam, and steel plates has not been included due to the number of geometric variables and steps that would be required which is not the focus of these calculations.

$$P_{lcell} = \frac{P_{act} + P_{beam}}{2}$$
$$P_{lcell} = \frac{12.78 + 1.94}{2} = 7.36\ kip$$

Load in the external load cells for Test 4 is ~7.58 kips. This is within adequate tolerance for the research team.

Appendix C. Concrete Compressive Strength Testing

Test Program:	Test No:	Truss Type:	Concrete Type:	Strength: (psi)
WTPD PCP	I-E-U30	Electro-Welded	Panel	3600
	I-E-U12		Panel	4670
	I-E-U38		Panel	4670
	I-E-U6		Panel	3730
	I-E-U49		Panel	3730
	II-E-U30-#4	Electro-Welded	Panel	6340
	II-E-U38-#4		Panel	7480
	II-E-U49-#4		Panel	7620
	II-E-U49-#5		Panel	10190
	III-E-U6-SC	Electro-Welded	Panel	7570
	III-E-U6-SW		Panel	10990
	III-E-U12-SW		Panel	-
	IV-H-U30	Hand-Welded	Panel	8150
	IV-H-U12		Panel	9770
	IV-H-U38		Panel	7820
	IV-H-U6		Panel	10900
	IV-H-U49		Panel	10900
	V-H-U30-#4	Hand-Welded	Panel	9950
	V-H-U38-#4		Panel	10000
	V-H-U49-#4		Panel	10000
	V-H-U49-#5		Panel	9950
	VI-H-U6-SW-C	Hand-Welded	Panel	8590
	VI-H-U6-SW-T		Panel	8590
	VI-H-U12-SW		Panel	8590
Full-Scale	01	Electro-Welded	Panel	8610*
	01	Electro-Welded	CIP	4890*
	02	Electro-Welded	Panel	8610*
	02	Electro-Welded	CIP	4890*
	03	Hand-Welded	Panel	8610*
	03	Hand-Welded	CIP	4890*
	04	Hand-Welded	Panel	8610*
	04	Hand-Welded	CIP	4890*
	05	Hand-Welded	Panel	8610*
	05	Hand-Welded	CIP	4890*
	06	Hand-Welded	Panel	8610*
	06	Hand-Welded	CIP	4890*

Test Program:	Test No:	Truss Type:	Concrete Type:	Strength: (psi)
	07	Electro-Welded	Panel	8610*
	07	Electro-Welded	CIP	4890*
	08	Electro-Welded	Panel	8610*
	08	Electro-Welded	CIP	4890*
	09	Electro-Welded	Panel	8610*
	09	Electro-Welded	CIP	4890*
	10	Hand-Welded	Panel	8610*
	10	Hand-Welded	CIP	4890*
Fatigue	01	Electro-Welded	Panel	-
	01		CIP	5800*
	02	Hand-Welded	Panel	-
	02		CIP	5800*
	03	Hand-Welded	Panel	10400
	03		CIP	4450
	04	Electro-Welded	Panel	9950
	04		CIP	5000

* These values are taken from 28-day compressive testing